IAHR AIRH

Supported by Spain Water and IWHR, China

IAHR 2017

37th IAHR WORLD CONGRESS

13-18 August, 2017

Kuala Lumpur, Malaysia

# IMPACTS OF POLLUTANTS ON THE ENVIRONMENT

# SECOND ORDER STATISTICS OF A JET IN AMBIENT TURBULENCE

ADRIAN C. H. LAI[(1)], PENG LIU[(2)], ADRIAN W. K. LAW[(3)] & E. ERIC ADAMS[(4)]

[(1)]Singapore-MIT Alliance for Research and Technology Centre, Singapore,
adrian.lai@smart.mit.edu
[(2)]The Hong Kong Polytechnic University, Hong Kong, China
pliuhkg@gmail.com
[(3)]Nanyang Technological University, Singapore,
cwklaw@ntu.edu.sg
[(4)]Massachusetts Institute of Technology, Boston, USA,
eeadams@mit.edu

## ABSTRACT

Jets and plumes can be seen in many natural and man-made environments and processes. The ambient which the jets discharge into is often not quiescent but weakly turbulent, which can somewhat change the mixing characteristics of the jet or plume. As a first step, to better understand the mixing of a jet in ambient turbulence, experiments are carried out in a 2.4 m (long) x 1.2 m (wide) x 2 m (tall) water tank. An array of submerged bilge pumps is placed at one end of the tank; each of them is switched on and off at random time and interval to generate an array of randomly pulsating jets. The pulsating jets are mixed in the tank and generated an approximately isotropic and homogeneous turbulence. A pure jet from a nozzle with diameter D = 1.0 cm discharged at an initial velocity $u_o$ = 0.63 m/s into the ambient turbulence (root-mean-square velocity ≈ 2 cm/s; integral length scale ≈ 9 cm). The instantaneous velocity field of the jet is then measured with Particle Image Velocimetry (PIV) at a distance of 10D – 30D from the source at a frequency of 50Hz. We then extract the velocity and spreading the rate of the jet in ambient turbulence. We also extract the second order statistics, such as the jet axial and shear stresses from the PIV measurements. It is shown that the jet momentum is conserved only if the jet second order statistics are taken into account, which previously have often been overlooked. The conservation of momentum is an important governing equation for predictive jet integral models, and an outline of such model will be given in this paper.

**Keywords:** Jets; plumes; ambient turbulence; second order statistics; integral models.

## 1 INTRODUCTION

Jets and plumes can be seen in many natural and man-made environments and processes. For example, partially treated wastewater is discharged into a marine environment in the form of jets to minimize environmental impact; the heat from humans and equipment in an indoor area gives rise to thermal plumes, which then affect the ventilation of the environment; sediment is often discharged into coastal waters for land reclamation and dredged waste disposal, and a sediment plume will sometimes form in the process. Quite often the ambient which the jets discharged into is not quiescent but weakly turbulent, which will affect the mixing of the jet or plume.

There are several studies in the past which attempted to investigate the effect of ambient turbulence on a jet or plume. Ching et al. (1995) performed experiments on a line plume in a turbulent ambient generated by an oscillating grid. It was found that the ambient turbulence did not significantly affect the plume initially, but the plume was completely destroyed by the turbulence when the plume velocity was somewhat less than twice of the turbulence intensity of the ambient. Law and Ho (2005) carried out their experiments of a non-buoyant round jet in oscillating grid generated turbulence, and similarly found that the jet velocity decayed very abruptly or even broke up close to the grid. The jet break up point was investigated in more detail by Guo et al. (2005) and Cuthbertson et al. (2006) using oscillating grid generated turbulence, but it was found that the break up point of the jet varied greatly depending on the experimental conditions. In all of these experiments, the turbulence generated was not homogeneous, and the size of the tank was not sufficiently large to avoid boundary effects, hence no solid conclusions could be drawn. To improve the homogeneity of the turbulence, Khorsandi et al. (2013) generated ambient turbulence using a random jet array. They then discharged a non-buoyant jet into an approximately homogeneous and isotropic turbulent field of different turbulence intensity. It was observed that the mean axial velocity of the jet was reduced by the turbulence, and the turbulence intensity and jet width were both increased. In all of these studies, it could be observed that the jet mixing characteristics could significantly be altered by the background turbulence, and in extreme cases is even broken up by the turbulence.

Integral models have been developed for predicting the mixing characteristics of a jet, which is important in assessing the impact of the jet to the surrounding environment. Although turbulence can noticeably affect the mixing of a jet and is often present in the ambient, these models do not account for its effects because it was believed that momentum conservation of the jet is not applicable (Khorsandi et al., 2013), and the variation of momentum after the jet interacted with the background turbulence is generally not known. In this paper, in order to better understand the effect of the ambient turbulence for the development of a predictive model, we performed experiments of a jet in ambient turbulence in the laboratory. Both the first and second order statistics of the jet, close and further from the source, were measured using particle image velocimetry (PIV). The conservation of momentum was assessed using the measured data, and finally the possibility of developing a predictive integral model which accounts for the effects of ambient turbulence was explored.

## 2 EXPERIMENTS

Experiments were carried out in a 2.4 m long x 1.2 m wide x 2.0 m deep glass tank. The experimental setup of this study is given in Figure 1. An isotropic turbulent background with low mean flow was generated using an array of bilge pumps mounted on a vertical panel covering an area of 1.2 m x 2.0 m, and programmed to turn on and off randomly (Variano and Cowen, 2008). Experiments were first carried out to characterize the generated turbulence. Then, a region in the tank was chosen with a roughly isotropic and homogeneous turbulent background with root-mean-square (rms) velocity 1.98 cm/s and negligible mean flow. The integral length scale of the region was calculated by integrating the area under the spatial autocorrelation function-distance curve of the rms velocity measured by experiments, and was found to be 8.9 cm. A turbulent jet was then discharged into the field of turbulence from a nozzle with internal diameter 1.0 cm and initial velocity $u_o$ = 63.0 cm/s (flow driven by gravity using a constant head tank and controlled by a rotameter), giving a Reynolds number of 6300. Particle Image Velocimetry (PIV) was used to measure the first and second order mixing characteristics of the jet. A Dantec Dual Power 100-100 Laser, was used to generate pulsed laser sheets of wavelength 532 nm, pulse interval 5000 μs, and energy 2x100 mJ at frequency 50Hz for the PIV measurements. Both the ambient fluid and the jet were seeded with neutrally buoyant particles, which scattered light when the pulsed laser passed through, giving rise to a region of illuminated particles. The particle images were then captured by a synchronized Charge Coupled Device (CCD) camera positioned perpendicularly to the laser sheets. The region of the jet that was captured ranged z = 10D – 30D, where z is the distance from the nozzle, and was within the region in which the jet had not been broken up by the ambient turbulence. A duration of 200 s of images was used for time averaging of the jet mixing characteristics, which had been checked to ensure statistical convergence. It should be noted that the problem of a jet in background turbulence can be divided into different regimes, and for this study we limited our scope to the case of the jet having a smaller length scale and a much larger velocity rather than the ambient turbulence. In all of the experimental runs, a reference case of the same jet discharging into quiescent ambient was also carried out for comparison.

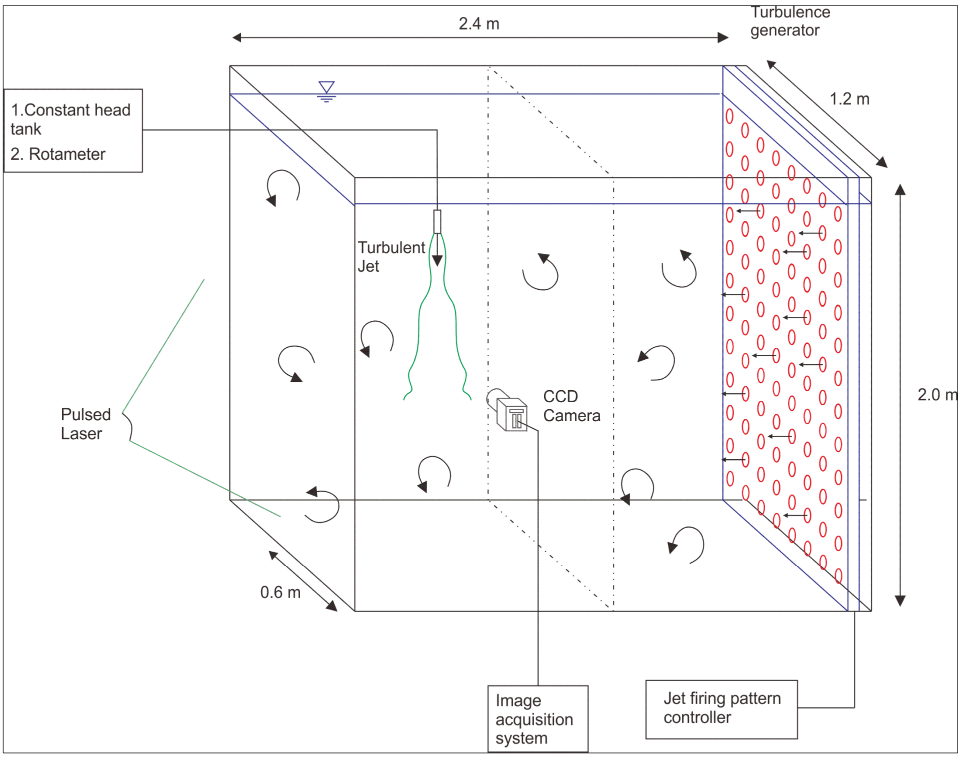


**Figure 1.** Experimental setup of this study.

 

## 3 RESULTS AND ANALYSIS

### 3.1 Centerline velocity and jet half-width

The centerline velocity $u_m$ of a round turbulent jet has been measured by a number of investigators, and its variation along the downstream distance is well established. Figure 2 shows the measured normalized centerline velocity of the jet with and without ambient turbulence. Without ambient turbulence, the best-fit line of the centerline velocity using the experimental data of the self-similar region can be expressed as

$$\frac{u_o}{u_m} = \frac{1}{C}\left(\frac{x}{D} - \frac{x_o}{D}\right) \qquad [1]$$

where, $C$ = 6.3 is an experimental constant and $x_o$/D = 2.9 is the virtual origin of the jet obtained in our experiments. Experimental data of past studies showed that C is typically ranged from 5 – 6.5, and $x_o$/D = 0 – 5.5 depending on the actual experimental conditions, which are also shown in Figure 2. Our data is generally consistent with the past studies, confirming the reliability of the instrumentation of this study.

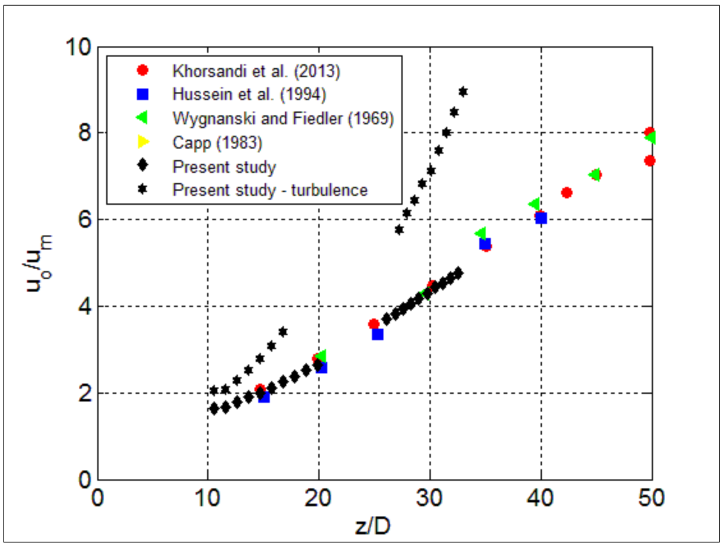


**Figure 2.** The measured normalized jet centerline velocity with or without ambient turbulence.

The results with the effects of ambient turbulence are also given in Figure 2. It can be seen that the centerline velocity of the jet decays faster than it did without ambient turbulence starting from z = 12D. The difference kept widening as the jet went downstream. At z = 30D, the velocity of the jet in turbulence is only about 60% of velocity of the jet in quiescent ambient. This shows that the effect of even a relatively weak turbulence (when the jet velocity is still an order of magnitude larger than the rms velocity of the ambient turbulence) can be significant.

The Gaussian half-width of the jet is defined as where the velocity falls to exp (-1) of the jet centerline velocity assuming a Gaussian velocity profile u(r) = $u_m$exp $(-r^2/b_g^2)$, where r is the radial distance from the jet centerline. The measured half-width with and without ambient turbulence is given in Figure 3. Without the turbulence, the spreading rate $db_g/dz$ is found to be 0.093, which is consistent with the measurements of other investigators of about 0.1. With the effect of ambient turbulence, the spreading rate is increased noticeably to 0.139, which is almost a 50% increase. The increase in spreading was due to the meandering of the jet by the large eddies of the ambient turbulence. The jet structure however is not very much affected being close to the source, since the jet velocity is still much larger than the ambient turbulence; the time averaged velocity profile is still approximately Gaussian for the range of downstream distances investigated.

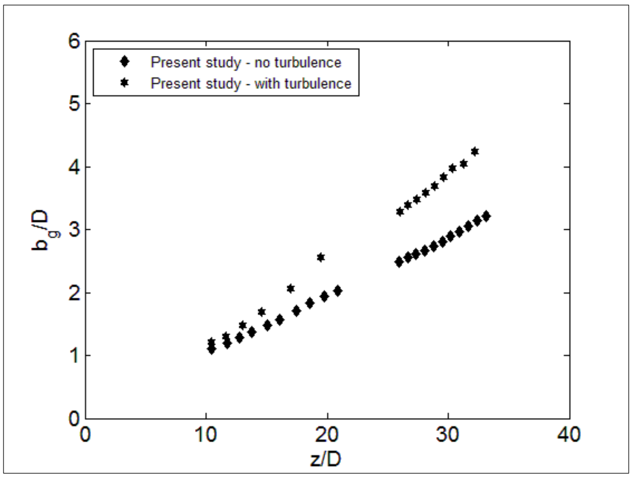


**Figure 3.** The measured Gaussian half-width of the jet with or without ambient turbulence.

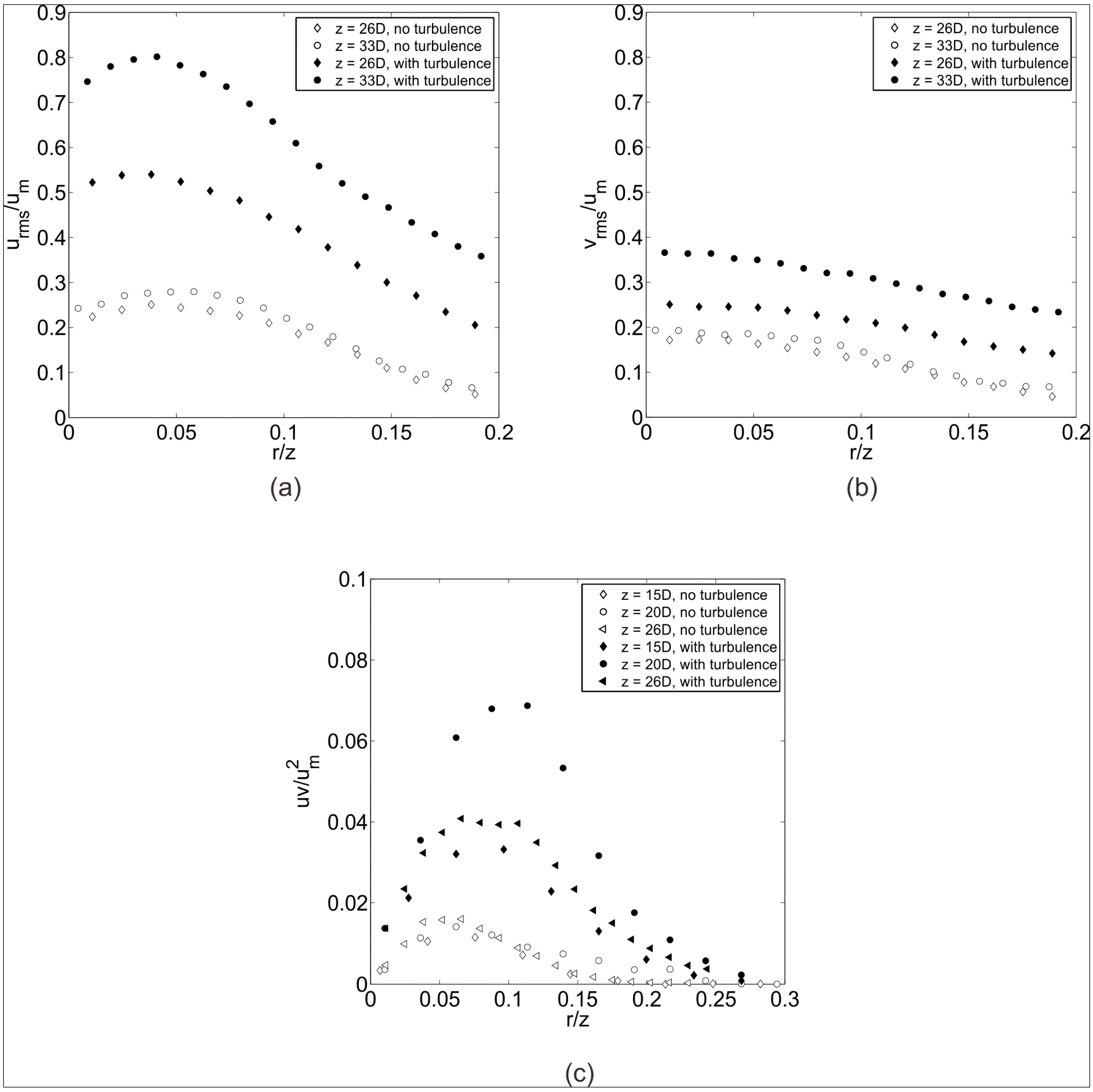


**Figure 4.** The second order statistics of a jet in quiescent ambient and with ambient turbulence. (a) the normalized turbulence intensity of the axial velocity; (b) the normalized turbulence intensity of the radial velocity; (c) the normalized turbulence shear stress.

 

3.2 Second-order statistics

The second-order statistics of a jet in quiescent and ambient turbulence were also obtained and are shown in Figure 4. Figure 4(a) shows the normalized turbulence intensity of the axial velocity of the jet at selected downstream distances. Without ambient turbulence, the turbulence intensity is consistent with the previous measurements of Wang and Law (2000), with a maximum intensity of 0.25, and can be appropriately scaled by the jet centerline velocity. The ambient turbulence can be seen to have significantly affected the turbulence intensity of the axial velocity. At z = 26D, the maximum normalized intensity reached 0.5, and even to 0.8 when the jet reached z = 33D, which is about 3 times that of the jet in quiescent ambient. This suggests that the mixing became more vigorous with the addition of the ambient turbulence. Figure 4(b) shows the normalized turbulence intensity of the radial velocity. The results without ambient turbulence were again consistent with Wang and Law (2000). With the ambient turbulence, the intensity also increases as the mixing becomes more vigorous, but the effect is weaker than that of the axial velocity, with the increase in intensity of only 2 times that of a jet in quiescent ambient at z = 33D. Figure 4(c) shows the shear stress of the jet with and without turbulence.

The ambient turbulence generally causes the shear stress inside the jet to increase, and also somewhat destroys the self-similarity of the profile. It can be seen that, without turbulence, the shear stress can collapse into a single curve by scaling with the jet centerline velocity (squared), which is no longer true with ambient turbulence. An interesting observation is that whether or not there was ambient turbulence, the shear stress external to the jet always fall close to zero. This suggests that the total momentum of the jet should be conserved, as there is no external force acting on the jet.

3.3 Momentum conservation

With ambient turbulence, it has been observed that the momentum integral defined only by the jet's first order mixing characteristics ($u_m$ and $b_g$) is not a constant, but decreases along the downstream distance (Khorsandi et al. 2013). A set of integral equations is difficult to be developed since the variation of the momentum along downstream is not known. The full momentum integral for an axisymmetric jet in homogeneous and isotropic ambient turbulence, which involves both the first and second order statistics of the jet, can be shown to be:

$$\frac{dM}{dz} = 2\pi \frac{d}{dz}\int_0^{\infty}[\overline{u^2} + \overline{u'^2} - \overline{v'^2}]rdr = 0 \qquad [2]$$

When there is no ambient turbulence, the contribution from the second order terms $u_{rms}^2$ and $v_{rms}^2$ to the integral are only of the order of 5% - 10% (Wang and Law 2000), and have negligible effects on the conservation of momentum. However, when there is ambient turbulence, as shown in section 3.2, the contribution from the second order terms increases noticeably, and needs to be included. Using our experimental results, we compare the momentum integral with and without considering the second order terms, and the result is shown in Figure 5. It can be seen that when the second order terms are accounted for, the momentum integral remains as a constant equal to the initial jet momentum. However, if only the first order terms are accounted for, the momentum integral can fall to only 0.5 of the initial jet momentum at z/D = 30, consistent with the finding of Khorsandi et al. (2013). This illustrates the importance to include the second order terms for momentum conservation with ambient turbulence.

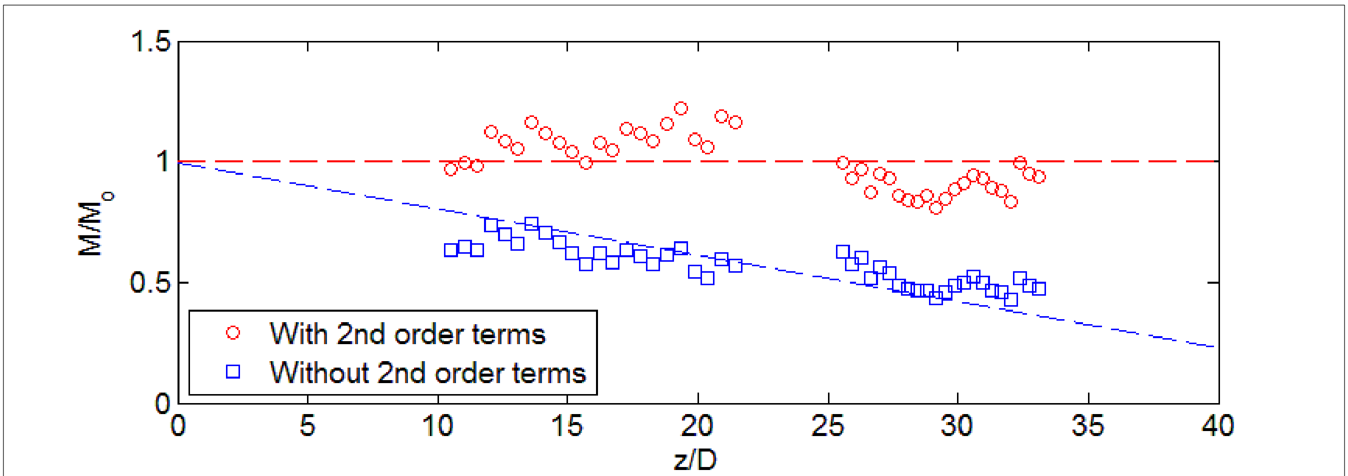


**Figure 5.** The ratio of the momentum integral to the jet initial momentum $M_o$ against downstream distance, with and without accounted for the second order terms.

 

3.4 Outline of an integral model for a jet in ambient turbulence

The conservation of momentum enables an integral model to be developed. An outline of such model will be given in this section. The changes in volume and momentum flux of the jet are given by:

$$\frac{dQ}{dz} = 2\pi\alpha b_g u_m; \quad \frac{dM}{dz} = 0 \qquad [3]$$

respectively. The centerline variables of the jet relate to the fluxes by:

$$u_m = \frac{2M}{k_M Q}; \quad b_g = \sqrt{\frac{k_M Q^2}{2\pi M}}; \quad k_M = 1 + \frac{M_T}{M_M} \qquad [4]$$

In eqs [3] and [4], α = 0.057 is the entrainment coefficient of the jet, and $k_M$ is the ratio of the total momentum with the second order terms ($M_T$) to that with only the first order mean flow terms ($M_M$). The effect of ambient turbulence will be reflected by the increase in $k_M$ over distance, which physically means that more momentum will be transported by the eddies or turbulence, rather than only the mean flow as in the case of quiescent ambient. The best-fit line to the data without second order terms of Figure 5 is calculated to be:

$$\frac{M_M}{M_o} = 1 - 0.0185\left(\frac{z}{D}\right) = \frac{1}{k_M} \qquad [5]$$

This equation can be used to compute the variation of $k_M$ with z. By solving eqs. [3] – [5], the jet mixing characteristics can be predicted. Figure 6 shows the predicted and observed jet centerline velocity decay with and without ambient turbulence. The prediction can be seen to be in reasonable agreement with the measurements, which suggests that the faster decay of the centerline velocity is due to the increasing portion of momentum being transported by the turbulence compared to the mean flow.

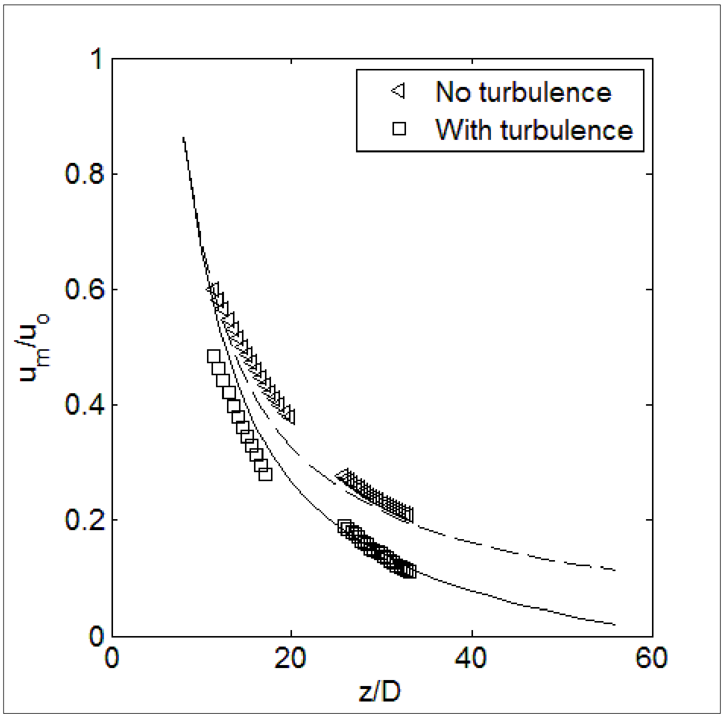


**Figure 6.** The predicted and observed centerline velocity of a jet with and without ambient turbulence. Solid line is the prediction for a jet in turbulence, and dashed line is that for a jet in quiescent ambient.

## 4 CONCLUSION

The effect of ambient turbulence on a turbulent jet is investigated experimentally in the present study. Both the first order and second order mixing characteristics of the jet were measured by PIV. For the first order statistics, the half-width of the jet is observed to be increased by the ambient turbulence. The mean centerline velocity of the jet is also observed to decay much faster than the case of a jet in quiescent ambient. For the second order statistics, the turbulence intensity of both the axial and radial velocity is observed to be increased by the ambient turbulence noticeably. The shear stress is also found to be increased by the ambient turbulence, but outside of the jet it always approaches zero. This is consistent with the theoretical prediction that the shear stress of a homogeneous and isotropic turbulence is zero. Since the shear stress external to the jet is zero, there is no external force acting on the jet, and total momentum will be conserved. Previous investigations showed that the jet momentum would decrease along the downstream distance in ambient turbulence if only the first order statistics were considered, and our PIV results were consistent with this observation. This however does not mean that the momentum conservation is violated; rather we show that the second order statistics also needs to be considered. Then, based on the conservation of momentum, we develops and outlines an integral jet model with the effect of ambient turbulence accounted for by a parameter representing the ratio of the total jet momentum transported by the mean flow to the total momentum. The comparison between model predictions and measurements are in good agreement, showing promise of a good model. A generalized model which also accounts for buoyancy, ambient turbulence length scale and intensity should now be developed.

## ACKNOWLEDGMENTS

This research is supported by the National Research Foundation Singapore under its Campus for Research Excellence and Technological Enterprise program. The Center for Environmental Sensing and Modeling is an interdisciplinary research group of the Singapore MIT Alliance for Research and Technology.

## REFERENCES

Capp, S.P. (1983). Experimental Investigation of the Turbulent Axisymmetric Jet*, Phd Dissertation*. University at Buffalo, SUNY.

Ching, C.Y., Fernando, H.J.S. & Robles, A. (1995). Break Down of Line Plumes in Turbulent Environments. *Journal of Geophysical Research*, 100(C3), 4707–4713.

Cuthbertson, A.J.S., Malcangio, D., Davies, P.A. & Mossa, M. (2006). The Influence of a Localized Region on Turbulence on the Structural Development of a Turbulent, Round, Buoyant Jet. *Fluid Dynamics Research,* 38, 683–698.

Guo, Y., Malcangio, D., Davies, P. A. & Fernando, H.J.S. (2005) A Laboratory Investigation into the Influence of a Localized Region on Turbulence on the Evolution of a Round Turbulent Jet. *Fluid Dynamics Research*, 36, 78–89.

Hussein, H.J., Capp, S.P. & George, W.K. (1994). Velocity-Measurements in a Highreynolds-Number, Momentum-Conserving, Axisymmetrical, Turbulent Jet. *Journal of Fluid Mechanics,* 258, 31–75.

Khorsandi B., Gaskin S. & Mydlarski L. (2013). Effect of Background Turbulence on an Axisymmetric Turbulent Jet. *Journal of Fluid Mech*anics, 736, 250–286.

Law, A.W.K. & Ho, D.W.F. (2005). *Further Investigations on Jet Spreading in Oscillating Grid Turbulence. In Environmental Hydraulics and Sustainable Water Management.* Taylor & Francis Group.

Lee, J.H.W. & Chu, V.H. (2003). *Turbulent Jets and Plumes: A Lagrangian Approach.* Springer, 390.

Variano E.A. & Cowen E.A. (2008). A Random-Jet-Stirred Turbulence Tank. *Journal of Fluid Mech*anics, 604, 1–32.

Wang, H. & Law, A.W.K. (2002). Second-Order Integral Model for a Round Turbulent Buoyant Jet. *Journal of Fluid Mechanics,* 459, 397–428.

Proceedings of the 37th IAHR World Congress
August 13 – 18, 2017, Kuala Lumpur, Malaysia

# MODELING AND MEASURING OF INTERFACES IN SEWER SYSTEMS

KATHARINA TEUBER[1], MARIA GRÜNEBERGER[2], DANEISH DESPOT[3], DIETMAR STEPHAN[4], MATTHIAS BARJENBRUCH[5] & REINHARD HINKELMANN[6]

[1,6] Chair of Water Resources Management and Modeling of Hydrosystems, TU Berlin, Germany,
katharina.teuber@uwi.tu-berlin.de, reinhard.hinkelmann@wahyd.tu-berlin.de
[2,4] Chair of Building Materials and Construction Chemistry, TU Berlin, Germany,
grueneberger@tu-berlin.de, stephan@tu-berlin.de
[3,5] Chair of Urban Water Management, TU Berlin, Germany,
daneish.despot@tu-berlin.de, matthias.barjenbruch@tu-berlin.de

## ABSTRACT

This paper presents the research focusing on interfaces in sewer systems as it is carried out within the DFG Research Training Group Urban Water Interfaces. During its transportation, wastewater in sewer systems undergoes a number of physical, biological and chemical processes and transformations. Under certain conditions such as high detention times, the formation of hydrogen sulfide ($H_2S$) in sewer systems leads to odor in the sewer atmosphere, and after a biogenic oxidation to sulfuric acid ($H_2SO_4$) to corrosion at sewer walls. In 1998, the restoration costs for corroded sewers in Germany has been estimated to be in a range of billions of US $ (Kaempfer and Bernd, 1999). High concentrations of odorous substances in the atmosphere can even lead to death of sewer workers. Within the research training group, three dissertation projects focus on two driving aspects: The enhanced understanding of odor and corrosion mechanisms and the development of a CFD simulation model. In order to gain a deeper understanding, a research pilot plant owned by the Berliner Wasserbetriebe (BWB) is operated. The work of this group enables a deeper in-detail understanding of $H_2S$ formation in sewer systems and can therefore lead to an improvement of existing models as well as to developments that enable a detailed analysis of odor and corrosion problems in sewers.

**Keywords:** Hydrogen sulfide ($H_2S$); Computational Fluid Dynamics (CFD); sewer systems; odor; corrosion.

## 1 INTRODUCTION

Every year damages of sewers due to corrosion cause high costs for sewer maintenance. At the same time, high hydrogen sulfide ($H_2S$) concentrations in the sewer atmosphere are a health risk for sewer workers. The processes leading to odor and corrosion as well as the empirical and conceptual description of these processes have been investigated for more than 70 years (e.g. Parker, 1945; Gilchrist, 1953; Thistlethwayte 1972). However, within the last 20 years a deeper understanding has been gained thanks to the efforts of research groups in Denmark and Australia (Rootsey & Yuan, 2010; Rootsey et al., 2012; Hvitved-Jacobsen et al., 2013). Conceptual model approaches have been developed in order to estimate corrosion risks. The aim of our research is to gain a deeper insight into the influence of small-scale structures such as obstacles and drop structures in sewers, to evaluate the comparability of different laboratory tests for sewer corrosion and to develop a Computational Fluid Dynamics (CFD) simulation model that is able to account for three-dimensional effects.

In order to better understand the processes investigated, the main processes leading to odor and corrosion shall be outlined in the following (see Figure 1). Under anaerobic conditions in sewage, sulfate present in the wastewater can be reduced to sulfide by sulfate-reducing bacteria (SRB) residing in the biofilms on the walls of sewer pipes (Sharma et al., 2008). Sulfide is diffused from the biofilm into the water phase as $H_2S$. Influenced by the pH value and the temperature, different amounts of sulfide as $H_2S$ and bisulfide ion ($HS^-$) are present in the water phase. As described by the air-water equilibrium, emission of $H_2S$ from the water into the air phase can occur. This process depends on factors such as the air and water phase velocities, pH value, temperature and the concentration of oxygen and nitrate. The air-water equilibrium for a volatile compound such as $H_2S$ can be described by Henry's law which describes the relative amount of a volatile compound in the gas phase as a function of its relative occurrence in the water phase under equilibrium conditions and at constant temperature. The temperature dependency of Henry's law can be described by different equations for example, the Van't Hoff equation. The concentration of $H_2S$ in the air phase defines the intensity of odor. Another process taking place at the air - water interface is reaeration which is the transfer of oxygen across the air - water interface. This process is the only way to supply oxygen to the water phase and therefore influences the potential of aerobic and anaerobic processes in the wastewater (Hvitved-Jacobsen et al., 2013).

 

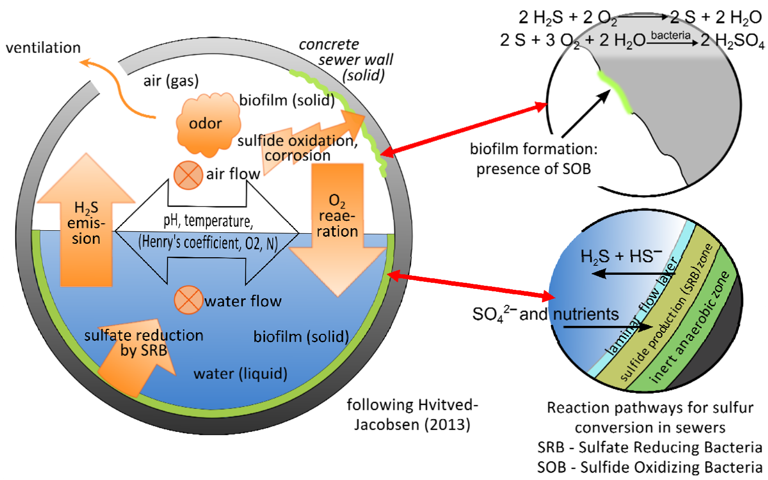


**Figure 1.** Interface processes in sewer systems

At moist concrete pipe walls, $H_2S$ can be oxidized to sulfuric acid ($H_2SO_4$) by aerobic microbial reactions (Hvitved-Jacobsen et al., 2013). Sulfuric acid can lead to the corrosion of the building material of the sewer system, especially of concrete and other cement-bound materials. A combined attack of the cement stone mineral's chemical dissolution and of expansive mineral formation (e.g. gypsum) can result in corrosion rates up to 1 cm $yr^{-1}$ or higher, even for concretes developed for such conditions (Grengg et al., 2015).

The research is carried out in three different sub-projects focusing on different interfaces in sewer systems as well as applying different principles. The projects collaborate in diverse states and exchange results of their investigations. Measurements of $H_2S$ emissions as well as corrosion rates are performed in a research pilot plant. The findings of this research pilot plant are used in order to validate a CFD model describing $H_2S$ emissions across the air - water interface. Corrosion rates are measured on a laboratory scale, a pilot plant scale and on a sewer scale. Different concrete samples are compared and different laboratory tests are compared among each other in order to generalize the test procedure for corrosion at the sewer atmosphere - biofilm - sewer wall (concrete) interface.

In the following, the respective projects are presented. In Section 2, the experiments planned in the research pilot plant is outlined. Section 3 presents the different tests that were performed in order to investigate corrosion rates. An overview of the development of the CFD model is given in Section 4.

## 2 PILOT PLANT INVESTIGATIONS

The research pilot plant provided by Berliner Wasserbetriebe (BWB) facilitates a unique opportunity for performing experiments under realistic but controlled conditions (Figure 2). Here, wastewater from a wastewater pumping station in Berlin is directly fed into the experimental sewer pipes of the research pilot plant. The facility comprises of two pressure sewers with diameters of 100 mm that act as a fermenter, providing anaerobic conditions for the wastewater to reach the required levels of septicity and thus adequate $H_2S$ formation ( Figure ***3***). The wastewater is then conveyed into two corresponding gravity sewers having a length of 25 m each and a diameter of 400mm. The experimental sewer lines are duplicated so that one is used for experiments dealing with containment strategies and the other is used as a reference line for comparison. The concrete samples outlined in Section 3.2 will be placed in both the experimental line and the reference line. Sensor probes are used for continuous measurements in both the liquid and gas phases which can be accessed digitally by storage on a database. Measurement of pH values, temperature, dissolved oxygen (DO), equivalent chemical oxygen demand $(COD)_{eq}$ and equivalent suspended solids ($TS_{eq}$) in the water phase can be made at various sampling points of the pilot plant setup. The scan spectro::lyser$^{TM}$ UV-VIS spectrometer probes (s::can Messtechnik GmbH, Austria) are used for continuous measurement of total dissolved sulfides and nitrate concentration in the liquid phase. As for the gas phase, it is possible to measure the $H_2S$, temperature and relative humidity. The $H_2S$ concentration in the gas phase is measured using the Kemira H2S-Guard$^{TM}$.

The experimental devises are used to further understand the key physicochemical and biochemical processes responsible for odor and corrosion in four different experiments. The experiments will be outlined in the following.

 

**Figure 2.** Research pilot plant

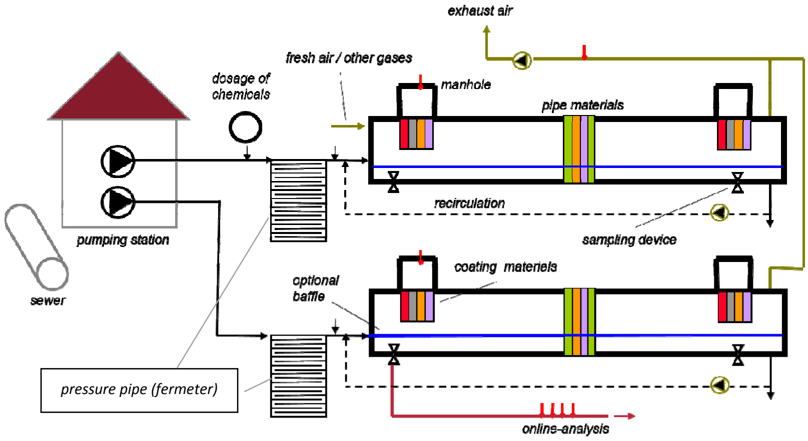


**Figure 3.** Schematic drawing of the research pilot plant

2.1 Sulfide formation in pressure or rising mains

Severe problems are associated with the microbial reduction of sulfate to sulfides in sewer systems, especially in pressurized flows (Hvitved-Jacobsen et al., 1995). Previous studies on sulfide production in pressure mains have resulted in a number of empirical formulas which are still used in praxis and are based on parameters such as biochemical oxygen demand (BOD), chemical oxygen demand (COD), sulfate concentration and temperature etc. (Thistlethwayte, 1972; Boon & Lister, 1975; Pomeroy & Parkhurst, 1977; Hvitved-Jacobsen et al., 1988; Nielsen et al., 1998). In this investigation, the mostly used empirical formulas are to be evaluated using statistical analysis to determine the relationships of the key parameters promoting sulfide formation in pressure sewers, especially sulfide production at the biofilm - wastewater interface. The main goal of the experiments carried out in the first stage is to gain an improved understanding of the conversion processes within the sewer sulfur cycle under anaerobic conditions.

2.2 Elevated $H_2S$ emissions in gravity sewers due to flow interruptions caused by the accumulation of gross solids (debris / solid materials)

Gross solids are of particular concern for sewer systems since they can cause maintenance problems such as blockages and their sedimentation can increase the formation of toxic gases (e.g. sulfide and methane) (Rutz, 2016). The sewer blockage formation process is attributed by materials such as plastics, wet-wipes etc. that enter into gravity sewers. The accumulation of gross solids in gravity sewers can contribute to the emission of $H_2S$ emission in two ways: Due to a disruption of the flow regime, turbulence effects can occur at the surrounding regions of the obstacle and a higher amount of pollutants develops due to the accumulation of sediments (Ashley, 2004).

Until now, the influence of these small-scale structures in the water phase on the emissions has not been quantified. Investigating this relation can lead to better predictions in simulation models as well as better recommendations for countermeasures. The aim of this experiment is to quantify the levels of $H_2S$ emitted into the sewer atmosphere at these hotspots with respect to different hydraulic conditions (Figure 4). The highlighted interface for this experiment is the wastewater - sewer atmosphere interface in gravity sewers.

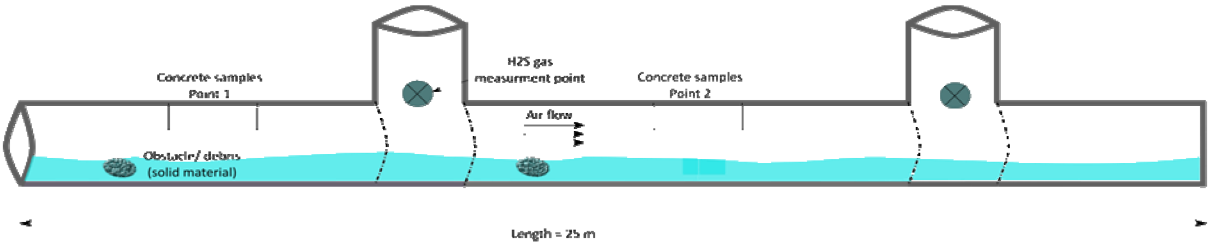


**Figure 4.** Experiment 2 – Elevated $H_2S$ emissions due to gross solids in wastewater

2.3 Investigation of $H_2S$ emissions at drop structures of sewer systems

The release or emission of $H_2S$ to the sewer atmosphere is known to be related to turbulence, pH, temperature and wastewater constituents (Matias et al., 2016). Drop structures found at manholes and transfer zones of sewer networks in sewers lead - similar to small-scale obstacles - to changed flow conditions and therefore facilitate increased $H_2S$ emissions. Previous efforts in understanding the $H_2S$ emission processes at drop structures of sewer systems have been only elaborated in laboratory experiments (i.e. with artificial wastewater) (Matias et al., 2016). Extending these investigations to a pilot scale study can help to verify the laboratory experiments to more realistic conditions (sewer geometry and real wastewater). The knowledge obtained from this investigation provides essential information to predict the effects of sulfides in wastewater infrastructures, and has the potential to substantially improve the design and management approach of sewer systems (Matias et al., 2016).

A drop structure as displayed in **Error! Reference source not found.** will be added to the pilot plant and different parameters will be varied. Again, the $H_2S$ emissions into the sewer atmosphere will be measured. As in the previous experiment, the wastewater - sewer atmosphere interface is the main focus. The tailwater depth will be calculated by using the validated CFD model which will be described in Section 4.

2.4 Impact of countermeasures at hotspots

In a fourth experiment, the impact of different countermeasures at hotspots is being tested. Problems of odor and corrosion in sewers are solved by several methods which have been intensively investigated. Today, most water companies and operators of sewer networks rely on several chemicals which have been proven to be effective in controlling sulfides in sewers. Chemical dosing of oxygen, nitrate, iron salts caustic, free nitrous acids and magnesium hydroxide ($Mg(OH)_2$) are all examples of effective chemicals that are most widely used (Ganigué et al., 2016). Recent research on the application of countermeasures for controlling and reducing sulfides has been carried out on the optimization of the dosage strategies. Two optimization techniques that can be used are: (1) to consider the dosage location and response time for the chemicals to take effect, (2) online dosing control strategies.

The countermeasures to be used in this research project were selected with respect to the optimization techniques mentioned above. The first countermeasure application is based on a new method proposed by Auguet et al. (2015) which studied the effectiveness of downstream nitrite dosage. This study was conducted using a lab-scale sewer system and until now there is no report on its application to field studies. Evaluation of this method under more realistic sewer network conditions can be studied in the pilot plant setup. A further step in this investigation will consider an online dosing control strategy.

The second countermeasure application is based on the online control of $Mg(OH)_2$ dosing. This investigation follows Ganigué et al. (2016) which developed an online control algorithm for the optimized dosing of $Mg(OH)_2$ for sulfide mitigation in sewers. The use of $Mg(OH)_2$ for sulfide control in sewer systems in Germany is undocumented. Therefore, an assessment of this chemical dosing usage will also be made during this investigation.

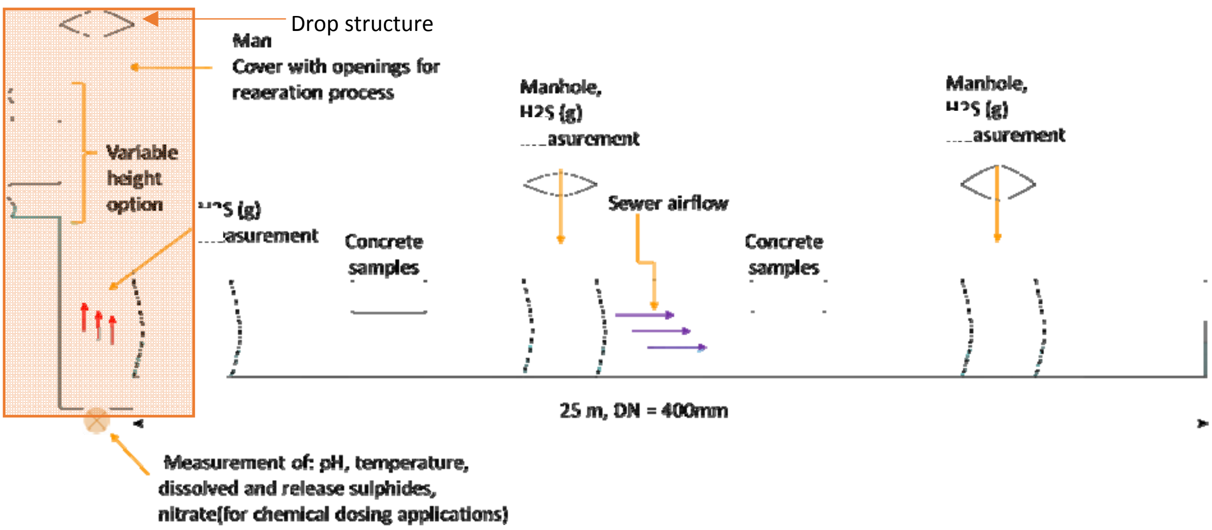


**Figure 5.** Experiment 3 – Pilot plant scale investigation of $H_2S$ emissions at drop structures

## 3 INVESTIGATIONS OF CORROSION PROCESSES IN SEWER AND LABORATORY TESTS

In the second research topic, corrosion processes in sewers at the interfaces of sewer atmosphere, biofilm and concrete sewer is being investigated. The use of concrete with a higher resistance against biogenic sulfuric acid corrosion (BSC) can increase the lifetime of sewer system components and reduce rehabilitation and replacement costs. In the past, much research on the development and testing of high resistance concrete has been done and a large variety of laboratory performance tests for acid resistance of concrete has been developed (e.g. De Belie et al., 2002; Petersen & Lohaus, 2006; Fourie & Alexander, 2007; ÖNORM B4710 appendix K, 2007; Hüttl et al., 2008). Those performance tests have not been experimentally compared. Also, most laboratory performance tests have not been directly compared to BSC in sewer systems by using the same concrete mixtures. Therefore, concrete samples in a sewer pilot plant is compared with the same concrete mixtures tested in four laboratory performance tests developed in Germany and

 

Belgium. The test developed by the Materialprüfungsanstalt (MPA) Berlin-Brandenburg (hereafter MPA Berlin-Brandenburg test) is performed in the original facility of MPA-Berlin-Brandenburg (now Kiwa Berlin) at TU Berlin. The facilities according to the LPI test and the E DIN 19573 appendix B test were installed at TU Berlin for this project. The TAP test is performed in the original facility at the Magnel Laboratory for Concrete Research at Ghent University (Belgium). A special focus lies on the time laps effect of the laboratory performance tests and the corrosion mechanisms and sulfate containing components on the interface between sewer atmosphere, biofilm and concrete.

### 3.1 Concrete and mortar types

Five concrete types with different binders and water/binder value (w/b) are produced to be tested in the pilot plant and in three laboratory performance tests. The different compositions result in varying acid resistances. The use of concrete with low, medium and high acid resistance allow a comprehensive comparison of the pilot plant processes and the laboratory performance tests. Table 1 presents the composition of the five concrete types and their assumed acid resistances. A maximum grain size of 16 mm and the grading curve between A16 and B16 according to DIN (2008) appendix L for all concrete types were chosen.

The laboratory performance test after E DIN 19573 appendix B (E DIN, 2013) requires mortar samples. The binder composition and w/b values of the five mortar types are equivalent to the concrete types. For each mortar type 450 g binder and 1350 g CEN-Reference-Sand DIN (2005) are used.

### 3.2 Pilot plant acid resistance tests

The concrete samples are positioned in the concrete sample point 1 (see Figure 4) of both gravity pipes in the pilot plant. Six cuboids per concrete type are stored in each gravity pipe. The cuboids' edge lengths are 150 mm x 100 mm x 40 mm. As a reference sample, another six cuboids per concrete type are stored over water in a closed container at 20°C. One cuboid per concrete type is taken from each gravity pipe of the pilot plant every six months. Also, one cuboid per concrete mixture of the reference samples is being taken for analysis every six months. Results are evaluated using the parameters monitored in the pilot plant, such as $H_2S$ concentration in the sewer gas phase.

**Table 1.** Composition and assumed acid resistances of concrete types used for acid resistance tests. Cement types are classified after DIN (2011). MS: microsilica, FA: hard coal fly ash.

| **Concrete type** | **1** | **2** | **3** | **4** | **5** |
|---|---|---|---|---|---|
| Type of binder | white CEM I 42.5 R (dw) | CEM I 42.5 R | CEM III B 42.5 N-NA | CEM III B 42.5 N-NA | CEM I 42.5 R – MS – FA |
| $m_{binder}/V_{concrete}$ [kg/m$^3$] | 360 | 360 | 360 | 373 | 350* |
| w/b value | 0.45 | 0.45 | 0.45 | 0.35 | 0.42 |
| assumed acid resistance | very low | low | medium | high | high |

* Cement 270 kg/m$^3$; microsilica 27 kg/m$^3$; hard coal fly ash 53 kg/m$^3$.

### 3.3 Laboratory performance tests

All concrete types are analyzed using the MPA Berlin-Brandenburg (Hüttl et al., 2008), the LPI (Petersen & Lohaus, 2006), and the TAP test (De Belie et al., 2002). All mortar types are examined according to E DIN (2013). An overview of the four tests is given in Table 2.

### 3.4 Analysis of concrete and mortar specimens

Concrete and mortar specimens from the pilot plant and the laboratory performance tests are analyzed with reflected-light microscopy of polished samples and polarizing light microscopy of thin sections to measure the damage depth. In addition, scanning electron microscopy with energy-dispersive X-ray spectroscopy is performed. Powder X-ray diffraction is done to characterize minerals formed during the experiments. Micro X-ray fluorescence spectroscopy is performed to produce element maps of polished samples and to measure the damage depth. The proton consumption is calculated using the titrated acid in E DIN 19573 appendix B test. The concrete degradation and surface roughness is measured by laser measurements during the TAP test (see De Belie et al., 2002).

Since for all tests the same concrete types are being used, the corrosion in the pilot plant and in the laboratory performance tests can be directly compared. New information is being gained on the applicability of laboratory acid resistance tests concerning sewer systems. The time lapse effect of the laboratory performance test is estimated. Thereby more detailed insights are gained concerning corrosion mechanisms caused by BSC.

 

**Table 2.** Testing parameters of the four laboratory performance tests.

| Testing parameter | MPA Berlin-Brandenburg test | LPI-test | E DIN 19537 appendix B test (bath test) | TAP test |
|---|---|---|---|---|
| ***Test specimen:*** | | | | |
| Type | concrete | concrete or mortar | mortar | concrete |
| Geometry | 4x15 cuboids: 150 mm x 100 mm x 40 mm | 2x4 concrete cuboids: 70 mm x 35 mm x 150 mm 2x6 mortar cuboids: 40 mm x 20 mm x 160 mm | 5 cuboids: 40 mm x 40 mm x 80 mm | cylinder: d = 270 mm, h= 70 mm |
| Testing age | 28 days* | 28 days* | 28 days* | 28 days* |
| *Testing medium* | | | | |
| Type | sulfuric acid | sulfuric acid* | sulfuric acid | sulfuric acid or acetic/lactic acid mix |
| Concentration | pH 3.5 | pH 3.0* | pH 4.0 | sulfuric acid: pH 0.8 – 1.0 acetic/lactic acid mix: pH 2.0 – 2.2 |
| ***Performance*** | | | | |
| Test duration | 12 weeks | 12 weeks* | 4,000 h | dependent on testing procedure |
| Testing facility | 5 tanks (45 l), 1 reservoir tank (80 l) | tank (13 l) | tank (4 l) | tank (2 l) |
| Acid renewal | every 2 weeks | every week* | every 1,000 h | after every attack cycle |
| Constant pH | yes (automatic titration) | yes (automatic titration) | yes (automatic titration) | no |
| Mixing of medium | circulation of medium | rotation of sample in acid tank (150 s per revolution) | magnetic stirrer | Rotation of sample in acid tank (1.04 revolution per h) |
| Abrasion | manual brushing of a part of the samples once per week | automatic brushing of a part of the samples every 150 s | none | automatic brushing after every attack cycle |
| ***Evaluation*** | | | | |
| Analysis | thin-section polarizing light microscopy and mass loss | thin-section polarizing light microscopy | proton consumption during the test | laser measurements |
| Assessment criterion | measured damage depth in comparison with reference concrete | measured damage depth | calculated damage depth | concrete degradation, surface roughness |

*Parameters can be changed according to the behavior and application of the building material.

## 4 DEVELOPMENT OF A THREE-PHASE CFD SIMULATION MODEL

In the third project, a CFD simulation model is developed in order to numerically describe formations across the wastewater - sewer atmosphere interface. So far, existing model approaches (Sharma et al., 2008; Hvitved-Jacobsen et al., 2013) are one-dimensional approaches, neglecting three-dimensional flow effects in sewage and air. The three-dimensional model approach is able to verify these assumptions and can be an extension of these models in respect to a more detailed analysis of hydraulic aspects.

The work carried out in this research divides in three different parts. The first step is a validation of the water phase described by the numerical model concerning different hydraulic conditions. Results obtained within this working package is presented in Section 4.2. Because of the fact that sewer systems are focused on in the work of this group of researchers, the consideration especially focuses on flow in closed conduits. After the first validation step is completed, the model is used to support the experimental work in the pilot plant in hydraulic questions. Possible applications are the estimation of the tailwater depth in the experiment outlined in Section 2.3. The two remaining working steps are the validation of the air phase behavior in closed systems as well as the implementation of transport as well as mass transfer processes depending on factors such as Henry's law in order to describe $H_2S$ formations. At a later stage, the model could even be extended to describe corrosion effects at the atmosphere - biofilm - sewer wall (concrete) interface and interact with the research project outlined in Section 3.

### 4.1 Numerical model

Surface water flow is calculated by using the two-phase flow solver interFoam based on a volume of fluid (VOF) approach for one- and two-phase flows as it is implemented in the open source model OpenFOAM. Both phases are considered as one fluid with rapidly changing fluid properties, therefore one set of Navier-Stokes-equations is solved. The phases are distinguished by an additional transport equation for the volume fraction which is used as a marker to describe the distribution of the phases throughout the domain. The equations can be formulated as follows (Rusche, 2002):

 

Mass conservation equation:

$$\nabla \cdot \vec{U} = 0 \qquad [1]$$

Momentum conservation equation:

$$\frac{\partial \rho \vec{U}}{\partial t} + \nabla \cdot (\rho \vec{U}\vec{U}) = -\nabla prgh + \nabla \cdot (\mu \nabla \vec{U}) + (\nabla \vec{U}) \cdot \nabla \mu - \vec{g} \cdot \vec{x} \nabla \rho \qquad [2]$$

where prgh is a specific pressure, describing the static pressure minus hydrostatic pressure:

$$prgh = p - \rho g h \qquad [3]$$

Volume of Fluid equation:

$$\frac{\partial \alpha}{\partial t} + \nabla \cdot (\alpha \vec{U}) + \nabla \cdot ((1-\alpha) U_r \alpha) = 0 \qquad [4]$$

with the following parameters:

$$\rho = \alpha \rho_w + \rho_a (1-\alpha) \qquad [5]$$

$$\mu = \alpha \mu_w + \mu_a (1-\alpha) \qquad [6]$$

where $\vec{U}$ is the velocity field [m/s]; ρ is the density [m³/s]; t is time [s]; p is pressure [Pa]; μ is dynamic viscosity [Ns/m²]; $\vec{g}$ is acceleration vector due to gravity [m/s²]; $\vec{x}$ is a spatial position vector [m]; α is volume fraction or indicator function [-]; $U_r$ is the relative velocity between the phases [m/s]; the subscripts a and w denote different fluids air and water.
The indicator function α is defined as:

$$\alpha = \begin{cases} 1 & \text{fluid water} \\ 0 < \alpha < 1 & \text{transitional region} \\ 0 & \text{fluid air} \end{cases} \qquad [7]$$

The water surface is considered as the area described by a volume fraction α = 0.5. For single-phase test cases the volume fraction α is 1 and constant over the whole domain and during the simulation time.

A special definition of boundary conditions for two-phase flows is necessary in order to obtain stability of simulations in closed ducts. The upper and lower walls are defined as no-slip conditions. Depending on the fact whether the simulations are two-or three-dimensional, the sidewalls are defined as no-slip conditions for three-dimensional cases and as empty boundary conditions for two-dimensional cases. The empty boundary condition in OpenFOAM is a special boundary condition for two-dimensional model setups. The definition of inlet and outlet is displayed in Figure 6. The inlet is divided in two parts, an inlet for the air phase, where a total pressure is defined. The second part is the inlet for the water phase, defined by a fixed discharge or flow velocity. At the outlet, a constant pressure is defined leading to a free outflow of the water without definition of a certain upstream water level. This upstream water level is achieved by adding a weir structure in the proximity of the outlet to the model geometry. This type of outlet boundary condition has originally been outlined for open systems with top atmospheric boundaries by Bayón-Barrachina & López-Jiménez (2015). For a more detailed description of further properties, such as the chosen boundary conditions for each test case and the turbulence models, the reader is referred to Teuber et al. (2017).

4.2 Validation of the water phase behavior

In order to secure the applicability of the chosen numerical model, flow properties such as the water flow velocity and the water surface behavior described by the VOF approach have been validated (Teuber et al. 2016; 2017).

 

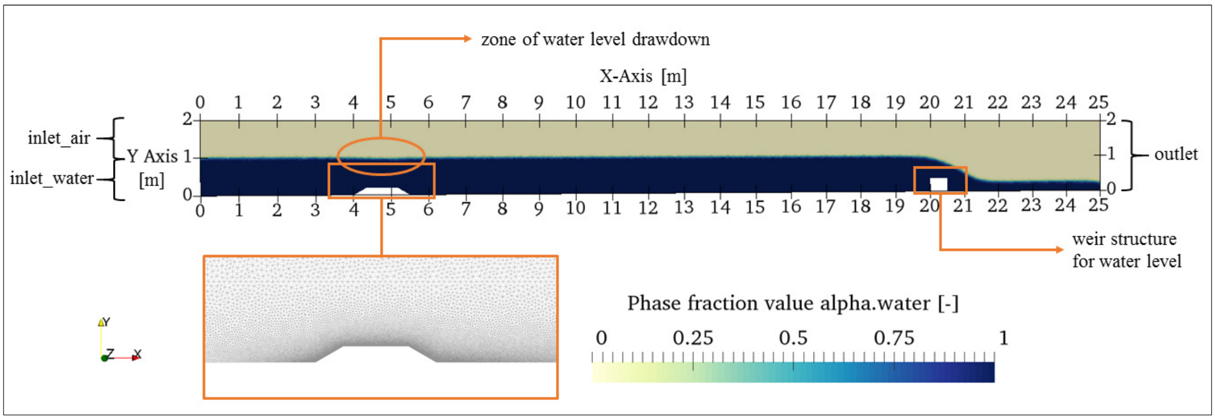


**Figure 6.** Model domain of water surface validation case

First, a validation of the water velocity was performed by using experimental results of single-phase water flow over a ground sill in a closed duct by Almeida et al. (1993). Different Reynolds averaged (RANS) turbulence models and Large Eddy Simulations (LES) were compared as well. The RANS models investigated were the Standard k-ε (Launder & Sharma, 1974), k-ω (Wilcox, 1988) and k-ω Shear Stress Transport (SST) model (Menter, 1993, 1994). As the subgrid-scale model for the LES simulations, the Smagorinsky model (Smagorinsky, 1963) was chosen. The results led to the conclusion that the chosen RANS models as well as the LES simulations lead to a good approximation of the experimental results. Due to the nature of the different turbulence models, the LES simulations were able to capture fluctuations in the flow velocity which can be of interest for some application areas. With this advantage of LES comes the disadvantage of a higher necessary mesh resolution which leads to significantly increased computation times.

In order to validate the behavior of the water surface, two-phase flow over a ground sill was simulated. The basic setup of the model domain is displayed in Figure 6. Simulations were performed for different two- and three-dimensional model setups with variations concerning the structure of the sill, discharge, water level and the flow regime. Since fluctuations of the flow velocity were of minor interest, the k-ε turbulence model was used. The water level drawdown was compared to analytical solutions obtained by using continuity and Bernoulli's equation. A detailed discussion of the results can be found in Teuber et al. (2016). Overall, the results showed a good agreement of the simulations with measured water velocities and a reasonable behavior of the water - air interface. However, the numerically computed water level drawdown was smaller than the analytically calculated drawdown. Explanation can be found in the treatment of single losses. The three-dimensional CFD model is able to account for single losses caused by the structure of the sill whereas the analytical solution is a one-dimensional solution that neglects single losses.

In a last step, simulations have been performed in a complex sewer geometry described in Bayón-Barrachina et al. (2015), proving the applicability of the simulations under demanding hydraulic conditions. This geometry contains different hydraulic structures such as weirs, different flow regimes and a hydraulic jump. The simulation results were compared to experimental measurements carried out on a 1:20 scale model as well as to CFD simulations previously performed by Bayón-Barrachina et al. (2015) by using a different model setup (open system, without upper wall). A detailed analysis will be published in Teuber et al. (2017). The results showed a good agreement between both the existing simulation model as well as the experimental results and lead to the conclusion, that the solver is applicable to complex hydraulic cases in closed conduits such as sewer systems.

Overall, the simulations performed show that the solver is able to simulate different hydraulic cases. The chosen turbulence models were comparable in their accuracy, however, the LES simulations were able to account for fluctuations in the velocity under increased computational effort. A second validation step will be to analyze the accuracy of the air-phase behavior.

## 5 CONCLUSIONS

In this paper, we present the research as it is carried out in the sewer interfaces group within the DFG Research Training Group Urban Water Interfaces. Different sub-projects focus on a deeper understanding of $H_2S$ formations at and across the wastewater - biofilm, the wastewater - sewer atmosphere and the sewer atmosphere - biofilm - sewer wall (concrete) interface.

The first project conducts experimental investigations on a pilot plant in order to gain an enhanced understanding of sulfide formations in pressure mains as well as on investigating the influence of flow interruptions caused by gross solids and drop structures. Furthermore, the effects of different countermeasures at hotspots are analyzed. In another project, this research pilot plant is used in order to investigate BSC in sewers. The main goal is to investigate different laboratory performance tests and to compare them among each other as well as to concrete probes installed in the pilot plant. In the third project, a CFD simulation model is being developed in order to describe $H_2S$ emissions across the wastewater - sewer atmosphere interface. First results show, that the model is able to accurately describe the behavior of the water phase. Therefore, the model can be used in order to estimate different hydraulic properties within the sewer pilot plant. On the other hand, results concerning $H_2S$ formations obtained by the sewer pilot plant can be used to validate extended CFD model.

The added value of the work carried out by this group lies in the detailed insight into $H_2S$ formation processes and sensitivity analyses that can be carried out. The influence of gross solids or drop structures on the $H_2S$ release can be investigated on a pilot plant scale. The validated CFD model can be used to investigate the effect of measures such as i.e. changed discharges or ventilation measures on $H_2S$ emissions. These findings can be integrated into existing model approaches in order to improve predictions. The development of a CFD model can generalize the findings of the investigations in the pilot plant to different conditions. The detailed analysis of different laboratory performance tests helps to generalize the development of acid-resistant concrete.

## ACKNOWLEDGEMENTS

The funding provided by the German Research Foundation (DFG) within the Research Training Group *Urban Water Interfaces* is gratefully acknowledged. Parts of the simulations were computed on the supercomputers of Norddeutscher Verbund für Hoch- und Höchstleistungsrechnen in Berlin. The sewer pilot plant is provided by the Berliner Wasserbetriebe (BWB). We also thank the Kompetenzzentrum Wasser Berlin for providing scan probes, the Kiwa (Berlin) for providing the apparatus for the MPA Berlin-Brandenburg test, and the Magnel Laboratory of the University Ghent for providing the TAP apparatus.

## REFERENCES

Almeida, G., Durao, D. & Heitor, M. (1993). Wake Flows Behind Two-Dimensional Model Hill. *Experimental Thermal and Fluid Science*, 7(1), 87-101.

Ashley, R.M. (2004). *Solids in Sewers: Characteristics, Effects and Control of Sewer Solids and Associated Pollutants.* IWA Publishing, Scientific and Technical Report, 3, 164-207.

Auguet, O., Pijuan, M., Guasch-Balcells, H., Borrego, C.M. & Gutierrez, O. (2015). Implications of Downstream Nitrate Dosage in Anaerobic Sewers to Control Sulfide and Methane Emissions. *Water Research,* 68, 522–532.

Bayón-Barrachina, A. & López-Jiménez, P.A. (2015). Numerical Analysis of Hydraulic Jumps Using Openfoam. *Journal of Hydroinformatics*, 4(17), 662-677.

Bayón-Barrachina, A., Vallés-Morán, F.J. & López-Jiménez, P.A. (2015). Numerical Analysis and Validation of South Valencia Sewage Collection System Diversion. *36th IAHR World Congress*, The Hague, The Netherlands.

Boon, A.G., & Lister, A.R. (1975). Formation of Sulphide in Rising Main Sewers and its Prevention by Injection of Oxygen. *Progress in Water Technology*, 7(2), 289-300.

De Belie, N., Monteny, J. & Taerwe, L. (2002). Apparatus for Accelerated Degradation Testing of Concrete Specimens. *Material Structure*, 35(7), 427-433.

DIN (2008). *Tragwerke Aus Beton, Stahlbeton Und Spannbeton – Teil 2: Beton – Festlegung, Eigenschaften, Herstellung Und Konformität – Anwendungsregeln Zu DIN EN 206-1*.

DIN (2005). *Prüfverfahren Für Zement – Teil 1: Bestimmung Der Festigkeit*; Deutsche Fassung EN 196-1:2005.

DIN (2011). *Zement – Teil 1: Zusammensetzung, Anforderungen Und Konformitätskriterien Von Normalzement*; Deutsche Fassung EN 197-1:2011.

E DIN (2013). *Mörtel Für Neubau Und Sanierung Von Entwässerungssystemen Außerhalb Von Gebäuden.*

Fourie, C.W. & Alexander, M.G. (2007). A Dynamic Hydrochloric Acid Test for Evaluating Acid Resistance of Sewer Pipe Concrete. *RILEM Workshop on Performance of Cement-Based Materials in Aggressive Aqueous Environments – Characterisation, Modelling, Test Methods and Engineering Aspects*, Ghent, Belgium, 98-107.

Ganigué, R., Jiang, G., Sharma, K., Chen, J., Vuong, L. & Yuan, Z. (2016). Online Control of Magnesium Hydroxide Dosing for Sulfide Mitigation in Sewers. Algorithm Development, Simulation Analysis, And Field Validation. *Journal of Environmental Engineering*, 142(12), 04016069.

Gilchrist, F.M.C. (1953). Microbiological Studies of the Corrosion of Concrete Sewers by Sulphuric Acid Producing Bacteria. *South African Chemist*, 7(8), 214–215.

Grengg, C., Mittermayr, F., Baldermann, A., Böttcher, M.E., Leis, A., Koraimann, G., Grunert, P. & Dietzel, M. (2015). Microbiologically Induced Concrete Corrosion: A Case Study from a Combined Sewer Network. *Journal of Cement and Concrete Research*, 77, 16-25.

Hüttl, R. (2008). Flugaschenbetone Mit Erhöhtem Säurewiderstand Im Kühlturm- Und Wasserbau – *Historie, Stand Der Technik Und Bewertungskriterien*. BVK/VGB Fachtagung, Frankfurt A.M., Germany.

 

Hvitved-Jacobsen, T., Jütte, B., Nielsen, P.H., & Jensen, N.A. (1988). Hydrogen Sulphide Control in Municipal Sewers. *Pretreatment in Chemical Water and Wastewater Treatment*. Springer Berlin Heidelberg, 239-247. DOI: 10.1007/978-3-642-73819-7_19

Hvitved-Jacobsen, T., Raunkjær, K. & Nielsen, P.H. (1995). Volatile Fatty Acids and Sulfide in Pressure Mains. *Water Science and Technology*, 31(7), 169-179.

Hvitved-Jacobsen, T., Vollertsen, J. & Nielsen, A.H. (2013). *Sewer Processes: Microbial and Chemical Process Engineering of Sewer Networks* (Vol. 2). CRC Press.

Kaempfer, W. & Berndt, M. (1999). Estimation of Service Life of Concrete Pipes in Sewer Networks. *Durability of Building Materials and Components*, 1, 36-45.

Launder, B.E. & Sharma, B.I. (1974). Application of The Energy Dissipation Model of Turbulence to the Calculation of Flow Near a Spinning Disc. *Letters in Heat and Mass Transfer*, 1(2), 131-137.

Matias, N.M., Nielsen, A.H., Vollertsen, J., Ferreira, F. & Matos, J.S. (2016). Reaeration and Hydrogen Sulfide Release at Drop Structures. *8th International Conference on Sewer Processes and Networks*, Rotterdam, The Netherlands.

Menter, F.R. (1993). Zonal Two-Equation K-Ω Turbulence Models for Aerodynamic Flows. *AIAA 24th Fluid Dynamics Conference*, Orlando, USA.

Menter, F.R. (1994). Two-Equation Eddy-Viscosity Turbulence Models for Engineering Applications. *AIAA Journal*, 32 (8), 1598-1605.

Nielsen, P.H., Raunkjær, K., & Hvitved-Jacobsen, T. (1998). Sulfide Production and Wastewater Quality in Pressure Mains. *Water Science And Technology*, 37(1), 97-104.

ÖNORM B 4710-1:2007-10 (2007). *Beton – Teil 1: Festlegung, Herstellung, Verwendung Und Konformitätsnachweis* (Regeln Zur Umsetzung Der ÖNORM EM 206-1 Für Normal- Und Schwerbeton).

Parker, C. (1945). The Corrosion of Concrete. 1. The Isolation of A Species of Bacterium Associated with the Corrosion of Concrete Exposed To Atmospheres Containing Hydrogen Sulphide. *The Australian Journal of Experimental Biology and Medical Science*, 23(3), 14-17.

Petersen, L. & Lohaus, L. (2006). Entwicklung Eines Prüfstandes Für Parameterstudien Zum Säurewiderstand Von Hochleistungsbetonen. *Internationale Baustofftagung Ibausil*, Weimar, Germany, 2 0637-2 0644.

Pomeroy, R.D. & Parkhurst, J.D. (1977). Forecasting of Sulfide Buildup Rates in Sewers. *Progress in Water Technology*, 9(3), 621.

Rootsey, R. & Yuan, Z. (2010). New Insights into Sewer Odour and Corrosion. *6th International Conference on Sewer Processes and Networks*, Queensland, Australia.

Rootsey, R., Melchers, R., Stuetz, R., Keller, J. & Yuan, Z. (2012). Taking Control of Odours and Corrosion in Sewers. *Australia's National Water Conference and Exhibition*, Sydney, Australia.

Rusche, H. (2002). Computational Fluid Dynamics of Dispersed Two-Phase Flows at High Phase Fractions, Phd Thesis. Imperial College London, University of London.

Rutz, M. (2016). Laboratory Investigation of Physical Disintegration of Gross Solids in the Sewer, Msc. Thesis. ETH Zürich.

Sharma, K., De Haas, D., Corrie, S., O'Halloran, K., Keller, J. & Yuan, Z. (2008). Predicting Hydrogen Sulfide Formation in Sewers: A New Model. *Journal of The Australian Water Association*, 35(2), 132-137.

Smagorinsky, J. (1963). General Circulation Experiments with the Primitive Equations: I. The Basic Experiment*. *Monthly Weather Review*, 91(3), 99-164.

Teuber, K., Broecker, T., Barjenbruch, M. & Hinkelmann, R. (2016). High-Resolution Numerical Analysis of Flow Over a Ground Sill Using Openfoam. *Proceedings of the 12th International Conference on Hydroscience And Engineering (ICHE)*, Tainan, Taiwan.

Teuber, K. Broecker, T., Bayón-Barrachina, A., Nützmann, G. & Hinkelmann, R. (2017). CFD-Modelling of Free-Surface Flows in Closed Conduits Using the Volume of Fluid Approach. *Journal of Hydraulic Research*, *Under Submission.*

Thistlethwayte, D.K.B. (1972). *The Control of Sulfides in Sewerage Systems*. Ann Arbor Science Publishers, Inc. Mich., 173

Wilcox, D.C. (1988). Re-Assessment of the Scale-Determining Equation for Advanced Turbulence Models. *AIAA Journal*, 26(11), 1299-1310.

Proceedings of the 37th IAHR World Congress
August 13 – 18, 2017, Kuala Lumpur, Malaysia

# PRELIMINARY ENVIRONMENTAL PROFILE STUDY OF INANAM RIVER CATCHMENT, SABAH

KOK HOU KU[1], TANIA GOLINGI[2],CHING SIN LIM[3], YABI YANGKAT[4] & VITALIS MODUYING[5]

[1,2,3] DHI Water and Environment (M) SdnBhd, Kota Kinabalu, Malaysia,
kkh@dhigroup.com; tag@dhigroup.com; csl@dhigroup.com
[4, 5]Environment Protection Department Sabah, Kota Kinabalu, Malaysia,
yabi.yangkat@sabah.gov.my; vitalis.moduying@sabah.gov.my

## ABSTRACT

This paper describes a preliminary environmental profile study for the Inanam catchment in Sabah, Malaysia. The study includes the identification an inventory of pollution sources, determination of catchment pollution loads, assessment of ecological and socio-economic sensitive receptors, determination of water quality objectives and assessment of water quality conditions under various conditions. To support the environmental profile study, a water quality model that simulates hydrologic, hydrodynamic and water quality processes is developed and used to assess and establish the existing water quality condition of the relevant reaches of Inanam, Likas and Darau Rivers. The result of the study shows that most of the Inanam River falls within Class II water quality under the National Water Quality Standards for Malaysia, however the downstream areas near the river mouth are Class III. Likas River is presently a Class III river, deteriorating to Class IV in the lower reaches. The water quality in Darau River currently falls within Class III, although nearing Class II. These results reflect the major land use patterns, where the rivers within the forested and undeveloped catchments are in good condition, while conditions deteriorate rapidly downstream as a result of runoff from industrial, commercial and residential areas. Future catchment development scenarios and various action plans for pollution prevention measures are established and tested in the model to assess their effectiveness in terms of a Water Quality Index (WQI). Pollution prevention measures tested include point loads discharge complied with either Standard A or B, together with non-point loads control, connecting domestic waste to sewer and treated, and point sources are treated to Standard B compliance. The modelling result indicates that the compliance to either Standard A or B together with non-point loads control measure shows a significant positive impact on the overall water quality within the study area.

**Keywords:** Water Quality; Water Pollution; Environmental Profile; Pollution Prevention.

## 1 INTRODUCTION

The Inanam catchment is located in the north-east of Kota Kinabalu, Sabah and comprises the Inanam, Likas and Darau Rivers. The Inanam catchment has been undergoing rapid urbanization development in the recent years with expansion of residential, commercial and industrial areas into previous forest and open space areas. This has contributed further to the deterioration in the water quality of the major rivers and drainage systems within the catchment area. The water quality in Likas Bay at the mouth of the Inanam River is subsequently affected.

The overall Inanam catchment area is approximately 95 km$^2$, and can be sub-divided into three main (sub-)catchments, namely Inanam (50 km$^2$), Likas (25 km$^2$) and Darau (20 km$^2$). Inanam River originates from the Crocker Range to the east and runs westward through Kg. Kiansam then through Inanam town. In the upper and middle reaches, Inanam River is a natural river. It then turns into a man-made channel at the confluence with Kilabu River near Kg. Tatahan and Kg. Pamatadan. Further downstream, Inanam River joins Likas River (also a man-made channel at this location), near Taman Kemajuan before joining Darau River at the Likas river bridge near the rivermouth before discharging into the Likas bay. In the upper reaches, the Inanam sub-catchment is mostly rural, with batches of agricultural land. In the lower reaches, the sub-catchment is urbanised with a mixture of residential, commercial and industrial areas.

The Likas sub-catchment, about half the size of the Inanam catchment, is the most urbanized sub-catchment within the study area. Likas River is essentially a man-made channel fed upstream by Shantung Hill and "Bukit Padang", both located in the Southern part of the catchment. The channel runs to the north through several residential developments. Further downstream, the land use changes with Likas River going through several industrial areas before converging with Inanam River.

The Darau sub-catchment is currently undergoing significant developments which include residential and commercial developments.

 

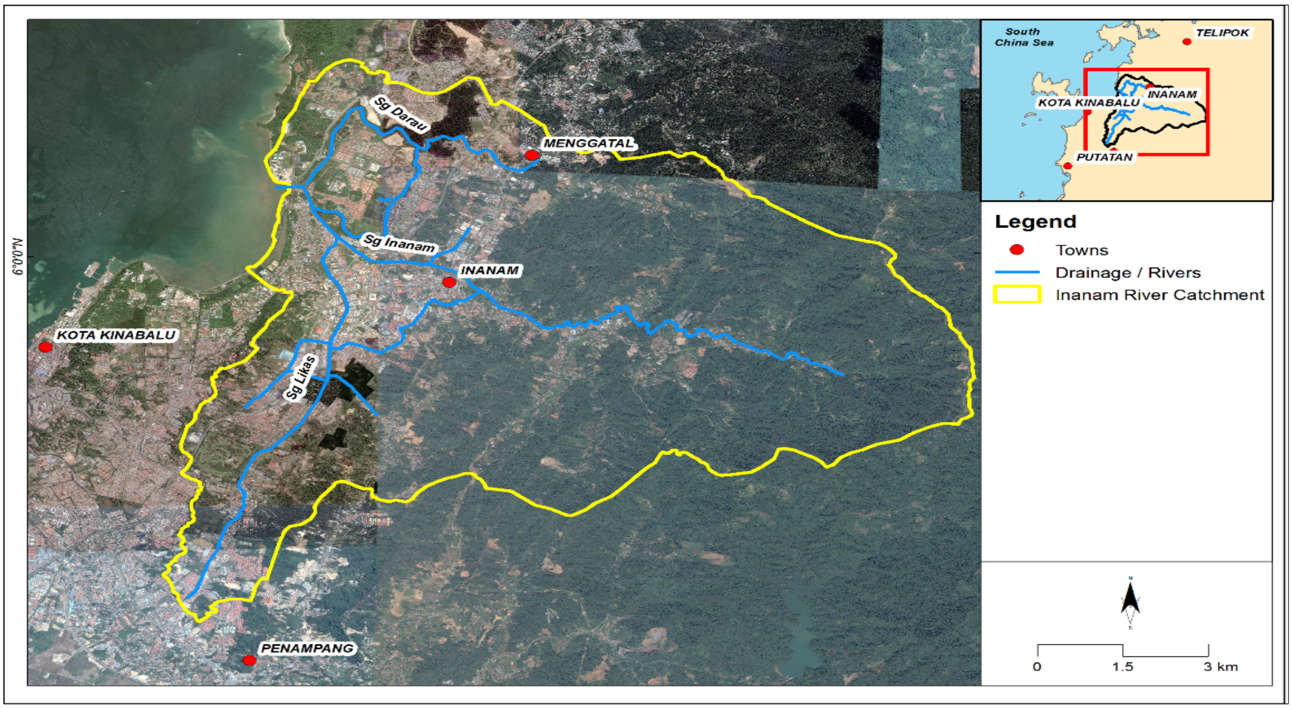


**Figure 1**. Study extent (Background: Google Satellite Image).

## 2 SOURCES OF POLLUTANTS

The main sources of pollutants have been identified as domestic sources releases (sewerage and wastewater), point sources releases (industrial, pig and poultry farms and waste water treatment plants) and non-point sources mainly from agricultural pollution.

### 2.1 Domestic sources

Untreated sewage discharged into the aquatic environment is a major concern in the catchment. Biological processes are rapid in tropical conditions, which lead to a rapid die-off of, for instance, *E. coli* bacteria. This is, however, not enough to mitigate health risks associated with discharging of large volumes of untreated sewage (Environment Conservation Department, 2002). Unsightly and foul smelling “drains” can be seen in the area of interest, particularly in Likas River and the lower reaches of Inanam River.

Another key component of domestic pollution source to be considered is the effect of high nutrient load. An illustration of adverse impact of high concentration of nutrients in the receiving waters is the explosive growth of freshwater weed (water hyacinth). Abnormal quantities of hyacinth lead to a depletion of oxygen in the receiving body (drain, river, enclosed bay).

### 2.2 Point sources

Point sources are independent of rainfall runoff (constant flux). Most of the water issues identified within the study area are related to point source, particularly in the urban landscape. Point sources within the study area consist of industries (e.g. food processing, workshop, gas stations, wet markets, and restaurants), pig and poultry farms, and Waste Water Treatment Plants (WWTPs).

### 2.3 Non point sources

Non-point sources in contrast are dependent on the rainfall runoff (flux that varies). Fertilizers, pesticides and herbicides used for agriculture to enhance production can increase nutrient loads into waterways and harm the environment. A good illustration of this often occurs on golf courses; if not managed properly, fertilizers needed to maintain greens and fairways in good condition can drain into water features, causing mass fish kills and foul smelling water. Focusing on the Inanam catchment, non-point sources are of less importance and magnitude as agricultural practices are limited to the upper Inanam catchment.

## 3 WATER QUALITY STANDARDS

The water quality standards to assess and classify the water quality classes together with corresponding water usage (refer Table 1 and 2) and status (refer Table 3) within the rivers and drains located within the Inanam catchment is based on Department of Environment (DOE) Water Quality Index (WQI) detailed in the National Water Quality Standards for Malaysia (NWQS).

 

The WQI is calculated using a series of sub-index (SI) values for each water quality parameter (refer Eq. [1]):

$$WQI = 0.22*SIDO + 0.19*SIBOD + 0.16*SICOD + 0.15*SIAN + 0.16*SISS + 0.12*SIpH \quad [1]$$

Where:

- SIDO is the sub-index for DO
- SIBOD is the sub-index for BOD
- SICOD is the sub-index for COD
- SIAN is the sub-index for ammonia
- SISS is the sub-index for suspended sediment
- SIpH is the sub-index for pH

Each sub-index is a formula derived from the concentrations of the relevant water quality parameter. Concentrations can be based upon best fit equations to a large collation of water quality samples or derived from numerical modelling

**Table 1.**DOE Water Quality Index Classes (National Water Quality Standards for Malaysia, NWQS).

| Parameter | DOE Classes | | | | | |
|---|---|---|---|---|---|---|
| | **I** | **IIa** | **IIb** | **III** | **IV** | **V** |
| DO | 7 | 5 - 7 | 5 - 7 | 3 - 5 | <3 | <1 |
| BOD | 1 | 3 | 3 | 6 | 12 | >12 |
| COD | 10 | 25 | 25 | 50 | 100 | >100 |
| SS | 25 | 50 | 50 | 150 | 300 | 300 |
| AN | 0.1 | 0.3 | 0.3 | 0.9 | 2.7 | >2.7 |
| pH | 6.5 - 8.5 | 6 - 9 | 6 - 9 | 5 - 9 | 5 - 9 | - |
| **WQI** | **> 92. 7** | **76.5 - 92.7** | | **51.9 - 76.5** | **31.0 - 51.9** | **< 31.0** |

**Table 2.** DOE classes and corresponding water usage.

| Class | Water Supply | Fishery | Water uses |
|---|---|---|---|
| I | Practically no treatment necessary | Very sensitive aquatic species | Conservation of natural environment |
| IIa | Conventional treatment required | Sensitive aquatic species | |
| IIb | - | - | Recreational use with body contact |
| III | Extensive treatment | - | - |
| IV | - | - | Irrigation |
| V | - | - | None |

**Table 3.**WQI ranges and corresponding river status for main water quality parameters.

| Water Quality Parameters | Index Range | | |
|---|---|---|---|
| | **Clean** | **Slightly Polluted** | **Very Polluted** |
| Water Quality Index (WQI) | 81 - 100 | 60 - 80 | 0 - 59 |
| Biochemical Oxygen Demand (BOD) | 91 - 100 | 80 - 90 | 0 - 79 |
| Ammoniacal Nitrogen ($NH_3$-N) | 92 - 100 | 71 - 91 | 0 - 70 |
| Suspended Solids (SS) | 76 - 100 | 70 - 75 | 0 - 69 |

## 4 NUMERICAL MODELLING

### 4.1 Overview

Establishing the dynamics of water quality, including replicating the existing situation and the performance of prospective pollution reduction interventions, was most effectively accomplished using computer-based modelling tools. The central focus of this study had been to establish models for relevant reaches of Inanam, Likas and Darau Rivers. These models simulated the hydrologic, hydrodynamic and water quality processes throughout the catchment. The modelling tools developed for this study consisted of the following components (refer Figure 2):

 

- Land based pollution load model (LOAD and SEAGIS): Simulating generation and transport of pollutants and suspended sediment throughout the catchment;
- Hydrologic model (i.e. Rainfall Runoff, MIKE 11 RR): Simulating rainfall on the catchments and the subsequent runoff into the river system;
- River hydrodynamic model (MIKE 11 HD): Simulating water levels and flows in the Inanam river system;
- Water Quality model (MIKE 11 WQ): Simulating transport and fate of pollutants in the river system.

The applied modelling tools were used in conjunction with available data and analyses to describe the existing situation and, by implementing proposed pollution reduction options and comparing the differences to the existing situation, assess the effectiveness and fine-tune the mitigation options. The combined modelling system was flexible, built-in with GIS with each component integrated with the others (i.e. the effect of changing one feature in the overall model can be seen in all facets and areas).

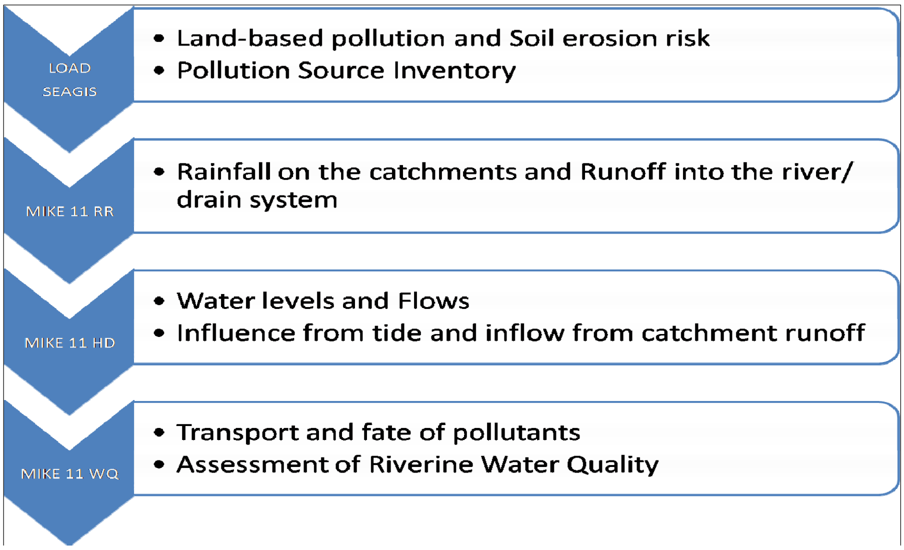


**Figure 2.**Overview of modelling tools.

4.2 Rainfall Runoff Modelling

The aim of the rainfall runoff modelling is to simulate rainfall on the catchments and the subsequent runoff into the river/ drainage system. Rainfall Runoff modelling was carried out using DHI's MIKE 11 NAM and Urban-A hydrological models.

The study area was divided into a series of sub-catchments, each representing in-flows into the Inanam, Darau and Likas river systems. The catchment delineation reflects the runoff pattern from the individual sub-catchments (refer Figure 3). Undeveloped, rural upstream sub-catchments were modelled using MIKE 11 NAM model, while the other sub-catchments, representing downstream predominantly urban areas, were modelled using Urban-A model (DHI, 2013).

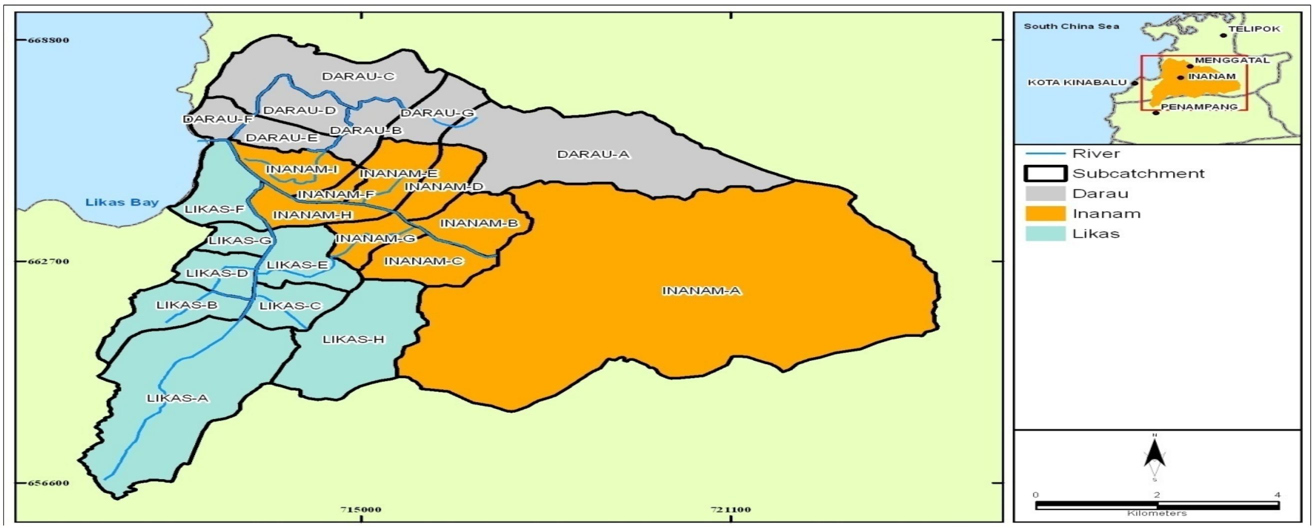


**Figure 3.**Sub-catchments used in the hydrological modeling.

4.3 Catchment/ Land Based Pollution

An issue with catchment inflow is the potential for contamination from pollution sources. Catchment runoff transports suspended sediments, nutrients, pollutants and fresh water. Sediment concentrations depend heavily on land use in the catchment area and, more specifically, changes in land use (for example, land clearing increases soil erosion). Nutrients and pollutants depend on industry, agriculture, livestock and population density in the catchment area.

A pollution load model had been developed that used identified point and non-point pollution sources and runoff generated by the rainfall-runoff model to predict the likely concentrations and types of pollution contained in runoff. The load assessment, considered hydrological, agricultural, population and land use information to predict the following:

- Quantification of non-point or diffuse sources of pollution to identify potential affected areas.
- Estimation of pollutant loads originating from urban sources such as industries, households, sewers and treatment facilities.
- Estimation of the pollutant quantity and concentration that reaches the receiving body via the use of calibrated load reduction factors and pollutant decay coefficients.

The total annual load per catchment determined for the present study area is shown in Table 4.

**Table 4.**Total annual LOAD per catchment.

| Catchment | BOD total (kg/yr) | P total (kg/yr) | NH4 total (kg/yr) | NO3 total (kg/yr) | E-coli Total (10^12/yr) |
|---|---|---|---|---|---|
| Inanam | 1,694,794 | 111,636 | 291,450 | 518,133 | 160,922 |
| Likas | 2,328,779 | 81,393 | 507,578 | 69,215 | 364,284 |
| Darau | 741,926 | 37,346 | 197,986 | 59,139 | 111,971 |

4.4 Hydrodynamic Modelling

Hydrodynamic conditions (the motion of water) in the river or drain govern the mixing of runoff water with ambient water. River/drain modelling was carried out using DHI's MIKE 11 1-d hydrodynamic (HD) model covering Inanam, Darau and Likas Rivers, and their main tributaries.

The model geometry consisted of river cross sections data extracted from bathymetry surveys conducted by DHI. Where appropriate, the model geometry made use of concrete drain cross sections acquired from the Department of Irrigation and Drainage (DID). The model boundaries consisted of catchment runoff derived from the rainfall-runoff. Open boundary conditions were applied at each upstream end of the model whereas, along the river reaches, catchment inflows were incorporated as distributed sources (i.e. the flow was distributed along the river reaches within the model domain). Tidal variations were applied to the downstream end of the model (i.e. Likas Bay).

  / ISSN 1562-6865 (Online) - ISSN 1063-7710 (Print)

4.5 Riverine Water Quality

The water quality modelling consisted of two components, as follows:

- An advection dispersion model - Simulating saline intrusion, flushing characteristics and movement of conservative substances;
- A water quality model - Simulating the movement and interactions of various water quality components (e.g. BOD, DO).

In order to capture spatial and temporal variations in the runoff and pollution loading, an integrated approach for hydrology and pollution load had been applied. The aim was to identify pollution sources and determine their impact upon water quality in the river system. By integrating all components, the relative importance of the various factors relating to water quality (land use, rainfall, tidal conditions, etc) can be assessed in an integrated manner. The modelling works, which included:

- Link to rainfall runoff and catchment load;
- Incorporation of advection and dispersion processes;
- Establishment and calibration of combined catchment pollution source (including suspended sediments) and riverine water quality models;
- Establishment of water riverine quality conditions and the major contributing pollutant sources.

## 5 WATER QUALITY MODEL CALIBRATION

Calibration was performed in conjunction with the catchment pollution model, where water quality process rates were adjusted as well as catchment specific pollution load retention parameters. The measurements used to compare model predictions were from long term samples collected from Alam Sekitar Malaysia Sdn. Bhd. (ASMA) and specific water quality sampling performed for this study.

Temporally, individual samples were separated by a month or more. As water quality conditions were highly variable according to diurnal cycles, flow rates, tidal conditions, etc. this tended to make the data look quite scattered, however the total number of points available over the long term was suitable to derive average conditions.

In turn, to quantify the accuracy of model predictions, model results for a typical hydrological year were compared to the average ASMA data (average values taken from the period 1998-2009). Table 5 shows the average concentrations of each parameter extracted from the model at ASMA stations located in Inanam, Likas and Darau Rivers, respectively (refer Figure 4). Comparison of model predictions to measurements is generally good. Although there are differences when looking at individual observations, the simulated and measured values are, on average, within the same range of magnitude.

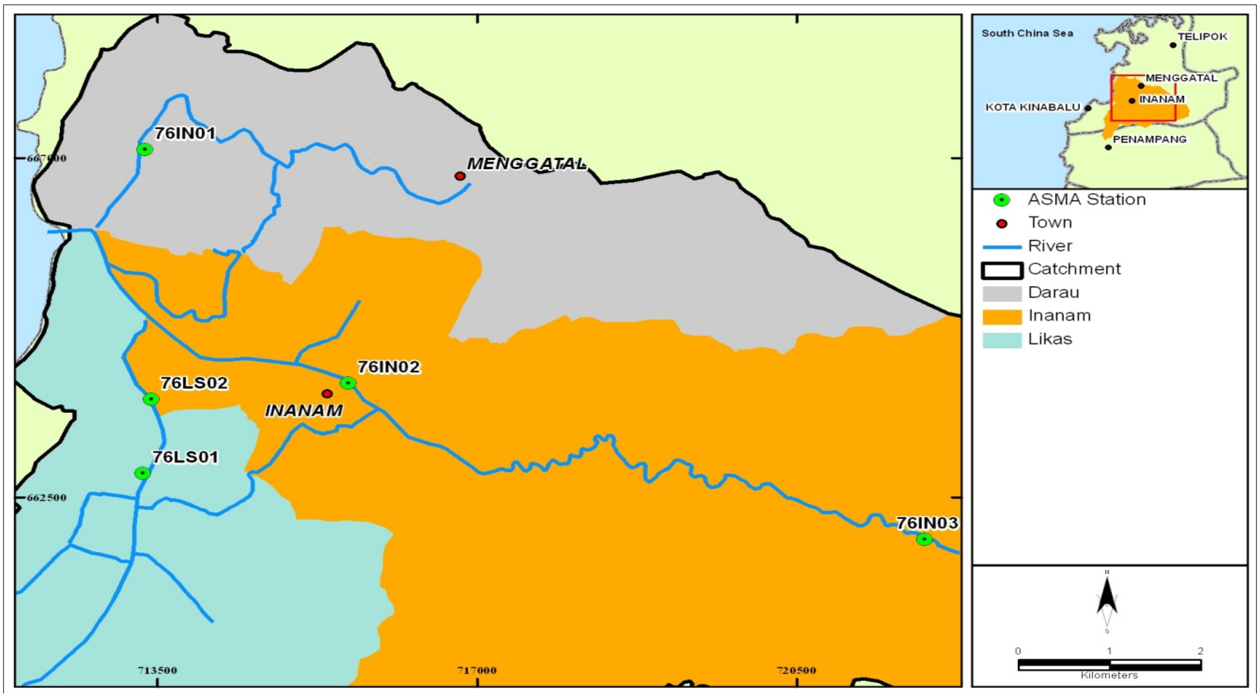


**Figure 4.** ASMA water quality stations located within Inanam catchment.

**Table 5.**Comparison between observed and simulated concentrations of water quality parameters at ASMA stations located at Inanam (76IN02), Likas (76LS01), Darau (76IN01) rivers.

| Parameter | Concentration (in mg/l unless stated otherwise) | | | | | |
|---|---|---|---|---|---|---|
| | 76IN02 | | 76LS01 | | 76IN01 | |
| | Observed | imulated | Observed | imulated | Observed | imulated |
| DO | 6.3 | 6.3 | 3.3 | 4.2 | 4.5 | 4.1 |
| TEMPERATURE (Degrees) | 27.4 | 28.0 | 28.7 | 28.0 | 29.0 | 28.0 |
| AMMONIA | 0.4 | 0.6 | 3.2 | 2.9 | 0.9 | 0.6 |
| NITRATE | 0.7 | 0.9 | 0.2 | 0.4 | 0.4 | 0.1 |
| BOD | 2.4 | 2.6 | 8 | 8.7 | 3.2 | 3.0 |
| E Coli (1/100 mL) | 17,476 | 11,585 | 70,161 | 90,436 | 25,283 | 19,034 |
| COD | 24.4 | 27.6 | 40.8 | 48.4 | 52.5 | 62.8 |
| TSS | 82.7 | 84.7 | 29.1 | 35.6 | 40.3 | 76.4 |

## 6 EXISTING RIVERINE WATER QUALITY

The water quality evaluation for existing condition at the study area was conducted using the DoE Water Quality Index (WQI) to classify the river reaches into three (3) categories, namely, ‘Clean’, ‘Slightly Polluted’ and ‘Polluted’ (refer Figure 5). The model shows that within the study area, only 16% of the total river length is classified as ‘Clean’. The majority of the river reaches are ‘Slightly Polluted’ (65%), with a significant portion (19%) of the river system is ‘Polluted’. Overall, Likas River is the most polluted river, with 23% of the river being ‘Polluted’ and a further 71% ‘Slightly Polluted’. nanam River is also 24% ‘Polluted’; however, only 39% is ‘Slightly Polluted’ with up to 37% of the river classified as ‘Clean’. Darau River meanwhile is almost entirely ‘Slightly Polluted’. The modeling results confirm the water quality status published in the Malaysia Environmental Quality Report (Department of Environment, 2009; Department of Environment, 2010).

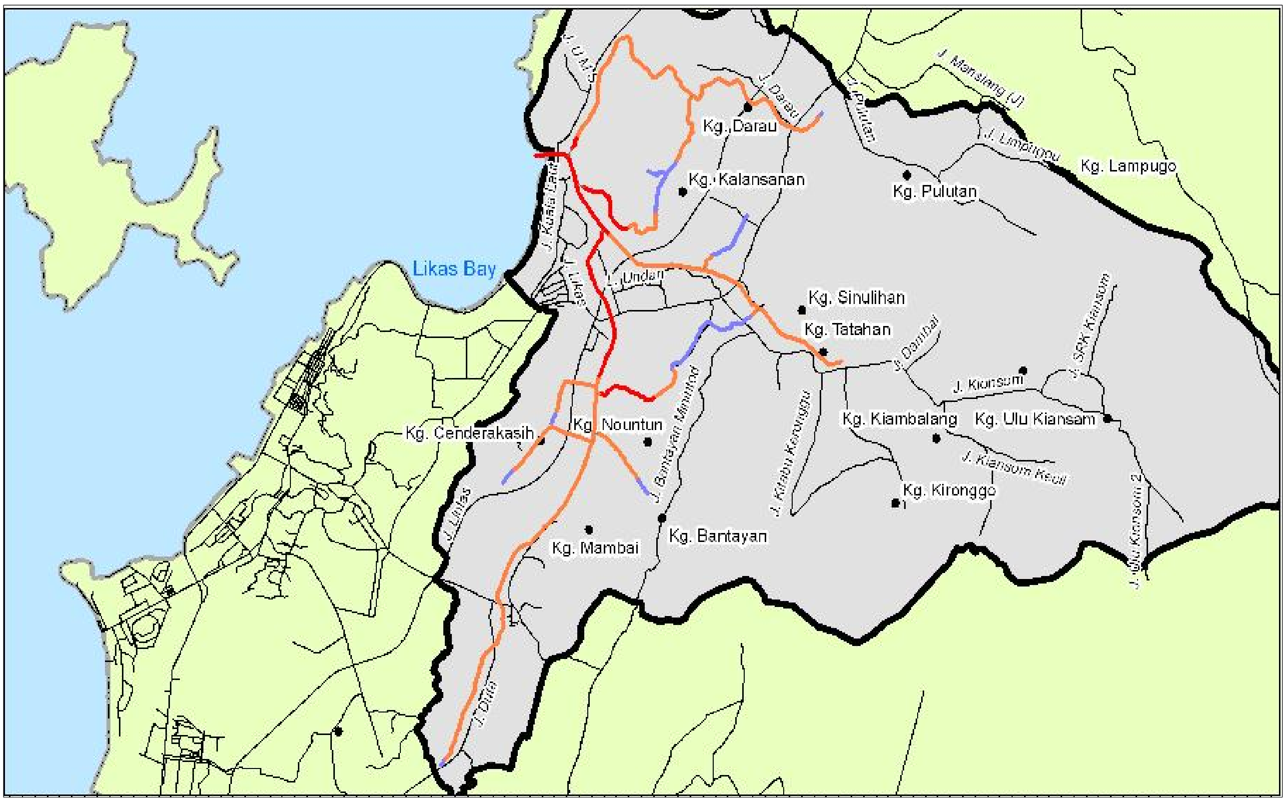


**Figure 5.** Existing river water quality status for the study area (Blue: ‘Clean’, Orange: ‘Slightly Polluted’, and Red: ‘Very Polluted’).

 

## 7 ASSESSMENT OF SCENARIOS

Different model scenarios were developed and tested to provide insight into the relevant issues and major concerns relating to the water quality within the Inanam river system. The developed scenarios aimed to assist in providing indicators, assess the effectiveness of proposed actions and provide guidance to support the development of water quality management options within the study area.

The following scenarios had been considered and tested:

- Scenario I - Existing Condition: This is the present (baseline) catchment condition (i.e. as of year 2011).
- Scenario II – Pristine Condition: This scenario represents the natural situation where all point source loads are excluded, and non-point loads are representative of natural vegetation.
- Scenario III – “do-nothing”: This scenario aims at representing the likely catchment condition in year 2030 if no changes to the existing procedures of management, treatment and enforcement are made. It is an extrapolation of the existing condition (i.e. Scenario I).
- Scenario IVa – WQ Standard Compliance (Level 1): This scenario assumes that all pollution loads are compliant with Water Quality Standard B discharge levels. For distributed sources, it is assumed that river reserve and agricultural management guidelines are implemented; non-point loads are 20% less than existing and suspended sediment loads are 40% less than existing.
- Scenario IVb – WQ Standard Compliance (Level 2): This scenario assumes that all point sources pollution loads are compliant with Water Quality Standard A discharge levels. For distributed sources, it is assumed that river reserve and agricultural management guidelines are implemented; non-point loads are 40% less than existing and suspended sediment loads are 80% less than existing.
- Scenario V – Full Domestic Waste Treatment: This scenario assumes that sullage (domestic waste not connected to sewerage network) is sewered and fully treated.
- Scenario VI – Point Sources Treatment: This scenario assumes that point sources from all livestock (pigs, poultry) and industries are treated to Standard B compliance. STP and WWTP discharges points are treated to the highest possible efficiency.

Figure 6 and Figure 7 show examples of simulated water quality index (WQI) values for river stretches along Inanam River and Likas River, while Figure 8 shows overview of the river water quality status within the study area for Scenario III (Future scenario in year 2030).

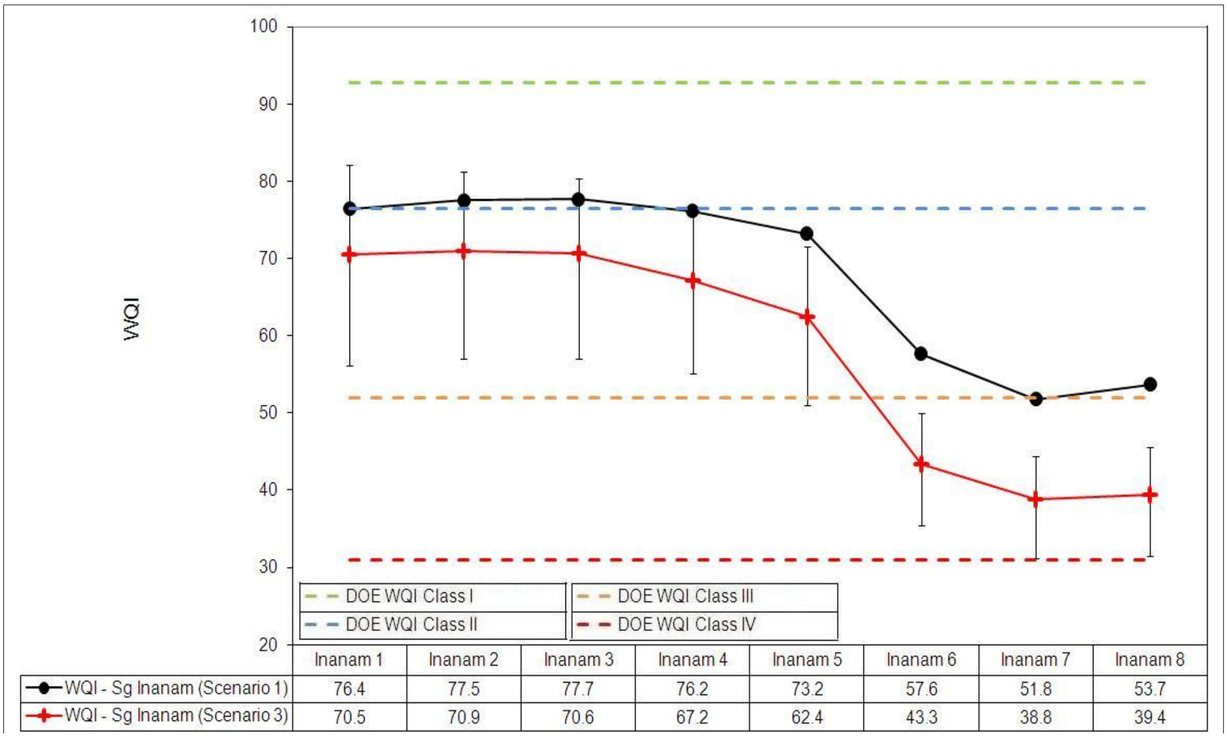


**Figure 6.** River water quality status for the study area for Scenario III (WQI – Inanam River).

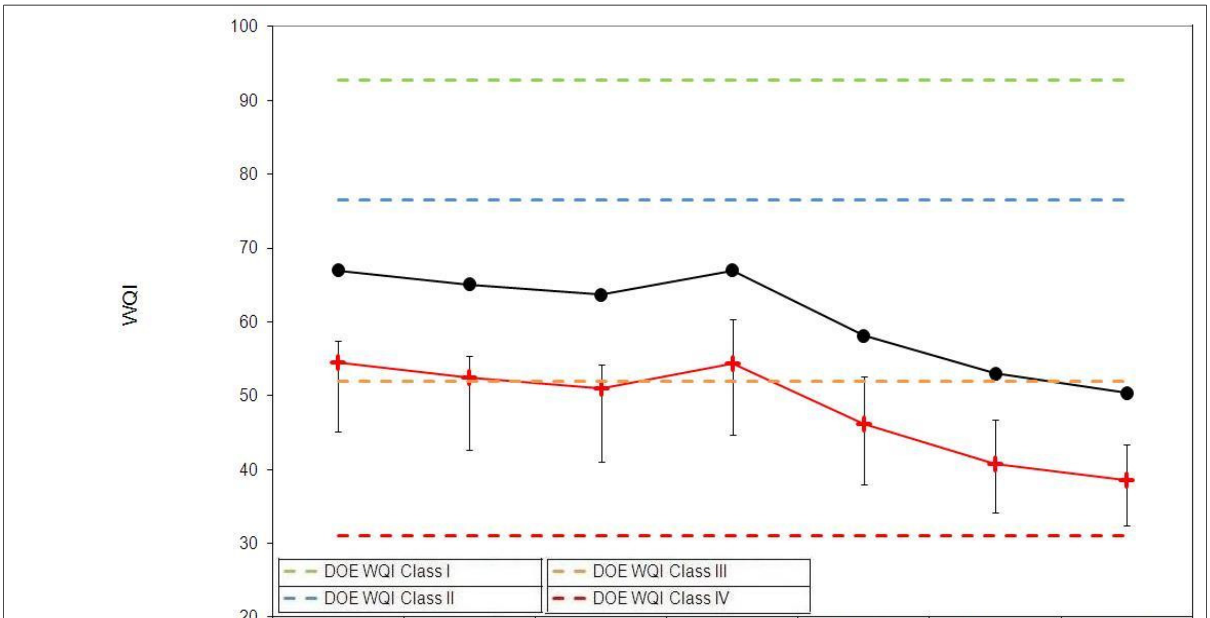


| | Likas 1 | Likas 2 | Likas 3 | Likas 4 | Likas 5 | Likas 6 | Likas 7 |
|---|---|---|---|---|---|---|---|
| WQI - Sg Likas (Scenario 1) | 66.9 | 65.0 | 63.7 | 67.0 | 58.1 | 53.0 | 50.4 |
| WQI - Sg Likas (Scenario 3) | 54.6 | 52.4 | 51.0 | 54.3 | 46.2 | 40.8 | 38.5 |

**Figure 7.** River water quality status for the study area for Scenario III (WQI – Likas River)

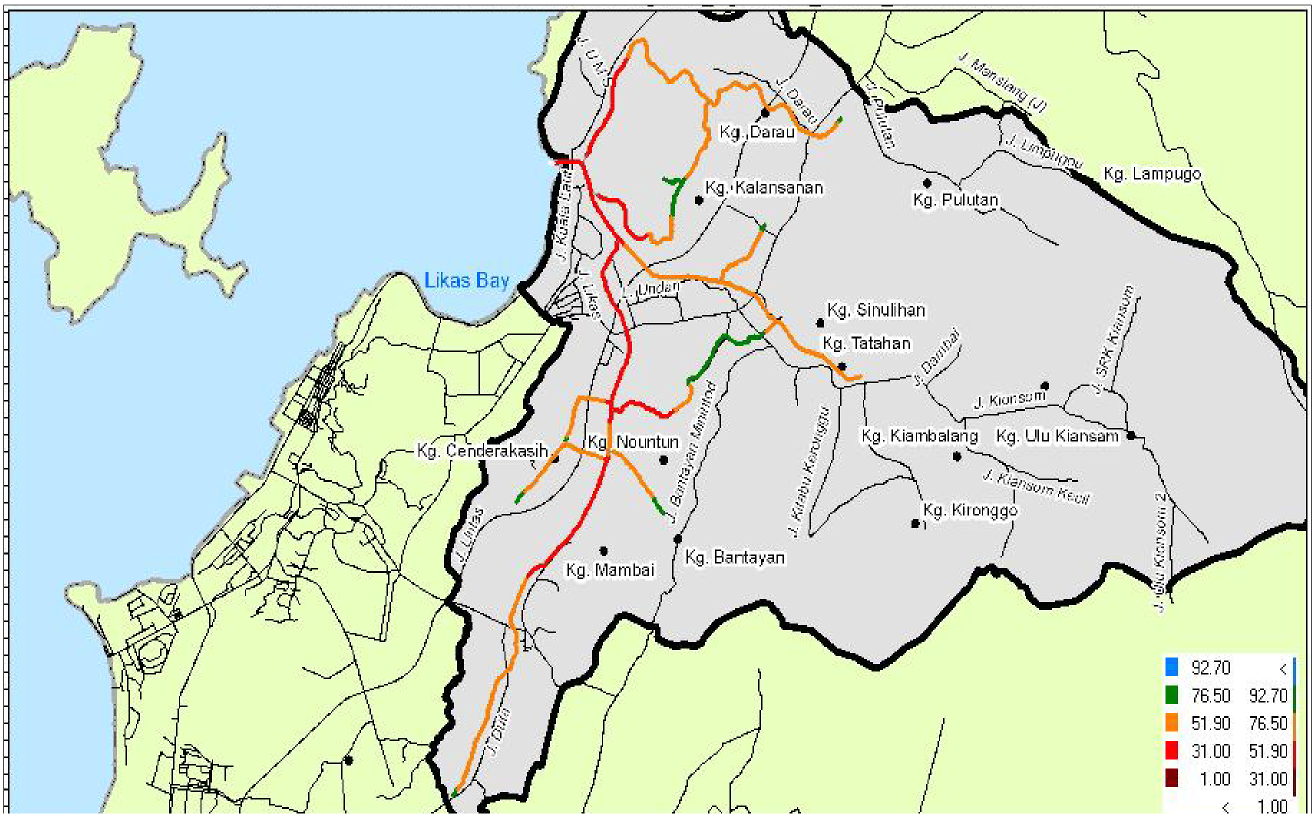


**Figure 8.** Overall riverine water quality index class for Scenario III
(Blue: 'Class I; Green: 'Class II', Orange: 'Class III', Red: 'Class IV' and Brown: 'Class V').

## 8 CONCLUSION

The result of the study shows that most of the Inanam River presently falls within Class II water quality (conventional treatment required for water supply and suitable for sensitive aquatic species) under the National Water Quality Standards for Malaysia, however the downstream areas near the river mouth are Class III (extensive water treatment required for water supply, suitable for common of economic value and tolerant aquatic species and fit for livestock drinking). The Likas River is presently a Class III river, deteriorating to Class IV (fit for irrigation purpose) in the lower reaches. It is also classified under the DOE river classification scheme as 'slightly' to 'very polluted'. The water quality in Darau River meanwhile currently falls within Class

 

III, although nearing Class II. These results reflect the major land use patterns, where the rivers within the forested and undeveloped catchments are in good condition, while conditions deteriorate rapidly downstream as a result of runoff from industrial, commercial and residential areas.

Mitigation of pollution through measures targeting domestic wastes, point source effluents and implementation of best management practices, as simulated in Scenario IVa/b, show a significantly positive impact on water quality for all rivers within the study area. In particular, this can improve the water quality of the lower reaches of Likas River by up to 44% (based on Water Quality Index), resulting in a Class III water quality classification. Improvements to downstream Inanam River is also up to 36% improvement in the WQI with resulting Class II/III river. The water quality improvement downstream Darau River is more moderate, with up to 20% improvement in the WQI. This is however sufficient to bring Darau River into Class II standard. The findings of this study can assist in providing indicators, assess the effectiveness of proposed mitigation or improvement actions and provide guidance to support the development of water quality management options to improve the overall water quality within the study area.

**ACKNOWLEDGMENTS**

The study which is the subject of this paper has been carried out by DHI Water & Environment (M) Sdn. Bhd. for the Environment Protection Department Sabah. The authors wish to acknowledge the support and assistance provided by the Environment Protection Department Sabah in the preparation of this paper.

**REFERENCES**

Department of Environment Malaysia, (2009). *Malaysia Environmental Quality Report 2009*, Department of Environment, Malaysia, Ministry of Natural Resources and Environment, Malaysia.

Department of Environment Malaysia DOE, (2010) *Malaysia Environmental Quality Report 2010*, Department of Environment, Malaysia, Ministry of Natural Resources and Environment, Malaysia.

DHI, (2013). *A Modelling System for Rivers and Channels* - MIKE 11 Reference Manual.

Environmental Conservation Department, (2002). *Wastewater Treatment in Sabah - Survey Report*, Environmental Conservation Department, Sabah, Malaysia.

 

Proceedings of the 37th IAHR World Congress
August 13 – 18, 2017, Kuala Lumpur, Malaysia

# EFFECT MECHANISM OF FLOW VELOCITY ON IRON RELEASE FROM PIPE SURFACES IN DRINKING WATER DISTRIBUTION SYSTEMS

MANJIE LI[1], ZHAOWEI LIU[2], YONGCAN CHEN[3] & YONGYAN WU[4]

[1,2,4] State Key Laboratory Hydroscience and Engineering, Tsinghua University, Beijing 100084, China,
limanjie14@mails.tsinghua.edu.cn; liuzhw@tsinghua.edu.cn; wuyongyan12@mails.tsinghua.edu.cn
[3] Southwest University of Science and Technology, 59 Qinglong Road, Mianyang 621010, Sichuan, China,
chenyc@tsinghua.edu.cn

## ABSTRACT

Iron release from corroded pipe surfaces is the primary cause of water quality deterioration in drinking water distribution systems. It is generally recognized that an appropriate increase of flow velocity would reduce iron release. However, there are two contradictory viewpoints about this effect mechanism. One declares that the accelerated flow provides more oxygen to preserve the integrity of the iron corrosion scale, a protective layer against further corrosion and iron release. The other statement holds that the raised shear stress applied in pipe surfaces brought by the increase of velocity improves the strength of scale layers and thus reduces the discoloration potential. In this study, a bench-scale testing was conducted to investigate the effect mechanism of flow velocity on iron release. A more than 20-year-old pipe section was used and the water quality parameters, such as pH, dissolved oxygen, turbidity, color, iron, chloride and sulfate, were determined.

**Keywords:** Iron release; corroded pipe; flow velocity; dissolved oxygen; shear stress.

## 1 INTRODUCTION

Water quality deterioration issues in drinking water distribution systems (DWDS) have drawn more and more attention, since they are closely related to human health. Among them, red water resulted from iron release is the most pervasive one as it affects the aesthetic quality of drinking water and could be perceived directly by customers (Tuovinen et al., 1980; Sarin et al., 2004a; 2004b; Imran et al., 2005a; 2006).

Old and corroded iron pipes are the main source of iron pollutant in this issue, particularly the unlined cast iron pipes, which still account for a large proportion in DWDS worldwide (Davies et al., 1997; Veschetti et al., 2010; Swietlik et al., 2012; Wang, 2015). Well-developed corrosion scales inside the pipe walls can protect the pipe metal from further corrosion. However, under disturbance, corrosion scales will release iron materials into bulk water, aggravating turbidity and color of the drinking water and thus leading to red water (Tuovinen et al., 1980; Sarin et al., 2004a; 2004b; Imran et al., 2005a; 2006).

Relevant researches mainly focus on the mechanism of iron corrosion as well as the influencing factors of iron release. Generally, it is recognized that appropriate increase of flow velocity would reduce iron release from the aged pipes. However, there are two contradictory viewpoints about this effect mechanism.

Sarin et al. (2004a) declares that in the final analysis, it is the interaction between dissolved oxygen (DO) and corrosion scales rather than the effect of velocity on iron release. As accepted, the corrosion rate of clean iron surface increases with increasing DO, which serves as the oxidizer and electron acceptor (McNeill and Edwards, 2001). However, as for the aged pipe surface covered with corrosion scales, enough oxidants can prevent the scales from being reduced and dissolved and thus preserve the integrity of this protective layer (Sarin et al., 2004a). And, accelerated flow renews the water body in DWDS and provides sufficient DO to the pipe surfaces.

The other opinion proposes that the discoloration in DWDS is a physical process of sedimentation and release of particulates, which mainly depends on the hydraulic condition and flow shear stress within the pipes. It claims that the raised shear stress applied on pipe surfaces brought by the increase of velocity impedes particle accumulation from bulk water to pipe walls, improves the strength of scale layers and thus reduces the discoloration potential (Boxall and Dewis, 2005; Boxall and Saul, 2005; Boxall and Prince, 2006; Vreeburg and Boxall, 2007; Husband and Boxall, 2010; Sharpe et al., 2010).

In this study, a bench scale testing was conducted to discuss these two viewpoints about the effect mechanism of flow velocity on iron release.

## 2 MATERIALS AND METHODS

A more than 20-year-old iron pipe section excavated from an experimental system in Tsinghua University, Beijing, China was adopted for study. Several segments were cut from this pipe section and the bench-scale testing systems were constructed in the previous research (Li et al., 2016), as shown in Figure 1. The detailed design principle and construction of the testing systems can be found in the relevant works (Mi et al., 2012a; 2012b; Li et al., 2016). These systems were operated under stagnation condition for 17 days to investigate the effects of pipe materials on scale characteristics and water quality variations, since this pipe section is a hybrid one assembled of unlined cast iron pipe and galvanized iron pipe.

According to the findings by Li et al. (2016), after disturbance, water quality in each system tended to stabilize in final. Afterwards, the three systems made of unlined cast iron pipe segments were continuously used for this study. Bulk water in the testing system was mobilized by an electric stirrer, whose rotation rate can be changed.

Rotation rates of the electric stirrers were set in five values, namely, 15 r/min, 30 r/min, 60 r/min, 90 r/min, and 120 r/min. Each rotation rate was kept for 4 days, with a hydraulic retention time (HRT) of 20 h. Water was discharged completely from the pipe systems every day and fresh tap water was fed into the systems in the meanwhile.

Water samples taken from the bench test systems were prepared for water quality measurement. Temperature, pH and DO were determined using a HACH HQ40d (USA) electrochemistry tester and corresponding electrodes. Turbidity was measured by a HACH 2100Q (USA) meter. Spectrophotometry (HACH DR3900, USA) was utilized to determine the color, iron content, chloride and sulfate. Color was measured as Pt-Co method unit.

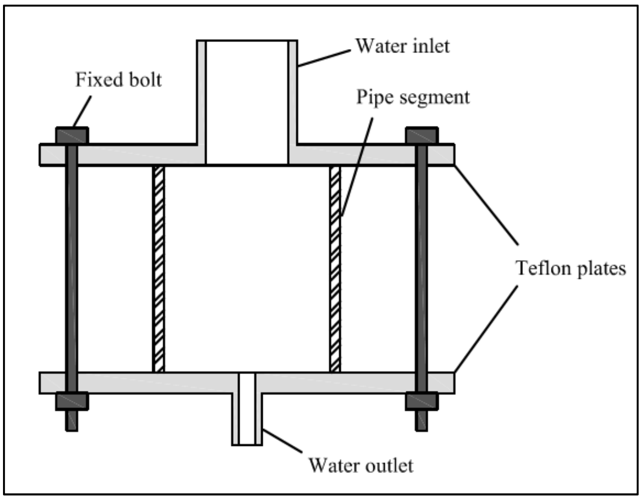


**Figure 1**. Schematic diagram of bench-scale pipe test system.

## 3 RESULTS AND DISCUSSIONS

### 3.1 Water quality variations

Figure 2 shows the variations of DO, pH, chloride, sulfate, iron, turbidity and color with the increase of rotation rate of stirrers. Each given value is the average deriving from the four ones measured at the same rotation rate. The value at 0 r/min is the datum measured in the final stable phase from the last testing (Li et al., 2016), which was operated under stagnation condition. The average parameters of source water are also given in the figure for ease of comparison. On the whole, the variation trends of water quality are similar among the three systems, even some parameters of the water samples are approximate.

#### 3.1.1 DO and pH

As drawn in Figure 2a, DO contents in the bulk water rise with the increase of rotation rate and the consequent enhancement of aeration. Moreover, the relationship between the DO concentration and rotation rate within 30 r/min appears to be linear. When rotation rate of stirrers is greater than 60 r/min, DO content roughly stays constant, since it gets close to the saturation point under the certain temperature (9.08 mg/L at 20℃). Similarly, the pH value shown in Figure 2b linearly increases in the beginning and stabilizes after the rotation rate reaching 60 r/min. The subtle variation of pH might be resulted from the ion transfer between bulk water and pipe surfaces.

Figure 3a shows the typical DO variation (at 30 r/min) within a HRT. DO content in water body rises rapidly right after starting stir and aeration. In the latter 10 hours, it tends to stabilize and DO increases slightly.

#### 3.1.2 Chloride and sulfate

Figures 2c and 2d give the variations of chloride and sulfate concentrations, respectively. In general, the chloride and sulfate increase as the rise of flow velocity. At the low rotation rate (about < 30 r/min), the chloride and sulfate concentrations drop below the background values in the source water after interaction, yet they exceed the datum at the high rotation rate (about > 30 r/min). This can be interpreted as the effects of shear stress on the sediment-release process of these substances.

Under the low flow velocity or even stagnation condition, the chloride and sulfate ions deposit from bulk water to pipe surfaces for scale formation. Many researches have verified that chloride and sulfate would be absorbed from bulk water to the scale surface or even form green rust, a kind of hydrated ferrous-ferric compounds (Tuovinen et al., 1980; Olowe et al., 1988; Drissi et al., 1994; Refait et al., 1998; Swietlik et al., 2012; Yang et al., 2012). However, as flow velocity increases, the impact of shear stress overcomes that of gravitation and attraction as well as the strength of scale layers. Then, the corrosion scale layers are disturbed and these substances are released to water body.

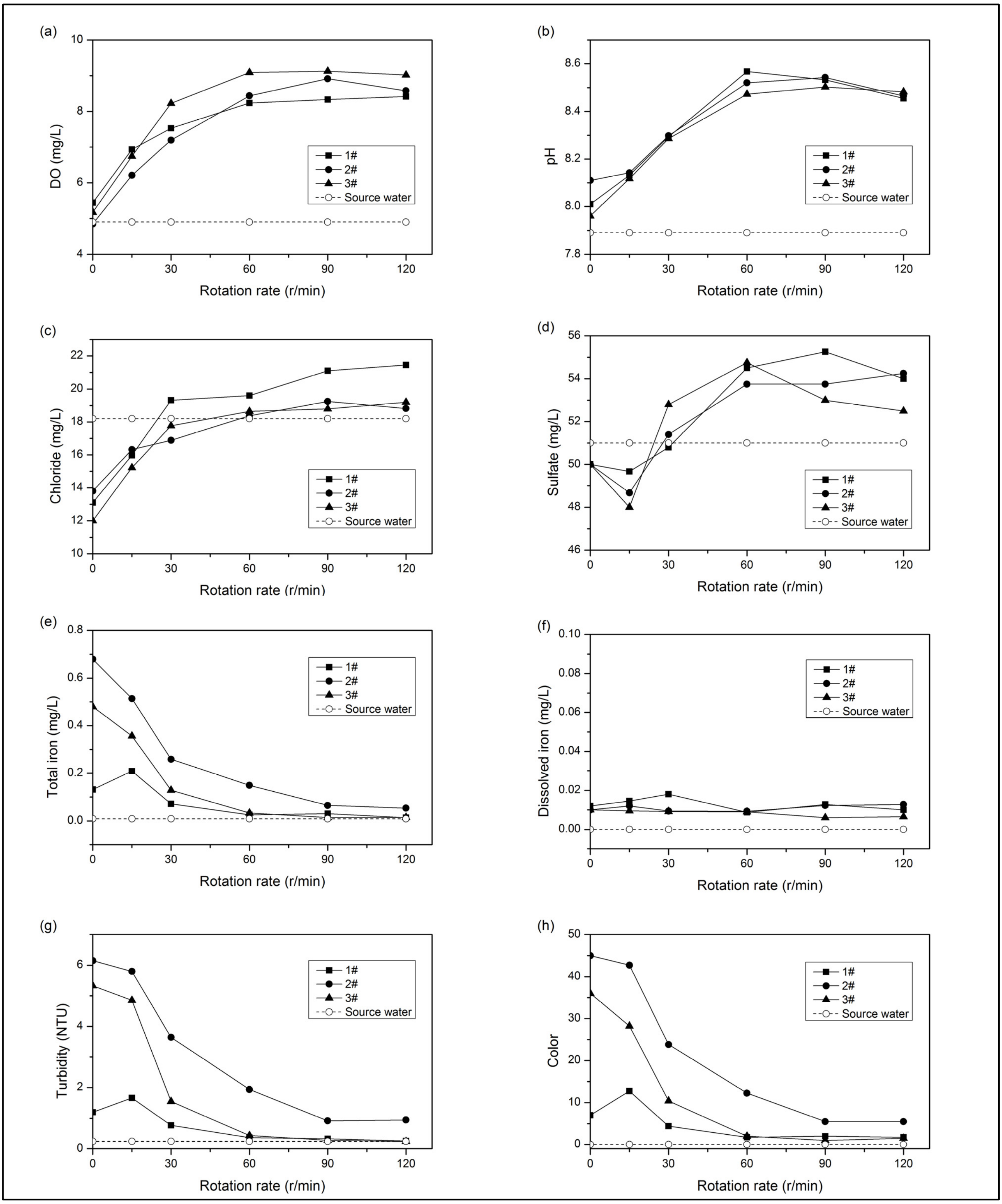


**Figure 2**. Variations of water quality parameters with increasing rotation rate of stirrers: (a) DO, (b) pH, (c) chloride, (d) sulfate, (e) total iron, (f) dissolved iron, (g) turbidity, and (h) color.

 

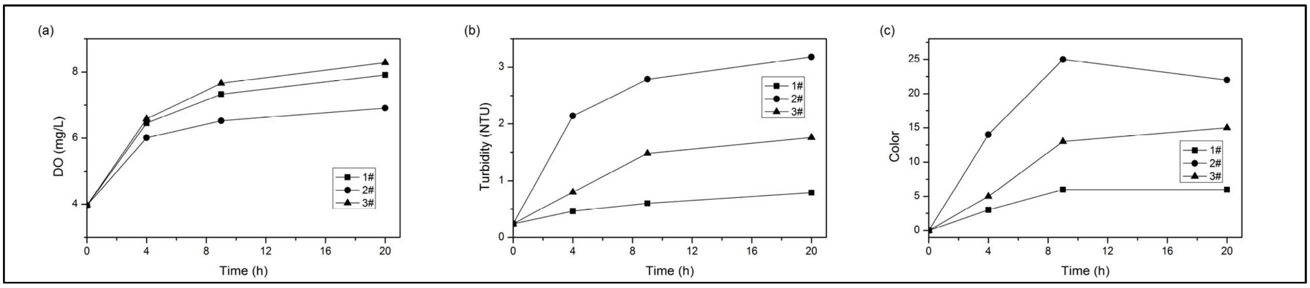


**Figure 3**. Variations of DO, turbidity and color within a HRT (at 30 r/min): (a) DO, (b) turbidity, and (c) color.

### 3.1.3 Iron, turbidity and color

Judging from Figures 2e, 2g and 2h, variation patterns of the total iron and turbidity, color are highly approximate, in terms of variation trends and amplitudes. This demonstrates a great contribution of iron release to red water issue, which has been discussed in detail previously (Sarin et al., 2003; Imran et al., 2005a; 2005b; Li et al., 2016). As shown in Figures 2e and 2f, the dissolved iron accounts for a small proportion of total and nearly remains steady, indicating that iron is mainly released in particulate form.

Generally, the iron release and turbidity, color of water were alleviated by increasing flow velocity. At low rotation rate (<15 r/min), the effective prevention of red water provided by accelerated flow velocity is less significant. Even a slight rise in the iron concentration (or turbidity, color) with was observed in sample 1#. The iron release (or turbidity, color) was markedly reduced between 15 – 60 r/min and leveled off afterwards.

Figures 3b and 3c show the variations of turbidity and color within a HRT (at 30 r/min), respectively. Similar to DO concentration, turbidity and color rapidly increase at the beginning and level off after 10 hours.

### 3.2 Effect mechanism of velocity

The experimental results in this study verify the finding that an appropriate increase of flow velocity can reduce iron release in DWDS. Moreover, which theory mentioned in Section 1 can better explain these variations?

The DO rise resulted from enhancement of aeration is in reasonable analogy to the DO supplement brought by accelerated flow in real DWDS. According to the DO theory, a sufficient DO content preserve the integrity of corrosion scales in pipe surfaces. If so, the release of chloride and sulfate would mitigate, corresponding to the decreasing iron concentration, with increasing flow velocity, this is not the case.

Then suppose that the discoloration in DWDS is a totally physical process supported by the shear stress theory. How would it be? The raised shear stress due to the velocity increase would cause the instant disturbance to the scale layers, leading to a sharp rise in iron release and subsequently strengthening the erosion resistance. Also, this cannot be detected in our study.

In summary, neither the DO theory nor the shear stress one could perfectly interpret the effect mechanism of flow velocity on iron release. The discoloration in DWDS is more probably a complex physic-chemical process. It is speculated that the structural damage comes with the rapid increase of shear stress and leads to the release of chloride, sulfate and iron. However, the increasing DO oxidates iron immediately and re-deposits it to pipe surface again. This is rather the re-formation of corrosion scale layers. The effect extents might differ among different components in the corrosion scales. What is more, a sophisticated experimental method and device should be designed to further investigate the hypothesis.

## 4 CONCLUSIONS

In this study, bench-scale testing systems were constructed to investigate the effect mechanism of flow velocity on iron release in DWDS. Primary conclusions can be drawn as follows:

a) With the increasing flow velocity and subsequent rise in DO content and shear stress, the iron release and turbidity, color of water are alleviated, while the release of chloride and sulfate is aggravated.
b) Neither the DO theory nor the shear stress one could perfectly interpret the effect mechanism of flow velocity on iron release. The discoloration in DWDS is more probably a complex physic-chemical process, which might be time-dependent and need further investigation.

## ACKNOWLEDGEMENTS

This work was supported by National Science and Technology Support Project of China (No.2015BAB07B09).

## REFERENCES

Boxall, J.B. & Dewis, N. (2005). Identification of Discolouration Risk through Simplified Modelling. *World Water & Environmental Resources Congress 2005*, 1-10.

Boxall, J.B. & Saul, A.J. (2005). Modeling Discoloration in Potable Water Distribution Systems. *Journal of environmental engineering*, 131(5), 716-725.

Boxall, J.B. & Prince, R.A. (2006). Modelling Discolouration in a Melbourne (Australia) Potable Water Distribution System. *Journal of Water Supply: Research and Technology-AQUA*, 55(3), 207-219.

Davies, C., Fraser, D.L., Hertzler, P.C. & Jones, R.T. (1997). USEPA's Infrastructure Needs Survey. *American Water Works Association. Journal*, 89(12), 30.

Drissi, H., Refait, P. & Génin, J.M. (1994). The Oxidation of Fe (OH) 2 in the Presence of Carbonate Ions: Structure of Carbonate Green Rust One. *Hyperfine Interactions*, 90(1), 395-400.

Husband, S., Boxall, J.B. & Williams, R. (2010). Discolouration Risk Management for Trunk Mains. *In Water Distribution Systems Analysis* 2010, 535-542.

Imran, S.A., Dietz, J.D., Mutoti, G., Taylor, J.S., Randall, A.A. & Cooper, C.D. (2005). Red water Release in Drinking Water Distribution Systems. *Journal (American Water Works Association)*, 97(9), 93-100.

Imran, S.A., Dietz, J.D., Mutoti, G., Xiao, W.Z., Taylor, J.S. & Desai, V. (2006). *Optimizing source water blends for corrosion and residual control in distribution systems*. Journal of American Water Works Association 98 (5), 107-115.

Li, M.J., Liu, Z.W., Chen, Y.C. & Hai, Y. (2016). Characteristics of Iron Corrosion Scales and Water Quality Variations in Drinking Water Distribution Systems of Different Pipe Materials. *Water Research*, 106, 593-603.

McNeill, L.S. & Edwards, M. (2001). Review of Iron Pipe Corrosion in Drinking Water Distribution Systems. *Journal of American Water Works Association*, 93(7), 88-100.

Mi, Z.L., Zhang, X.J., Chen, C., Lu, P.P., Wang, J. & Gu, J.N. (2012). Influence of Sulphate and Alkalinity Change on Iron Release in Drinking Water Distribution System. *China Water & Wastewater*, 28(1), 31-34.

Mi, Z.L., Zhang, X.J., Chen, C., Chen, P.J. & Du, J.D. (2012). Controlling Iron Release in Drinking Water Distribution System Fed with Desalinated Seawater. *China Water & Wastewater*, 28(19), 37-40.

Olowe, A.A., Genin, J.M. & Bauer, P. (1988). Hyperfine Interactions and Structures of Ferrous Hydroxide and Green Rust II in Sulfated Aqueous Media. *Hyperfine Interactions*, 41(1), 501-504.

Refait, P., Abdelmoula, M. & Génin, J.M.R. (1998). Mechanisms of Formation and Structure of Green Rust One in Aqueous Corrosion of Iron in the Presence of Chloride Ions. *Corrosion Science*, 40(9), 1547-1560.

Sarin, P., Snoeyink, V.L., Bebee, J., Jim, K.K., Beckett, M.A., Kriven, W.M. & Clement, J.A. (2004). Iron Release from Corroded Iron Pipes in Drinking Water Distribution Systems: Effect of Dissolved Oxygen. *Water Research*, 38(5), 1259-1269.

Sarin, P., Snoeyink, V.L., Lytle, D.A. & Kriven, W.M. (2004). Iron Corrosion Scales: Model for Scale Growth, Iron Release, and Colored Water Formation. *Journal of Environmental Engineering*, 130(4), 364-373.

Świetlik, J., Raczyk-Stanisławiak, U., Piszora, P. & Nawrocki, J. (2012). Corrosion in Drinking Water Pipes: The Importance of Green Rusts. *Water research*, 46(1), 1-10.

Sharpe, R.L., Smith, C.J., Boxall, J.B. & Biggs, C.A. (2010). *Pilot scale laboratory investigations into the impact of steady state conditioning flow on potable water discolouration*. Water Distribution System Analysis 2010, 494-506.

Sharpe, R.L., Smith, C.J., Boxall, J.B. & Biggs, C.A. (2010). Pilot Scale Laboratory Investigations into the Impact of Steady State Conditioning Flow on Potable Water Discolouration. *In Water Distribution Systems Analysis* 2010, 494-506.

Tuovinen, O.H., Button, K.S., Vuorinen, A., Carlson, L., Mair, D.M. & Yut, L.A. (1980). Bacterial, Chemical, and Mineralogical Characteristics of Tubercles in Distribution Pipelines. *Journal of American Water Works Association*, 72(11), 626-635.

Veschetti, E., Achene, L., Ferretti, E., Lucentini, L., Citti, G. & Ottaviani, M. (2010). Migration of Trace Metals in Italian Drinking Waters from Distribution Networks. *Toxicological & Environmental Chemistry*, 92(3), 521-535.

Vreeburg, I.J. & Boxall, J.B. (2007). Discolouration in Potable Water Distribution Systems: A Review. *Water research*, 41(3), 519-529.

Wang, L. (2015). Effects of water source switching by South-to-North Water Diversion Project on distribution systems in Beijing and countermeasures. *Master Dissertation*, Tsinghua University.

Yang, F., Shi, B.Y., Gu, J.N., Wang, D.S. & Yang, M. (2012). *Morphological and physicochemical characteristics of iron corrosion scales formed under different water source histories in a drinking water distribution system*. Water Research, 46, 5423-5433.

Yang, F., Shi, B., Gu, J., Wang, D. & Yang, M. (2012). Morphological and Physicochemical Characteristics of Iron Corrosion Scales Formed Under Different Water Source Histories in a Drinking Water Distribution System. *Water Research*, 46(16), 5423-5433.

 

# NUMERICAL MODELING AND PRELIMINARY ANALYSIS ON DISPERSION OF LIQUID EFFLUENT FOR INLAND NUCLEAR POWER PLANTS

HAIWEN ZHANG[(1)], PING JI[(2)], YIJUN ZHAO[(3)], JUE YUAN[(4)], XIAOLI CHEN[(5)], LI ZENG[(6)]

[(1,2,3,4,5,6)] China Institute of Water Resources and Hydropower Research, Beijing 100038, China,
haiwenzhang@hotmail.com

## ABSTRACT

A numerical modeling and preliminary analysis on dispersion of liquid effluent for the purpose of site selection of inland power plants is presented in this study. A 3D environmental hydraulic modeling by using MIKE 3 Flow model based on a flexible mesh approach has been carried out for simulating the effluent concentration due to the liquid effluent accompanied with cooling water discharge in rectangular channel. A series of scenarios with different ratios of width to water depth ($\beta = B/h$) and various ratios of ambient flow discharge to outfall discharge ($\gamma = Q_a/Q_o$) have been simulated. Considering the specific limit on the concentration of radioactive liquid effluent ($^3H$) on the cross-section at 1 km downstream from the outfall for inland nuclear power plants in China, the concentration on this specific cross-section has been analyzed on the basis of the modeling results. Approximate estimations of the mean concentration and the maximum depth-averaged concentration on this cross-section have been established, which could be used as a reference for the site selection of inland power plants.

**Keywords:** Numerical modeling; dispersion; liquid effluent; inland power plant.

## 1 INTRODUCTION

The discharge of radioactive liquid effluents is one of the main issues for nuclear power plants. The permissible limits on the amount of radioactive effluents are normally prescribed by the standards and regulations. In China, a specific limit on the concentration of radioactive liquid effluent (Tritium, $^3H$) on the cross-section at 1 km downstream from the outfall is required for inland nuclear power plants, which is described in "Regulations for environmental radiation protection of nuclear power plants" issued by Ministry of Environmental Protection (2011). In order to maintain the effluent concentration within the permissible limits, it is important to study the dispersion of liquid effluent for plant siting decision and Environmental Impact Assessment (EIA). Numerical modeling is a key approach for the study.

A 3D environmental hydraulic modeling by using MIKE 3 Flow model based on a flexible mesh approach (FM) has been carried out in this study. The dispersion of liquid effluent accompanied with cooling water discharge in generalized rectangular channel has been simulated for the purpose of site selection of inland power plants.

## 2 METHODOLOGY

### 2.1 Model description

MIKE 3 developed by DHI Water & Environment is a comprehensive software system designed for the simulation of three-dimensional flows and environmental processes where stratification due to the density variations is an important phenomenon to simulate. A model of MIKE 3 HD FM (DHI, 2009) has been applied for the simulation of dispersion of liquid effluent in this study. The model is based on the numerical solution of the three-dimensional incompressible Reynolds averaged Navier-Stokes equations, subject to the assumptions of Boussinesq and of hydrostatic pressure. Thus, the model consists of continuity, momentum, temperature, salinity, transport and density equations and is closed by a turbulent closure scheme. The free surface is taken into account using a sigma-coordinate transformation approach.

The continuity equation is written as:

$$\frac{\partial u}{\partial x}+\frac{\partial v}{\partial y}+\frac{\partial w}{\partial z}=S \qquad [1]$$

and the two horizontal momentum equations for the *x*- and *y*- components read:

 

$$\frac{\partial u}{\partial t}+\frac{\partial u^2}{\partial x}+\frac{\partial vu}{\partial y}+\frac{\partial wu}{\partial z} = fv-g\frac{\partial \eta}{\partial x}-\frac{1}{\rho_0}\frac{\partial P_a}{\partial x}-\frac{g}{\rho_0}\int_z^{\eta}\frac{\partial \rho}{\partial x}dz+F_u + \frac{\partial}{\partial z}\left(v_t\frac{\partial u}{\partial z}\right)+u_sS \quad [2]$$

$$\frac{\partial v}{\partial t}+\frac{\partial v^2}{\partial y}+\frac{\partial uv}{\partial x}+\frac{\partial wv}{\partial z} = -fu-g\frac{\partial \eta}{\partial y}-\frac{1}{\rho_0}\frac{\partial P_a}{\partial y}-\frac{g}{\rho_0}\int_z^{\eta}\frac{\partial \rho}{\partial y}dz+F_v + \frac{\partial}{\partial z}\left(v_t\frac{\partial v}{\partial z}\right)+v_sS \quad [3]$$

where $t$ is the time, $x$, $y$ and $z$ are the Cartesian coordinates, $\eta$ is the surface elevation, $d$ is the still water depth, $h= \eta + d$ is the local water depth, $u$, $v$ and $w$ are the velocity components in the $x$, $y$ and $z$ directions, respectively, $f = 2\Omega\sin\Phi$ is the Coriolis parameter, $\Omega$ is the angular rate of revolution and $\Phi$ is the geographic latitude, $g$ is the gravitational acceleration, $\rho$ is the density of water, $\rho_0$ is the reference density of water, $P_a$ is the atmospheric pressure, and $v_t$ is the vertical eddy viscosity. $S$ is the magnitude of the discharge due to point sources and ($u_s$, $v_s$) is the velocity by which the water is discharged into the ambient water. The horizontal stress terms are described using a gradient-stress relation, which is simplified to:

$$F_u=\frac{\partial}{\partial x}\left(2A\frac{\partial u}{\partial x}\right)+\frac{\partial}{\partial y}\left(A\left(\frac{\partial u}{\partial y}+\frac{\partial v}{\partial x}\right)\right) \quad [4]$$

$$F_v=\frac{\partial}{\partial x}\left(A(\frac{\partial u}{\partial y}+\frac{\partial v}{\partial x})\right)+\frac{\partial}{\partial y}\left(2A\frac{\partial v}{\partial y}\right) \quad [5]$$

where $A$ is the horizontal eddy viscosity.

The surface and bottom boundary conditions for $u$, $v$ and $w$ are:

At $z = \eta$,

$$\frac{\partial \eta}{\partial t}+u\frac{\partial \eta}{\partial x}+v\frac{\partial \eta}{\partial y}-w=0, \quad \left(\frac{\partial u}{\partial z},\frac{\partial v}{\partial z}\right)=\frac{1}{\rho_0 v_t}(\tau_{sx},\tau_{sy}) \quad [6]$$

At $z = -d$,

$$u\frac{\partial d}{\partial x}+u\frac{\partial d}{\partial y}+w=0, \quad \left(\frac{\partial u}{\partial z},\frac{\partial v}{\partial z}\right)=\frac{1}{\rho_0 v_t}(\tau_{bx},\tau_{by}) \quad [7]$$

where $\vec{\tau}_b=(\tau_{bx},\tau_{by})$ and $\vec{\tau}_s=(\tau_{sx},\tau_{sy})$ are the bottom and surface wind stresses, respectively.

$$\frac{\vec{\tau}_b}{\rho_0}=c_f\vec{u}_b|\vec{u}_b| , \quad \vec{\tau}_s=\rho_a c_d\vec{u}_w|\vec{u}_w| \quad [8]$$

in which $c_f$ is the drag coefficient, $\vec{u}_b$ = ($u_b$, $v_b$) is the flow velocity above the bottom. $\rho_a$ is the density of air, $c_d$ is the drag coefficient of air, and $\vec{u}_w$ = ($u_w$, $v_w$) is the wind speed 10 m above the sea surface.

The fluid is assumed to be incompressible. Hence, the density, $\rho$ does not depend on the pressure, but is only dependent on the temperature, $T$.

The transport of temperature, $T$, follows the general advection-dispersion equation as:

$$\frac{\partial T}{\partial t}+\frac{\partial uT}{\partial x}+\frac{\partial vT}{\partial y}+\frac{\partial wT}{\partial z}=F_T+\frac{\partial}{\partial z}\left(D_v\frac{\partial T}{\partial z}\right)+\widehat{H}+T_sS \quad [9]$$

where $\widehat{H}$ is a source term due to heat exchange with the atmosphere. $D_v$ is the vertical turbulent (eddy) dispersion coefficient. $T_s$ is the temperature of the source. $F_T$ is the horizontal dispersion terms defined by:

$$F_T=\left[\frac{\partial}{\partial x}\left(D_h\frac{\partial}{\partial x}\right)+\frac{\partial}{\partial y}\left(D_h\frac{\partial}{\partial y}\right)\right]T \quad [10]$$

 

where $D_h$ is the horizontal dispersion coefficient (Rodi, 1984).

The transport for the effluent concentration, $C$ is given by:

$$\frac{\partial C}{\partial t} + \frac{\partial uC}{\partial x} + \frac{\partial vC}{\partial y} + \frac{\partial wC}{\partial z} = F_c + \frac{\partial}{\partial z}\left(D_v \frac{\partial C}{\partial z}\right) - k_p C + C_s S \quad [11]$$

in which $k_p$ is the linear decay rate of the effluent, $C_s$ is the concentration of the effluent at the source, $D_v$ is the vertical dispersion coefficient, and $F_c$ is the horizontal diffusion term defined by:

$$F_c = \left[\frac{\partial}{\partial x}\left(D_h \frac{\partial}{\partial x}\right) + \frac{\partial}{\partial y}\left(D_h \frac{\partial}{\partial y}\right)\right] C \quad [12]$$

where $D_h$ is the horizontal dispersion coefficient.

The spatial discretization of the primitive equations is performed using a cell-centered finite volume method. The spatial domain is discretized into non-overlapping element/cells. In the horizontal plane an unstructured grid is used while in the vertical domain a structured discretization is used. For the time integration, a semi-implicit approach is utilized where the horizontal terms are treated explicitly and the vertical terms are treated implicitly.

The advantage of the flexible mesh is that the mesh can be designed to accurately resolve the details around islands, structures, intake/outfalls and land/water boundaries while the same grid apply a coarse resolution in areas of less interest.

## 2.2 Modeling scenarios

In this study, we focus on generalized straight rectangular channel. Figure 1 shows the model domain and the location of the outfall. The width of the channel ($B$) is set to 100 m and the length of the channel is 4500 m with the outfall located at 500 m from the upstream boundary. The constant water depth of the channel varies from 1.25 m to 15 m. The liquid effluent focuses on non-decaying radionuclide discharged intermittently along with cooling water. The excess water temperature of the cooling water is 8 ºC as compared to the ambient channel water. The time series of normalized effluent concentration discharged from the outfall with the maximum value of 1 is shown in Figure 2. The period of effluent discharge is 2.5 hours with about 6-day interval.

The liquid effluent along with cooling water is discharged from the bottom on the side, as shown in Figure 3 for the sketch. The constant cooling water discharge from the outfall ($Q_o$) is set to be 10 m$^3$/s with a speed of 1 m/s perpendicular to the bank. The current speed of the ambient flow varies from 0.1 m/s to 0.8 m/s. Table 1 presents the modeling scenarios in this study. The ratio of the ambient flow discharge to the outfall discharge ($\gamma = Q_a/Q_o$) and the ambient Froude number ($Fr = U/(gh)^{0.5}$) for each scenario are also presented in the table.

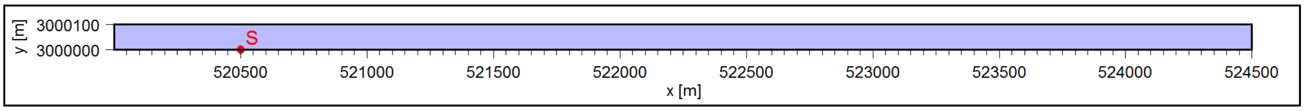


**Figure 1**. Model domain with location of the outfall.

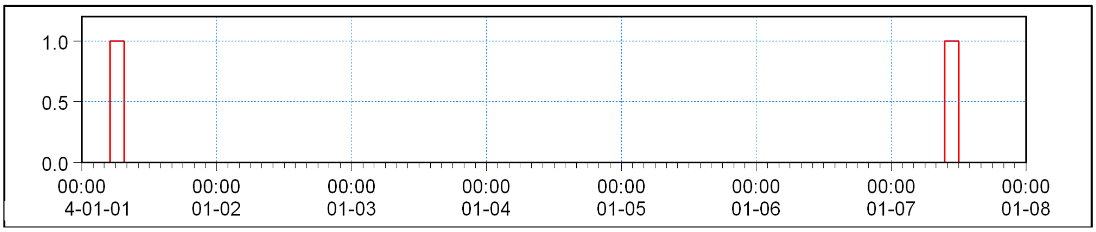


**Figure 2**. Time series of normalized effluent concentration discharged from the outfall.

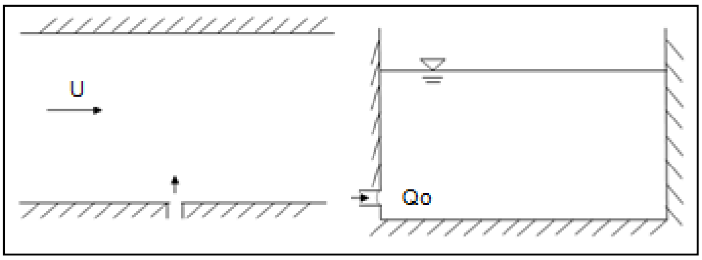


**Figure 3**. Sketch of the outfall discharge, top view (left) and side view (right).

 

**Table 1**. Modeling scenarios in the study ($Q_o$ = 10m$^3$/s).

| Scenarios | Width *B* [m] | Water depth *h* [m] | *β=B/h* | Ambient current speed *U* [m/s] | *γ=Q$_a$/Q$_o$* | *Fr=U/(gh)$^{0.5}$* |
|---|---|---|---|---|---|---|
| Scen-01 | 100 | 15 | 6.67 | 0.4 | 60 | 0.033 |
| Scen-02 | 100 | 15 | 6.67 | 0.2 | 30 | 0.016 |
| Scen-03 | 100 | 15 | 6.67 | 0.1 | 15 | 0.008 |
| Scen-04 | 100 | 10 | 10 | 0.4 | 40 | 0.040 |
| Scen-05 | 100 | 10 | 10 | 0.2 | 20 | 0.020 |
| Scen-06 | 100 | 10 | 10 | 0.1 | 10 | 0.010 |
| Scen-07 | 100 | 7.5 | 13.33 | 0.8 | 60 | 0.093 |
| Scen-08 | 100 | 7.5 | 13.33 | 0.4 | 30 | 0.047 |
| Scen-09 | 100 | 7.5 | 13.33 | 0.2 | 15 | 0.023 |
| Scen-10 | 100 | 7.5 | 13.33 | 0.1 | 7.5 | 0.012 |
| Scen-11 | 100 | 5 | 20 | 0.8 | 40 | 0.114 |
| Scen-12 | 100 | 5 | 20 | 0.4 | 20 | 0.057 |
| Scen-13 | 100 | 5 | 20 | 0.2 | 10 | 0.029 |
| Scen-14 | 100 | 5 | 20 | 0.1 | 5 | 0.014 |
| Scen-15 | 100 | 2.5 | 40 | 0.4 | 10 | 0.081 |
| Scen-16 | 100 | 2.5 | 40 | 0.2 | 5 | 0.040 |
| Scen-17 | 100 | 2.5 | 40 | 0.1 | 2.5 | 0.020 |
| Scen-18 | 100 | 1.25 | 80 | 0.2 | 2.5 | 0.057 |
| Scen-19 | 100 | 1.25 | 80 | 0.1 | 1.25 | 0.029 |

2.3 Model set up

As described above, the model domain of the channel is 100 m wide, and 4500 m long with different water depth. Figure 4 shows the model grid in the whole (horizontal) domain and zoomed in local area. The model grid is generated in combination of triangular and quadrangular mesh with a fine resolution of 1 m around the outfall. Being a compromise between resolving the outfall characteristics and computation time, 10 equidistant Sigma layers have been used for the vertical mesh in the model. The outfall is located at Layer 2 (Layer 1 corresponds to the bottom).

Bed resistance is one of main calibration parameters for the model set up. In the previous studies on the power plants in Hunan province in China, the calibrated Manning numbers (*n*) varied from 0.02 s/m$^{1/3}$ to 0.04 s/m$^{1/3}$ (Zeng, 1997; Chen, 2010). As the proposed site of inland power plant is located in Hunan province, a roughness height corresponding to the Manning number (*n*) of 0.032 s/m$^{1/3}$ is applied in this study.

The Smagorinsky formulation (Smagorinsky, 1963) with a default coefficient of 0.28 has been utilized for the horizontal eddy viscosity. The turbulence module log-law formulation has been applied for the vertical eddy viscosity. The dispersion coefficients are determined by doing sensitivity tests.

For the boundary conditions, the specified velocities have been applied for the upstream and downstream boundary conditions in order to have a certain stable water level at the outfall. A simulation period of 25 hours is selected to ensure that the effluent concentration is down to zero in the whole domain.

It is noted that, as the liquid effluent is discharged accompanied with cooling water, the distribution of concentration is influenced by the buoyancy effect due to the temperature difference. Therefore, the effluent concentration and the temperature of cooling water are simulated simultaneously in the modeling (Zhang, 2015).

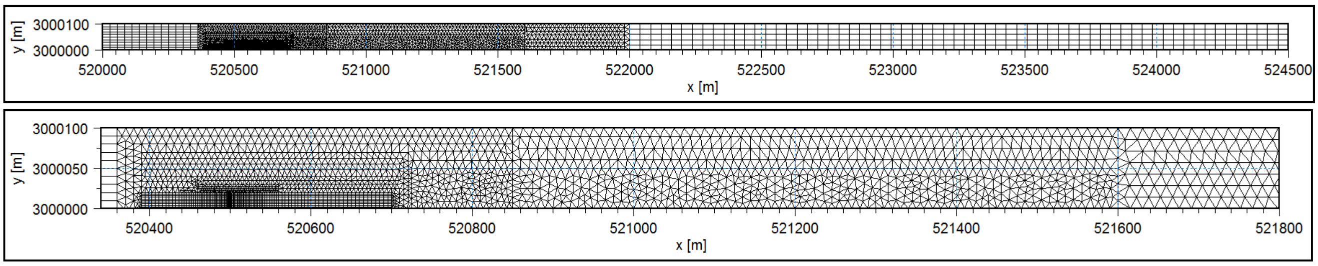


**Figure 4**. Model grid in the whole domain (upper) and the local area (lower).

 

# 3 MODEL RESULTS AND ANALYSIS

## 3.1 Distribution of the maximum effluent concentration

The distributions of effluent concentration have been simulated for all the scenarios with different water depths and ambient current speeds. As the effluent concentration is discharged intermittently, the concentration in the domain changes with time. Thus, the maximum concentration during the simulation period at each element has been picked first, which is the basis for the data analysis in the following section. Figure 5 shows the maximum concentration during the whole period at the surface, the intermediate layer and the bottom in the local area for Scen-12 with the water depth of 5 m and current speed of 0.4 m/s. The maximum dispersed area of the effluent occurs at the surface among the vertical layers. The comparison of the maximum concentration at the surface between the scenarios with different ambient current speeds is shown in Figure 6. The dispersed area of the effluent increases as the ambient current speed decreases.

Considering the specific limit on the concentration of radioactive liquid effluent ($^{3}H$) on the cross-section (y-z) at 1 km downstream from the outfall for inland nuclear power plants in China, the concentration on this specific cross-section for each scenario has been extracted from the model results and analyzed. Figure 7 and Figure 8 show the maximum concentration distributed on this cross-section with water depth of 5 m and 15 m, respectively. Again, the dispersed area of the effluent increases as the ambient current speed decreases. As the water depth becomes deeper, the maximum concentration on the cross-section decreases.

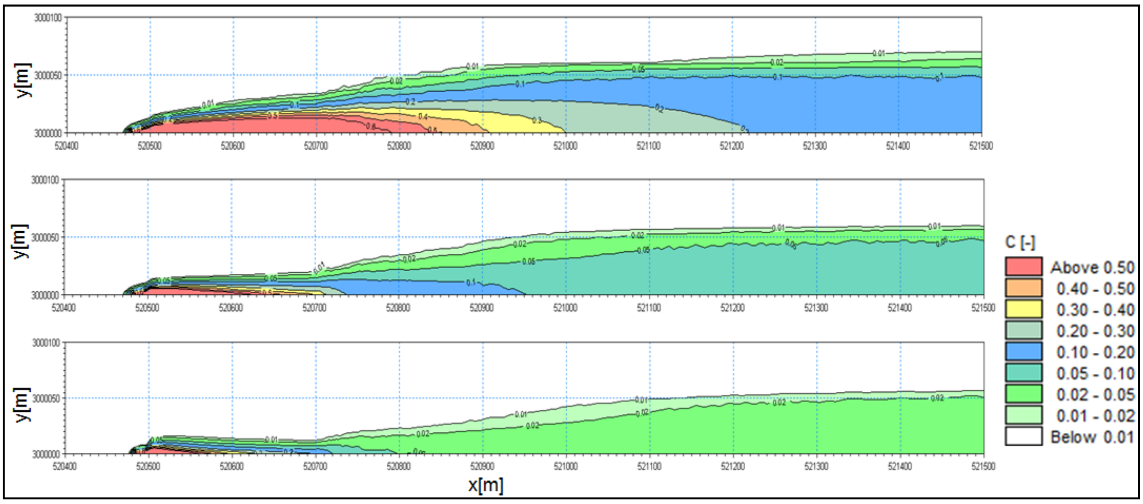


**Figure 5**. The maximum concentration at the surface (upper), the intermediate layer (middle) and the bottom (lower) for Scen-12 with h = 5 m and U = 0.4 m/s in local area.

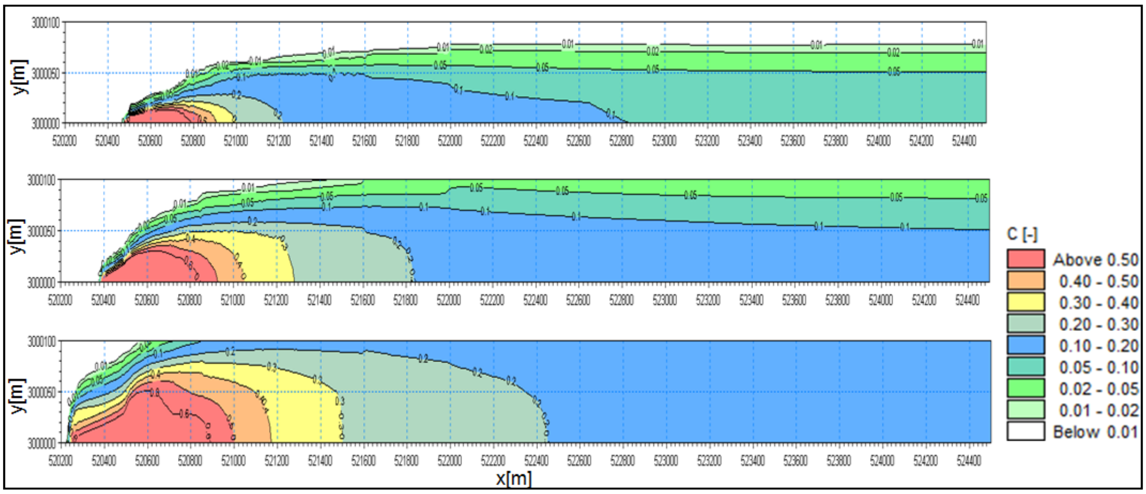


**Figure 6**. The maximum concentration at the surface in the whole domain for the scenarios with h = 5 m, U = 0.4 m/s (upper), U = 0.2 m/s (middle), U = 0.1 m/s (lower).

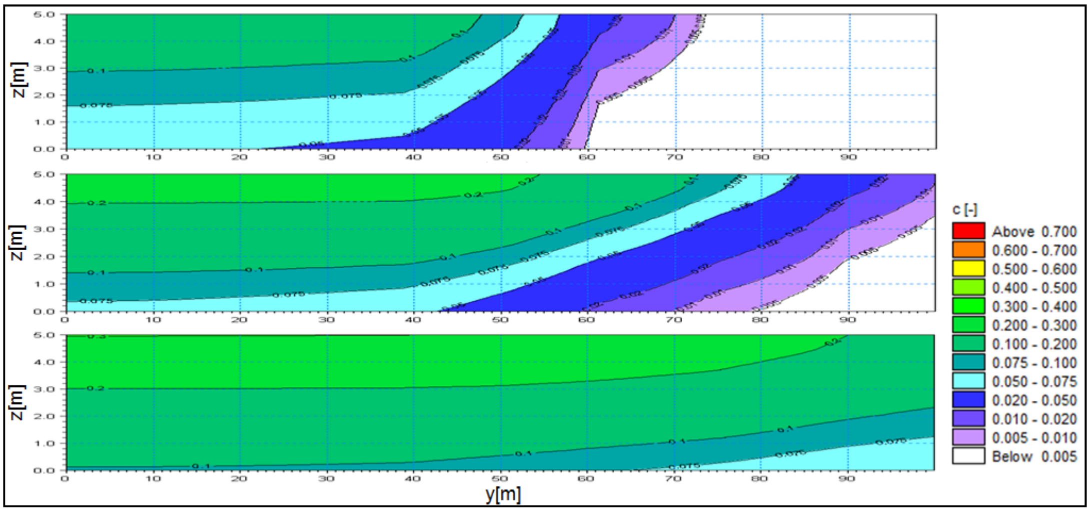


**Figure 7**. The maximum concentration on the cross-section (y-z) at 1 km downstream from the outfall for the scenarios with h = 5 m, U = 0.4 m/s (upper), U = 0.2 m/s (middle), U = 0.1 m/s (lower).

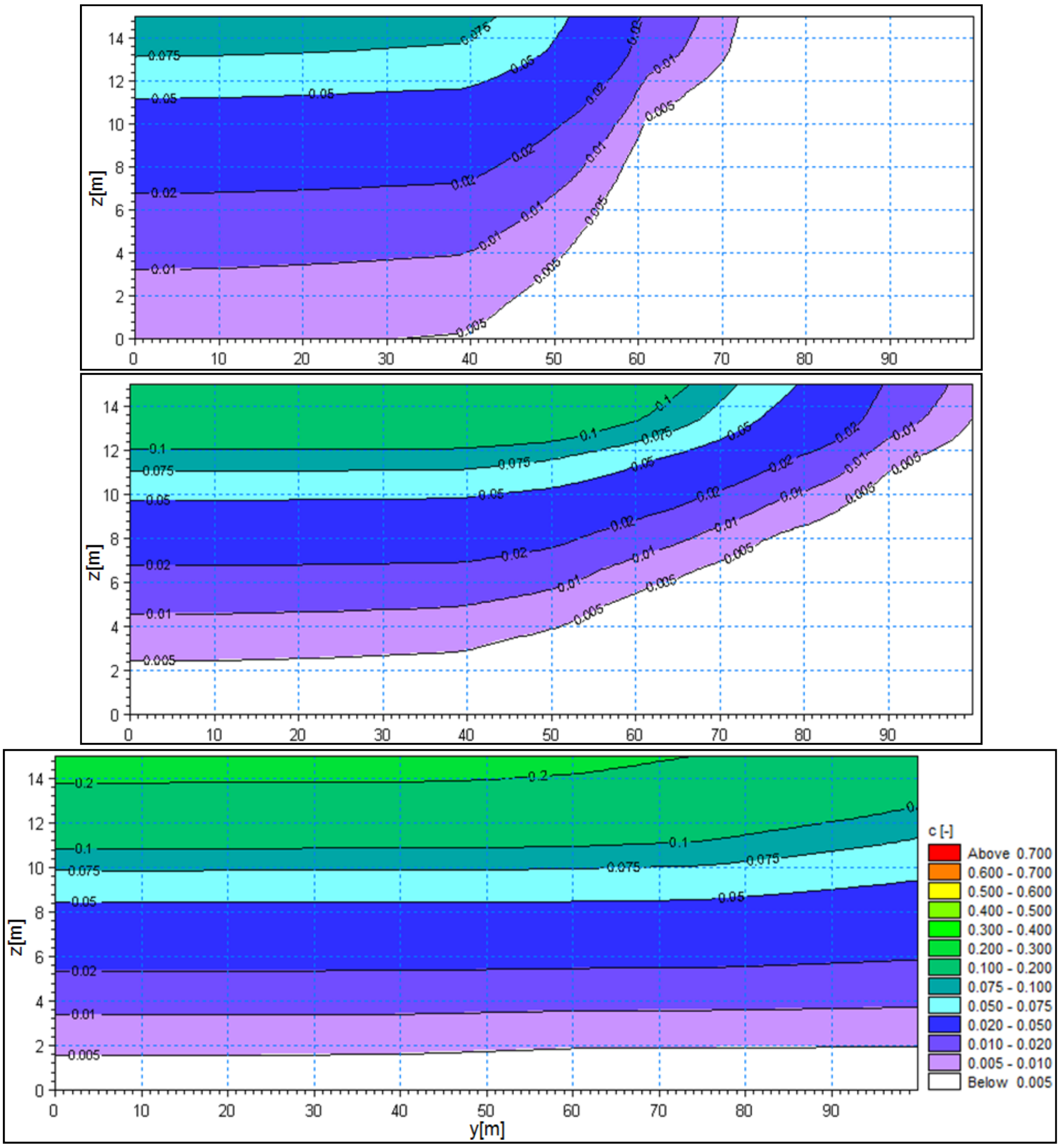


**Figure 8**. The maximum concentration on the cross-section (y-z) at 1 km downstream from the outfall for the scenarios with h = 15m, U = 0.4 m/s (upper), U = 0.2 m/s (middle), U = 0.1 m/s (lower).

 

3.2 Analysis of the concentration on the specific cross-section

We focus on the concentration on the cross-section at 1 km downstream from the outfall, due to the concentration limit on this specific cross-section for inland nuclear power plants in China as mentioned above.

The mean value of the maximum concentration during the simulation period (mean concentration for short, $C_{mean}$) on this specific cross-section for each scenario has been counted and shown in Figure 9. The maximum depth-averaged concentration ($C_{max}$) on this cross-section has also been counted and shown in Figure 10 for all the scenarios. Both $C_{mean}$ and $C_{max}$ increase as expected when the water depth becomes shallower or the ambient current speed goes down.

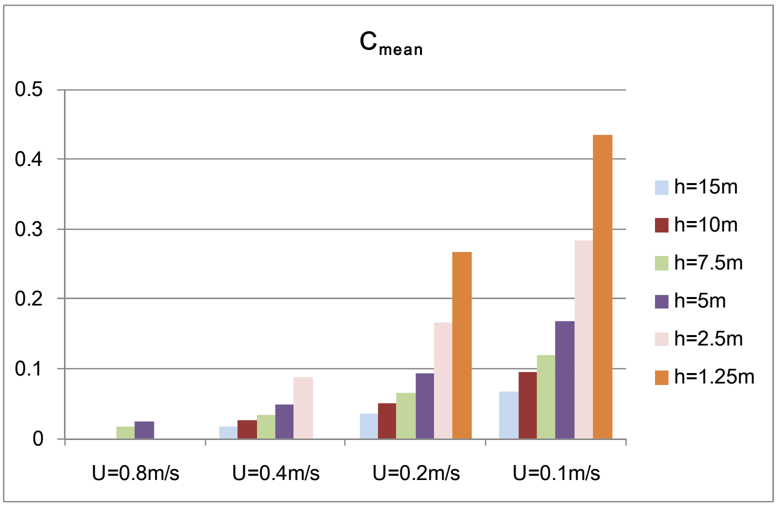


**Figure 9**. Mean concentration on the cross-section at 1 km downstream from the outfall.

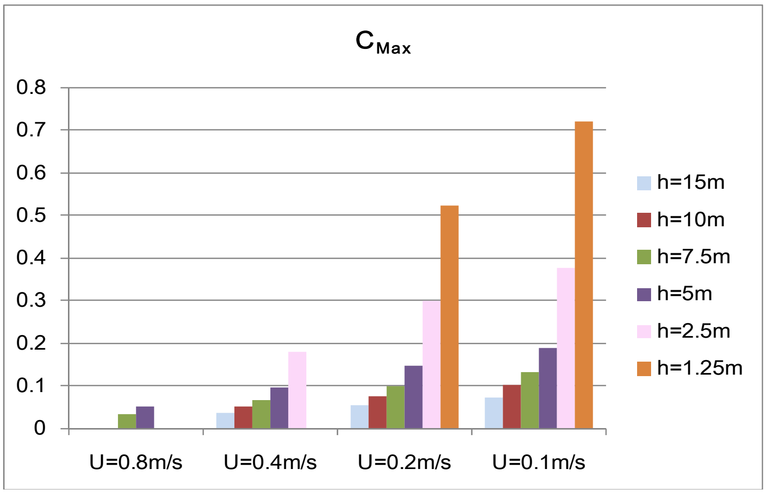


**Figure 10**. Maximum depth-averaged concentration on the cross-section at 1 km downstream from the outfall.

Taking reference of the study on the heat dispersion of cooling water for inland power plants (Zhang et al., 2015), it is assumed that the mean concentration ($C_{mean}$) and the maximum depth-averaged concentration ($C_{max}$) on the cross-section can be expressed by a function of the ratio of width to water depth ($\beta$), the ratio of ambient flow discharge to outfall discharge ($\gamma$) and the ambient Froude number ($Fr$), and written as:

$$C_m = f(\gamma, \beta, Fr) \quad [13]$$

in which $C_m$ denotes the mean concentration ($C_{mean}$) or the maximum depth-averaged concentration ($C_{max}$) on the cross-section.

A direct relation between the mean concentration ($C_{mean}$) on the cross-section and the ratio of ambient flow discharge to outfall discharge ($\gamma$) is found and shown in Figure 11. $C_{mean}$ decreases gradually as the ratio $\gamma$ goes up. Based on this relation, the mean concentration ($C_{mean}$) on the cross-section can be approximately estimated by the following expression:

$$C_{mean}=0.629\gamma^{-0.859} \quad [14]$$

 

According to Eq. [13], the relation among the maximum depth-averaged concentration ($C_{max}$) on the cross-section, the ratio of ambient flow discharge to outfall discharge ($\gamma$), the ratio of width to water depth ($\beta$) and the ambient Froude number ($Fr$) have been analyzed. A fitting curve has been found for the relation between $C_a$ ($C_a = C_{max}\beta^{-2/3}$) and the combined parameter of $\gamma_a$ ($\gamma_a = \gamma Fr^{1/2}$) for all the scenarios, as shown in Figure 12. Based on this curve, the maximum depth-averaged concentration ($C_{max}$) on the cross-section can be approximately estimated by:

$$C_{max}=0.0228\beta^{2/3}(\gamma Fr^{1/2})^{-0.389} \qquad [15]$$

The approximate estimations of the mean concentration ($C_{mean}$) and the maximum depth-averaged concentration ($C_{max}$) on the cross-section at 1 km downstream from the outfall obtained above in Eq. [14] and Eq. [15] could be used as reference for site selection of inland nuclear power plant in China.

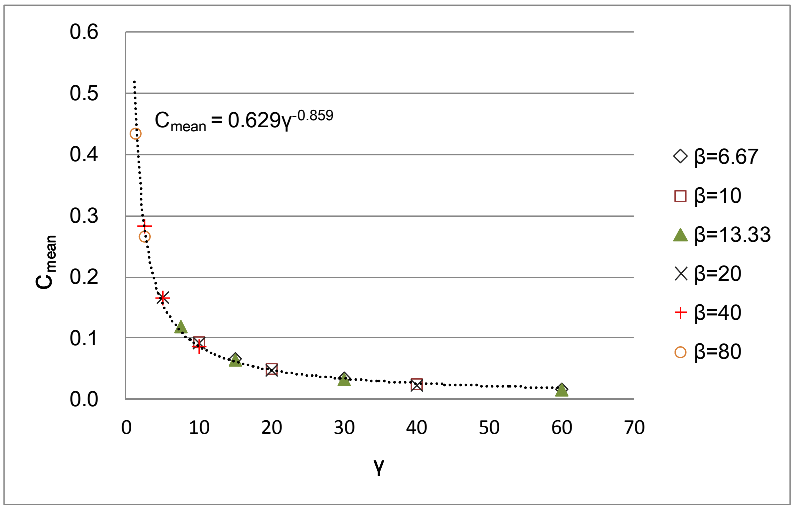


**Figure 11**. Relation between $C_{mean}$ and $\gamma$.

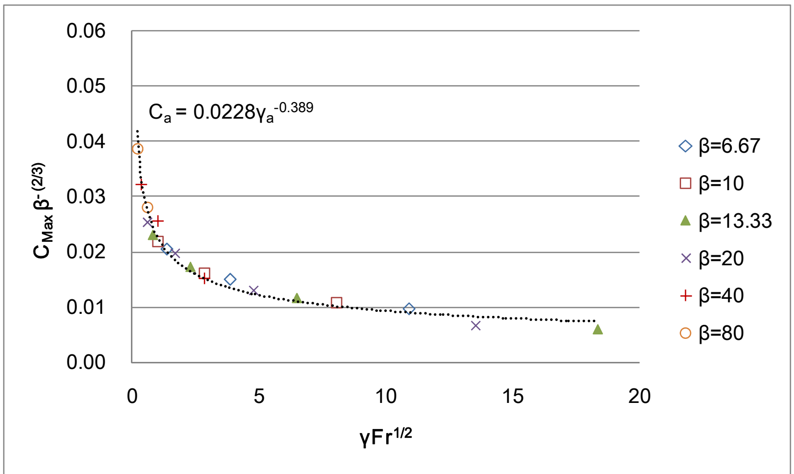


**Figure 12**. Relation between $C_a$ ($C_a = C_{max}\beta^{-2/3}$) and $\gamma_a$ ($\gamma_a = \gamma Fr^{1/2}$).

## 4 CONCLUSIONS

A numerical modeling using MIKE 3 HD with flexible mesh has been carried out to study the dispersion of liquid effluent for the purpose of the site selection of inland power plants. A series of scenarios with different ratios of width to water depth and various ratios of ambient flow discharge to outfall discharge in straight rectangular channel have been simulated. Based on the modeling results, the mean effluent concentration and the maximum depth-averaged concentration on the cross-section at 1 km downstream from the outfall have been analyzed. Approximate estimations of the mean concentration and the maximum depth-averaged concentration on this cross-section have been established, which could be used as a reference for site selection of inland nuclear power plant in China.

 

**REFERENCES**

DHI. (2009). MIKE 21 & 3 Flow Model FM Hydrodynamic and Transport Module Scientific Documentation. *DHI Water & Environment,* 1-24.

Rodi, W. (1984). Turbulence Models and Their Application in Hydraulics.

Zeng, P. (1997). Report of Numerical Modeling Study on Cooling Water for Zhuzhou Power Plant in Phase II. *China Institute of Water Resources and Hydropower Research,* 5-8.

Chen, X. (2010). Report of Numerical Modeling Study on Effluent Discharge of Changde Nuclear Power Plant in Hunan Province. *China Institute of Water Resources and Hydropower Research,* 13-16.

Smagorinsky, J. (1963). General Circulation Experiments with the Primitive Equations: I. The Basic Experiment. *Monthly weather review,* 91(3), 99-164.

Zhang, H., Ji, P., Zhao, Y., et al. (2015). Numerical Modeling Study on Heat Dispersion of Cooling Water for Inland Power Plants. *E-proceedings of the 36th IAHR World Congress*.

Proceedings of the 37th IAHR World Congress
August 13 – 18, 2017, Kuala Lumpur, Malaysia

# NUMERICAL SIMULATION OF SEDIMENT TRANSPORT AND SUSPENDED SOLID DISTRIBUTION DUE TO THE DAMAGE OF RECLAMATION WALL IN MINAMATA BAY

EDISTRI NUR FATHYA[(1)], SHINICHIRO YANO[(2)], AKITO MATSUYAMA[(3)] & AKIHIDE TADA[(4)]

[(1)] Dept. of Maritime Engineering, Kyushu University, Fukuoka, Japan,
edisfathya@gmail.com
[(2)] Dept. of Urban and Environmental Engineering, Kyushu University, Fukuoka, Japan,
yano@civil.kyushu-u.ac.jp
[(3)] National Institute for Minamata Disease, Japan,
[(4)] Division of System Science, Nagasaki University, Japan

## ABSTRACT

More than 25 years after the dredging and reclamation projects of high mercury-contaminated sediment were conducted, the possibility of sludge leakage from the reclaimed area to Minamata Bay may threaten the lives of the marine environment and people around the bay. The inevitable problem could occur because the wall sheet will deteriorate as time goes by. In order to predict the condition of sediment leakage, we conduct the numerical simulation of sediment transport and suspended solid (SS) distributions from the reclaimed wall area to the bay. Delft3D software including the rectangular variable grid and 40 tidal components as boundary condition is imposed, also we assume a part of the wall in the north and south part collapsed and for one day in rainy season, the high contaminated sediments including mercury are released to the bay. The results show that SS distribution to the Minamata Bay is more significant when the south part of reclamation wall collapses than the north part. In the upper layer, when the low tide occurs, barotropic and baroclinic flow move SS to southwest direction entering Minamata Bay and the results of baroclinic flow show a faster current velocity and larger area of distribution than barotropic flow. On the other hand, at high tide, the SS can be distributed around the northern area. After 30 days, both barotropic and baroclinic flows finally spread and move the SS to Fukuro Bay, which is a small semi-enclosed bay at the head of Minamata Bay, and the sediment above seabed to south entering the Minamata Bay. From the result, in the upper layer, it can be assumed that baroclinic flow is significantly distributing SS to Minamata Bay. Meanwhile, in deeper layer, barotropic and baroclinic flow almost have a similar contribution in transporting the sediment from reclamation wall to the bay.

**Keywords:** Lifetime of reclamation wall; sediment transport; suspended solid; mercury; Minamata bay.

## 1 INTRODUCTION

The Minamata disease tragedy that occurred 60 years ago was caused by methylmercury (MeHg) contamination produced by the inorganic mercury disposal by a chemical factory for around 40 years (Minamata City, 2007). Furthermore, this problem has been resolved by dredging and reclamation projects of high contaminated bottom sediment around Minamata Bay. The project which conducted by Kumamoto prefectural government was held on 1977 to 1990. The project carried out around 1.5 million ton of high contaminated sediment from the bay to the coastal area. Over around 2.1 km$^2$ bay area, which contained more than 25 ppm of Hg, was dredged and reclaimed into 0.58 km$^2$ enclosed area in the coastal region (Balogh et al., 2015).

Before dredged the high contaminated bottom sediment, the projects started with the installation of boundary nets to prevent the mixing of contaminated and non-contaminated fish (Hirose and Yamaguchi, 1990). The suction dredging by cutterless suction dredgers was chosen to prevent the sediment mixing and muddiness during the dredging work (Hirose and Yamaguchi, 1990; Yoshinaga, 1995). The sludge containing methylmercury accumulated in the bay on the reclamation area as thick as 4 m at the most (Kashiranui, 2014). Meanwhile, in the inner bay, the mercury basically only occurred in an upper thin layer of bottom sediment. For effective dredging work, the 50 cm of bottom sediment in the bay area was dredged and reclaimed it into the reclamation area (Yoshinaga, 1995). Sediment discharged into the reclamation area was kept under water and covered with a sandproof membrane, particular volcanic ash earth and mountain soil (Hirose and Yamaguchi, 1990). The land is now 40 ha amenities called Eco-park with athletic fields, a rose garden, etc. (Kashiranui, 2014).

After the remediation project, the concentration of mercury in Minamata Bay was reducing significantly from around 2,700 ppm to 8.85 ppm (Tomiyasu et al., 2006). However, the sludge with a high amount of methylmercury remains underground and so does the fear of leak of the sludge as the walls are naturally deteriorating (Kashiranui, 2014). Moreover, the project was held around 30 years ago and it is inevitable that the strength of the reclamation wall in present condition is reducing and might release sediment which was reclaimed to the shore. That incident may threaten the lives of the marine environment and people around the bay.

In order to predict the condition of sediment leakage, we try to simulate in case that the incident occurs by numerical simulation of sediment and suspended solid (SS) distribution from the reclaimed wall area to the bay. We assume the sediment leakage occurs when it rains. When it rains, the sediment around reclamation area would be released from the collapsed walls of reclamation and then the sediment that contains high Hg concentration can enter into the bay with the rain water. Furthermore, the possibility of leakage occurs in the mean of normal rainfall around the bay.

## 2 NUMERICAL MODELING

The numerical simulation of this study is based on Yano et al. (2014) and Fathya et al. (2016a). All of the model parameters and settings are adapted from their study. Here, we used the same domain and grid system to simulate the effect of the damaged wall in the sediment transport and SS distribution around Minamata Bay.

### 2.1 Computational domain and grid

We consider the large area in western part of Kyushu Island include the Ariake Sea and Yatsushiro Sea as our domain (Figure 1) in order to minimize error due to boundary condition. The concerning area is Minamata Bay (red box in Figure 1), which is around 3 km$^2$ large size. Therefore, to get precise result, the variable grid that had been applied in Fathya et al. (2016a) is also applied to the domain here and is divided into three grid sizes, first 250 m grid size as the original grid size by Yano et al. (2014), second is 125 m, and the finest is 62.5 m, which Minamata Bay and its surrounding are included. The variable grid system is made by grid module in DELFT3D software. In addition, for the vertical coordinate system, we divide it into five layers σ-coordinate system.

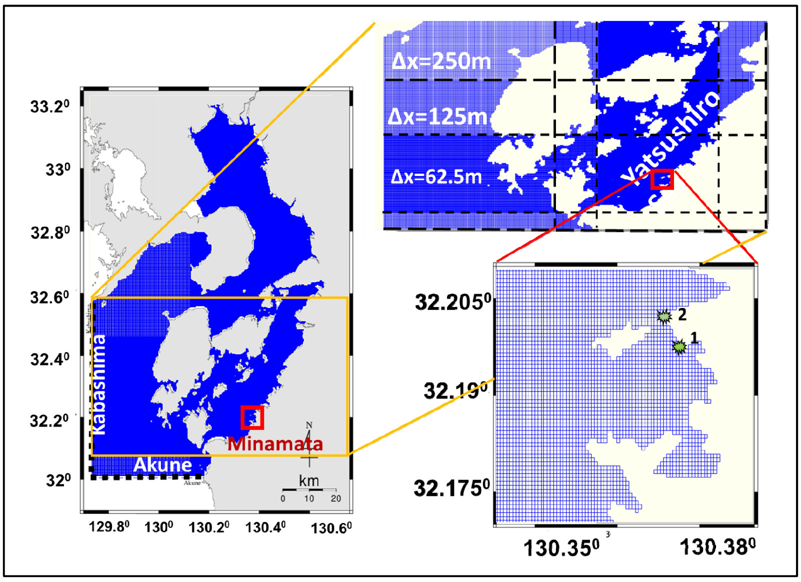


**Figure 1**. Computational domain, grid system, and Minamata Bay grid.

The damage walls are assumed to occur in the south and north part from the reclamation wall (green dots in Figure 1). The simulation is conducted in two times, first, we assumed only the south wall that collapses and second, the damaged wall is on the north side.

### 2.2 Calculation method

The 3D hydrodynamic simulation is conducted by Delft3D in the coastal area. Delft3D is hydro-based software, which includes the flow and sediment transport model, morphological model, ecosystem model, wave model, and so on. The SS distribution is simulated by flow module in Delft3D and also it is used to simulate sediment transport by adapting the moving wall boundary model for a tidal flat area. The horizontal eddy viscosity is evaluated by the sub-grid scale (SGS) model and vertical eddy viscosity is evaluated by k-ε turbulent model including buoyancy effect terms. For the erosion and deposition processes of bottom sediment, from Yano et al. (2014) the Ariathrai-Patheniades equation and Krone's equation were used (Eq. [1] and [2]).

$$E = \begin{cases} M\left(\frac{\tau_b}{\tau_{cr,e}} - 1\right) : \tau_b > \tau_{cr,e} \\ 0 \quad : \quad \tau_b \le \tau_{cr,e} \end{cases} \qquad [1]$$

$$D = \begin{cases} wc_b\left(1 - \frac{\tau_b}{\tau_{cr,d}}\right) : \tau_b < \tau_{cr,d} \\ 0 \quad : \quad \tau_b \ge \tau_{cr,d} \end{cases} \qquad [2]$$

where $E$ : erosion flux (kg/m$^2$/s), $M$ : erosion parameter (kg/m$^2$/s), $D$: deposition flux (kg/m$^2$/s), $w$ : settling velocity (m/s), $c_b$: suspended solid (SS) concentration in the bottom layer (kg/m$^3$), $\tau_b$: bottom shear stress (N/m$^2$), $\tau_{cr,e}$: critical bottom shear stress for erosion, and $\tau_{cr,d}$ : critical bottom shear stress for deposition.

2.3 Boundary conditions, input parameter and scenarios

The two lines on left and below sides, the lines that connected Kabashima and Akune are set as the open boundary (Figure 1). Along the lines, the 40 tidal constituents are installed as tidal input. The major components, $M_2$ and $S_2$, and other components were obtained from field measurement at several tide gauge stations by Yano et al. (2010).

Model parameters for erosion and deposition processes are based on the study by Yano et al. (2014). They used Nakagawa and Yoshida (2008) values for the parameters: *i.e.,* $w$ = 0.0018 m/s, $M$ = 3.3x10$^4$ kg/m$^2$/s, and $\tau_{cr,d}$ = 1.0 N/m$^2$. They considered that re-suspension of bottom sediment occurs in Minamata Bay where tidal current is weak normally, so they set the $\tau_{cr,e}$ at small value of 0.001 N/m$^2$.

Scenarios for the wall damage incident are set when rainy season around June and July. The mean normal rainfall around Minamata and Yatsushiro Sea is 40 mm/hour (Yano et al., 2006). In addition, the reclamation area of Hg sediment is around 0.58 km$^2$, then the flow of SS is calculated as (Eq. [3]):

$$SS\ discharge(m^3/s) = reclamation\ area(m^2) \times rainfall\ mean(m/s) \qquad [3]$$

resulting SS discharge in leaked wall which containing Hg is around 6.47 m$^3$/s. This value is set in the north and south points of damage (green dots in Figure 1). Also, we compare the conditions without riverine freshwater inflow (barotropic) and with freshwater inflow (baroclinic).

The SS concentration leaked from the damaged wall is set to a high value, considering the high mercury concentration around 25 to 2,700 ppm, which has been dredged and reclaimed in Minamata Bay. As the wall collapses, the sediment in reclamation area is released to the bay for about one day and to see the effect of tidal, we set the time of releasing on the neap tide, spring tide, and transition times between them.

The initial bottom sediment around reclamation wall is also set with 1 m thickness value. The horizontal distribution of cumulative deposition thickness of sediment can be considered as a horizontal pattern of total Hg in bottom sediment (Yano et al., 2014). The sediment transport and also hydrodynamic conditions of previous studies (Yano et al., 2010; Yano et al., 2014; Fathya et al., 2016a; Fathya et al., 2016b) have been validated by field observation data and resulting quite good agreement. Considering to similar simulation and conditions and also there is no sufficient data for validating the result of present study, here, we attempt to describe how the SS and sediment transport pattern if the reclamation wall collapses and releasing high concentration Hg to the Minamata Bay.

## 3 RESULTS

### 3.1 Result of suspended solid distribution

#### 3.1.1 South wall damage

Figure 2 shows the results of suspended solid (SS) distribution in the surface layer without freshwater input (barotropic condition) when the south wall of reclamation collapses and when the low tide occurs. The SS is released to the bay in four times: at neap tide, the transition time from neap to spring tide, spring tide, and at spring to the neap tide. The red color is indicating the high concentration of SS that contained Hg and has concentration around 0.01 kg/m$^3$ or equivalent to 10 ppm. This value is set in order to make the area of SS distribution more visible. Meanwhile, the blue color indicates the low concentration of SS. It can be seen that at low tide, the SS is moving toward southwest entering Minamata Bay and at spring tide (Figure 2c), the transport is slightly farther than at neap tide (Figure 2a). Meanwhile, at transition times, the transport is in between the neap and spring tide cases. These differences can be caused by the differences of current velocity, which is high at spring tide and low at neap tide.

 

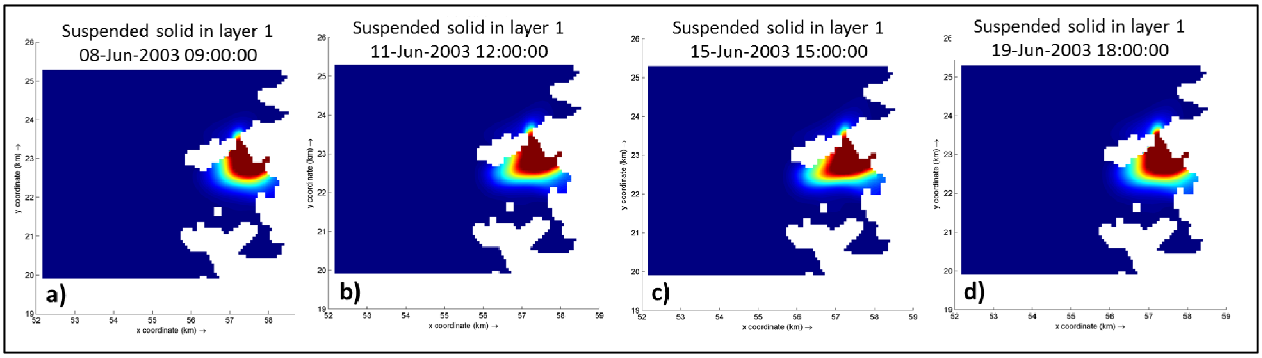


**Figure 2**. SS distribution by the damage of south reclamation wall without freshwater inflow in surface layer at low tide on a) the neap tide, b) the neap to spring tide, c) the spring tide, d) the spring to neap tide.

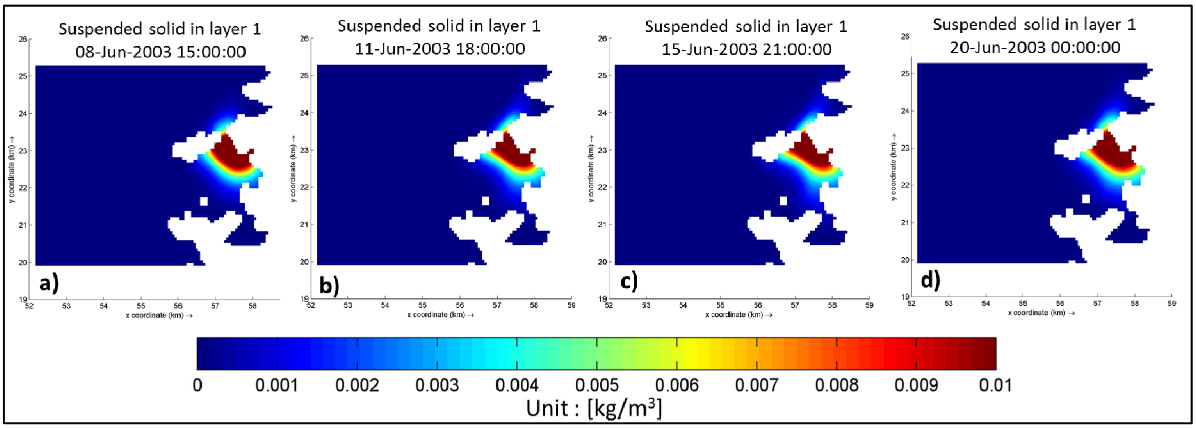


**Figure 3**. SS distribution by the damage of south reclamation wall without freshwater inflow in surface layer at high tide on a) the neap tide, b) the neap to spring tide, c) the spring tide, d) the spring to neap tide.

Meanwhile, at high tide (Figure 3), the transports of SS are quite similar in each time. The SS also moves to Minamata Bay, but it is not as far as low tide occur (Figure 2). There is also no significant difference among the spring, neap, and transition tide. The tidal current at high tide that moves SS to the shore is not as fast as at low tide moves SS entering the bay.

In the case with riverine freshwater inflow (baroclinic), the SS distribution results are shown in Figures 4 and 5. Different from the barotropic case, here, the SS transports are seen significant where the red color is spreading almost in the entire area of the bay. From these results, the baroclinic flow can be expected to be more significant for transporting the SS than barotropic flow. The freshwater inflow has an important role of hydrodynamic conditions around the bay. Although not so significant, the difference also can be seen at low tide in spring tide (Figure 4c) and the area of SS spreading from the damaged wall to Minamata Bay is larger than in the neap tide (Figure 4a).

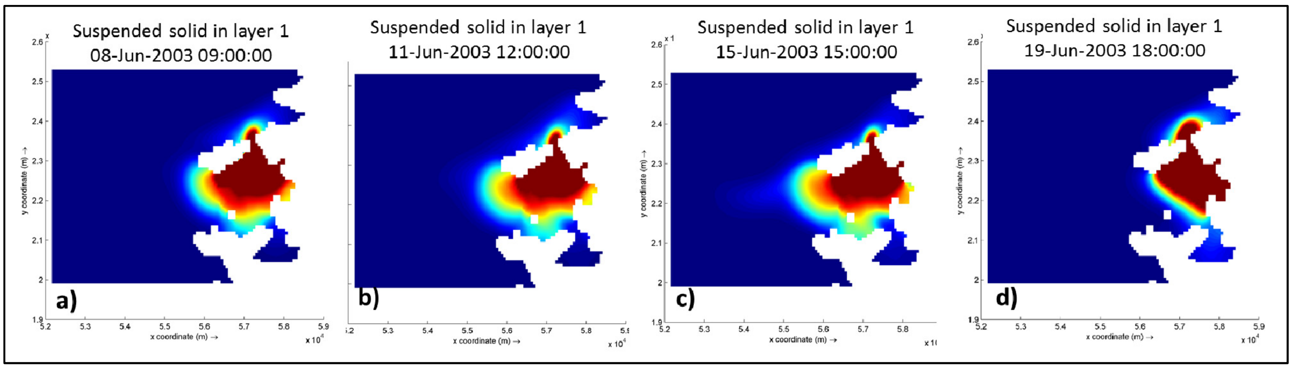


**Figure 4**. SS distribution by the damage of south reclamation wall with freshwater inflow in surface layer at low tide on a) the neap tide, b) the neap to spring tide, c) the spring tide, d) the spring to neap tide.

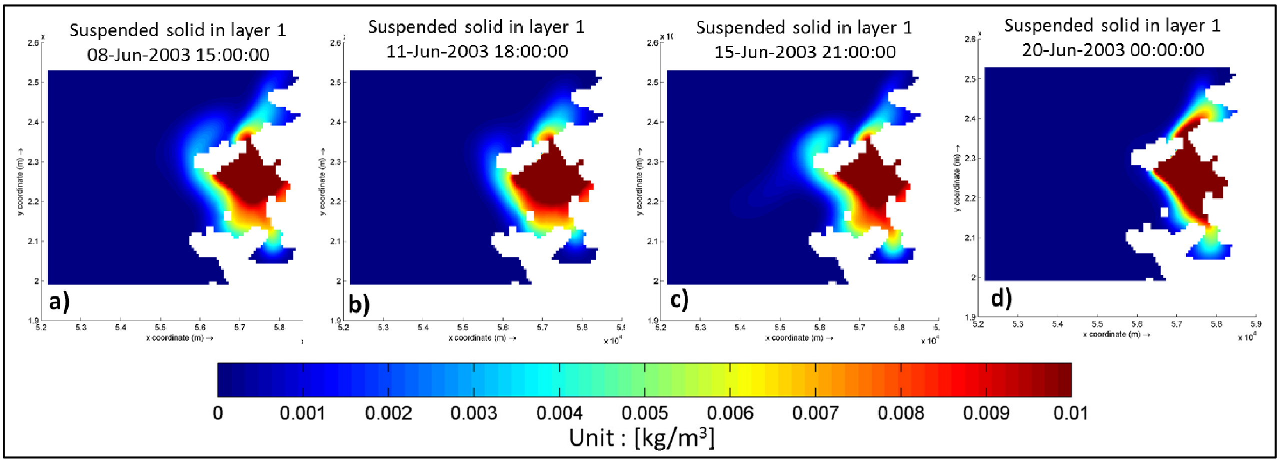


**Figure 5**. SS distribution by the damage of south reclamation wall with freshwater inflow in surface layer at high tide on a) the neap tide, b) the neap to spring tide, c) the spring tide, d) the spring to neap tide.

At high tide (Figure 5), the areas of distribution in the neap and spring tide are quite similar, and it can be seen that the SS moves toward northeast entering the bay, in opposite direction when low tide occurs. This result also indicates that the baroclinic flow is possible to make the magnitude of current in the neap and spring tide quite similar and different with the barotropic flow, because of the effect of freshwater inflow and stratification around the bay.

### 3.1.2 North wall damage

Figure 6 shows the SS distributions in the surface layer when the north part of the reclamation wall collapses in barotropic condition and when the low tide occurs. Meanwhile, Figure 7 shows the result of high tide condition. Here, the transport of SS at the neap, spring, and transitions times also do not show significance difference. However, the transport at spring tide (Figure 6c) is slightly larger than at neap tide (Figure 6a). Likewise the low tide condition, the high tide condition (Figure 7) also shows a similar pattern of transport, but here, the northern transport is more visible than at low tide.

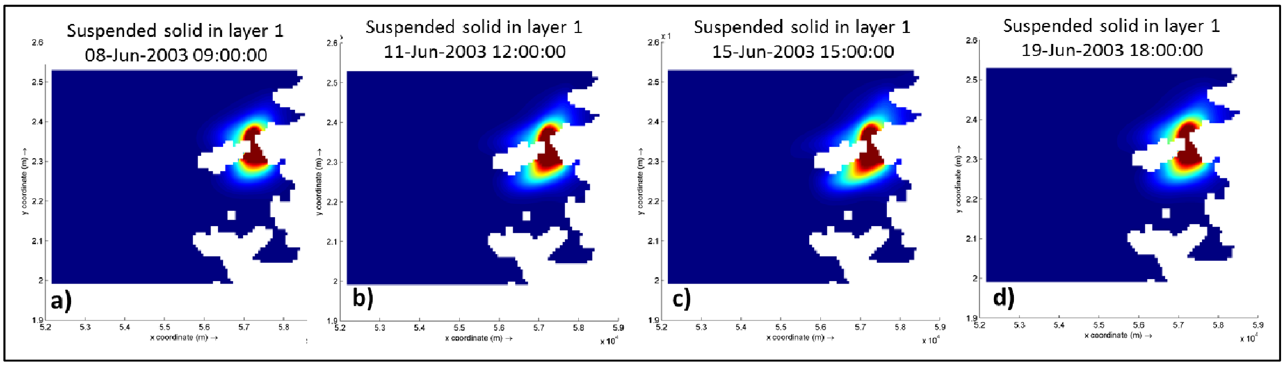


**Figure 6**. SS distribution by the damage of north reclamation wall without freshwater inflow in surface layer at low tide on a) the neap tide, b) the neap to spring tide, c) the spring tide, d) the spring to neap tide.

The damage of north part on reclamation wall could move the SS around the reclamation area and Koiji Island, the small island in front of it. Area of distribution is also smaller than the case that the south part of reclamation wall collapses because the island can block the spreading of SS to Minamata Bay. Here, we can see that on the north side of Minamata Bay, the SS transports at high tide (Figure 7) is farther than that at low tide (Figure 6) due to the position of wall damage.

The influence of freshwater inflow is shown in Figures 8 and 9 below. Similar to the previous case, we can also see that the baroclinic flow gives a significance difference to the SS distribution around the bay. At low tide (Figure 8), the SS moves towards the bay. While at high tide (Figure 9) it is seen moving to the shore and north part from the bay. The distribution of SS in north wall damage seems less spread than the case of south wall collapse as we can see that the red zone with higher SS is not as much as the case of the south wall damage.

 

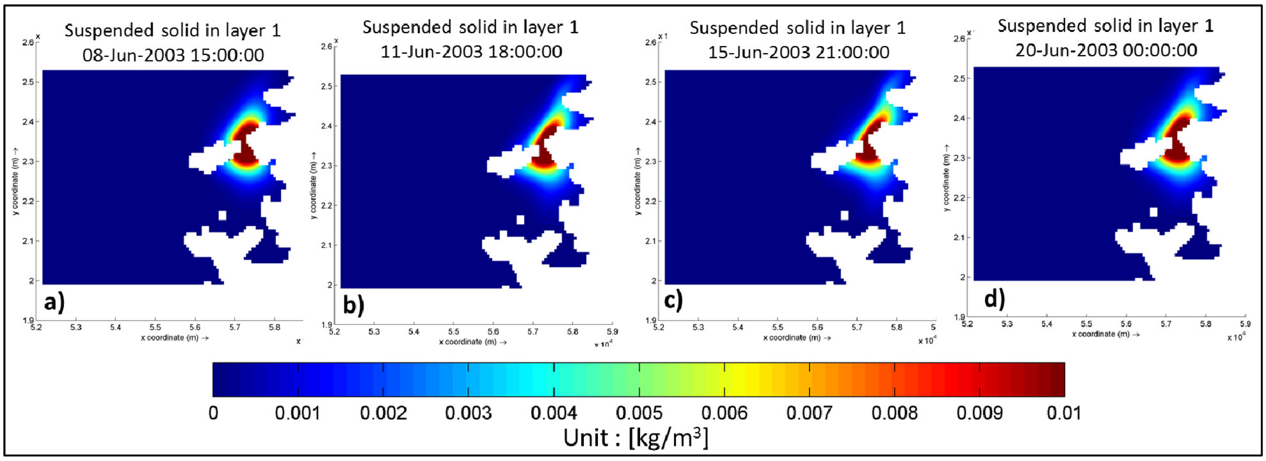


**Figure 7**. SS distribution by the damage of north reclamation wall without freshwater inflow in surface layer at high tide on a) the neap tide, b) the neap to spring tide, c) the spring tide, d) the spring to neap tide.

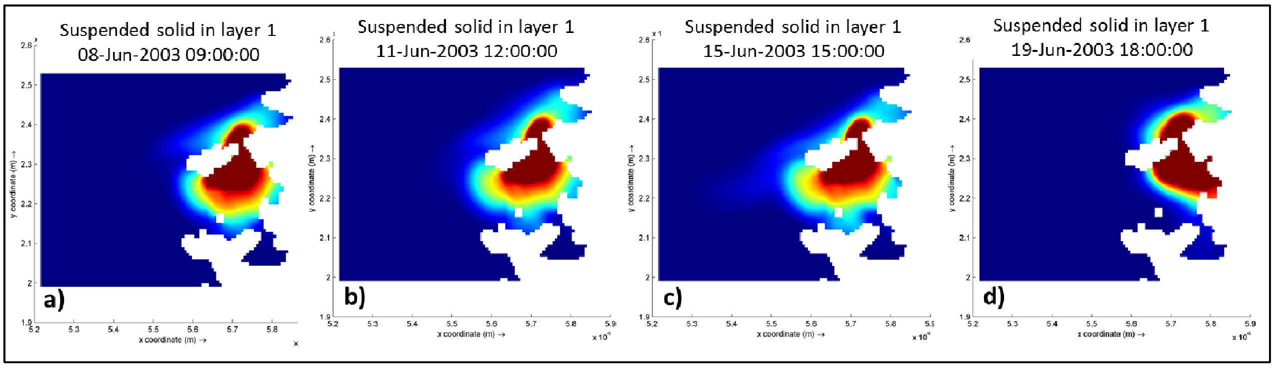


**Figure 8**. SS distribution by the damage of north reclamation wall with freshwater inflow in surface layer at low tide on a) the neap tide, b) the neap to spring tide, c) the spring tide, d) the spring to neap tide.

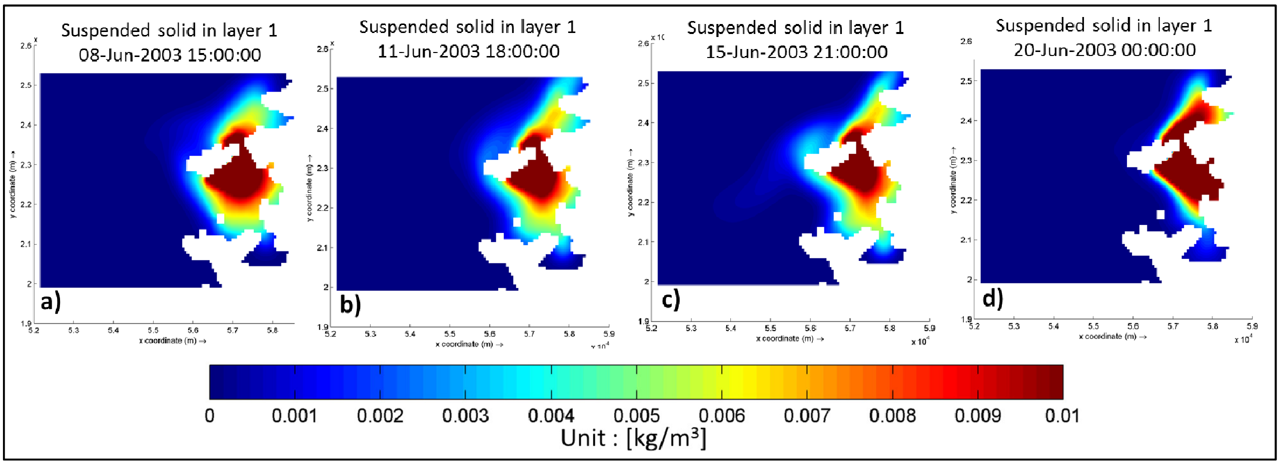


**Figure 9**. SS distribution by the damage of north reclamation wall with freshwater inflow in surface layer at high tide on a) the neap tide, b) the neap to spring tide, c) the spring tide, d) the spring to neap tide.

### 3.1.3 Suspended solid transport after 30 days

After 30 days, the SS movement in each condition (on the surface and at the bottom layer) is shown in Figure 10 and Figure 11 below, respectively. Figure 10a and 10b show the SS transport when the south part of reclamation wall collapses and Figure 10c and 10d when north wall collapse in barotropic condition. Meanwhile, Figure 11a and 11b as well as Figure 11c and 11d show results in baroclinic condition when south wall and north wall collapse, respectively. After 30 days, the SS concentration around the bay is reducing and the plots here show that the highest concentration (red color) is around 1 x $10^{-3}$kg/$m^3$ or equivalent to 1 ppm of SS concentration.

The results of SS transport in the surface (Figure 10a and 10c) and bottom (Figure 10b and 10d) on barotropic condition show quite a similar pattern where the SS mostly transported to Fukuro Bay, a small semi-enclosed bay in Minamata Bay. It is expected to be in the same pattern because the barotropic condition did not calculate the stratification effect and resulting in a similar pattern and direction of SS transport. The position of the damaged wall also gives different results, which the SS released from south wall damage (Figure 10a and 10b) has a much higher concentration of SS than the one from north wall damage (Figure 10c and 10d). As explained above, the south wall damage is more exposed to the bay than the north wall damage, which is blocked by Koiji Island. That can be the cause of the higher concentration of SS in Fukuro Bay when south wall collapse than when the north wall collapse.

Meanwhile, the results of the baroclinic case (Figure 11) show that the SS concentration after 30 days almost washed away from the bay. Only a small amount of SS concentration is also found in Fukuro Bay. On the surface layer (Figure 11a and 11c), the SS has been removed from Minamata Bay whereas at the bottom layer (Figure 11b and 11d), a small amount of SS seem still been concentrated in Fukuro Bay. This result indicates that the baroclinic flow in the surface layer is faster than in bottom layer.

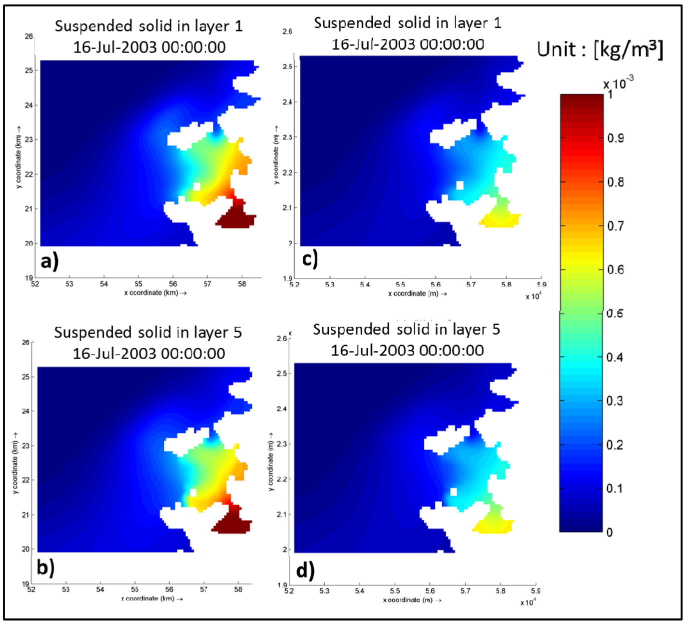


**Figure 10**. SS distribution after 30 days without freshwater inflow by the damage of south reclamation wall in a) Surface and b) Bottom layer and the damage of north reclamation in c) Surface and d) Bottom layer.

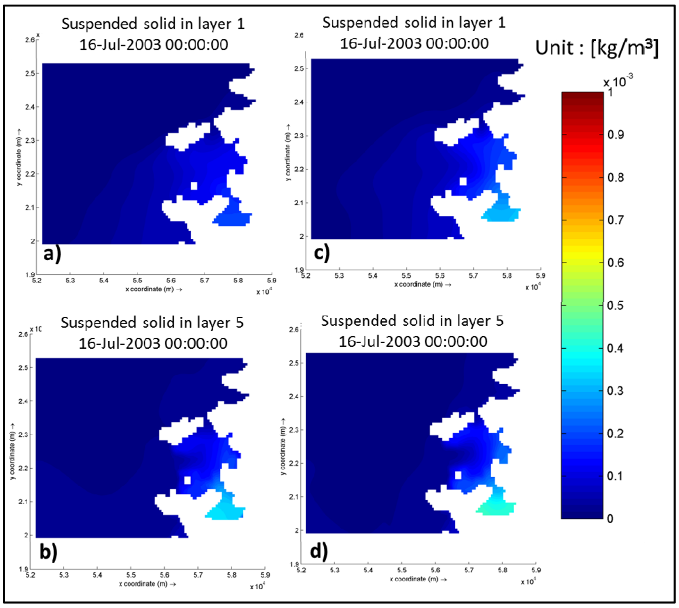


**Figure 11**. SS distribution after 30 days with freshwater inflow by the damage of south reclamation wall in a) Surface and b) Bottom layer and the damage of north reclamation in c) Surface and d) Bottom layer.

## 3.2 Result of sediment transport

The cumulative of erosion and deposition of sediment around reclamation wall after two months are shown in Figure 12 below. Red color indicates deposition and blue color indicates erosion. Figure 12a shows the sediment transport result in barotropic condition and Figure 12b in baroclinic condition. Both barotropic

  / ISSN 1562-6865 (Online) - ISSN 1063-7710 (Print)

and baroclinic flows make a similar pattern of sediment transport where the sediments tend to move to south entering Minamata Bay. The currents above seabed in barotropic and baroclinic conditions around the reclamation wall are not really high as mention by Fathya et al. (2016b) due to the shallow depth and narrow area between the reclamation wall and Koiji Island. Also, because the amount of initial sediment is relatively small, the sediment pattern results can be seen below.

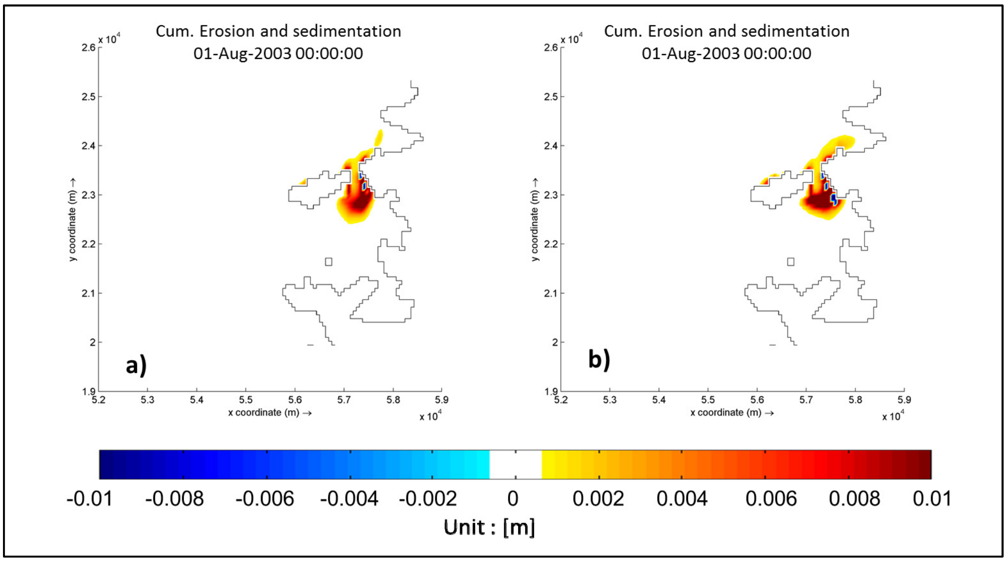


**Figure 12**. Cumulative erosion and deposition of sediment around reclamation wall in Minamata Bay after 2 months a). Without freshwater inflow and b). With freshwater inflow.

On the other hand, the SS concentrations at bottom sediment after two months are shown in Figure 13 below. Different from sediment transport, the SS transport between barotropic and baroclinic conditions are not similar. It can be seen that the barotropic flow moves SS tend to south enter Minamata Bay (Figure 13a) whereas the baroclinic flow moves SS to the north (Figure 13b). The directions of transport here are quite similar to the result of Yano et al. (2014), which showed southern transport by the barotropic flow and northern transport by the baroclinic flow.

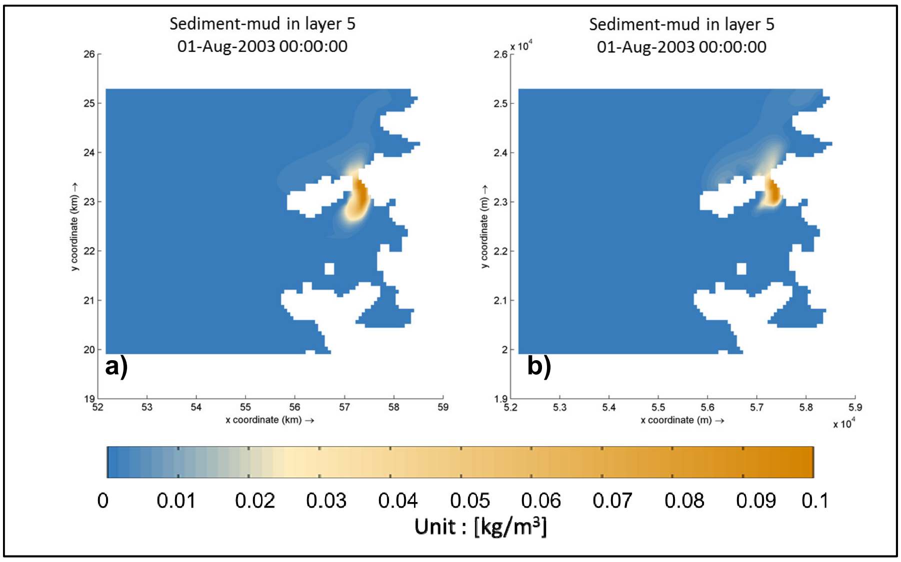


**Figure 13**. Suspended solid distribution in sediment around reclamation wall in Minamata Bay after 2 months a). Without freshwater inflow and b). With freshwater inflow.

## 4 CONCLUSIONS

The results of numerical simulation of SS and sediment transport by the leaked sediment in Minamata Bay reclamation area can differ in several conditions as follow:

1. In the upper layer, the barotropic flow moves SS to southwest direction entering Minamata Bay as well as the baroclinic flow but with faster current speed and resulting larger area of distribution than by barotropic flow. In the bottom layer, the barotropic flow gives a similar pattern of distribution.

 

Meanwhile, the baroclinic flow here is reducing and only moves SS to the area around the reclamation wall;
2. The SS distribution is more significant when the south part of reclamation wall collapses than the north part;
3. The distribution also depends on the tide. When the high tide occurs, a higher concentration can be distributed around the northern area. On the other hand, at low tide, it moves south-westward;
4. After 30 days, both barotropic and baroclinic flows finally spread and move the SS to Fukuro Bay, which is a small semi-enclosed bay in Minamata Bay and the sediment above seabed to south entering Minamata Bay.

From the results, in the upper layer, it can be assumed that baroclinic flow is significantly distributing SS to Minamata Bay whereas in deeper layer barotropic and baroclinic flows almost have a similar contribution in transporting the sediment from reclamation wall to Minamata Bay. Also, it can be expected that the SS transport is intense in baroclinic condition. It spreads to the whole area of Minamata Bay. Although after around two months the SS concentration is reducing, it can be expected that there is still a small amount of SS in Fukuro Bay.

The damage of reclamation wall in Minamata Bay could lead a big disaster for the marine organism and human living in surrounding area. By simulating the SS and sediment transport when the incident occurs, the distribution of high Hg-contaminated sediment can be estimated for a solution to prevent environmental damage and see how far the leaked mercury spreads.

## ACKNOWLEDGEMENTS

The study was supported by JSPS KAKENHI Grant Number 24360200.

## REFERENCES

Balogh, S.J., Tsz-Ki Tsui, M., Blum, J.D., Matsuyama, A., Woerndle, G.E., Yano, S. & Tada. A. (2015) Tracking the Fate of Mercury in the Fish and Bottom Sediments of Minamata Bay, Japan, using stable mercury isotopes, *Environment Science Technology*, 49(9), 5399–5406.

Fathya, E.N., Yano, S., Tada, A. & Matsuyama, A. (2016a). Numerical Simulation of Fine Sediment Transport in Minamata Bay using Variable Grid. *Proceeding of the 20th IAHR-APD Congress 2016.*

Fathya, E.N., Yano, S., Tada, A., Matsuyama, A. & Riogilang, H. (2016b). Impact of Reclamation Project on Mercury-Contaminated Sediment Transport from Minamata Bay into the Yatsushiro Sea. *Journal of JSCE, Ser. B2 (Coastal Engineering),* 72(2), 1285-1290.

Hirose & Yamaguchi. (1990). Mercury Sediment Disposal Work in Minamata Bay. *Civil Engineering in Japan,* Vol. 13(421).

Kanshiranui Planning General Incorporated Association. (2014). *Preparatory Study for Minamata Field Work* (http://www.mkplan.org/download/downloadfiles/kisogakusyuu_en2014.pdf).

Minamata City. (2007). Minamata Disease: Its History and Lesson. *Kumamoto: Minamata City.*

Nakagawa, Y., & Yoshida, H. (2008). Field Observation and Modeling of Suspended Fine Sediment Load in Ariake Bay, Japan. *Proceedings in Marine Science*, 9, 155-163.

Tomiyasu, T., Matsuyama, A., Eguchi, T., Fuchigami, Y., Oki, K., Horvat, M., ... & Akagi, H. (2006). Spatial Variations of Mercury in Sediment of Minamata Bay, Japan. *Science of the Total Environment*, 368(1), 283-290.

Yano, S., Tai, A., Ohfuchi, Y., Tada, A., Matsuyama, A. & Rajar, R. (2006). Field Observation of SS Transport at Mouth of the Minamata Bay. *Annual Journal of Coastal Engineering,* JSCE, 53, 326-330.

Yano, S., Winterwerp, J.C., Tai, A. and Saita, T. (2010). Numerical Experiments on Features of Nonlinear Tide and Its Influences on Sediment Transport in the Ariake Sea and Yatsushiro Sea. *Journal of JSCE, Ser. B2 (Coastal Engineering)*, 66(1), 341-345.

Yano, S., Kawase, H., Hisano, A., Riogilang, H., Tada, A. & Matsuyama, A. (2014). The Effect of Salinity Stratification on Sediment Transport in Minamata Bay. *Proceeding of the 19th IAHR-APD Congress 2014*, in USB memory.

Yoshinaga, K. (1995). Mercury-Contaminated Sludge Treatment by Dredging in Minamata Bay. In *Dredging, Remediation, and Containment of Contaminated Sediments*. ASTM International.

STP 1293, K.R. Demars, G.N. Richardson. R. N. Yong, and R. C. Chaney, Eds., *American Society for Testing and Materials*, Philadelpia, 182-191.

 

# PREDICTING DIFFUSE SOURCE POLLUTION FOR A NUTRIENT-SENSITIVE RIVER BASIN WITH THE SWAT MODEL

ALPER ELÇI[(1)] & SELMA AYAZ[(2)]

[(1)] Department of Environmental Engineering, Dokuz Eylül University, Buca/Izmir, Turkey
alper.elci@deu.edu.tr
[(2)] Environment and Cleaner Production Institute, Tübitak Marmara Research Center, Gebze/Kocaeli, Turkey
selma.ayaz@mam.tubitak.gov.tr

## ABSTRACT

Nutrient-sensitive river basins require special attention with respect to monitoring and controlling point source and diffused source discharges. Water quality models that simulate spatial and temporal changes in surface water quality are important tools in the management of river basin. Particularly, the prediction of diffuse source pollution is an important phase in surface water quality modeling studies. The objective of this study is to predict the spatial and temporal distribution of diffuse source pollution loads for a nutrient-sensitive river basin in north-western Turkey using the GIS-based version of the SWAT model. The results of this study are subsequently used as input data in a related study that involves the development of a surface water quality model for the Mudurnu river. The study area is significant since the Mudurnu river is one of 663 water bodies in the country that are classified as nutrient-sensitive. Primary input data for the SWAT model comprise of land cover data, digital elevation, soil texture map and meteorological records. Average monthly flow rates of surface runoff, lateral subsurface flow, seepage from groundwater, evapotranspiration and deep aquifer recharge are calculated for all sub-basins. The model is calibrated with an automated procedure against measured monthly discharge data. Nutrient loads for each sub-basin are estimated considering basin-wide data on chemical fertilizer and manure usage, population data for septic tank effluents and information about land cover. Diffuse source contaminant loads predicted for each sub-basin indicate that the total annual nitrogen load ranges from 4.6 to 32.78 kg/ha/yr, averaging 15.2 kg/ha per year. Total annual phosphorus load varies between 0.27 – 7.23 kg/ha/yr with an average annual basin load of 2.8 kg/ha. It is concluded that the results from this study are comparable to values published for similar nutrient-sensitive basins and can be directly utilized in related surface water quality modeling studies.

**Keywords:** Simulation; river water quality; SWAT model; nutrients; calibration.

## 1 INTRODUCTION

Nutrient-sensitive river basins require special attention with respect to monitoring and controlling point source and diffused source discharges. It is also crucial for these basins to set attainable water quality targets for sustainability of the river's ecosystem. Water quality models that simulate spatial and temporal changes in surface water quality are important tools in the management of river basin. Particularly, the prediction of diffuse source pollution is an important phase in surface water quality modeling studies. The SWAT model (Arnold et al., 2012) is widely used to simulate river discharge and nutrient loads from river basins of various sizes (e.g. Gassman et al., 2006; Tripathi et al., 2004).

The objective of this study is to predict the spatial and temporal distribution of diffuse source pollution loads for a nutrient-sensitive river basin in north-western Turkey using the GIS-based version of the SWAT model. This study is a component of a water quality modeling study (Tubitak-MAM, 2016) that involves prediction of the overall water quality status of the Mudurnu river and prediction of nutrient concentrations and biological quality indicators based on pollutant reduction scenarios. The purpose is to obtain contaminant loads originating from various diffuse contaminant sources in the basin that are subsequently used as input data in a related study that involves the development of a surface water quality model for the Mudurnu river.

## 2 SITE DESCRIPTION

The Mudurnu river basin is located in the Marmara Region of Turkey and has a drainage area of 2380 km$^2$. The mean annual precipitation in the basin is recorded as 836 mm and the mean minimum and maximum temperatures on long-term record are 6.4 °C and 17.8 °C, respectively. The river has a length of 130 km and drains water primarily from agricultural lands and forests (Figure 1). Agricultural lands and forests cover 50.1% and 42.8 % of the total river basin area, respectively. Soil texture in the basin comprises of luvisols, calcaric fluvisols, calcic cambisols and orthic acrisols. The site is also characterized by land slope, which is an important factor in the generation of surface runoff, therefore important in the occurrence of diffuse source pollution. The basin features mostly land slopes greater than 10%, except for the downstream of the basin, where slopes less than 1% are observed. The study area is significant since the Mudurnu river is one of 663 water bodies in the country that are classified as nutrient-sensitive (Tubitak-MAM, 2016). As for diffuse pollution loads, it is estimated that about 43,000 people are living in residential areas that have no sewerage system and therefore are connected to septic tanks for wastewater disposal. Agriculture is important for the population living in the Mudurnu river basin. The total area reserved for agriculture is 5622 ha. Chemical fertilizer use is estimated as 13561 t per year. Manure originating from livestock is also used as fertilizer. Manure production rate are approximated using livestock animal numbers; based on official records the number of cows and cattle is about 29200 and sheep and goats 10500. Furthermore, there are two dumpsites within the boundaries of the basin that are estimated to have a minor contribution to the overall diffuse pollution load.

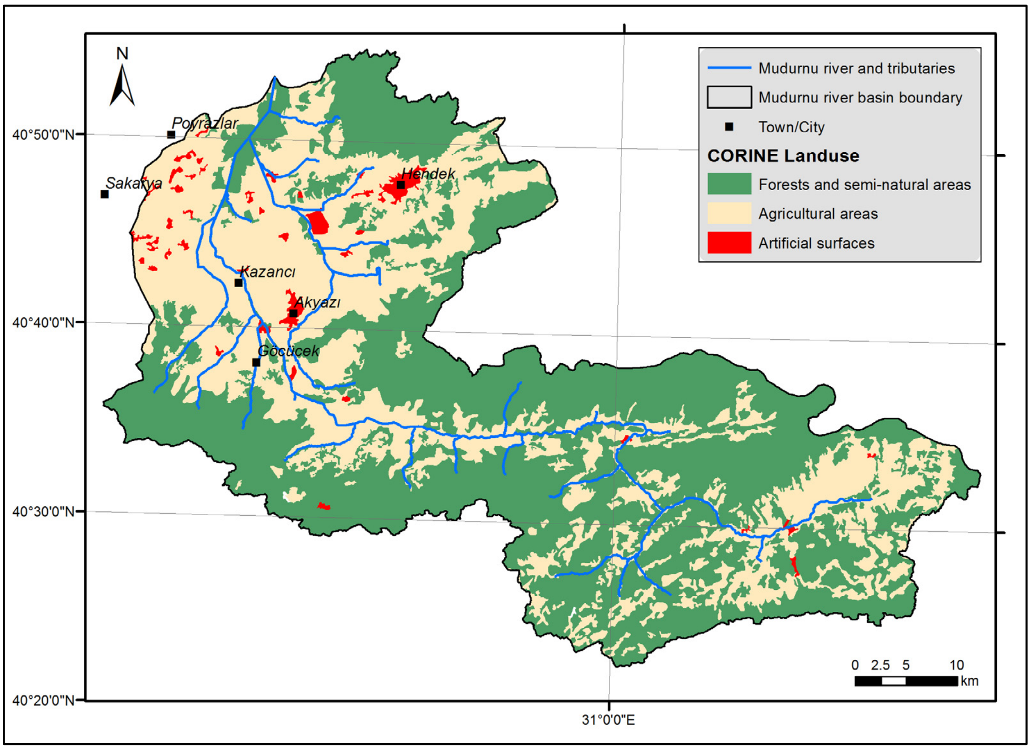


**Figure 1.** Landuse distribution in the Mudurnu river basin.

## 3 MODEL APPLICATION

SWAT, an abbreviation for soil and water assessment tool, is a semi-distributed, process-based hydrologic and water quality model (Arnold et al., 2012) developed by the U.S. Department of Agriculture (USDA). Major model components in SWAT include hydrology, weather, sedimentation, soil temperature, crop growth, nutrients, pesticides, and agricultural management. This model is widely used for river basin scale studies dealing with water management. ArcGIS compatible ArcSWAT (version 2012.10.8) is used for this study, which is basically an interface to the SWAT model (version 2015).

Primary input data for the SWAT model comprise of CORINE land cover data, digital elevation map, soil texture map and meteorological records. Additionally, locations and number of septic tanks, locations of dump sites and information about fertilizer consumption and manure production are required for data input. The number of septic tanks is approximated using the population count that is not connected to the sewer system. Consequently, center points of residential areas not connected to the sewerage system were assumed as representative locations for septic tanks. Using the information about fertilizer consumption, it is estimated that on an elemental basis 646.2 kg/ha of nitrogen and 92.5 kg/ha of phosphorus is applied annually. Manure production is calculated from livestock animal numbers. Production unit rates per livestock animal are assumed as 0.3 kg N/t animal per day and 0.1 kg P/t animal per day for cattle and cows; 0.42 kg N/t animal per day and 0.06 kg P/t animal per day for sheep and goats. These unit rates were based on a study by Tanik et al. (2013). Eventually, elemental nutrient input originating from manure application is determined as 297.3 kg N/ha and 96.6 kg P/ha per year.

For diffuse pollution modeling purposes, the basin is divided into 34 sub-basins and 243 hydrologic response units (HRUs). Sub-basins are derived from 30-m resolution ASTER digital elevation map. Furthermore, a HRU is established based on land use, soil class and land slope and unique combinations of these properties constitute a single HRU, therefore properties are assumed homogeneous within a HRU. The meteorological variables required by SWAT are precipitation, solar radiation, relative humidity and wind speed on a daily basis, also minimum and maximum daily temperatures. Missing records are filled in using the internal SWAT weather generator, which utilizes long-term statistical data pertaining to the relevant meteorological station. Runoff flow rates are simulated using the Soil Conservation Service's Curve Number Method (Mockus, 1969). Potential evapotranspiration (PET) for each HRU is estimated using the Penman-Monteith method and then adjusted into actual evapotranspiration using antecedent and current soil water conditions.

As a first step of the modeling process, average monthly flow rates of surface runoff, lateral subsurface flow, seepage from groundwater, evapotranspiration and deep aquifer recharge are calculated for all sub-basins. SWAT evaluated these hydrologic components to finally compute discharge rates for all reaches of the river. These discharge rates are numerically assigned to outlet points that are located downstream of each sub defined sub-basin. The most downstream outlet point represents the outlet point for the entire river basin. Here the Mudurnu river merges with the Sakarya river, a major river in northwestern Turkey. Simulated discharge values at the basin outlet are compared to measured monthly discharge data to evaluate performance of the model. The SUFI-2 algorithm in the SWAT-CUP software (Abbaspour, 2011) is used for sensitivity analysis and model calibration. Model parameters adjusted during the calibration were curve number (CN2), groundwater revap coefficient (GW_REVAP), threshold depth of water in the shallow aquifer required from return flow to occur (GWQMN) and available water capacity of the soil (SOL_AWC). Several statistics, including the coefficient of determination ($R^2$), root mean square error (RMSE) and Nash-Sutcliffe (NS) efficiency are used to facilitate the calibration process and evaluate the accuracy of model flow predictions. In the second step of the modeling process, the flow-calibrated model is run to simulate diffuse source nitrogen and phosphorus loads originating from the sub-basins. The simulation time is defined for a 5-year period (1.1.2012 – 31.12.2016) with a warm-up period of 3 years. The calibration period spans from May 2015 to April 2016.

# 4 RESULTS

## 4.1 Simulation of River Discharge

The model is calibrated with an automated calibration procedure against measured monthly river discharge data. Comparing modeled discharge rates at the outlet of the river basin (Figure 2) with measured values yield a satisfactory calibration performance with $R^2$ at 0.72, RMSE at 13.7 $m^3/s$ and a NS coefficient of 0.72. The mean simulated and measured discharge rate for the calibration period is 31.94 $m^3/s$ and 31.05 $m^3/s$, respectively. It is important to note that discharge rates from all point sources in the basin are added to the simulated river flow rate assuming that point source discharge are constant for the entire year.

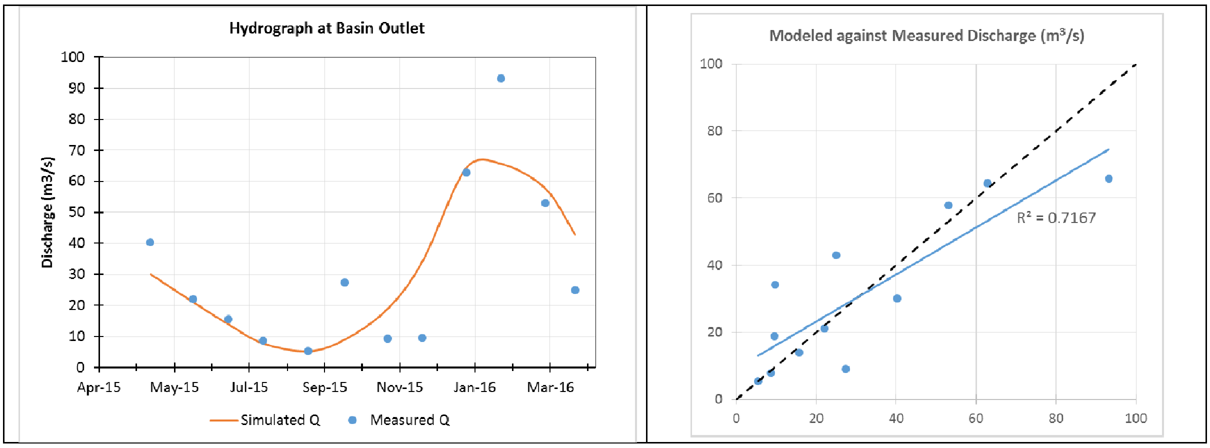


**Figure 2.** Comparison of simulated river discharge against measured data.

## 4.2 Simulation of Nutrient Loads

Diffuse source nutrient loads to the river are predicted for each sub-basin with the SWAT model. Model results for nitrogen loads are broken down as nitrate (surface runoff, lateral subsurface flow and groundwater components) and organic nitrogen. Phosphorus loads are reported as soluble mineral form, organic phosphorus and mineral phosphorus sorbed to sediment particles. Results are reported in this study as sums, i.e. total nitrogen and total phosphorus and only for the calibration period of May 2015 – April 2016. Spatial distribution of total nitrogen loads is shown in Figure 3. As can be seen, results indicate that the total annual nitrogen load ranges from 4.61 to 32.78 kg/ha/yr, averaging 15.2 kg/ha per year. The distribution of loads is very heterogeneous and appear to be correlated with the relative area of land use class reserved for agriculture. The dominant components of the total nitrogen load are nitrate coming from groundwater and organic nitrogen flowing to the river via surface runoff. Mineral nitrogen in surface runoff is relatively insignificant.

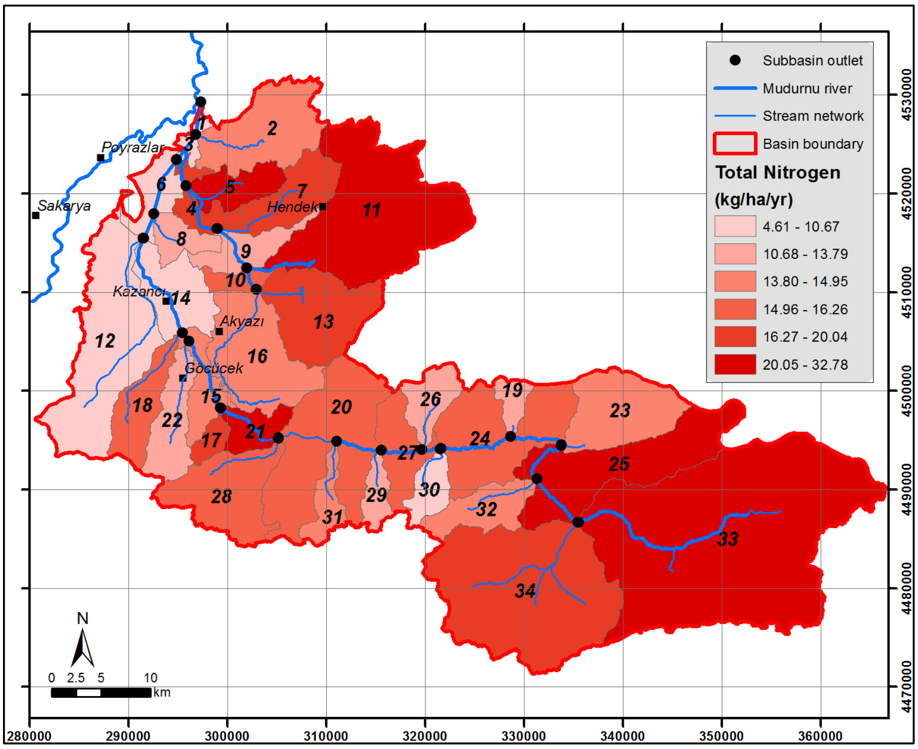


**Figure 3.** Total nitrogen annual unit loads predicted by the SWAT model.

Model results for phosphorus is given in Figure 4. Total annual phosphorus load varies between 0.27 – 7.23 kg/ha/yr with an average annual basin load of 2.84 kg/ha. The highest load is expected to occur in sub-basin 21, an area dominated by agricultural activities. Total nitrogen loads are also highest in this sub-basin. The most significant component of the total phosphorus load is mineral phosphorus sorbed to sediment particles. Therefore, erosion appears to be a controlling factor of diffuse source phosphorus inputs to the river.

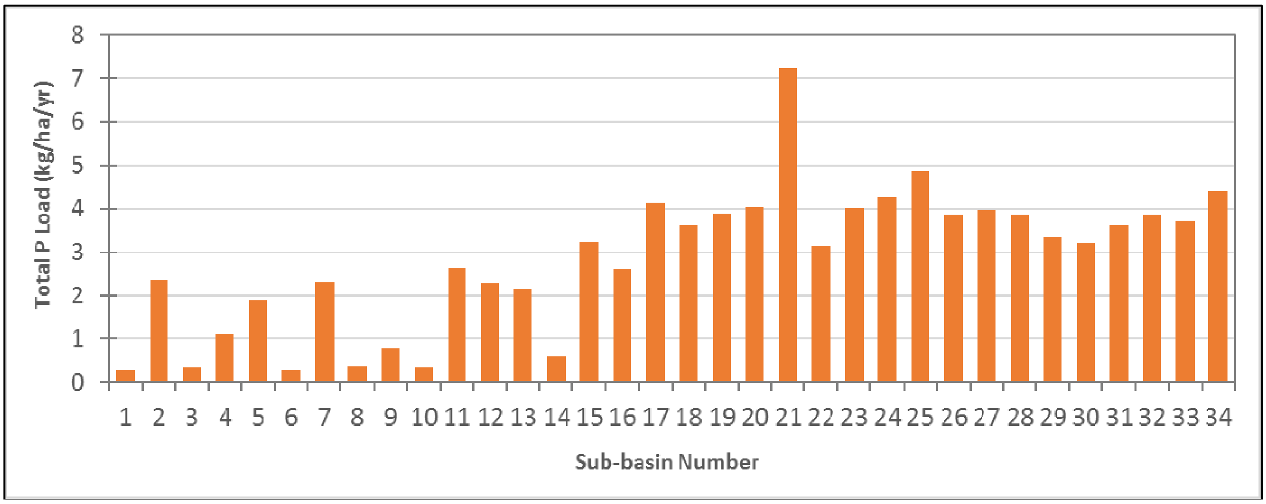


**Figure 4.** Total phosphorus annual unit loads predicted by the SWAT model.

## 5 CONCLUSIONS

Probably the most important input data for a surface water quality models are pollutant loads from point and diffuse sources. Diffuse source nutrient loadings are estimated for the Mudurnu river basin using the well-known SWAT model are presented in this paper. Model results are invaluable since they can be used as inputs for subsequent pollutant transport models, land use impact studies, water and land management scenario studies and also climate change impact studies. It is evident that the results from this study are comparable to values published for similar nutrient-sensitive basins and therefore can be directly utilized in related surface water quality modeling studies. However, to improve accuracy of predictions, SWAT model parameters must be also calibrated against water quality data measured at several outlet points throughout the river basin. This process can become complicated if major point nutrient sources are present in the basin. In such a case, the model parameters that are related to pollutant transport in the river reach must also be included in the calibration process, which eventually leads to a multi-parameterized optimization problem. Nevertheless, the study has shown that river discharge can be simulated with good agreement with measured data and that reasonable values for nutrient loads can be obtained.

## ACKNOWLEDGEMENTS

This study was supported by the Directorate General for Water Management, Ministry of Forestry and Water Affairs of the Turkish Republic. The authors would like to thank the Directorate's staff for their involvement in the study.

## REFERENCES

Abbaspour, K.C. (2011). *SWAT-CUP4: SWAT Calibration and Uncertainty Programs - User Manual*, Department of Systems Analysis, Integrated Assessment and Modelling (SIAM), EAWAG. Swiss Federal Institute of Aquatic Science and Technology, Duebendorf, Switzerland, 106.

Arnold, J.G., Moriasi, D.N., Gassman, P.W., Abbaspour, K.C., White, M.J., Srinivasan, R., Santhi, C., Harmel, R.D., van Griensven, A., van Liew, M.W., Kannan, N. & Jha, M.K. (2012). SWAT: Model use, Calibration, and Validation. *Transactions of the ASABE,* 55, 1491-1508.

Gassman, P.W., Osei, E., Saleh, A., Rodecap, J., Norvell, S. & Williams, J. (2006). Alternative Practices for Sediment and Nutrient Loss Control on Livestock Farms in Northeast Iowa. *Agriculture, Ecosystems & Environment*, 117(2), 135-144.

Mockus, V. (1969). *Hydrologic Soil-Cover Complexes*. SCS National Engineering Handbook: section 4. *Hydrology*, 10, 11-24.

Tanik, A., Ozalp, D. & Seker, D.Z. (2013). Practical Estimation and Distribution of Diffuse Pollutants Arising from a Watershed in Turkey*. International Journal of Environmental Science and Technology,* 10(2), 221-230.

Tripathi, M.P., Panda, R.K., Raghuwanshi, N.S. & Singh, R. (2004). Hydrological Modeling of a Small Watershed using Generated Rainfall in the Soil and Water Assessment Tool Model. *Hydrological Processes*, 18, 1811-1821.

Tubitak-MAM. (2016). *The Determination of Sensitive Areas and Water Quality Targets for Turkey on a Watershed Basis*, Final Report. Environment and Cleaner Production Institute of the Tubitak Marmara Research Center, Gebze/Kocaeli, Turkey, 893.

Proceedings of the 37th IAHR World Congress
August 13 – 18, 2017, Kuala Lumpur, Malaysia

# 2D NUMERICAL APPROACH FOR EVALUATION OF WEIR OPERATION STRATEGIES ON HARMFUL ALGAL BLOOM CONTROL

IL WON SEO[1] & JUN SONG KIM[2]

[1,2] Department of Civil Engineering,Seoul National University, Seoul, Republic of Korea
seoilwon@snu.ac.kr; hyde17k@snu.ac.kr

## ABSTRACT

Due to climate change, multi-purpose weirs are built across the rivers in South Korea to resolve drought problems. As for change of flow condition by these hydraulic structures, weir operation strategies have been considered as crucial part to control harmful algal bloom (HAB). HAB impairs ecological values in river ecosystems as this green-colored biomass of cyanobacteria involves toxicity and bad odor. This study is aimed at investigating effective approaches of pulse discharge from weirs to restrain HAB, using a 2D finite element model (FEM). In this study, the depth-averaged advection-dispersion-reaction model (ADRM) is used to analyze the transport and growth characteristics of cyanobacteria in the shallow water flow. Furthermore, the spatial-temporal measurements in the Nakdong River, South Korea are used to derive a water temperature function to calculate the growth rate of cyanobacteria and calibrate the model. As a result of the model calibration, simulation results showed a good agreement with the spatial measurements as showing average MAPE less than 13 %. Using the calibrated model, several weir operation scenarios with the pulse discharge from Gangjeong weir located at the upstream of the study area are simulated, varying duration time, frequency and total volume of the discharge. According to the simulation results, the reduction rate is not proportional to the frequency and duration time but increasing with the optimal combination of the both variables as ranging from 3.82 to 4.45 % in the reduction rate at a fixed amount of the flushing water.

**Keywords**: Harmful algal bloom (HAB); pulse discharge; depth-averaged advection-dispersion-reaction model (ADRM); water temperature function; Nakdong River.

## 1 INTRODUCTION

High biomass of cyanobacteria is well known as a harmful algal bloom (HAB) that causes water quality deterioration with bad odor and toxicity such as microcystin and anatoxin, filter clogging in water intake facilities, and even kill aquatic animals by hypoxia (Paerl and Huisman, 2009). The HAB is a result of eutrophication triggered by urban and agricultural runoff which involves excessive nutrient loadings. In streams, cyanobacteria propagate by uptake of nutrients such as phosphorus (P) and nitrogen (N), satisfying certain environmental conditions, especially optimal water temperature, light intensity, and stable water condition by low velocity. Thus, cyanobacteria have commonly considered as a biological indicator to assess symptoms of eutrophic level in the aquatic systems. The Nakdong River in South Korea was selected as a study river since it is one of serious eutrophic rivers because of effluent with high concentration of P and N, which is introduced from its tributaries where many wastewater treatment plants (WWTPs) and sewage treatment plants (STPs) are located. Due to climate change, this eutrophic river has suffered aberrant drought events in the last decade. Therefore, several multi-purpose weirs were constructed to treat the recent water shortage problem. However, this artificial flow control by the weirs has impeded the natural river flow, hereby accelerating HAB during summer by increasing the water retention time (Kim et al., 2007). In this study, proper weir operation strategies with variation of duration time, frequency and total volume of pulse discharge from the weir were investigated to effectively diminish HAB, using a 2D numerical model.

The objectives of the present study include the following:

(a) Collection of spatial and temporal distribution of cyanobacteria through a portable sensor and in-situ water quality monitoring systems.
(b) Derivation of a water temperature function to compute growth rate of the cyanobacteria, using the temporal measurement data.
(c) Application of empirical functions to the numerical model, and calibration of model parameters, using the spatial measurement data.
(d) Investigation of effect of change in the weir operation variables (duration time, frequency and total volume of the pulse discharge) on the magnitude of HAB, using the calibrated model.

 

## 2 FIELD STUDY

### 2.1 Study area

The Nakdong River has served as an essential water supply source in the south eastern area of South Korea with a drainage area of about 23,817 $km^2$ and length of 525 km to provide drinking water for 13 million of local households. However, many WWTPs and STPs are located along the main channel and its tributaries, and effluent discharge from these facilities have led to increase in eutrophic level of the Nakdong River. Especially, the water quality of a study area defined as about 17.2 km long section between Gangjeong weir and Dalseong weir, as shown in Figure 1, was significantly vulnerable to high nutrient loading with heated or cooling water from the Kumho River, which is the largest tributary of the Nakdong River and involves huge industrial runoff from Seongseo industrial complex.

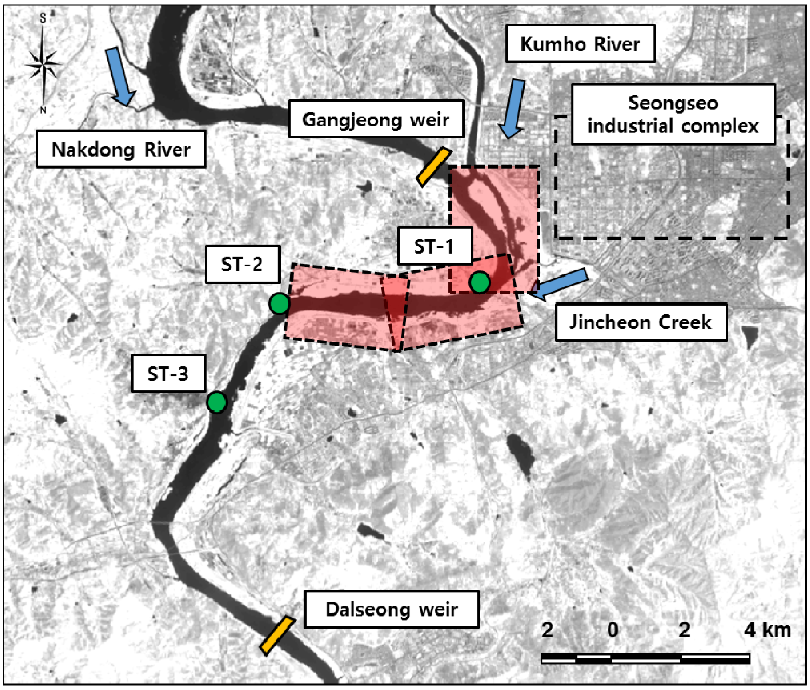


**Figure 1.** Study area (green circles and red-shaded areas for temporal and spatial data, respectively).

### 2.2 Data collection

To collect temporal water quality variables, measurements of 5-minute interval were conducted at three different locations, ST-1, ST-2 and ST-3 (Figure 1), implementing in-situ water quality monitoring systems featured with YSI 6600 V2 sonde and solar-powered data logger, as shown in Figure 2. This multi-parametric water quality sonde is used to measure water temperature (WT), dissolved oxygen (DO), pH, electric conductivity (EC), turbidity (Turb) and chlorophyll-a (Chl-a) and cell count of cyanobacteria (BGA) during April to June, 2016. Furthermore, spatial distribution of cyanobacteria was scanned by a portable sensor, bbe AlgaeTorch 10 in October 10, 2016. Before the confluence zone with the Kumho River and Jincheon Creek, the four-point measurements and two-point measurements for each cross-section in the Nakdong River and Kumho River, respectively were achieved. The five-point measurements were conducted at further cross-sections in the main channel up to 8.7 km downstream of Gangjeong weir, as shown in Figure 2.

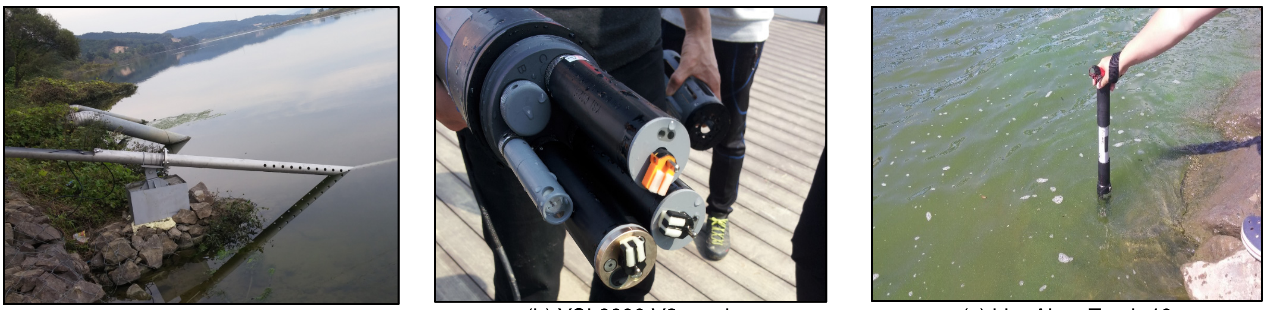

(a) Monitoring station, ST-3 (b) YSI 6600 V2 sonde (c) bbe AlgaeTorch 10

**Figure 2.** In-situ water quality monitoring system.

 

2.3 Results of measurements

All the temporally measured values by the in-situ water quality monitoring systems were converted to daily-averaged values for noise data reduction, and simple statistics of measurements are summarized in Table 1. In this study, BGA was used as an indicator of cyanobacteria because Chl-a can represents cells of diatom or chlorophyta rather than those of cyanobacteria.

**Table 1.** Statistics of water quality variables measured at monitoring stations.

| Variables | ST-1 (n = 25) | | ST-2 (n =56) | | ST-3 (n = 72) | |
|---|---|---|---|---|---|---|
| | Std. dev. | Mean | Std. dev. | Mean | Std. dev. | Mean |
| WT (˚C) | 1.16 | 25.09 | 2.48 | 23.06 | 4.17 | 20.55 |
| DO (mg/l) | 1.57 | 5.54 | 1.76 | 8.00 | 1.95 | 10.44 |
| pH | 1.22 | 6.30 | 0.37 | 7.49 | 0.46 | 8.13 |
| EC (µS/cm) | 36.36 | 441.57 | 50.29 | 411.04 | 103.89 | 424.41 |
| Turb (NTU) | - | - | 2.43 | 0.59 | 19.82 | 7.67 |
| Chl-a (mg/m3) | - | - | 5.78 | 9.87 | 7.87 | 12.61 |
| BGA (cells/ml) | 1182 | 3876 | 1641 | 3129 | 2855 | 4588 |

In the study site, the distribution of water temperature was not spatially homogeneous due to discharge from WWTPs located along the Kumho River and Jincheon Creek. Therefore, derivation of a proper water temperature function was indispensable to increase the model accuracy. During the monitoring period, predominant species of cyanobacteria was Microcystis and Aphaiozomenon. Imamura (1981) experimentally exhibited that growth rate of these groups had exponential relationship with water temperature (Imamura, 1981), thereby generally adopting Eppley equation to calculate the growth rate of cyanobacteria (Chapra, 2008).

$$f(T) = \theta^{T-T_{ref}} \quad [1]$$

where $f(T)$ is water temperature limiting function; $\theta$ is water temperature coefficient; $T$ is water temperature; and $T_{ref}$ is reference water temperature. According to the measurements in this study, Eppley equation showed high discrepancy with the measured BGA as r = 0.43. Therefore, the modified optimal water temperature equation was proposed in this study, and it showed better performance as well illustrating the sharp growth of cyanobacteria from 23 ˚C to further increase, compared to the former equation, as shown in Figure 3.

$$f(T) = \exp\left[-\gamma(T_{opt} - T)^2\right] + b \quad [2]$$

where $\gamma$ is shape parameter of the curve; $T_{opt}$ is optimal water temperature; and $b$ is intercept. These parameters were tuned as $\gamma$ = 0.04, $T_{opt}$ = 31 ˚C, and $b$ = 0.15 with r = 0.49.

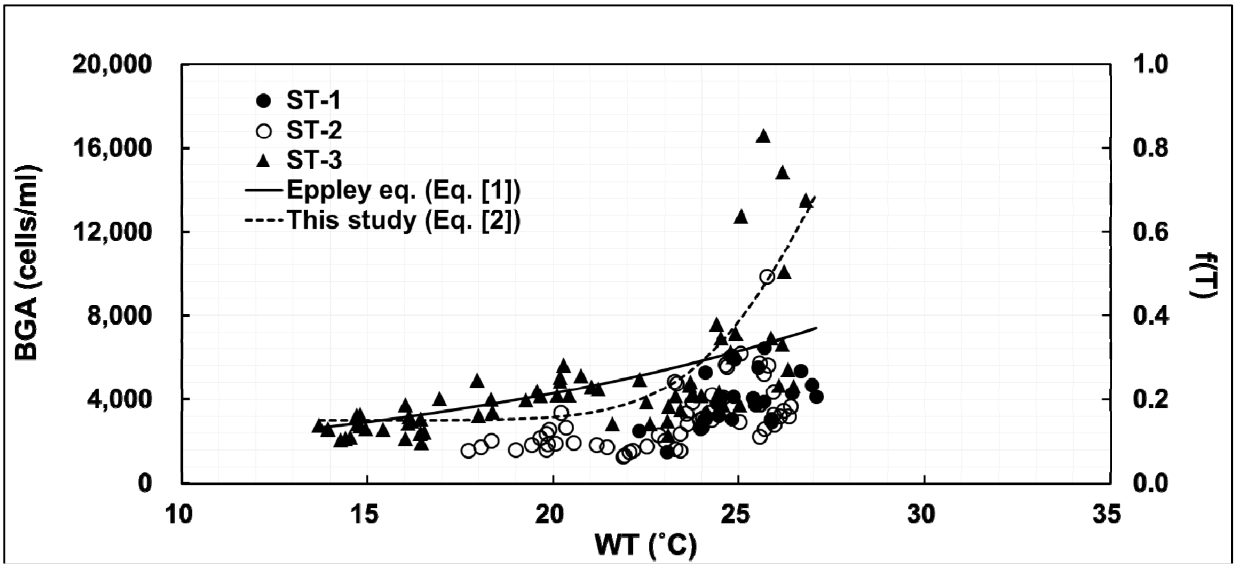


**Figure 3.** Empirical function to calculate growth rate with water temperature.

  / ISSN 1562-6865 (Online) - ISSN 1063-7710 (Print)

For the spatial measurements, BGA was collected at total 192 points with 85 points at 17 cross-sections after the confluence zone, as shown in Figure 4. The measurements were accomplished, assuming the steady state condition for velocity and concentration field. According to the measurement results, high concentrations of BGA were observed at river banks adjacent to ST-2 due to not only the transverse mixing effect of high concentration of nutrient from the Kumho River on water quality of the Nakdong River around this area but also penetration of high light intensity into shallow water zones occurred around the river banks. The latter phenomena created a favorable condition for increasing the growth rate of cyanobacteria by photosynthesis.

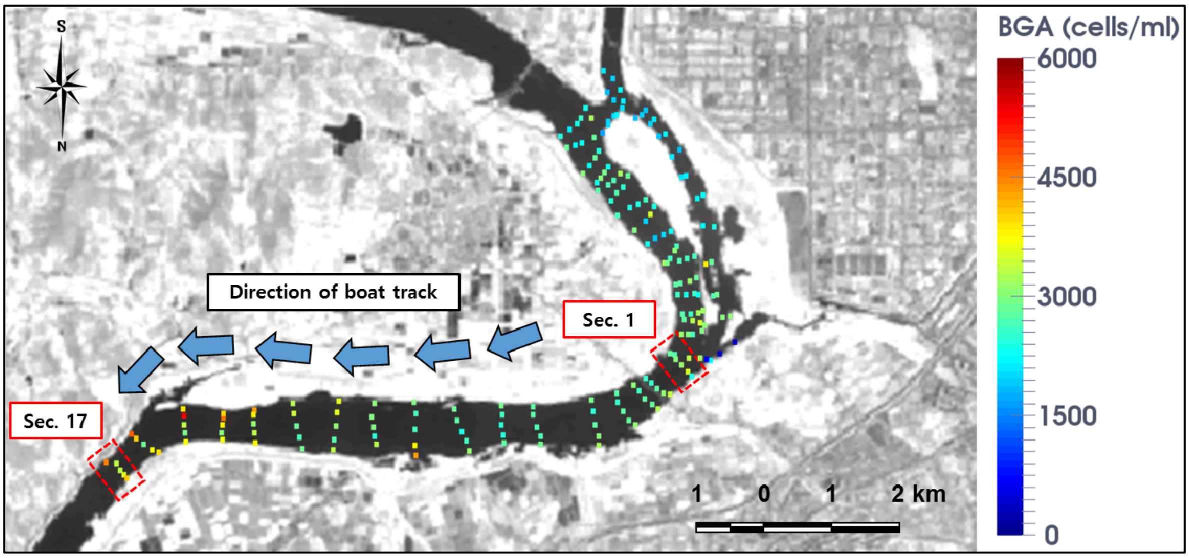


**Figure 4.** Spatial distribution of BGA (no. of sections ordered from Sec. 1 to 17 by boat track).

## 3 NUMERICAL MODELS

### 3.1 Hydrodynamic model

Open-channel flows are commonly considered as a shallow water problem, neglecting the effect of vertical motions. In this study, a shallow water flow model, Hydro Dynamic Model-2D (HDM-2D) was used to obtain hydraulic properties such as 2D velocity field and water depth for solving hydraulic behavior of cyanobacteria. This finite element model (FEM) adopted a combination of structured and unstructured grids in order to efficiently describe complex geometry of the real river systems. Governing equations of HDM-2D consist of continuity equation and momentum equation also known as a shallow water equation express as (Seo and Song, 2010):

$$\frac{\partial h}{\partial t} + h\nabla \cdot \underline{u} + \underline{u} \cdot (\nabla h) = 0 \qquad [3]$$

$$\frac{\partial \underline{u}}{\partial t} + (\underline{u} \cdot \nabla)\underline{u} = -g\nabla(H+h) + \frac{1}{h}\nabla \cdot (h\nu\nabla \underline{u}) - \frac{gn^2}{h^{4/3}}\underline{u}\|\underline{u}\| \qquad [4]$$

where $t$ = time; $\underline{u}$ = $(u_1, u_2)$ is depth-averaged velocity vector in $x$ -, $y$ -directions respectively; $\underline{u}$ = gravitational acceleration; $H$ = bottom elevation; $h$ = water depth; $\nu$ = kinematic viscosity; $n$ = Manning's roughness coefficient; and $\|\underline{u}\|$ = Euclid norm of velocity.

### 3.2 Pollutant transport model

As most rivers in real systems have channel width and length much larger than water depth, it satisfies that vertical mixing is rapidly completed ahead of transverse and longitudinal mixing. Therefore, a depth-averaged advection-dispersion-reaction model (ADRM), Contaminant Transport Model-2D (CTM-2D) was used to analyze transport of cyanobacteria, simultaneously considering its reaction processes in streams. Governing equation of CTM-2D can be written as (Lee and Seo, 2007):

$$\frac{\partial (hC)}{\partial t} + \nabla \cdot (h\underline{u}C) - \nabla \cdot (h\mathbf{D} \cdot \nabla C) + \mathbf{R}(C,t) = 0 \qquad [5]$$

where $C$ = depth-averaged concentration; $\mathbf{D}$ = tensor of dispersion coefficients; and $\mathrm{R}(C,t)$ = reaction term for a non-conservative pollutant.

3.3 Water temperature model

The study area involved inputs of cold or warm water from the tributaries. As a consequence, the distribution of water temperature was spatially not homogeneous. Assuming the heat pollutants as a non-conservative material, its reaction in the water body can be related to the exchange of heat with the atmosphere as the internal energy conservation analogous to the mass conservation. Therefore, the internal-energy equation can be expressed as a conservation of water temperature equation. In this study, the change of water temperature due to atmospheric exchange was assumed to be a proportional relationship with the temperature difference between the water surface and an equilibrium temperature as (Edinger et al., 1974):

$$R(T,t) = \frac{K_H(T_e - T)}{\rho c_p h} h \qquad [6]$$

where $K_H$ is heat exchange coefficient; $T_e$ is heat equilibrium temperature; $\rho$ is density of water; $\boldsymbol{I}$ = light intensity; and $c_p$ is specific heat of water. $T_e$ can be given as follow:

$$T_e = T_d + \frac{I}{K_H} \qquad [7]$$

where $T_d$ is dew point temperature.

3.4 Cyanobacteria growth model

The growth characteristics of cyanobacteria are based on a photosynthetic process with uptake of nutrients, depending on water temperature and solar radiation. Thus, the cyanobacteria growth model described as a reaction term consisted of three limiting functions: nutrient function, light intensity function, and water temperature function which was derived from the temporal measurements in this study. The reaction term to calculate the growth rate, including decay and settling effects can be written as (Thomann and Muller, 1987):

$$\mathbf{R}(C_{\mathbf{cyano}}, t) = \left(\mu_{\mathbf{max}} \cdot f(P,N) \cdot f(I) \cdot f(T) - k\theta^{T-20} - \frac{\omega}{h}\right) C_{\mathbf{diatom}} \qquad [8]$$

where $C_{\mathrm{cyano}}$ = depth-averaged concentration of diatom; $\mu_{\max}$ = maximum growth rate; $f(P,N)$ = nutrient weighting function; $f(I)$ = light intensity weighting function; $f(T)$ = water temperature weighting function; $k$ = respiration, death and excretion rate; and $\omega$ = settling velocity.

The nutrient function for the cyanobacterial growth is generally expressed as a Monod equation. In this study, the equation was combined with Liebig's law of minimum for the multiple nutrients as expressed below:

$$f(P,N) = \mathbf{min}\left(\frac{P}{P + K_P}, \frac{N}{N + K_N}\right) \qquad [9]$$

where $P$ = depth-averaged concentration of phosphate; $K_P$ = half saturation constant of phosphate; $N$ = depth-averaged concentration of nitrate; and $K_N$ = half saturation constant of nitrate.

The intensity of solar radiation is attenuated as it penetrates into the water column, depending on water transparency. Additionally, cyanobacteria cell can be destructed if the light intensity exceeds the saturating value. Combination of those processes with Steele's light function can be described as:

$$f(I) = \frac{I \cdot e^{-k_e h}}{I_s} \cdot e^{\left(1 - \frac{I \cdot e^{-k_e h}}{I_s}\right)} \qquad [10]$$

where $k_e$ = light attenuation rate; and $I_s$ = saturating light intensity.

 

### 3.5 Model calibration

As a result of the model calibration with comparison between the simulated values and measured value at Sec. 1, 6, 11 and 17, the model combined with the water temperature function retrieved from the temporal measurement data showed the fairly good accuracy with the average MAPE less than 13 %. The model modified with the water temperature function and light intensity function, perfectly illustrated the particular transverse distribution of cyanobacteria, which showed high concentration skewed to the river banks, where relatively higher growth rate was calculated by higher water temperature, available light intensity, and long water retention time compared to that calculated around the main flow zones due to the stronger light attenuation with higher water depth, and short water retention time, as shown in Figure 5.

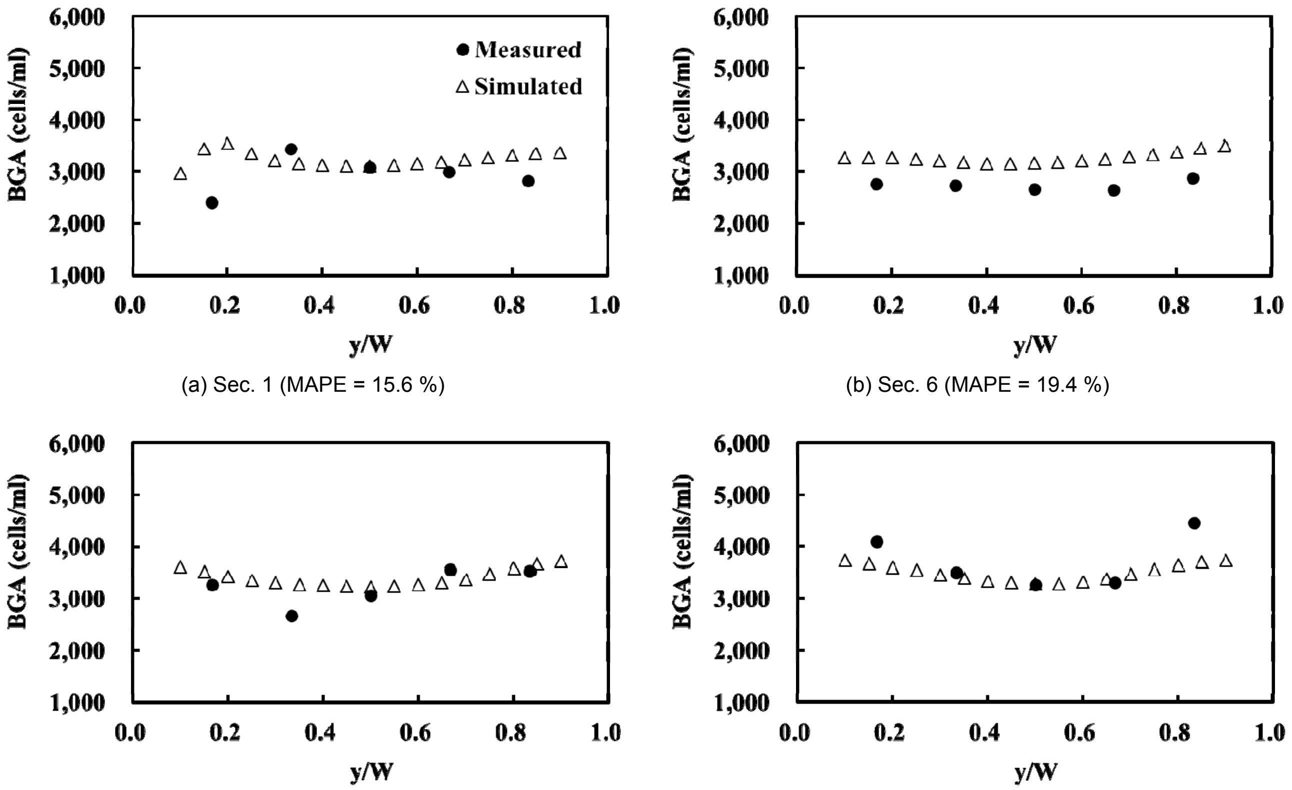


(a) Sec. 1 (MAPE = 15.6 %)

(b) Sec. 6 (MAPE = 19.4 %)

(c) Sec. 11 (MAPE = 9.4 %)

(d) Sec. 17 (MAPE = 6.5 %)

**Figure 5.** Results of model calibration (y = distance from left bank and W = channel width).

## 4 WEIR OPERATION SCENARIOS

Using the calibrated model, weir operation scenarios with the pulse discharge were simulated, controlling discharge as the upstream boundary at Ganjeong weir in the study area. The simulations were performed for 48 hours with the scenarios following as the case PD 1 to PD 4 with variation of duration time, frequency and total volume of the pulse discharge, as described in Figure 6. The total volume of the discharge were set as a constant value ($V = 1.73 \times 10^7$ $m^3$) except for the case PD4 ($V = 0.86 \times 10^7$ $m^3$). For the normal operation, the discharge from the weir was 200 $m^3/s$ while it increased to 400 $m^3/s$ when the weir gate was open. The discharges from the Kumho River and Jincheon Creek were fixed as 30 $m^3/s$ and 4 $m^3/s$. The distributions of BGA and water temperature in the model calibration were used for the initial condition.

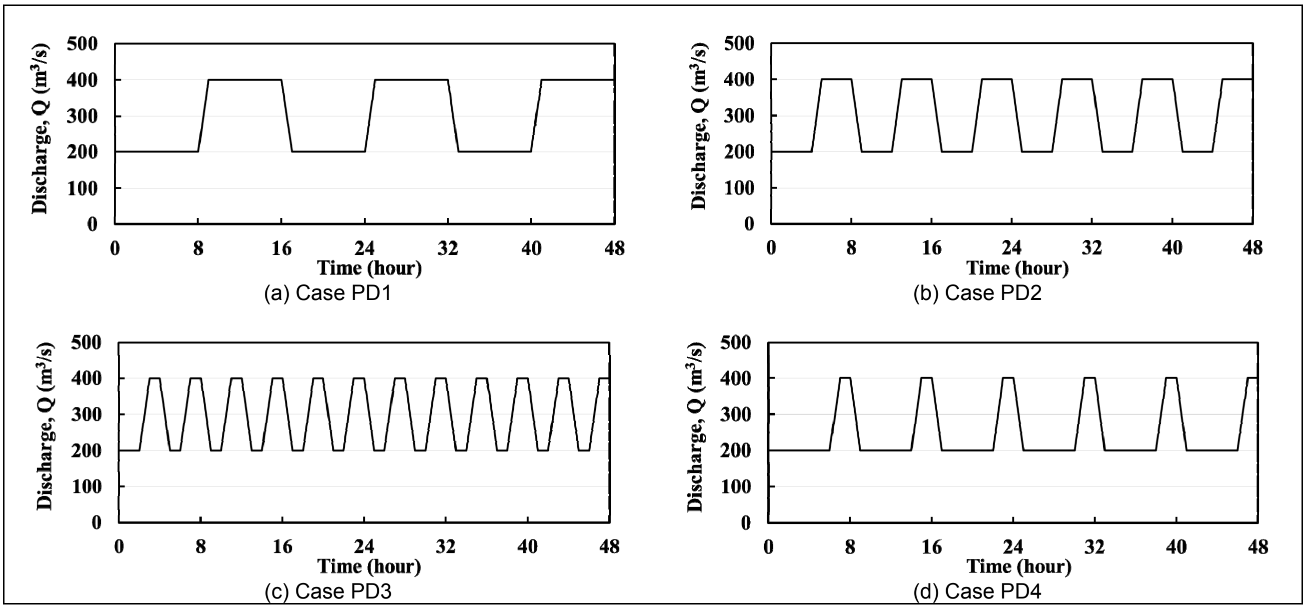


**Figure 6.** Scenario cases with variation of upstream boundary condition for HDM-2D.

From the results of the scenario simulation, average percentages of HAB reducted after 48 hours at Sec. 17, where a water intake facility was located, were 3.95 %, 4.45 %, 3.82 % and 2.60 % from the case PD1 to PD4, respectively, as shown in Figure 7. The case PD4 showed the poorest performance in the HAB reduction owing to the total volume of this case half of that in other cases. Comparison between the remaining cases, the case PD2 exhibited the greatest reduction effect on HAB. In the case PD1, the duration time with no pulse discharge events allowed BGA recovered up to the initial state. Furthermore, the frequent discharge with the short duration time was not effective to restrain the cyanobacterial growth. In this study, therefore, the case PD2 representing 6 times of the pulse discharge with 4 hours for each flushing event was evaluated as an optimal weir operation scenario for restraining HAB if the amount of water for the pulse discharge was assigned at a fixed level.

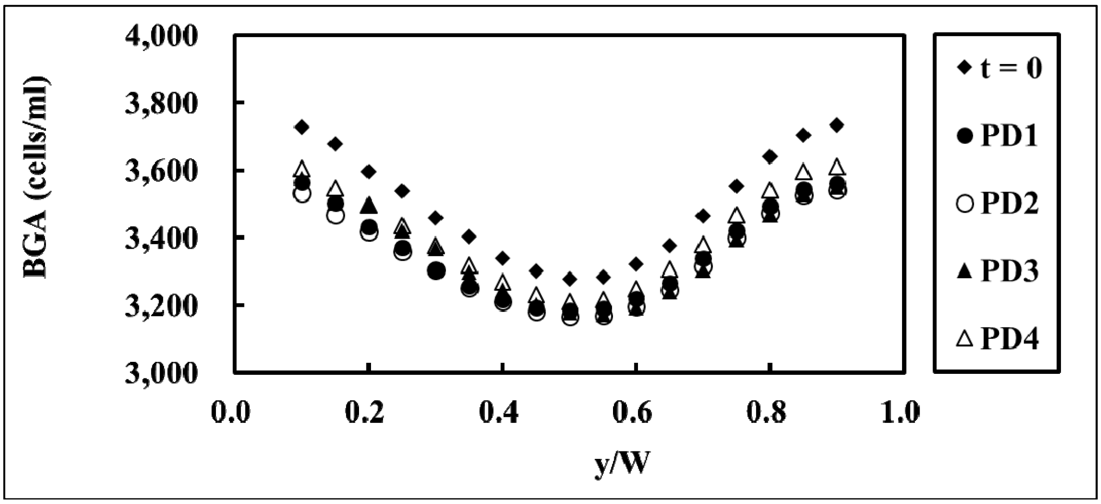


**Figure 7.** Result comparison of scenario cases at Sec. 17 after 48 hours.

## 5 CONCLUSIONS

In this study, a water temperature equation, which adopted the optimal function rather than a conventional exponential form, was proposed to calculate the growth rate of cyanobacteria from the temporal measurement data. In the model calibration, the 2D ADRM modified with this function showed the acceptable accuracy with the average MAPE less than 13 % as compared with the spatial measurement data. As a result of the weir operation scenario evaluation using the calibrated model, the case PD2 showed the best performance in the HAB reduction in the Nakdong River.

## ACKNOWLEDGEMENTS

This research was supported by a grant (11-TI-C06) from Advanced Water Management Research Program funded by Ministry of Land, Infrastructure and Transport of Korean government. This work was conducted at the Engineering Research Institute and the Integrated Research Institute of Construction and Environment in Seoul National University, Seoul, Korea.

**REFERENCES**

Chapra, S.C. (2008). *Surface Water-Quality Modeling*. Waveland press, 844.

Edinger, J.E., Brady, D.K. & Geyer, J.C. (1974). *Heat Exchange and Transport in the Environment.* Report No. 14 (No. NP-2900127). Johns Hopkins Univ., Baltimore, MD (USA). Dept. of Geography and Environmental Engineering.

Imamura, N. (1981). Studies on the Water Blooms in Lake Kasumigaura. *Proceedings-International Association of Theoretical and Applied Limnology*, 21, 652-658.

Kim, D.K., Cao, H., Jeong, K.S., Recknagel, F. & Joo, G.J. (2007). Predictive Function and Rules for Population Dynamics of Microcystis Aeruginosa in the Regulated Nakdong River (South Korea), discovered by evolutionary algorithms. *Ecological modelling*, 203(1), 147-156.

Lee, M.E. & Seo, I.W. (2007). Analysis of Pollutant Transport in the Han River with Tidal Current Using A 2D Finite Element Model. *Journal of Hydro-Environment Research*, 1(1), 30-42.

Paerl, H.W. & Huisman, J. (2009). Climate Change: A Catalyst for Global Expansion of Harmful Cyanobacterial Blooms. *Environmental Microbiology Reports*, 1(1), 27-37.

Seo, I.W. & Song, C.G. (2010). Development of 2D Finite Element Model for the Analysis of Shallow Water Flow. *Journal of the Korean Society of Civil Engineers*, 30(2B), 199-209.

Thomann, R.V. & Mueller, J.A. (1987). *Principles of Surface Water Quality Modeling and Control*. Pearson, 644.

Proceedings of the 37th IAHR World Congress
August 13 – 18, 2017, Kuala Lumpur, Malaysia

# DYNAMICS OF SEDIMENT CLOUD AND CLUMP REGIMES

JENN WEI ER[(1)]

[(1)] School of Civil and Environmental Engineering, Nanyang Technological University, Singapore.
e-mail Jer001@ntu.edu.sg
[(1)] Center for Environmental Sensing and Modeling, Singapore-MIT Alliance for Research and Technology Centre, Singapore

## ABSTRACT

With the continuous growth of population and economy in major coastal cities around the world, dredging and land reclamation have become two key activities to improve or maintain the navigation channels for maritime industry and to expand the land for infrastructure development. Both involve the open-water disposal of sediments either during the management of dredged material or during reclamation of the coastal area. The major concerns with the open-water sediment disposal include the loss of suspended sediments and/or associated contaminants into the ambient and the accuracy of sediment placement. Therefore, it is essential to analyze the near-source sediment dynamics for engineering assessment. In literature, the disposed sediment cloud is usually modeled as a group of dense particles released instantaneously into water forming a circulating vortex cloud, which descends through the water column as a thermal. However, this may not be the actual physical configuration. When the sediment volume is significant and requires a finite duration to be fully released, the sediment cloud appears as a starting plume with a thermal-like front head followed by a trailing stem instead. Also, even when the discharge volume is small enough to be treated as an instantaneous release, the formation of sediment clumps has been observed rather than the thermal if the source cloud number is below a certain threshold. The present study establishes for the first time a classification scheme based on physical length parameters to systemically categorize and analyze the different processes depending on the source conditions. The derivation of physical length parameters in the classification scheme is also discussed in the paper.

**Keywords**: Particle cloud; thermal; plume; clump.

## 1 INTRODUCTION

Open-water sediment disposal is often practiced in various activities such as land reclamation and management of dredged material, which involves the dumping of materials (reclaimed or dredged) into designated areas. In practice, these open-water disposal operations typically require the pre-approval from regulatory agencies, and the approval requirements include the evaluation of water quality impact in the water column (USEPA/USACE 1991, USEPA/USACE 1998). Hence, it is essential to be able to predict the fate and transport of the disposed sediments in the coastal environment with sufficient accuracy for the impact assessment.

Several engineering models as summarized in Table 1 have been developed to assess the dynamics of disposed sediments under various conditions and for different purposes. The transport processes of the disposed sediments in these models are categorized into near- and far-field regions (Figure 1), distinguished by the mechanisms that govern the mixing and dynamics of the sediment clouds. Sediment clouds within the near-field region are driven by momentum and buoyancy, which is induced by the density difference between the cloud and ambient fluid. From field evaluations, Bokuniewicz et al. (1978) summarized the fate of disposed sediments in this region into three sequential phases: (i) convective descent phase, during which the flow behavior is dominated by the release and source conditions; (ii) bottom collapse phase upon impact with the seabed, during which horizontal spreading occurs; and (iii) passive-transport dispersion phase (or intermediate far-field), when the sediments are carried by the ambient currents and turbulence.

In general, the dynamic behavior of disposed sediments in the convective descent phase under homogeneous stagnant ambient conditions can be divided into the conventional three regimes (Rahimipour and Wilkinson, 1992), including: (i) initial acceleration regime, within which the sediments become well mixed with water and descend as a solid body; (ii) thermal regime, within which the sediment cloud behaves self-similarly and starts to decelerate due to the entrainment of ambient stagnant water; and (iii) dispersive regime, within which the velocity of sediments slows to the level of individual particle settling velocity. This formation process is schematically explained in Figure 2(a). Again, previous studies and most of the engineering models are focused on the thermal regime, in which the sediment cloud is characterized by a coherent vortex ring structure. Its gross characteristics behave like a single-phase miscible thermal and can be modeled by using the asymptotic solutions:

 

$$\text{Two-dimensional thermal: } z \sim t^{2/3} \tag{1}$$

$$\text{Three-dimensional thermal: } z \sim t^{1/2} \tag{2}$$

where $z$ is the penetration depth and $t$ is the time. This is classified as the thermal-like formation process by Zhao et al. (2014), who found that this regime occurred following the instantaneous release of sediments with source cloud number, $Nc$ higher than $3.2 \times 10^{-2}$. The $Nc$ is defined as the ratio of the settling velocity ($w_s$) of individual particles to the characteristic circulation velocity ($w_t$) within the sediment cloud:

$$Nc = \frac{w_s}{w_t} = \frac{w_s}{\sqrt{B_o}/r_o} = \frac{w_s r_o}{\sqrt{B_o}} \tag{3}$$

where $B_o$ is the total excess buoyancy and $r_o$ is the initial equivalent cloud radius.

In recent studies, two new formation processes have been identified with different initial regimes: clump regime (Wen and Nacamuli, 1996; Zhao et al., 2014) and starting plume regime (Er et al., 2016). The clump regime (wake-like formation process) occurs also due to the instantaneous release of sediments, but with $Nc$ lower than $3.2 \times 10^{-2}$. As illustrated in Figure 2(b), the clump regime features fast descending sediment clump(s), with sediments shedding along its path. Thus, it differs significantly from the acceleration regime, which the sediments were well mixed with the ambient water and move together as a ballistic volume without losing to the wake. The transition from clump to thermal regime is however possible, if the sediment clump disintegrates within the region, whereby entrainment velocity at the rear of the leading vortex was strong enough to incorporate all the sediments lost in the wake into the sediment thermal.

The third formation process, with the starting plume regime, is expected when significant amounts of sediments were released during the disposal operation, and they require a finite duration to be fully discharged. During this period, the sediments were continuously released into the ambient fluid from the source. The sediment cloud (or sediment plume in this case) was characterized as a thermal-like front head followed by a trailing stem. The gross characteristics can be modeled as a single-phase starting plume with the asymptotic solutions expressed as:

$$\text{Two-dimensional starting plume: } z \sim t \tag{4}$$

$$\text{Three-dimensional starting plume: } z \sim t^{3/4} \tag{5}$$

Unlike the shedding of sediments in the clump regime, the sediments in the tail region will be continuously supplied into the front head in the starting plume regime. After the sediments were fully discharged, the sediment cloud will descend as a discrete thermal without a great amount of sediment loss to the environment.

The above comparison shows that these three formation processes exhibit significant differences in terms of the dynamic behaviors of the disposed sediments. In the event of a disposal operation, thermal-like formation process is preferred as the sediments are held within the coherent vortex ring during the descent. Otherwise, the formation of sediment clumps (wake-like formation process) may occur, and the sediments lost to the wake are vulnerable to be carried away by ambient currents. Hence, it is necessary to identify the formation process and to assess the transport of disposed sediments with the appropriate model. The objective of the present study is to propose a classification scheme to systemically categorize the different processes depending on the source conditions. The derivation of physical length parameters in the classification scheme is also discussed, and the scheme is examined with the experimental results reported in past studies.

## 2 CLASSIFICATION SCHEME

Figure 3 shows a schematic diagram of the classification scheme that classifies the formation processes of sediment clouds based on the comparison of physical length parameters that represent the dynamic influences on the cloud behavior. The scheme includes two dominant physical length parameters: the depth of descent when the acceleration regime is completed, $z_{a-t}$ and the depth of descent when the sediments are fully released, $z_e$; as well as a non-dimensional parameter: Cloud number, $Nc$.

In practice, the disposal can be operated from either a small volume (e.g. backhoe bucket) or large volume release (e.g. barge, hopper dredge). The former usually implies an instantaneous release, because the duration for sediments to be fully released is relatively short. To represent the effect of instantaneous release, we introduce the length parameter, $z_{a-t,}$ based on the length scale, $l_{a-t}$ (Luketina and Wilkinson 1998) that estimates the water depth required for the transition from acceleration to thermal regime. On the other hand, the latter release condition requires certain duration, $t_e$ for sediments to be fully discharged and the depth of the sediment cloud front at $t = t_e$ and it can then be defined as $z_e$, which represents the influence of continuous release.

In the classification, the first step was to determine the type of release (instantaneous or continuous release) by comparing $z_{a\text{-}t}$ and $z_e$. If the sediments were fully emptied from the source before the sediment cloud front reaches the $z_{a\text{-}t}$ (i.e. $z_{a\text{-}t} > z_e$), the sediment cloud will behave as an instantaneous release and experience either the P1 or P2 process, depending on the source cloud number, *Nc*. Otherwise, the sediment cloud will behave as a starting plume and develop as the P3 process.

**Table 1**. Engineering models or software.

| Model/Software | Related Publication(s) | Purpose and Contribution |
|---|---|---|
| K & C model | Koh and Chang (1973) | • Model the disposed sediments as single-phase miscible thermal<br>• Fundamental of DIFID, DIFCD and STFATE |
| DIFID & DIFCD | Brandsma and Divoky (1976) | • Modified K&C model, include long term diffusion |
| STFATE | Johnson and Fong (1995) | • Model the instantaneous disposal of material from hopper dredge<br>• Discretize the initial semi-continuous release into a sequence of sediment clouds |
| MDFATE | | • Simulate the change in bathymetry from numerous disposal events over a certain period |
| BSDM | Er et al. (2016) | • Include the realistic physical condition and geometrical factor of barge |

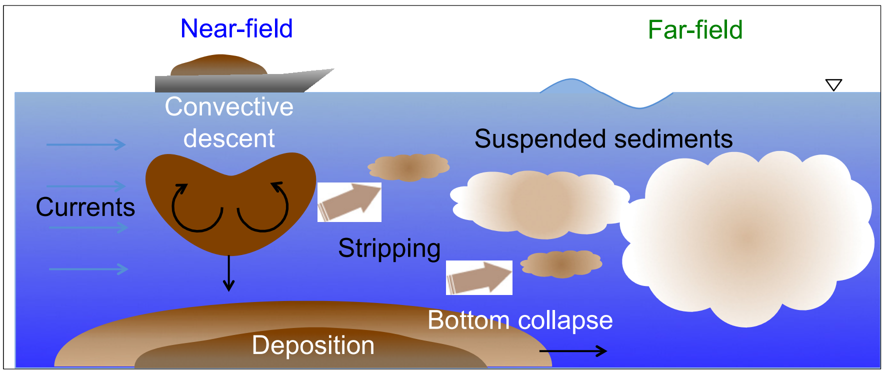


**Figure 1**. Transport of disposed sediments.

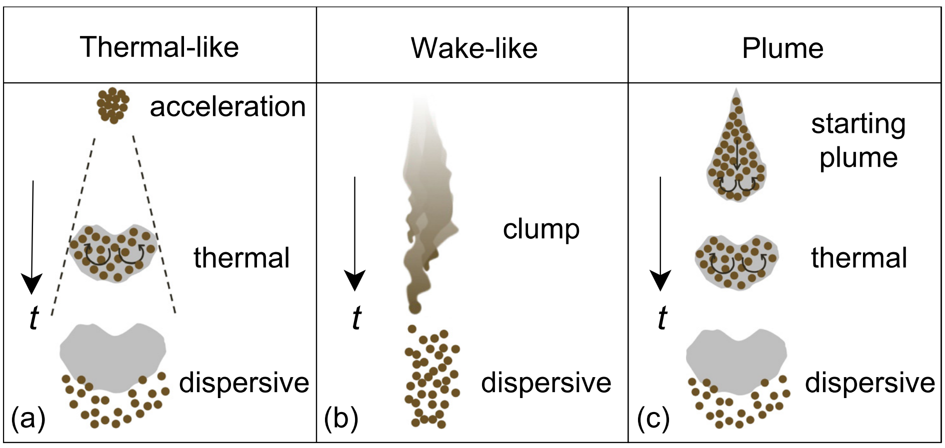


**Figure 2**. Formation process of sediment cloud (gray: entrained fluid, dots: sediment particles).

 

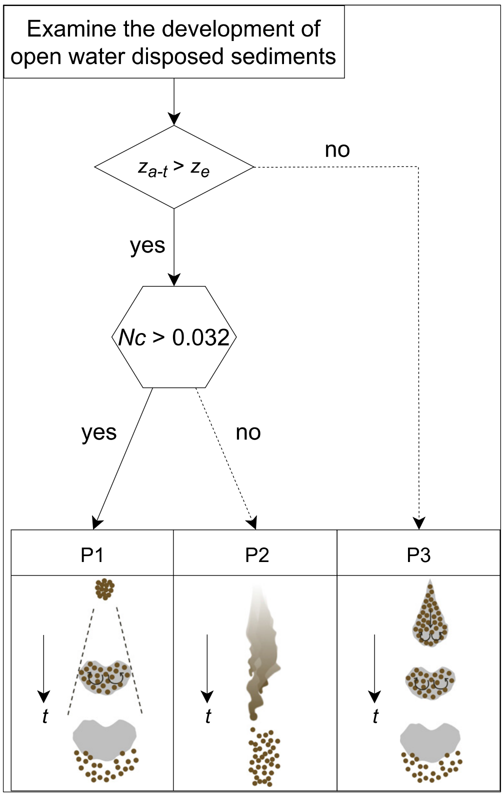


**Figure 3**. Classification of sediment cloud formation processes
(P1: thermal-like, P2: wake-like and P3: plume formation processes).

2.1 Acceleration Depth

The formula of $z_{a-t}$ can be derived through the length scale of acceleration regime, $l_{a-t}$ proposed by Luketina and Wilkinson (1998):

$$l_{a-t} \sim (m_o/\rho_a)^{1/3} \tag{6}$$

where $m_o$ is the mass of disposed sediments and $\rho_a$ is the density of ambient fluid, and

$$z_{a-t} = C_{a-t}\, l_{a-t} \tag{7}$$

where the value of $C_{a-t}$ can be determined from the data of previous experimental studies. Table 2 summarizes the value of $C_{a-t}$ from four different studies reported in the literature, which varies from 2.5 to 10.7. This significant variation can be directly attributed to the different release conditions, such as the release method, water content, formation number, and size of sediments. In the present study, a median value of 6.6 is adopted for the analysis.

**Table 2**. Summary of $C_{a-t}$ from previous studies.

| Previous Studies | $C_{a-t}$ |
|---|---|
| Luketina and Wilkinson (1998) | 4.1 |
| Gu and Li (2004) | 10.7 |
| Wang et al. (2014) | 6.9 – 10.4 |
| Zhao et al. (2012) | 2.5 – 5.9 |

2.2 Empty Depth

$z_e$ was previously determined by Er *et al.* (2016) as:

$$z_e = C_e \left( \frac{t_e \sqrt{g'}}{V_o^{1/6}} \right)^{a_e} V_o^{1/3} \tag{8}$$

where $g'$ is the reduced gravity, $V_o$ is the volume of release, $C_e$ and $a_e$ are 1.0 and 0.61, respectively, determined from experiments. The detailed derivation can be found in Er et al. (2016).

 

## 3 VERIFICATION

The wake-like formation process (P2) was first observed by Wen and Nacamuli (1996) and analyzed by Zhao et al. (2014) in a systematic manner. It is noted that the P2 process has been rarely reported since previous experimental studies had *Nc* typically larger than $3.2 \times 10^{-2}$ (Rahimipour and Wilkinson, 1992; Bühler and Papantoniou, 2001; Gu and Li, 2004; Zhao et al. 2012). The exception was Ruggaber (2000) who performed experiments with $Nc < 3.2 \times 10^{-2}$ but did not observe the formation of sediment clumps. This might be attributed to the fact that he mixed the particles first with water and then released them in suspension by constant stirring, which prevented the formation of sediment clumps.

Both P1 and P2 processes are due to the instantaneous release of sediments, while the P3 process is due to continuous release from the source at the beginning. Er et al. (2016) established an engineering model, BSDM (Barged Sediment Disposal Model) based on the P3 process, and verified the predictions with an experimental study by releasing large but finite amounts of sediment from a model barge through a bottom rectangular opening. With the additional development here, the full integration of the classification scheme (including P1 and P2) into BSDM and its comparison with available results is shown in Table 3. Clearly, the formation process observed in the previous studies generally agreed well with the predicted results by BSDM, except for two cases with coarser sediments for the P3 process. This might be due to the current classification scheme, only including the three-dimensional regime, whereas the sediment cloud released from a rectangular opening was in a two-dimensional regime before transiting to three-dimensional (Er et al. 2016).

**Table 3**. Examination of classification scheme with previous studies.

| $m_o$ (g) | $\rho_s$ g/cm3 | $d_{50}$ (mm) | $w_s$ (cm/s) | *Nc* | $z_{a\text{-}t}$ (cm) | $z_e$ (cm) | Predicted Process | Verify (T/*F*)# | Remarks |
|---|---|---|---|---|---|---|---|---|---|
| Rahimipour and Wilkinson (1992) | | | | | | | | | |
| 5.5 | 2.65 | 0.2 | 2.1 | $3.4 \times 10^{-2}$ | 11.6 | 3.12 | P1 | T | |
| 12.2 | 2.65 | 0.33 | 5.1 | $8.3 \times 10^{-2}$ | 15.2 | 5.61 | P1 | T | |
| Wen and Nacamuli (1996) | | | | | | | | | |
| 199.8 | 1.39 | 1.25 | 4.4 | $7.2 \times 10^{-2}$ | 38.6 | 4.47 | P1 | T | |
| 83.5 | 2.65 | 0.11 | 1.3 | $1.3 \times 10^{-2}$ | 28.9 | 9.99 | P2 | T | |
| Ruggaber (2000) | | | | | | | | | |
| 40 | 2.5 | 0.264 | 3.2 | $3.9 \times 10^{-2}$ | 22.6 | 1.71 | P1 | T | |
| 40 | 2.5 | 0.129 | 1.36 | $1.9 \times 10^{-2}$ | 22.6 | 2.21 | P2 | *F* | |
| 40 | 2.5 | 0.024 | 0.05 | $5.7 \times 10^{-4}$ | 22.6 | 4.08 | P2 | *F* | |
| Bühler and Papantoniou (2001) | | | | | | | | | |
| 86.1 | 2.6 | 1.95 | 18.8 | $3.9 \times 10^{-1}$ | 29.1 | 4.76 | P1 | T | |
| 44.7 | 2.6 | 1.95 | 18.8 | $2.2 \times 10^{-1}$ | 23.4 | 4.01 | P1 | T | |
| 21.5 | 2.6 | 1.95 | 18.8 | $2.5 \times 10^{-1}$ | 18.4 | 3.34 | P1 | T | |
| Gu and Li (2004) | | | | | | | | | |
| 7.8 | 2.6 | 0.89 | 14 | $2.2 \times 10^{-1}$ | 13.1 | 2.74 | P1 | T | |
| 7.8 | 2.6 | 0.45 | 6.3 | $9.7 \times 10^{-2}$ | 13.1 | 3.37 | P1 | T | |
| Zhao et al. (2012) | | | | | | | | | |
| 8.4 | 2.5 | 0.513 | 7.13 | $1.1 \times 10^{-1}$ | 13.4 | 2.98 | P1 | T | |
| Zhao et al. (2014) | | | | | | | | | |
| 5.5 | 2.5 | 0.256 | 2.92 | $5.0 \times 10^{-2}$ | 11.6 | 2.88 | P1 | T | |
| 5.5 | 2.5 | 0.120 | 0.93 | $1.6 \times 10^{-2}$ | 11.6 | 3.59 | P2 | T | |
| 5.5 | 2.5 | 0.068 | 0.35 | $6.0 \times 10^{-3}$ | 11.6 | 4.36 | P2 | T | |
| 448 | 2.5 | 0.256 | 2.92 | $2.4 \times 10^{-3}$ | 50.5 | 12.6 | P2 | T | |
| Er et al. (2016) | | | | | | | | | |
| 112 | 2.5 | 0.728 | 10.55 | $1.1 \times 10^{-1}$ | 31.8 | 18.5 | P1 | *F* | $L/W = 5$ |
| 112 | 2.5 | 0.728 | 10.55 | $1.1 \times 10^{-1}$ | 31.8 | 36.7 | P3 | T | $L/W = 40$ |
| 112 | 2.5 | 0.512 | 7.13 | $7.4 \times 10^{-2}$ | 31.8 | 22.6 | P1 | *F* | $L/W = 5$ |
| 112 | 2.5 | 0.512 | 7.13 | $7.4 \times 10^{-2}$ | 31.8 | 44.8 | P3 | T | $L/W = 40$ |
| 112 | 2.5 | 0.256 | 2.92 | $3.0 \times 10^{-2}$ | 31.8 | 33.7 | P3 | T | $L/W = 5$ |
| 112 | 2.5 | 0.256 | 2.92 | $3.0 \times 10^{-2}$ | 31.8 | 66.9 | P3 | T | $L/W = 40$ |
| 112 | 2.5 | 0.120 | 0.93 | $9.7 \times 10^{-3}$ | 31.8 | 52.1 | P3 | T | $L/W = 5$ |
| 112 | 2.5 | 0.120 | 0.93 | $9.7 \times 10^{-3}$ | 31.8 | 103 | P3 | T | $L/W = 40$ |
| Er (2016) | | | | | | | | | |
| 10 | 2.5 | 0.120 | 0.93 | $1.4 \times 10^{-2}$ | 11.9 | 16.7 | P3 | T | |

  / ISSN 1562-6865 (Online) - ISSN 1063-7710 (Print)

Note:

- For the sediments disposed from air, the discharged time ($t_e$) is calculated from Beverloo's equation (Mankoc *et al.* 2007)
- *L*: barge length and *W*: barge opening width
  [#] T: same formation process reported; *F*: different process reported

## 4 ENGINEERING APPLICATION

The application of the integrated BSDM to field conditions is demonstrated in Table 4. For the disposal with backhoe bucket, the amount of sediments involved was usually in the order of 1 m$^3$, depending on the bucket size. In the real operation, the sediments were usually lifted to mid-air before being released, and the sediment discharge time (and the subsequent $z_e$) can be estimated from the Beverloo's equation (Mankoc et al., 2007). With coarse sands, the P1 process can be expected. However, with fine sands and, the disposed sediments would descend as sediment clumps (P2) instead. On the other hand, for barge disposal, large amount of sediments, we will typically be involved (in the order of 1000 m$^3$). The disposed sediments would descend as starting plumes first before transiting to discrete sediment thermals when the sediments are fully discharged (P3).

It is important to note that the engineering models listed in Table 1 (e.g. STFATE) are for the thermal formation only (P1), and both clump-like and plume formation processes (P2 and P3) are not included. As discussed above, the occurrence of P1 is only when dumping coarse sands with a relatively small volume (backhoe bucket), which is an unlikely scenario in real disposal operations. The utilization of BSDM can therefore provide a more accurate assessment of the fate and transport of the sediments in coastal waters during the operation.

**Table 4**. Application of classification scheme on field conditions.

| $m_o$ (g/kg/ton) | $\rho_s$ g/cm$^3$ | $d_{50}$ (mm) | $w_s$ (cm/s) | $Nc$ | $z_{a\text{-}t}$ (cm) | $z_e$ (cm) | Predicted Process |
|---|---|---|---|---|---|---|---|
| Field – backhoe bucket (bucket size: 1 m × 1 m) | | | | | | | |
| 1000 kg (~ 1 m$^3$) | 2.5 | 0.068 | 0.35 | $8.0 \times 10^{-4}$ | 660 | 132 | P2 |
| 1000 kg (~ 1 m$^3$) | 2.5 | 0.100 | 14.7 | $3.2 \times 10^{-2}$ | 660 | 88.7 | P1 |
| Field – bottom-split barge (barge dimensions: 1000 m × 10 m × 1 m) | | | | | | | |
| 1000 ton (~ 1000 m$^3$) | 2.5 | 0.068 | 0.35 | $2.5 \times 10^{-4}$ | 6600 | 12400 | P3 |

## 5 CONCLUSIONS

In the present study, a classification scheme is established to systematically categorize the formation processes (P1: thermal-like, P2: wake-like and P3: plume) based on the source conditions. The scheme provides the prediction of the expected formation process. The verification was done by comparing with the experimental data reported in the past studies. In general, the predictions agreed well with the reported data. The scheme is now fully integrated into BSDM.

Looking ahead, the classification scheme will be further improved to account for various release conditions, and a model for assessing the dynamic of sediment clumps is under development.

## ACKNOWLEDGEMENTS

This research was supported by the National Research Foundation Singapore through the Singapore-MIT Alliance for Research and Technology's Center for Environmental Sensing and Modeling interdisciplinary research program.

## REFERENCES

Bokuniewicz, H.J., Gebert, J., Gordon, R.B., Higgins, J.L. & Kaminsky, P. (1978). *Field Study of the Mechanics of the Placement of Dredged Material at Open-Water Disposal Sites,* Technical Report D-78-7, U.S. Army Engineer Waterways Experiment Station, Vicksburg, Miss.

Brandsma, M.G. & Divoky, D.J. (1976). *Development of Models for Prediction of Short-Term Fate of Dredged Material Discharged in the Estuarine Environment,* Contract Report D-76-5, U.S. Army Engineer Waterways Experiments Station, Vicksburg, Miss.

Bühler, J. & Papantoniou, D.A. (2001). On the Motion of Suspension Thermals and Particle Swarms. *Journal of Hydraulic Research*, 39(6), 643-653.

Er, J.W. (2016). Open Water Disposal of Barged Sediment, *Ph.D. Thesis*. School of Civil and Environmental Engineering, Nanyang Technological University.

Er, J.W., Law, A.W.K., Adams, E.E. & Zhao, B. (2016). Open Water Disposal of Barged Sediments. *Journal of Waterway, Port, Coastal, and Ocean Engineering (ASCE)*, 142(5), 1-16.

Gu, J. & Li, C. (2004). Modeling Instantaneous Discharge of Unsorted Particle Cloud in Ambient Water by an Eulerian-Lagrangian Method. *Journal of Hydraulic Research*, 42(4), 399-405.

Johnson, B. H. & Fong, M. T. (1995). *Development and Verification of Numerical Models for Predicting the Initial Fate of Dredged Material Disposed in Open Water, Report 2. Theoretical Developments and Verification Results* (No. WES/TR/DRP-93-1). U.S. Army Engineer Waterways Experiment Station, Vicksburg, MS.

Koh, R.C.Y. & Chang, Y.C. (1973). *Mathematical Model for Barged Ocean Disposal of Wastes*, Technical report, U.S. Army Engineer Waterways Experiment Station, Vicksburg, Miss.

Luketina, D. & Wilkinson, D. (1998). The Transition to the Swarm Phase for a Particle Cloud. *Proceedings, 13th Australasian Fluid Mechanics Conference*. Melbourne, Australia.

Mankoc, C., Janda, A., Arevalo, R., Pastor, J., Zuriguel, I., Garcimartín, A. & Maza, D. (2007). The Flow Rate of Granular Materials through an Orifice. *Granular Matter*, 9(6), 407-414.

Rahimipour, H. & Wilkinson, D. (1992). Dynamic Behaviour of Particle Clouds. *Proceedings, Eleventh Australasian Fluid Mechanics Conference, Vols 1 and 2*. University of Tasmania, Hobart, Australia.

Ruggaber, G.J. (2000). Dynamics of Particle Clouds Related to Open-Water Sediment Disposal, *Ph.D. Thesis*. Department of Civil and Environmental Engineering, Massachusetts Institute of Technology.

USEPA/USACE (1991). *Evaluation of Dredged Material Proposed for Ocean Disposal - Testing Manual,* (The Green Book).

USEPA/USACE (1998). *Dredged Material Proposed for Discharge in Waters of the U. S.* (Inland Testing Manual).

Wang, R.Q., Law, A.W.K. & Adams, E.E. (2014). Large-Eddy Simulation (LES) of Settling Particle Cloud Dynamics. *International Journal of Multiphase Flow*, 67, 65-75.

Wen, F. & Nacamuli, A. (1996). *The Effect of the Rayleigh Number on a Particle Cloud*. Hydrodynamics: Theory and Applications vol. 1 and 2. Balkema, 1275-1280.

Zhao, B., Law, A.W.K., Adams, E.E. & Er, J.W. (2014). Formation of Particle Clouds. *Journal of Fluid Mechanics*, *746*, 193-213.

Zhao, B., Law, A.W.K., Adams, E.E., Shao, D.D. & Huang, Z.H. (2012). Effect of Air Release Height on the Formation of Sediment Thermals in Water. *Journal of Hydraulic Research*, 50(5), 532-540.

 

# A GIS-BASED DRASTIC MODEL FOR ASSESSING GROUNDWATER VULNERABLE ZONES IN NAGPUR CITY, INDIA

SAHAJPREET KAUR GAREWAL[(1)] & AVINASH D. VASUDEO[(2)]

[(1,2)] Department of Civil Engineering, Visvesvaraya National Institute of Technology, Nagpur, India,
sahaj012@gmail.com; avinashvasudeongp@gmail.com

## ABSTRACT

Groundwater is fairly a ubiquitous resource. Increased exploitation, environmental degradation and usages of chemicals have threatened the groundwater quality and presently the aforesaid are the major issues faced by water resources engineers over the world. The possible contaminants in groundwater are practically unlimited; a wide range of pollutants are found in groundwater causing adverse effect on environment. The concern related to groundwater quality generally focuses on the impact of pollutants and quality degradation on human health. Proper management of groundwater is a primary concern, if done meticulously would ultimately lead to a cleaner and healthier environment. Assessment of groundwater vulnerability is one of most significant tool for planning, management and taking necessary remedial action on the affected areas. The present study evaluates the groundwater vulnerable zones of Nagpur city, using DRASTIC method within GIS environment. The groundwater quality and level data of Central Ground Water Board (CGWB) within Nagpur Municipal Corporation (NMC) limits are used to analyze the extent of groundwater contamination in the city. It was observed that all the studied parameters, such as F, Na, TDS, pH, EC, TH, Mg and Cl, were within permissible limit, except some isolated pockets but concentration of nitrate was above permissible limit and its presence mostly found in various parts of the city. Medial city Nagpur, which is not a prime hub of industries, is facing groundwater pollution. This may be due to typical stratigraphy or hydro-geology of the area and disposal of untreated city waste. From this study, it was found that for further prevention of the groundwater pollution, necessary remedial measure should be taken in the highly vulnerable zone of city and waste of the city should be handled properly.

**Keywords:** Groundwater; GIS; vulnerability; DRASTIC; pollutants.

## 1 INTRODUCTION

Groundwater is that component of the hydrological cycle, which is stored and moves slowly through the geological formation of earth. It is highly susceptible to contamination mostly in the urban areas due to the increasing urbanization and careless disposing of unwanted chemicals and wastes in the vicinity of industrial area. Contamination of groundwater is a concern worldwide due to its adverse impact on environment and human health. Protection of existing surface and groundwater resources against contamination and overexploitation is one of the most important aspects of Integrated Water Resource Management (Hamutoko et al., 2016). Once the contamination occurs to groundwater, it is very difficult or sometimes impossible to take corrective steps for remediation, considering the cost and its invisibility in nature (Johnson, 1979).

For effective planning and management of groundwater resources, it is necessary to take corrective measures for preventing groundwater contamination, which can be assessed by groundwater vulnerability assessment tool (Sener and Davraz, 2013). Groundwater vulnerability is an estimation of risk from contaminants, which travel from the land surface to groundwater under natural condition in most of the cases. The vulnerability assessment of an area is evaluated not only to create a scientific insight, but also to help the decision makers to arrive at a best decision from the available data and to take good scientific judgment for groundwater development.

Numerous researches have carried out extensive research to identify the most useful tool for vulnerability assessment in last few decades. A variety of methods have been developed to provide information about groundwater contamination like GOD (Foster, 1987), DRASTIC (Aller et al., 1987), SINTACS (Civita and De Maio, 1997), etc. These methods have been implemented in different regions over the world to evaluate the vulnerable areas for effective groundwater planning and management. The methods used for vulnerability assessment are mostly regional specific, which varies under different hydro-geological conditions. DRASTIC method is one of the most popular methods for groundwater vulnerability assessment among the available alternatives. Babiker et al. (2005), Baalousha (2006), Rahman (2008), Leone et al. (2009), Shirazi et al. (2013), Gupta (2014) and Hamutoko et al. (2016) has applied DRASTIC in thier respective study areas for vulnerability assessment. The groundwater vulnerability map generated using DRASTIC methodology is unique and is only acceptable for the defined hydro-geological properties of a specific area for which it is executed. The rates and weights assigned to DRASTIC parameters varies depending upon the hydro-geological properties of the area under study, hence the resultant groundwater vulnerability map can not be compared to different areas vulnerability map.

Due to the increasing urbanization in Nagpur city and careless disposal of city waste, overexploitation and quality degradation of groundwater have been reported in various regions. Nagpur is named after the Nag River flows within the city and causes adverse impact on the drainage system. Due to the disposal of untreated city waste directly in the water bodies, City Rivers are getting converted into sewers (Jain and Sharma, 2011). To investigate the groundwater condition of Nagpur city, the field data of quality parameters from different groundwater monitoring wells were analyzed. The data of these monitoring wells are regularly collected and maintained by Central Ground Water Board, Government of India (CGWB) and analyzed in perspective standards proposed by the Bureau of Indian Standards (BIS) for drinking water (IS-10500-91, revised 2003) by checking of the permissible limits to decide the suitability of groundwater.

For a proper planning, management and selecting effective remedial measure for the city, groundwater vulnerability assessment is very necessary. The objective of the present study is to evaluate groundwater vulnerability of the Nagpur city using DRASTIC method and to identify the parameters which are responsible for higher vulnerability index.

## 2 STUDY AREA

Nagpur city is located at Geographical centre of India (Figure 1) at mean altitude of 310.5m above the sea level. It lies between 21°00’ to 21°15’ North latitudes and 79°00’ to 79°15’ East longitude and covers a total area of about 218km$^2$ within NMC boundary. Nagpur is centrally urbanized city with a population of approximately 2,405,665. Nag and Pilli River are two major water bodies that flow within the urban setting of the city. Rivers traverses in the city towards East, where Nag River starts from the Western end of the city and Pilli River starts from North East of the city. The stratigraphy of city is followed by the Deccan trap and Archeans formation (Manzar, 2013). Massive basalt occupies a major portion of the city. The climate varies from hot summer where temperature rises to 45°C and drops to 12°C in cold winter. The average rainfall of the city is about 1100mm.

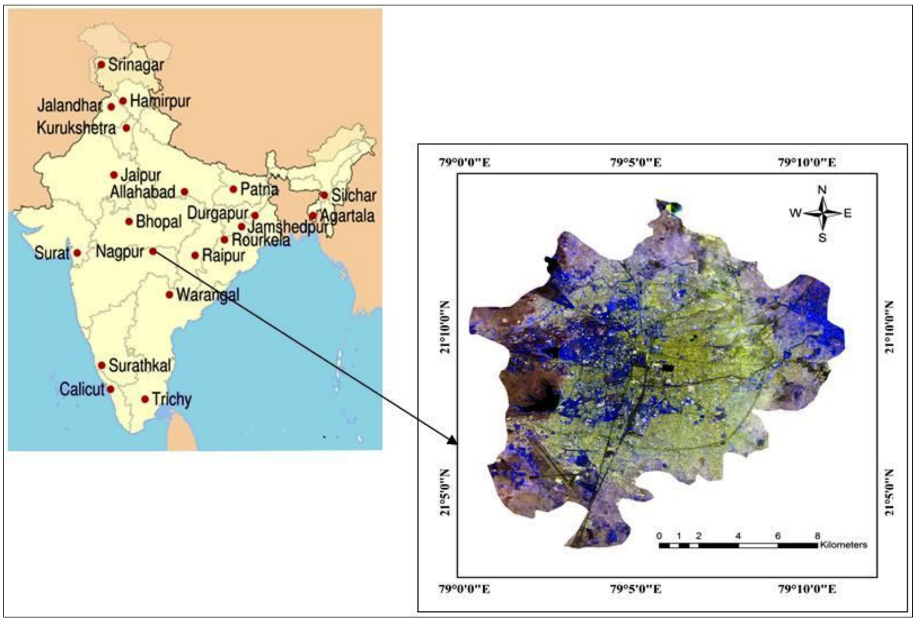


**Figure 1**. Map of the study area.

## 3 MATERIALS AND METHODOLOGY

A GIS based DRASTIC method was adopted to identify the vulnerable zones of Nagpur city. The detailed methodolog that was formulated for the present study is shown in Figure 2.The following steps are employed.

i. DRASTIC method was implemented to assess the groundwater vulnerability;
ii. Single parameter sensitivity analysis (SPSA) was carried to identify the most effective parameters;
iii. The resultant vulnerability map was correlated with quality parameters of the city to analyze how close the assessment is with the reality of plain.

  / ISSN 1562-6865 (Online) - ISSN 1063-7710 (Print)

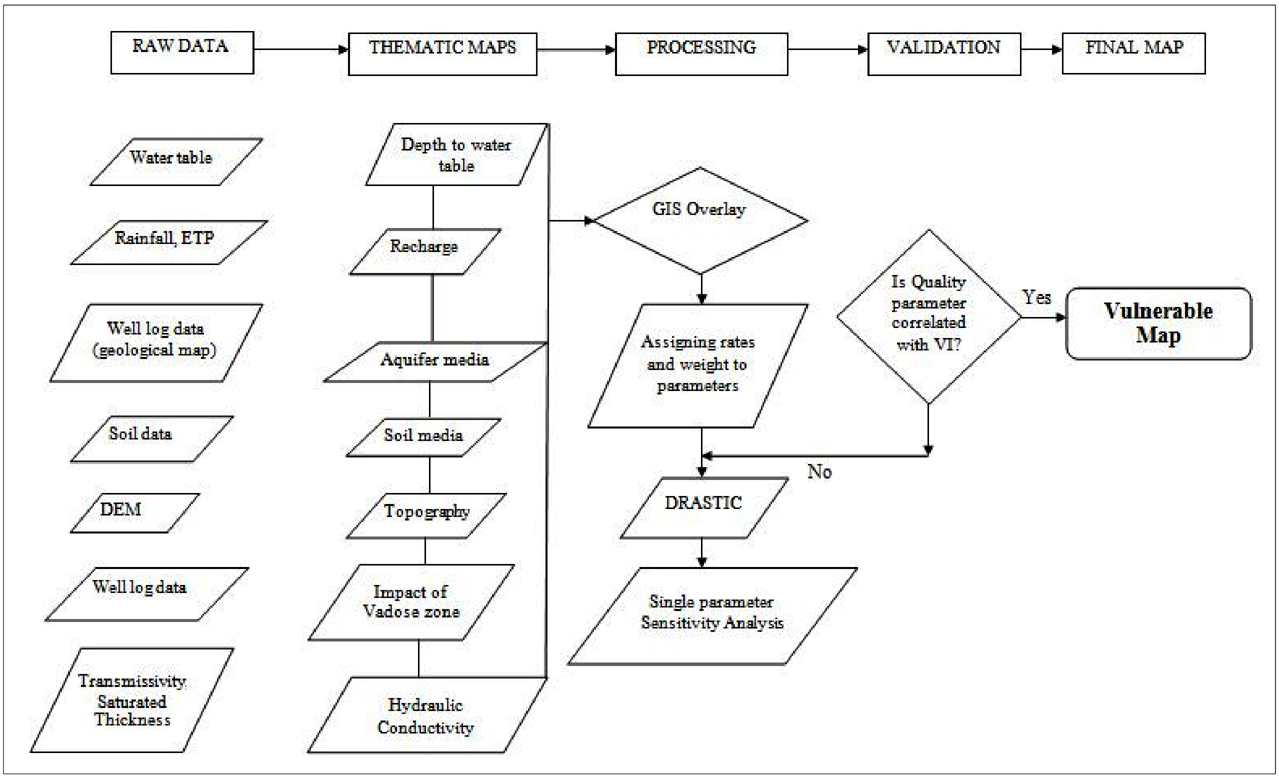


**Figure 2**. Overall methodology.

3.1 DRASTIC

DRASTIC is an overlay and index method used to find the intrinsic vulnerability of an area based on the factors affecting the transport and attenuation of contaminants. Vulnerability of an area is estimated based on the known factors of aquifers (Aller et al., 1987), such as:

- Depth to water table (D);
- Recharge (R);
- Aquifer media (A);
- Soil media (S);
- Topography (T);
- Impact of vadose zone (I);
- Hydraulic Conductivity (C).

Each parameter is classified to different sub-parameters depending on their characteristics and are rated on the scale of 1 to 10 based on the factors that they are contributing to contamination. Weights are assigned to each parameter from 1 to 5 according to their relative importance on groundwater vulnerability. Vulnerability index is computed as the weighted sum overlay of all the parameters using Eq. [1], as given below:

$$VI = D_rD_w + R_rR_w + A_rA_w + S_rS_w + T_rT_w + I_rI_w + C_rC_w \qquad [1]$$

where

VI is Vulnerability Index, r is the rating assigned to different sub-parameters, and w is the weight of the parameters.

The numerical rating and weights documented by Aller et al. (1987) using Delphi technique have been used worldwide and is adopted in the study for the assement of groundwater vulnerability shown in Table 1. All the thematic maps and vulnerability classification map was prepared using GIS technique in ArcGIS 10 software. Once the DRASTIC index is computed considering the intrinsic properties of aquifer, they are classifed into several zones characterized by different level of vulnerability.

3.2 Single parameter sensitivity analysis (SPSA)

SPSA was carried out to identify the effective parameter for vulnerability assessment and to mark the impact of individual parameter on the other parameters and vulnerability index. SPSA perceive the importance of the coordination of weight and rates of the parameter on overall vulnerability assessment of an area. In this analysis, ‘Effective weight’ of the parameter is evaluated using Eq. [2] and compared to the assigned theoretical weight of respective parameter (Babiker et al., 2005).

$$W = \frac{P_w P_r}{VI} \qquad [2]$$

where

W is the effective weight of the parameter, VI is the vulnerability index, and Pw and Pr are the weight and rates of respective parameter.

## 4. INPUT DATA FOR GROUNDWATER VULNERABILITY ASSESSMENT USING DRASTIC

Groundwater vulnerability of an area is estimated using known condition of aquifers. Each parameter used for vulnerability assessment has its significant impact on groundwater contamination. DRASTIC is GIS based method, thematic map of all the parameters are used as an input for estimating groundwater vulnerability. Thematic map for parameters are prepared using the data collected from different government departments, previous research projects and authorized websites.

### 4.1 Depth to water table

The depth to water table plays a crucial role for vulnerability assessment, it influences the time of contaminant to undergo physical, chemical and microbiological reaction. It is the depth of unsaturated media, which contaminants travels from land surface (source) to reach ground water table. It is obtained by the data of 45 monitoring wells of CGWB located at different zones within the city. The data collected from different zones are interpolated using Geostatisical analysis (kriging) and proceeded in Arc GIS environment to obtain map of depth to water table of the city and it varies from 0.7m to 15.2m below ground level (Table 1). In general, the greater the depth to water table, the lesser the chance of contamination will be.

### 4.2 Recharge

Recharge has a significant impact on vulnerability assessment. It helps in dilution and dispersion of the contaminants, depending on the concentration and hydrogeology of the area (Aller et al., 1987). The contaminant reaches to the groundwater with the amount of water infiltrate to recharge the aquifer. Rainfall is considered as the major source of recharge in the study area, the data of nearby rain gauge station are collected from India Meteorological Department (IMD). Net recharge is calculated as 30 to 40% of the rainfall (Baalousha, 2006; Gupta, 2014). The recharge varies from 396 mm to 433 mm within the study area (Table 1). The higher the groundwater recharge, the more the potential contaminant transport will be.

### 4.3 Aquifer media

Aquifer media refers to the hydro-geology of the area and defines the formation of rocks, which can yield an adequate quantity of water for use. Water stored in the aquifer moves through the various geological formations and the contamination migrations are affected by media through which it is travelling. It is obtained from litho log data acquire from CGWB and proceeded in ArcGIS software to digitize and generate raster map acceptable for DRASTIC proceeding, classifications, as shown in Table 1. The major portion of the study area is covered with Massive basalt (igneous rock) and other hard rock formation present in the area are Amgoan Gneissic complex (Metamorphic rock), Unclassified Gniess Tirodi (Metamorphic rock) and Intertrapean.

### 4.4 Soil media

Soil media plays a significant role for assessment of the groundwater vulnerability as it restricts the movement of contaminants through recharge. The soil map is collected from National Bureau of Soil Survey (NBSS), Nagpur, India. The map is scanned, geo referenced and converted in raster format supported for DRASTIC proceeding. The study area is mainly protected by clay, clayey loam and sand, as shown in Table 1. Finer grain soil limits the flow of contaminants to larger extent as compared to coarser grain soil.

### 4.5 Topography

Topography affects the infiltration rate of surface water by controlling the residence time, which governs whether contaminant will infiltrate into media or become the part of surface runoff. Flat topography is responsible for infiltration of contaminants, as time of contact for infiltration will be more and vice versa for steep slope. Slope of the study area is extracted from Digital elevation model (DEM) prepared using Cartosat imagery downloaded from government authorized website (Bhuvan). The city follows one sided topography, steeper in the West to milder on East varies from 2.7% to 23% (Table 1).

### 4.6 Impact of Vadose zone

The Vadose zone is defined as the unsaturated zone above the water table. Vadose zone is important for contaminant attenuation because various chemical, physical and microbiological reactions occur in this zone. Thickness of vadose zone is a depth of material by which the contaminants must pass before reaching the aquifer, hence the greater the depth, the lesser the contaminants will be. Thickness of vadose is calculate using an approach defined by (Li and Zhao, 2011), DEM and the depth of water table, which varies from 0.6m to 10.8m (Table 1).

4.7 Hydraulic conductivity

Hydraulic conductivity is the property of aquifer media, which governs the rate at which the groundwater water flow. The hydraulic conductivity depends on the properties of media and characteristics of the flowing water. The well log data of aquifer are used as input to form thematic map. Saturated thickness of aquifer is divided from transmissivity to obtain map showing hydraulic conductivity of the area. It varies from $10^{-6}$ to$10^{-4}$ m/s (Table 1). The higher the hydraulic conductivity of the area, the more the contaminants transportation will be, leading to the rise in the vulnerability index.

**Table 1**. Rates and weight of the parameters.

| **1. Depth to water (m)** | | | **2. Recharge(mm)** | | | **3. Aquifer Media** | | |
|---|---|---|---|---|---|---|---|---|
| Sub parameter | R | W | Sub parameter | R | W | Sub parameter | R | W |
| 0.7-2.61 | 10 | | 396-404 | 3 | | Intertrapean | 1 | |
| 2.62-3.87 | 9 | | 405-410 | 5 | | Massive basalt | 4 | |
| 3.87-4.69 | 8 | | 411-416 | 7 | 4 | Amgaon- Gneiss complex | 7 | 3 |
| 4.69-5.95 | 6 | 5 | 417-422 | 8 | | | | |
| 5.95-7.86 | 4 | | 423-433 | 9 | | Unclassified Gneiss-tirods | 8 | |
| 7.86-10.77 | 2 | | | | | | | |
| 10.77-15.2 | 1 | | | | | | | |

| **4. Soil media** | | | **5. Topography (%)** | | | **6. Impact of Vadose zone (m)** | | | **7. Hydraulic Conductivity(m/s)** | | |
|---|---|---|---|---|---|---|---|---|---|---|---|
| Sub parameter | R | W | Sub parameter | R | W | Sub parameter | R | W | Sub parameter | R | W |
| Clay loam | 3 | | <2.7 | 10 | | 0.6-3.2 | 8 | | $<10^{-6}$ | 5 | |
| Clayey | 7 | 2 | 2.7-5 | 9 | | 3.2-3.9 | 7 | | $10^{-5}$-$10^{-6}$ | 6 | |
| Alluvial | 8 | | 5-7.9 | 7 | | 3.9-4.5 | 6 | | $10^{-4}$-$10^{-5}$ | 8 | 3 |
| | | | 7.9-11 | 5 | 1 | 4.5-5 | 5 | 5 | $10^{-3}$-$10^{-4}$ | 9 | |
| | | | 11-16 | 4 | | 5-5.9 | 4 | | | | |
| | | | 16-23 | 3 | | 5.9-7 | 3 | | | | |
| | | | 23> | 1 | | 7-10.8 | 2 | | | | |

*R=rating and W=weight

## 5. RESULTS

The Groundwater vulnerability of study area is evaluated by contribution of seven intrinsic parameters of aquifer rated and weighted using already documented Delphi technique of Aller et al. (1987), as shown in Table 1.

5.1 DRASTIC

The groundwater vulnerability of the study area was acquired by DRASTIC approach. All the groundwater controlling parameters are combined to form a map showing areas less or more susceptible to groundwater contamination. The resultant vulnerability map is classified into five vulnerable zones, showing the areas under very high vulnerability to very low vulnerability using Natural Break (Jenks) method in ArcGIS software. The resultant map (Figure 3) shows 14.20% and 49.30% of the total study area lies under very high and high vulnerable zones, followed by 19.02%, 10.09% and 7.39% under moderate, low and very low vulnerable zones, respectively. The areas covered under high to very high vulnerable zones are at the higher risk as the vulnerability index value is high and are more susceptible to contamination. From the detailed examination of vulnerability map of the city, it was found that Central to North East part of the city are more vulnerable and at high risk zones, where the South zone of the city is found to be safe, having least vulnerability.

5.2 Single parameter Sensitivity analysis (SPSA)

For finding the factors that are more responsible for higher value of vulnerability index, a statistical summary of parameter was analyzed before SPSA was carried out. Table 2 shows the statistical summary of the parameters. The mean of all the parameters were examined to find their contributions on the vulnerability index, which follows the sequence of R > T > C > S > A > I > D.

**Table 2**. Statistical summary of governing parameters.

| | D | R | A | S | T | I | C |
|---|---|---|---|---|---|---|---|
| Min | 1 | 3 | 1 | 3 | 1 | 2 | 5 |
| Max | 10 | 9 | 8 | 8 | 10 | 8 | 9 |
| Mean | 4.47 | 8.24 | 5.52 | 6.7 | 8.22 | 5.51 | 7.07 |
| SD | 1.64 | 1.42 | 1.72 | 1.08 | 1.98 | 1.34 | 1.21 |

The SPSA analysis was carried to find out most effective parameters for vulnerability assessment. The result of SPSA is shown in Table 3 and it was found that Recharge, Topography, Conductivity, Soil media, Aquifer media and Impact of Vadose zone are the more effecting parameters and the depth to water level is the least effective, as its effective weight is less than the assigned theoretical weight.

**Table 3**. Single parameter sensitivity analysis.

| Parameter | Theoretical weight | Theoretical weight (%) | Effective weight (%) | | | |
|---|---|---|---|---|---|---|
| | | | Min. | Max. | Average | SD |
| D | 5 | 21.74 | 4 | 28 | 14.91 | 4.44 |
| R | 4 | 17.40 | 9 | 37 | 22.75 | 3.13 |
| A | 3 | 13.04 | 1 | 19 | 13.14 | 2.91 |
| S | 2 | 8.70 | 3 | 18 | 9.76 | 2.32 |
| T | 1 | 4.35 | 0 | 12 | 5.42 | 1.83 |
| I | 5 | 21.74 | 7 | 29 | 18.72 | 2.89 |
| C | 3 | 13.04 | 9 | 22 | 14.58 | 2.30 |

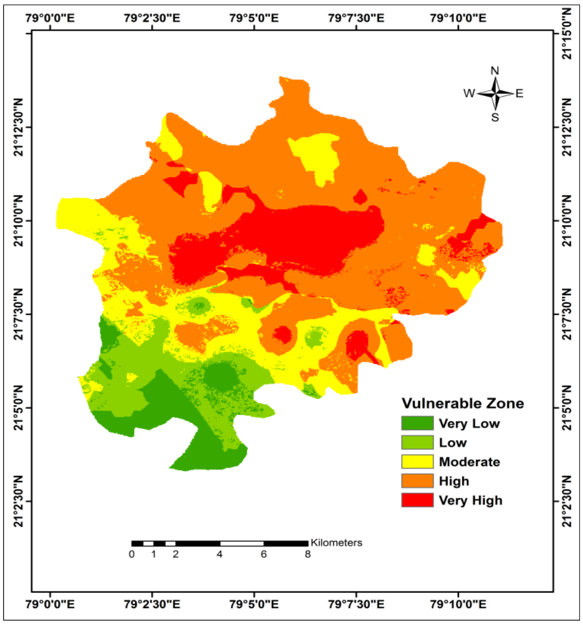


**Figure 3**. Vulnerability map of Nagpur city.

5.3 Validation

The Groundwater vulnerability map of Nagpur city evaluated using DRASTIC approach is regional specific, which needs to be validated. Of all the quality parameters documented in CGWB report, nitrate ($NO_3$), total dissolve solid (TDS), electrical conductivity (EC), sodium (Na), and magnesium (Mg) are used for validation of the vulnerability map. All the quality parameters are classified into five zones varying from very low to very high concentrations of contaminant (Figure 4).The vulnerability map of the city is also classified into five vulnerable zone varies from very low vulnerable zones, having the least vulnerability index, to very high vulnerable zones, having the higher value of vulnerability index. The concentration of quality parameters and vulnerability index of different monitoring wells are observed. Different regression techniques are used to find the correlation between the DRASTIC index and Quality parameters (Table 4).

 

**Table 4**. Correlation between DRASTIC index and Quality parameters.

| Correlation | Pearson coefficient | Kendall's coefficient | Spearman coefficient |
|---|---|---|---|
| DRASTIC with $No_3$ | 0.249 | 0.130 | 0.174 |
| DRASTIC with TDS | 0.327 | 0.213 | 0.324 |
| DRASTIC with EC | 0.306 | 0.238 | 0.358 |
| DRASTIC with Mg | 0.338 | 0.138 | 0.179 |
| DRASTIC with Na | 0.377 | 0.290 | 0.392 |

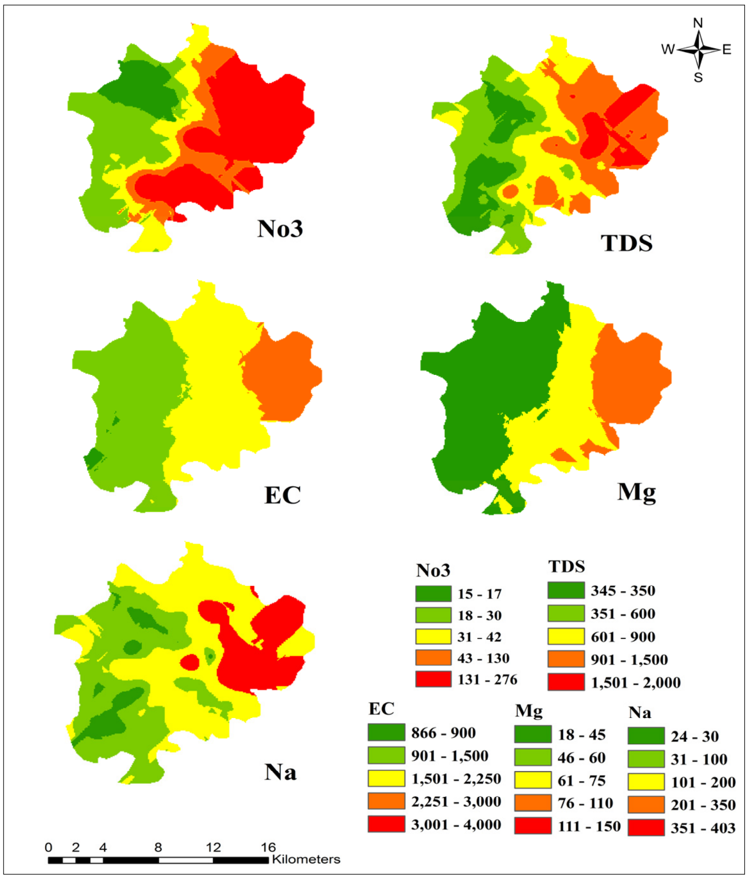


**Figure 4**. Spatial variation of contaminants within the city limit.

## 6. CONCLUSIONS

In this study, the Groundwater vulnerability of the city was evaluated using DRASTIC method. All the intrinsic parameters of an aquifer are included for the assessment of groundwater vulnerability. From the study of vulnerability map, it was found that:

i. Central to North-East part of the city are more vulnerable to contamination and at high risk zones;
ii. The results of statistical summary and single parameter sensitive analysis performed for all the parameters revealed that the recharge rate, topography, soil media and aquifer media are the main factors that are affecting the vulnerability of the area;
iii. Also, the groundwater hydraulic parameters like hydraulic conductivity and depth to water table influence the vulnerability;
iv. The higher vulnerability index on the Eastern part of the city is mainly due to one sided topography of the city, which is steeper towards the East and the dumping site is also located at East of the city.

### 6.1 Remedial measure

The various zones and observation wells of the city are found to be affected from higher concentration of contaminants. Hence, the following remedial measure can be adopted to reduce the contamination in the city:

i. Along with the lateral lining, it is recommended to provide bottom lining for canals to reduce the seepage losses;
ii. A larger diameter sanitary protection around the affected wells is necessary to restrict the boundary of contamination;
iii. As the river bodies are flowing within the urban setting the untreated city waste should not be disposed directly in the rivers without treatment;
iv. The capacity of the existing wastewater treatment plant should increase to handle larger city waste;
v. A proper proposal for disposing municipal solid waste collected from different zones of the city;

vi. Landfill sites must be selected very carefully, considering the hydro geological settings of area and away from the habitation;
vii. Rainwater harvesting practices should be adopted to enlarge the recharge of groundwater that helps in dilution of contamination.

**REFERENCES**

Aller, L., Lehr, J.H., Petty, R. & Bennett, T. (1987). DRASTIC: A Standardized System to Evaluate Groundwater Pollution Using Hydrogeologic Setting. *Jour. Geol. Soc. India ,* 29(1), 23-37.

Baalousha, H. (2006). Vulnerability Assessment for the Gaza Strip, Palestine Using DRASTIC. *Environmental Geology ,* 50(3), 405-414.

Babiker, I.S., Mohamed, M.A., Hiyama, T. & Kato, K. (2005). A GIS-Based DRASTIC Model for Assessing Aquifer Vulnerability in Kakamigahara Heights, Gifu Prefecture, Central Japan. *Sci. Total Environ.,* 345(1), 127-140.

Civita, M. & De Maio, M. (1997). *Un Sistema Parametrico per la Valutazione e la Cartografia della Vulnerabilita' degli Acquiferi All'inquinamento: Metodologia e Automatizzazione.* Pitagora Editrice, Bologna.

Foster, S.S.D. (1987). Fundamental Concept in Aquifer Vulnerability Pollution Risk and Protection Strategy. *Vulnerability of Soil and Groundwater to Pollutants*,38, 69-86.

Gupta, N. (2014). Groundwater Vulnerability Assessment Using DRASTIC Method in Jabalpur District of Madhya Pradesh. *International Journal of Recent Technology and Engineering,* 3(3), 36-43.

Hamutoko, J.T., Wanke, H. & Voigt, H.J. (2016). Estimation of Groundwater Vulnerability to Pollution Based on DRASTIC in the Niipele Sub-Basin of the Cuvelai Etosha Basin, Namibia. *Physics and Chemistry of the Earth, Parts A/B/C,* 93, 46-54.

Jain, S.K. & Sharma, V. (2011). *Contamination of Ground Water by Sewage,* Central Ground Water Board Ministry of Water Resources Government of India, Faridabad.

Johnson, C.C. (1979). Land Application of Waste - An Accident Waiting to Happen. *Ground Water*. 17(1), 69–72.

Leone, A., Ripa, M.N., Uricchio, V., Deak, J. & Vargay, Z. (2009). Vulnerability and Risk Evaluation of Agricultural Nitrogen Pollution for Hungary's Main Aquifer Using DRASTIC and GLEAMS Models. *Journal of Environmental Management ,* 90(10), 2969–2978.

Li, R. & Zhao, L. (2011). Vadose Zone Mapping Using Geographic Information Systems and Geostatistics: A Case Study in the Elkhorn River Basin, Nebraska, USA. In *Water Resource and Environmental Protection (ISWREP)*, 4, 3177-3179.

Manzar, A. (2013). *Ground Water Information Nagpur District.* CGWB, Nagpur.

Rahman, A. (2008). A GIS Based DRASTIC Model for Assessing Groundwater Vulnerability in Shallow Aquifer in Aligarh, India. *Applied Geography ,* 28(1), 32–53.

Sener, E. & Davraz, A. (2013). Assessment of Groundwater Vulnerability Based on a Modified DRASTIC Model, GIS and an Analytic Hierarchy Process (AHP) Method: the Case of Egirdir Lake Basin (Isparta, Turkey). *Hydrogeology Journal ,* 21(3), 701–714.

Shirazi, S.M., Imran, H.M., Akib, S., Yusop, Z. & Harun, Z.B. (2013). Groundwater Vulnerability Assessment in the Melaka State of Malaysia Using DRASTIC and GIS Techniques. *Environmental Earth Science ,* 70(5), 2293–2304.

 

Proceedings of the 37th IAHR World Congress
August 13 – 18, 2017, Kuala Lumpur, Malaysia

# TRACKING OF FLOATING OBJECTS ON RIVER SURFACE BY NUMERICAL SIMULATION

AKIHIKO NAKAYAMA(1), SEAK NI CHAI(2), HUAN TAO GOH(3) & KHAI CHIN NG(4)

(1,2,3) Universiti Tunku Abdul Rahman, Kampar, Malaysia,
akihiko@utar.edu.my
(4) Universiti Tenaga Nasional, Kuala Lumpur, Malaysia,
NkChing@uniten.edu.my

## ABSTRACT

In order to understand the effects of various objects that float on surfaces of rivers and channels, a method of tracking floating objects based on numerical flow simulation has been developed. The floating objects are assumed to be rigid bodies with no preferred directional characteristics but with given drag coefficient. The flow computation is a Large Eddy Simulation (LES) that models the effects of floating bodied by their drag forces. The calculation is applied to a river reach for which the flow and trajectory data are available. It is then applied to track assumed bodies in meandering river in Malaysia. The results show accumulation of bodies on the outer bank of bends as is observed at the site.

**Keywords:** river flow; numerical simulation; LES; floating objects.

## 1 INTRODUCTION

There are various objects that float on surfaces of rivers and channels that influence the aesthetic and other qualities of the natural and constructed streams. Large objects such as wood branches and debris that are washed into flows can not only influence the conveyance of the river streams but may impact the environment (Boogaard et al., 2016). Small trash like plastic bags and solid waste are impacting the ecology of the streams and the sea. The flow conveyance can be impeded during floods and overflow and inundation can be caused. River structures such as the bridge piers and intake facilities are also susceptible to blockages due to floating and suspended objects (Hamid and Abdullah, 2011). Management of these floating objects in rivers is becoming a major issue in developed and developing countries (Boogaard et al., 2016). Due to its detrimental effects, preventive measures are taken for the intake structures of hydropower stations (Hribernik et al., 2013). For prevention of debris clogging the intakes, diverter structures and trash traps are built. For the effective installment of such preventive devices or structures it is very important to know the characteristics of the movement of the floating objects with and without the devices. The trajectories of floating objects depend on the details of the surface flow, which is part of the complex three-dimensional free-surface flow. Therefore, the flow in natural rivers with complex geometries needs to be known before tracking the floating objects is performed.

There are a number of methods of finding particle trajectories, but most of them suffer statistical uncertainty due to the inadequate turbulence realization (e.g. Piterbarg and Ozgokmen, 2004). In order to find the effects of floating objects on river surfaces with strong turbulence effects, we have implemented the computation of the motion of floating objects in a Large Eddy Simulation (LES) code (called KULES, Nakayama, 2015) for rivers and channels. The objects that are intentionally or unintentionally disposed and washed in river streams are transported by the flow and influence the flow as well. The two methods of tracking have been considered. The first one assumes the mass and the size of the objects are negligible and the objects are regarded as passive particles. In this case, the flow calculation can be conducted without the effects of the floating objects. In the second method, the motion of each object is computed simultaneously with the flow. The object is assumed to have the same density as the water in the river but with an assumed drag coefficient. The displacement effects due to the existence of the bodies are neglected. The bodies are assumed to have no preferred direction and the resistance is assumed to act in the direction opposite of the flow and with a known drag coefficient. They approximate the motion of trash and small debris.

Trajectory calculation is done for two very different river reaches but with distinctive bends. The first one has a single sharp bend with high relatively large slope near mountains and the second one is a meandering reach with multiple bends in flat low land. Both are the stretches where trajectories of floating objects are difficult to predict.

## 2 CALCULATION METHOD AND EQUATIONS

In order to construct a method of tracking floating objects, we need to compute the flow itself. When the floating objects are small and the number of objects is small, we may neglect the effects of the objects on the flow and the flow can be independently computed by considering the objects as passive particles. But when the objects are large and their obstruction to the flow is significant, we need to compute the flow around the solid objects. In this case the thee-dimensional simulation of the flow around the objects must be considered and the two-way Fluid-Structure Interaction must be considered. We consider cases in which the individual shapes of the floating objects may not play important effects and interpret them as objects with flow resistance. It will apply to the cases of medium size objects like trash and small debris but not to cases with large objects with distinctive geometric features like wood trunks comparable to the width or the depth of of the flow.

In any case, the flow is simulated by the Large Eddy Simulation methodology. The scale of resolution is such that the details of the floating objects are not represented by the numerical grid but the large-scale three dimensional flow can be resolved. The method we use here is described in Nakayama (2015) together with basic verifications done in basic channel flows and a few applications to real rivers has also been done (Nakayama and Asami, 2016).

The equations of motion and the continuity equation with the effects of floating objects are

$$\frac{\partial u_i}{\partial t}+u_j\frac{\partial u_j}{\partial x_j}=-\frac{1}{\rho}\frac{\partial p}{\partial x_i}+g_i+\frac{\partial}{\partial x_j}\left[(\nu_t+\nu)\left(\frac{\partial u_i}{\partial x_j}+\frac{\partial u_j}{\partial x_i}\right)\right]+\frac{1}{2}C_D\lambda(V_i-u_i)V_R \qquad [1]$$

and

$$\frac{\partial u_j}{\partial x_j}=0 \qquad [2]$$

where $u_i$ is the components of velocity vector of water in the Cartesian coordinates $x_i$ with $x_3$ vertically taken positive upward, $p$ is the pressure, $g_i$ is the gravitational acceleration, $\nu$ and $\nu_t$ are the coefficients of molecular and subgrid viscosity, $C_D$ is the drag coefficient of the floating sold body with the frontal area per unit volume, $\lambda$, $V_i$ is the velocity of the rigid body, and $V_R$ is the resultant of flow velocity relative to the velocity of the body $[(u_i-V_i)(u_i-V_i)]^{1/2}$. Smagorinsky model is used for determining $\nu_t$. It is noted that the resistance in [1] is applied only at the free surface and the depth of the floating bodies are considered smaller than the computational grid size.

The vertical position of the free surface $h(x_1,x_2)$ is solved by requiring it to satisfy the kinematic free surface boundary condition

$$\frac{\partial h}{\partial t}+u_{s1}\frac{\partial h}{\partial x_1}+u_{s2}\frac{\partial h}{\partial x_2}=u_3+\gamma\frac{\partial h}{\partial x_1}+\gamma\frac{\partial h}{\partial x_2} \qquad [3]$$

where $u_{s1}$ and $u_{s2}$ are the velocity components on the free surface and the last two terms represent the effects of the subgrid surface fluctuation and $\gamma$ is the model coefficient, taken here as the same as the Smagorinsky eddy viscosity $\nu_t$.

The equation for the motion of the floating body is

$$M\frac{dV_i}{dt}=C_D A\frac{1}{2}\rho V_R\left(u_{si}-V_i\right),\qquad i=1,2 \qquad [4]$$

where $M$ is the mass of the floating body, and $A$ is the frontal area of it. It is noted that if the density of the floating solid object may be assumed equal to the water density it can be re-written as

$$\frac{dV_i}{dt}=C_D\lambda\frac{1}{2}V_R\left(u_{si}-V_i\right),\qquad i=1,2 \qquad [5]$$

The location $X_i$ of the body is computed by integrating this equation. It is noted that if the mass is small, [4] indicates that $V_i=u_{si}$ and the objects move with the flow.

The numerical method used to solve the above governing equations is based on a HSMAC method (Hirt and Cook, 1972) extended to free surface flows. The standard Smagorinsky model is used for the sub-grid scale effects. The motion of the free-surface is computed from the kinematic condition in the cells containing the free surface. The pressure in the cells containing the free surface is not computed but set as the pressure boundary condition that the pressure on the free surface is equal to the atmospheric. The solution algorithm is close to the VOF method (Hirt & Nichols, 1981) but is limited to the single-valued function of the horizontal coordinates. The velocity component normal to the free surface is computed from the momentum equations so the wetting front can advance over or retract from the dry ground. In the calculation, the motion of the wetting front is on the rough surfaces and is allowed only when the depth exceeds one half of the roughness height.

The boundary condition considers the wall model as done in the previous work Nakayama and Asami (2016) which explains more about the method used here. The bed roughness is incorporated as the roughness element height set in the boundary condition. The bed is considered fixed but the resistances due to the riparian vegetation are considered.

## 3 APPLICATION TO RIVER FLOW

### 3.1 Studied river reaches

Calculation was conducted for two different river reaches with distinctive plan forms. The first one is in a mountain area with a slope nearly 1/200. It is a mid reach of Ibogawa River in Hyogo Prefecture of western Japan. Figure 1 shows its location and the satellite image. The simulation calculation was conducted in the region enclosed by white box of about 2km x 2km. The river bends due to the mountainous terrain with hard rocks.

The second river reach for which simulation was conducted is in a low land in Perak, Malaysia. Figure 2 shows the location of this river and the aerial view of the simulated region in the city of Teluk Intan. Here the river meanders around in very flat low land near the Melaka Strait where it empties. The river makes almost 360 deg. wind within the area indicated by the white box. The radius of the curve is only about two times the river width and the effects of the bend are expected to be very strong.

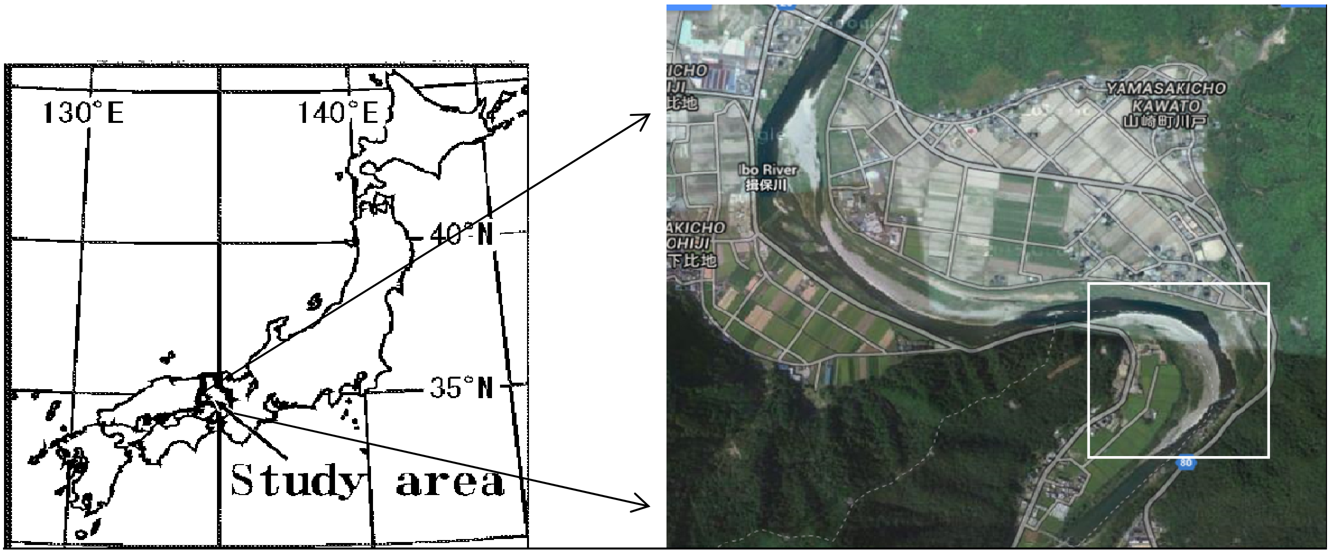


**Figure 1**. The river reach with a sharp bend of Ibogawa River in Japan. White box indicates the simulation region.

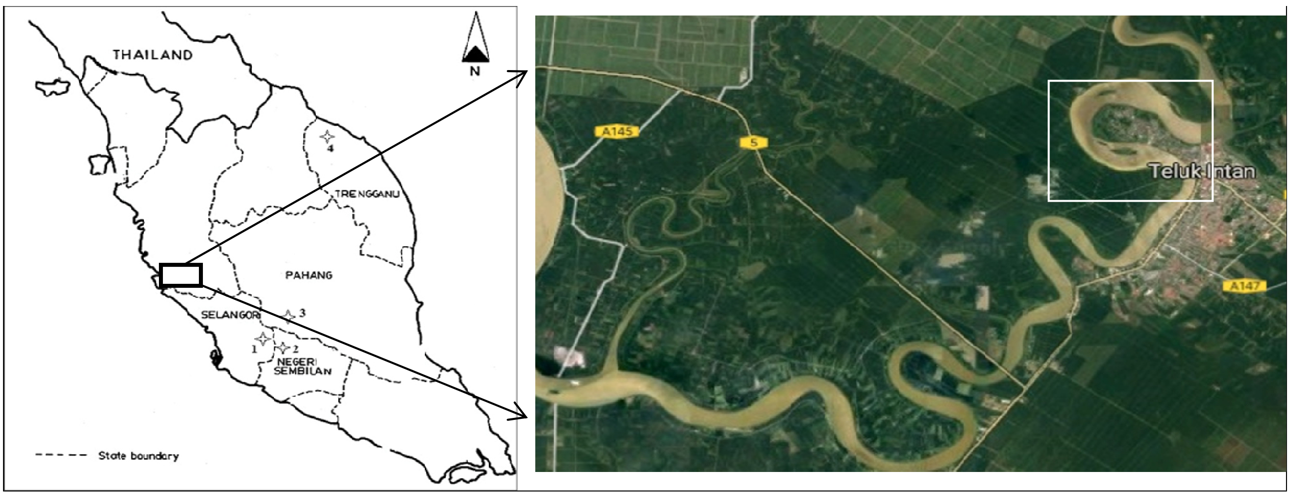


**Figure 2**. The meandering river reach of Perak River in Malaysia. White box indicates the simulation region.

Calculation was conducted starting from the flow condition with the flow rate lower than the target flow so the wetting front can be represented as the result of increasing flow rate. The main calculation is done for a steady state with constant flow rate. The initial flow field was generated by setting an approximate free surface level and the slope with logarithmic velocity distributions everywhere. Computation with the constant inflow rate for about one to two flow-through time was conducted. The flow rate for Ibogawa is 20m$^3$/s, while that for Perak River is 1500m$^3$/s.

The inflow section of the upstream segment is set as the turbulence developing region and the instantaneous velocity, pressure and the free surface elevations of the downstream section of this development region are recycled to the inflow section. In the recycling, the magnitude of the velocity is adjusted so that the total volume flow rate to follow the assumed hydrograph. This allows development of turbulent fluctuations at the inflow section. There are confluences of small tributaries. The inflow rate through these tributaries is prescribed but no turbulence developing region is introduced.

The condition at the downstream boundary depends on what is the state of the flow further downstream. If the slope is steep like in Ibogawa River low flow period, a free outflow condition is applied. For the low meandering case of Perak River, the downstream stage or the uniform flow condition is assumed at the downstream boundary.

3.2 Results of the flow simulation

The surface flow and the elevation of the surface calculated by the LES are shown in Figures 3 and 4. The average flow velocity for the Ibogawa River is about 1m/s and that for Perak River is 1.5m/s. The area covered in Ibogawa calculation is 1500m x 2000m and that in Perak River is 4000m x 5000m. The average slope of Ibogawa River reach is about 1/200 and that of Perak River is 1/4000. The Bend of Ibogawa is to the right and there is a steep slope of less than 1/100 after the first bend. Perak River bends first to the right and then to the left by nearly 360 degrees. The bed roughness is represented by the roughness height of 0.05cm for both rivers. In each of these cases the computational grid is a fixed rectangular grid of approximately 200 x 200 x 70 points and about 30 points lie across any flow section.

In Figures 3, the free surface is indicated by blue region and the arrows represent the surface velocity distribution across representative transverse sections. In Figure 4, the river flow region is indicated by the blue line and the elevation of the water surface is shown as color contours. In both cases, the surface flow is strongly influenced by the bend. In Ibogawa, the bend is only in one direction and the left bank is always the outer bank. In case of Perak River, the curve reverses three times. The strongest one is in the middle of the simulation region where flow turns almost 360 degrees.

The surface velocity distribution indicate there is strong secondary flow but also indicate changes in the velocity in wide part and narrow passages. In addition, islands of various sizes effect the local velocity and the turbulence as well.

(a) LES results

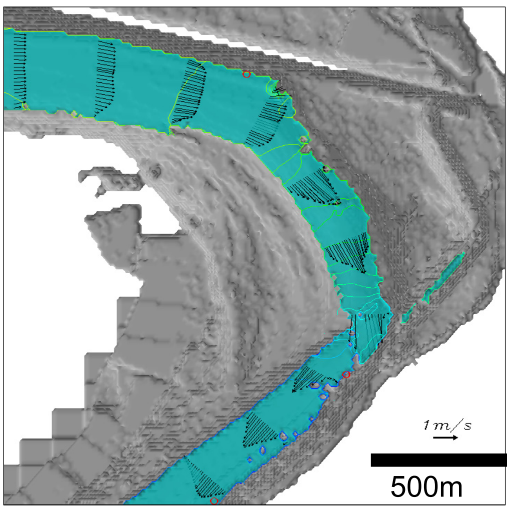


(b) Aerial photo

**Figure 3**. The average surface flow of Ibogawa River obtained by LES.

 

(a) LES results (b) Satellite image

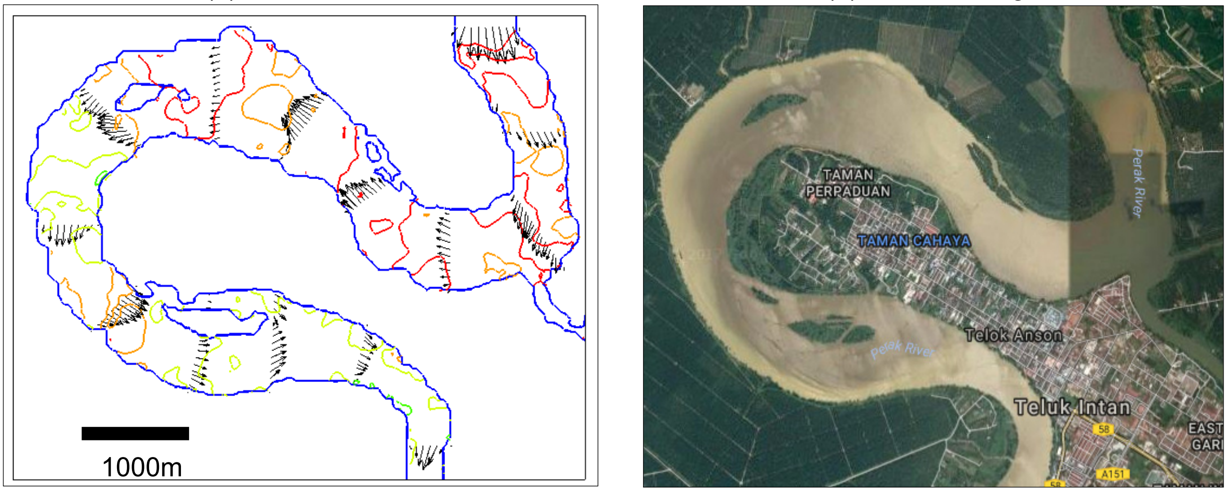


**Figure 4**. The average surface flow of Perak River obtained by LES.

## 4 SIMULATION OF MOTION OF FLOATING PARTICLES

Tracking of floating objects were conducted in the flow as shown above. In all cases, the size of the floating objects are assumed smaller than the computational grid and not explicitly represented as explained earlier. First the rows of particles are introduced at the upstream end and the positions of these particles are tracked using the equations shown in Section 2. The drag coefficients of the particles are assumed to be one. It is a typical value for round bluff bodies like spheres. The frontal area ratio $\lambda$ is assumed unity as well, the frontal area is assumed small so that the mass in the equation of motion of the body is set equal to that of water. The drag due to the objects is applied only in the grid cells that contain the objects. The parameters associated with the floating objects must be adjusted in specific applications and the situation with medium size objects are assumed in the present calculation.

Figure 5(a) to (c) show the particle tracking in Ibogawa River. Initially three rows of 150 particles are placed in three rows spanning the full river width on the surface at the upstream end as shown in Figure 5(a). The subsequent positions of these particles after release are tracked. Figure 5(b) is 60 seconds after the particles are released, and Figure 5(c) is the distribution 300 seconds after the release. It is seen that the particles placed in straight lines quickly lose the initial arrangement quickly due to the different flow speed and the turbulence. There is a sudden bend of something like 45 degrees and the flow is a rift on a high slope. Particles run down quickly in the center leaving slow moving particles near both banks. Then there is a second bend in the same direction, but here there is a sharp drop and downstream of it is like a pool and the speed is slow. There is a gathering of particles in the pool and slowly translate downstream.

(a) Initial time (b) 60 seconds after release (c) 300 seconds after release

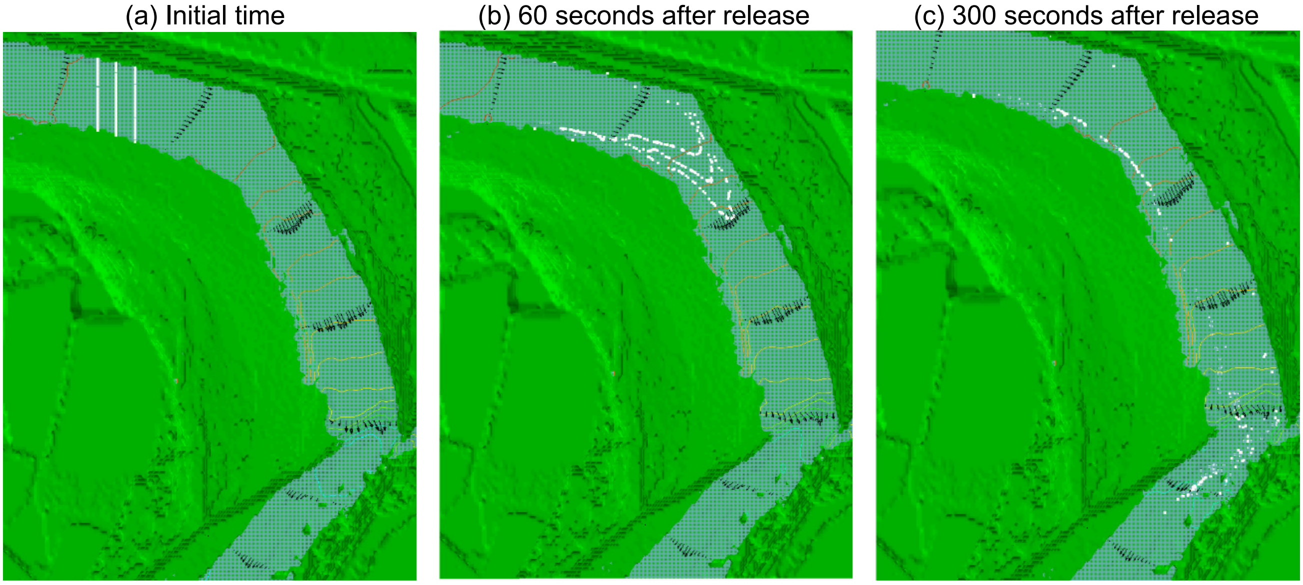

**Figure 5**. Simulation of tracking of small particles in Ibogawa River. White dots indicate particles.

Up to this stage, the floating objects tend to be either pushed towards outer bank or left in slow moving areas on the inner bank. As they pass around the bend those near the outer bank are bushed towards the outer bank. Those closer to the inner bank tend to get stuck near the bank. These characteristics are very important in designing such structures as trash traps or diverters. As the river drops suddenly near the downstream end where a pool is formed the flow loses its speed and particles gather again in the central region.

Figure 6 shows similar results but in larger scale with multiple bends in different directions. This time the objects are released along a single line across the river width. The trend around the first bend is similar to the case of Ibogawa River and the objects cling to the banks. The movement after the first bend is rather complicated with mixed effects of the second curve in the opposite direction. There is a slow flow region in a widened section after the first bend and the contraction following it. The observation at the site indicated that debris and trash were seen near the outer bank of the first bend. Around the large bend there is an island and that and the reversing curve made the motion rather complex.

We have conducted a field survey to investigate the characteristics of the floating objects. The simulation appears to represent the main feature of the motion of the light objects placed in upstream section.

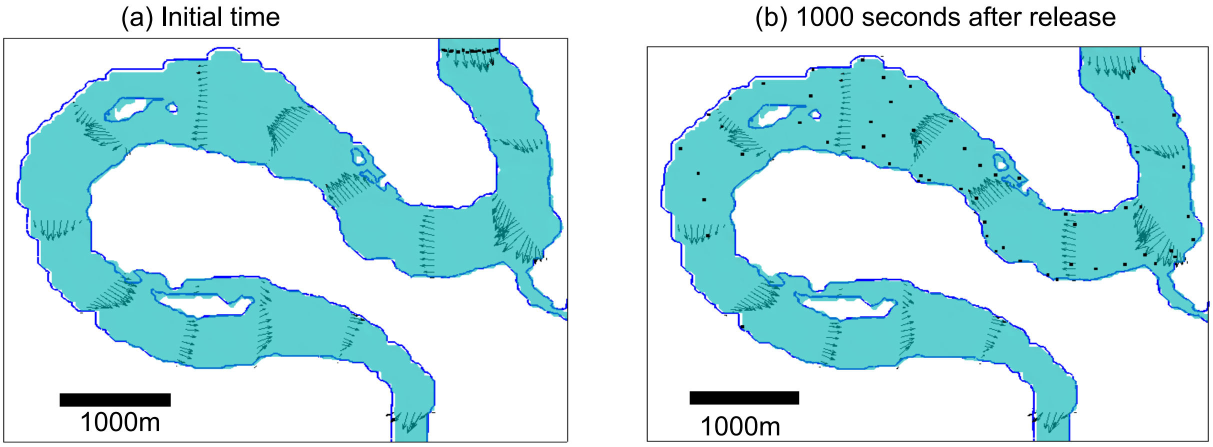


**Figure 6**. Simulation of tracking of small particles in Perak River. Dark dots indicate floating objects.

## 5 CONCLUSIONS

A LES based simulation method of tracking floating objects in rivers is developed. The flow computation is based on the three-dimensional LES analysis. The floating objects are modeled by the bodies with constant drag coefficient and the motion of multiple bodied has been solved together with the flow. These are intended to examine the trajectories of common objects on river surfaces such as trash and debris and to find the effective methods of controlling them.

It is found that the motion of relatively small objects with no characteristic shape can be predicted reasonably. The motion of floating objects around a sharp single bend shows some distinct trends on the trajectories. The particles tend to cling in the slow speed regions near the banks. Especially the objects that tend to accumulate near the outer bank (Figure 5(c)). When there are multiple bends of different directions in flat low land, the trends are complicated. Depending on the shapes and the characteristics of the banks they may be trapped or transported slowly (Figure 6(b)). Other than the inner bank of the bend, pool regions downstream of rapids tend to collect the objects.

The present study is a step towards finding solution to various problems caused by floating objects on rivers. In the case of large objects with characteristic geometric properties such as the shape and the size, drag coefficient of varying values and its dependency on the relative flow direction can be assumed. It is a useful alternative method to more elaborate and expensive full fluid-structure interaction simulation.

## REFERENCES

Boogaard, F., Vojinovic, Z. Chen, Y.-C., Kluck, J. & Lin, T.-P. (2016). High Resolution Decision Maps for Urban Planning: A Combined Analysis of Urban Flooding and Thermal Stress Potential in Asia and Europe. *In MATEC Web of Conferences*, 103, 04012.

Hamid, H.A. & Abdullah, K.Z. (2011). The Development of Trash Diverter System for Tenom Pangi Hydro Power Station Intake, Sabah. *Journal of Applied Sciences,* 11(11), 1973-1979.

Hirt, C.W. & Cook, J.L. (1972). Calculating Three-Dimensional Flow around Structure and Over Rough Terrain. *Journal of Computational Physics,* 10(2), 324–340.

Hirt, C.W. & Nichols, B.D. (1981). Volume of Fluid (VOF) Method for the Dynamics of Free Boundaries. *Journal of Computational Physics,* 39(1), 201-225.

 

Hribernik, A. Fike, M. & Hribernik, T.M. (2013). Economic Optimization of a Trashrack Design for a Hydropower Plant. *Journal of Trends in the Development of Machinery and Associated Technology*, 17(1), 161-164.

Nakayama, A. (2015). Large Eddy Simulation Method for Flow with Large Movement of Free Surface and Wetting Front, *E-Proceedings of the 36th IAHR World Congress*, Hague, Netherlands.

Nakayama, A. & Asami, K. (2016). *LES Simulation of Flow and Bed Shear Stress in a River Reach Taking into Account of Vegetation, Bushes, Cobble Bars and Large Boulders. In River Flow 2016,* 110-115. CRC Press.

Piterbarg, L.I. & Ozgokmen, T.M. (2004). Predictability of Lagrangian Particle Trajectories:Effects of Uncertainty in the Underlying Eulerian Flow. *Journal of Marine Res*earch, 62(1), 1-35.

 

# DILUTION STRATEGY FOR DESALINATION EFFLUENT

VINCENT H. CHU(1) & WIHEL ALTAI(2)

(1,2) Department of Civil Engineering, McGill University, Montreal, Canada,
vincent.chu@mcgill.ca

## ABSTRACT

A series of numerical simulations of the gravity-current head on the seafloor are conducted to study how the effluent from the seawater desalination plant is diluted so that strategy may be devised to minimize the impact of the effluent on the marine environment. In one simulation, the gravity-current head is produced by the release of the effluent from an instantaneous source. In the other simulation, the gravity-current head is produced by a continuous but intermittent source. The entrainment coefficient evaluated from the simulations of the gravity-current head, equal to a value of about 0.11, is a nearly constant independent of the density stratification in the current head. Existing studies of the desalination effluent have been focused on the dilution of the effluent by the negatively buoyant jet in the near field. In the simulation, when the dense effluent is discharged vertically in the form of fountain, gravity-current heads are produced on the seafloor by the asymmetric and intermittent releases of dense effluent from the fountain. The part of the dilution by the current heads on the seafloor is found from the simulation to be the greater than the dilution within the fountain. The results of these series of simulations have pointed to the need of the simulation in the far field. The significant effluent dilution on the surrounding marine environment must be included for the optimal design of the desalination facilities.

**Keywords:** Seawater desalination; negatively buoyant jet; fountain; density current; Lagrangian block advection.

## 1 INTRODUCTION

Desalination of seawater for potable water has become acceptable reality to some cities and coastal communities. More than 15,000 seawater desalination plants are operating around the world (Winter, 2015). The intake of seawater and the disposal of the brine back to the sea are designed to minimize the negative impact on the marine environment. The degree of the impact, however, is site-specific that depends not only on the disposal facility but also on the surrounding marine environment (Lattemann and Hopner, 2008). The brine from the desalination plant is denser than seawater of natural salinity. Mixing with the surrounding sea water is initiated by the negatively buoyant jet in the near field. The gravity current is the fall back of the negatively buoyant jet on the seafloor in the far field. The simulation for the spread of the gravity current on the seafloor is essential toward understanding the overall impact of the effluent to the surrounding marine environment. Most of the existing studies of the desalination-plant effluent have been focused on the mixing by the negatively buoyant jets (Zeitoun et al., 1970; Marti et al., 2012; Ahmad and Baddour, 2014). The mixing by the negatively buoyant jet however is ineffective. Much vertical momentum is needed to produce moderate dilution of the brine with the surround fluid by the jet (Chu, 1975; Robert and Tom, 1987; Zhang and Baddour, 1997; Kikkert et al., 2007; Jirka, 2008; Lai and Lee, 2012; Ahmad and Baddour, 2012; Voustrou et al., 2015). The goal of the present simulations therefore is to shift focus on the jet mixing and to ask the question how further mixing may be achieved as the effluent advances as gravity current on the seafloor.

Two series of simulation experiments are conducted. The first is the gravity-current head produced by the instant release of a small volume of dense fluid behind a tall lock gate. The entrainment associated with the development of the Kelvin-Helmholtz instability along the mix layer from the leading edge of the gravity-current head is determined from the simulation and correlate with the dimension and velocity of the current head. The second series of the simulations is the intermittent advance of the gravity-current heads on the seafloor due to the vertical discharge from a negatively buoyant jet. A stable and non-diffusive numerical method by Lagrangian advection of blocks of fluid developed by Chu and Altai (2012; 2015; 2016; 2017) is employed to do the numerical calculations.

## 2 GRAVITY-CURRENT HEAD PRODUCED BY AN INTANTANEOUS SOURCE

The gravity-current head produced by an instantaneous release of dense fluid from behind a lock gate is the first series of the simulations. Figure 1 and Figure 2 show the sequence of the images of the gravity-current head produced by the release from the lock gate of height ($H$) in a tank of a length ($L$), which is equal to four times the tank's height, $H_{\text{tank}}$. The dense fluid is released from a small lock of length ($L_o$) equal to one-eighth of the tank's height, $H_{\text{tank}}$, *i.e.,* $L_o/H_{\text{tank}} = 8$. The height of the lock is $H = H_{\text{tank}}$, $\frac{1}{2}H_{\text{tank}}$ and $\frac{1}{4}H_{\text{tank}}$, that is $H/L_o = 8$, 4 and 2, respectively, for the three simulation experiments referred to as the full-height, half-height

  / ISSN 1562-6865 (Online) - ISSN 1063-7710 (Print)

and quarter-height releases. The Lagrangian block advection simulation uses 384 blocks over the height of the tank and 1536 blocks along the length of the tank. The time-step sizes are such that the Courant number associated with the maximum velocity is 0.2. The buoyancy profiles ($g'/g_o$) of the gravity current are shown in the figures as the head advances toward the end of the tank. The dashed line in the figures defines the height ($H$) and the length ($L_o$) of the locks. These releases from a tall lock gate of small volume have produced prominent heads with a weak trailing current behind the heads that depends on the height of the lock. The full-height release with the aspect ratio of $H/L_o$ = 8 has produced the most coherent structure of the gravity-current head. The vorticity in the turbulent mixing layer feeding into the wake is able to organize itself to produce one highly coherent vortex within the gravity-current head for the full-height release shown by the image sequence in Figure 1. We see the detachment of this gravity current from the tank at the dimensionless time, $t\sqrt{gH}$ = 2.29 in Figure 1a, the multiple eddies in the wake in Figure 1b at time, $t\sqrt{gH}$ = 4.90 and the organization into one large coherent vortex in Figure 1c at time, $t\sqrt{gH}$ = 7.50. In contrast, the current head produced by the half-height release with $H$ = 4 $L_o$ in the image sequence shown in Figure 2 is less organized.

The close-up view in Figure 3 shows the development of the Kelvin-Helmholtz instability in the turbulent mixing layer from the leading edge the gravity-current head produced by the full-height release at the instant after the front has advanced a distance $x_f$ = 14.9$L_o$. The vorticity initiated from the leading edge of the gravity-current head moves along the layer to the back of the gravity-current head to form a wake. This produces a prominent circulation region in the wake region. The maximum velocity occurs at the impingement of the wake vortex on the floor. This full-height release has produced a gravity-current head without much of the trailing current that otherwise would be feeding from behind the head. This is remarkable as the head is now charging forward without much of the current that initiates it. The relation between the head and the gravity current in this full-height release is akin to the formation of a smoke ring and the perfect impulse that blows the ring.

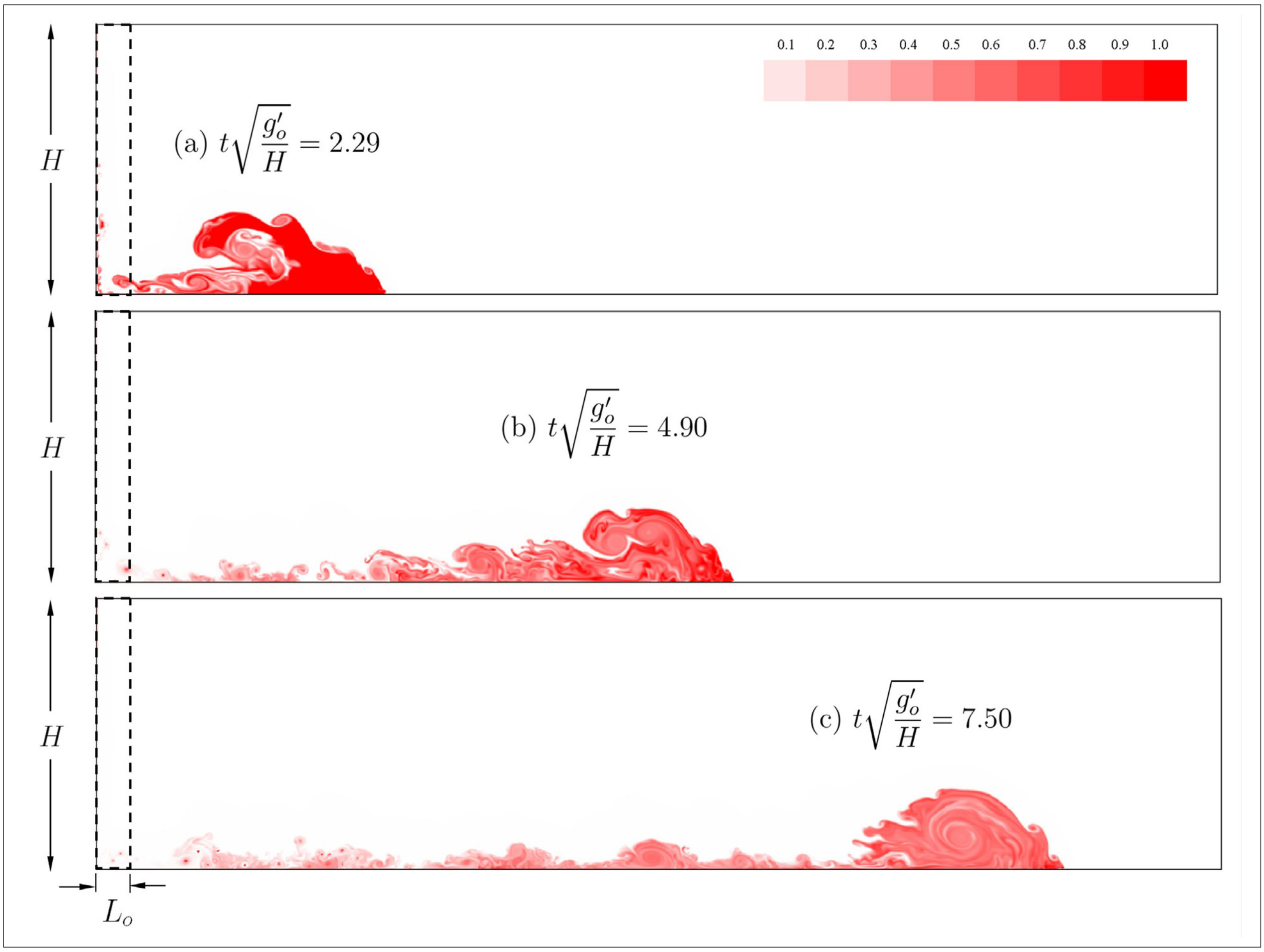


**Figure 1**. Development of the buoyancy profiles ($g'/g_o$) of the gravity-current head produced by the full-height release of a source fluid of length ($L_o$) and height ($H$ = 8 $L_o$). The dashed line marks the initial position of the source fluid of reduced gravity ($g'_o$) behind the gate.

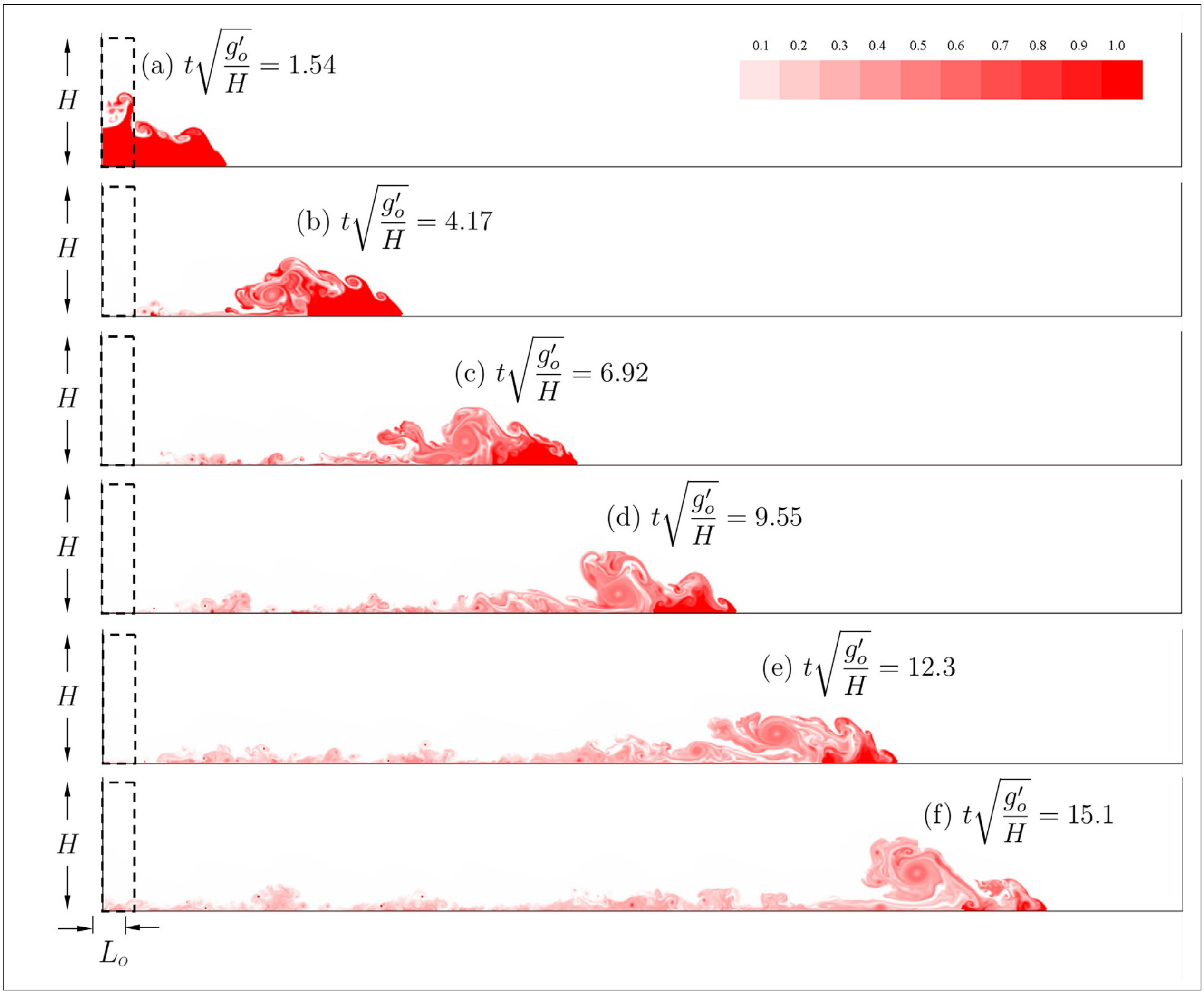


**Figure 2**. The buoyancy profiles ($g'/g_o$) of the gravity-current head produced by the half-height release of source fluid of a length ($L_o$) and a height ($H = 4\ L_o$). The dashed line marks the initial position of the source fluid of reduced gravity ($g'_o$).

The organization of the vorticity in the wake and the impingement of the coherent wake vortex on the floor have produced a maximum velocity ($u_{max}$) in the wake on the floor. The distance from the leading edge to the floor velocity maximum is ($x_f$ - $x_m$). This length ($x_f$ - $x_m$) and the maximum height ($h_m$) define the shape of the current head and determine the length of the mixing layer:

$$\frac{\ell_{mixlayer}}{L_o} = \frac{\sqrt{h_{max}^2 + (x_f - x_m)^2}}{L_o} = \sqrt{[\frac{h_{max}}{H}\frac{H}{L_o}]^2 + [\frac{(x_f - x_m)}{h_{max}}\frac{h_{max}}{H}\frac{H}{L_o}]^2} \qquad [1]$$

The numerical simulations have determined the maximum floor velocity ($u_{max}$), the length of the head ($x_f$ - $x_m$) and the height of the head ($h_m$). Table 1 lists the values of these key parameters: (a) $u_{max}/u_f$, (b) ($x_f$ - $x_m$)/$h_{max}$ (c) $h_{max}/H$, and (d) $\ell_{maxlayer}/H$. The nominal value of the floor maximum velocity is $u_{max}/u_f \sim 3.1$, 2.7 and 2.6 for the full-height, half-height and quarter-height release, respectively. There are considerable variations from the nominal values as the shape of the current head is modulating due to presence of large coherent eddies along the turbulent mixing layer initiated from the leading edge of the gravity-current head (Hallworth et al. 1996; Nogueira et al. 2014). The head length-to-height ratio that defines the shape of the gravity-current head has a nominal value of ($x_f$ - $x_m$)/$h_{max}$ ~ 1.3, 1.9 and 2.3. The head-height to the lock-height ratio has a nominal value of $h_{max}/H$ ~ 0.28, 0.42, 0.55, respectively. Details of the simulation results including the variations from the nominal values are given in a recent paper by Chu and Altai (2017).

 

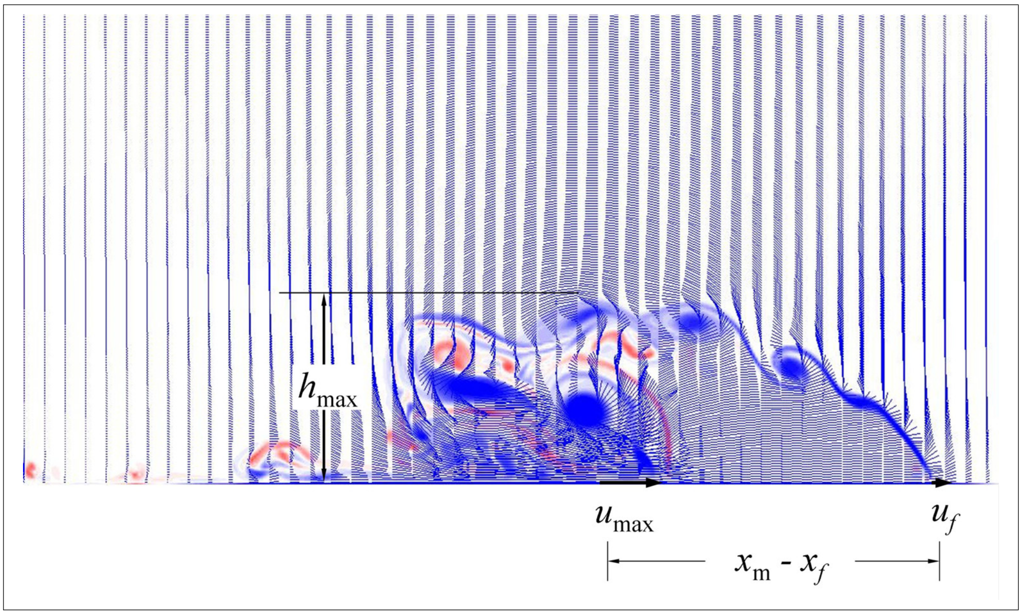


**Figure 3**. The vorticity pattern and the velocity vectors delineating the coherent structure of the gravity-current head produced by the full-height release, after the leading edge has advanced a distance, $x_f$ = 14.9 $L_o$. The height of the current head, $h_{max}$, and the distance from the leading edge to the location where the maximum floor velocity ($u_{max}$) occurs, ($x_m$ - $x_f$), defines the shape of the current head.

**Table 1**. Nominal values and the deviations from the values of the key parameters for the gravity-current head produced by the full-height, half-height and quarter-height releases.

| | | $u_{max}/u_f$ | $(x_f - x_m)/h_{max}$ | $h_{max}/H$ | $\ell_{mixlayer}/L_o$ |
|---|---|---|---|---|---|
| Full-height | ($H/L_o$= 8) | 3.1±0.3 | 1.3±0.4 | 0.28±0.1 | 3,67 |
| Half-height | ($H/L_o$= 4) | 2.7±0.7 | 1.9±0.5 | 0.42±0.8 | 3.61 |
| Quarter-height | ($H/L_o$= 2) | 2.6±0.8 | 2.3±1.5 | 0.55±0.8 | 2.76 |

## 3 ENTRAINMENT BY THE KELVIN-HELMHOLTZ INSTABILITY

The total volume of turbulent dense fluid in the gravity-current head including the wake behind the head, V, for every instant of time is determined from the simulations using a cut off at the 5 percent boundary where $g'/g_o$ = 0.05. The results in Figure 4 show this volume to increase continuously following a linear relation with the distance of advance $x_f$ on the floor due to entrainment of ambient fluid into the current head. The rates of the increase with the distance for the full-height, half-height and quarter-height releases are:

$$\frac{1}{L_o}\frac{dV}{dx_f} = 0.45, 0.36 \text{ and } 0.29, \text{ respectively.} \qquad [2]$$

These rates are not diminishing as the current head advance over the distance on the floor from $x_f = L_o$ to 20 $L_o$. This is remarkable as the gravity current on the floor is stably stratified. The density stratification does not seem to affect the entrainment process. We offer the following entrainment hypothesis to explain the observation. The Kelvin-Helmholtz instability along the mixing layer initiated at the leading edge of the advancing front is responsible for the entrainment. The rate of the entrainment is proportional to the length of the mixing layer, $\ell_{maxlayer}$, which are $\ell_{maxlayer}/L_o$ = 3.67, 3.61 and 2.76 for the full-height release ($H/L_o$ = 8), half-height release ($H/L_o$ = 4), and quarter-height release ($H/L_o$ = 2), respectively, as given in Table 1. With these values, the entrainment coefficients

$$\alpha = \frac{1}{\ell_{\text{mixlayer}}}\frac{dV}{dx_f} = 0.12,\ 0.10 \text{ and } 0.11, \qquad [3]$$

are obtained for the three simulations with the very different height-to-length ratios of $H/L_o$ = 8, 4 and 2, respectively. These values of the entrainment coefficients are nearly identical using the length of the mixing layer ($\ell_{maxlayer}$) to define the entrainment coefficient. The surrounding fluid enters the mixing layer over the length ($\ell_{maxlayer}$) where the buoyancy effect on mixing is negligible. This mechanism of the mixing by the Kelvin-Helmholtz instability explains why the entrainment coefficient is the same for the three current heads of different shapes and sizes. The fluid in the tail behind the wake of the head however is stably stratified. Further mixing is negligible once the entrained fluid leaves the end of the mixing layer to enter in the wake to form the stably stratified tail. Hallworth et al. (1996) has proposed the association of the entrainment process with the development of the Kelvin-Helmholtz instability. The value of the entrainment coefficient obtained in the laboratory experiment of Hallworth et al. (1996) was α = 0.079 based on their model I using a shape factor, $S = (2/\pi)^{1/2}$ and α = 0.065 based on model II using the measured shape factor ($S$). These values from the laboratory study are lower than the values given in Equation 3. Part of the reason for the difference in the value is due to the difference in the definition of the entrainment coefficient. The other reason for a smaller laboratory value of the coefficient could be due to the viscous effect, which can be significant in the laboratory. The development of the mixing layer from the leading edge is the most sensitive to the viscous effect at the leading edge where the Reynolds number defined by the initial thickness of the mixing layer is infinitesimally small. The Kelvin-Helmholtz stability would be suppressed if the Reynolds number of the layer is smaller than certain critical value.

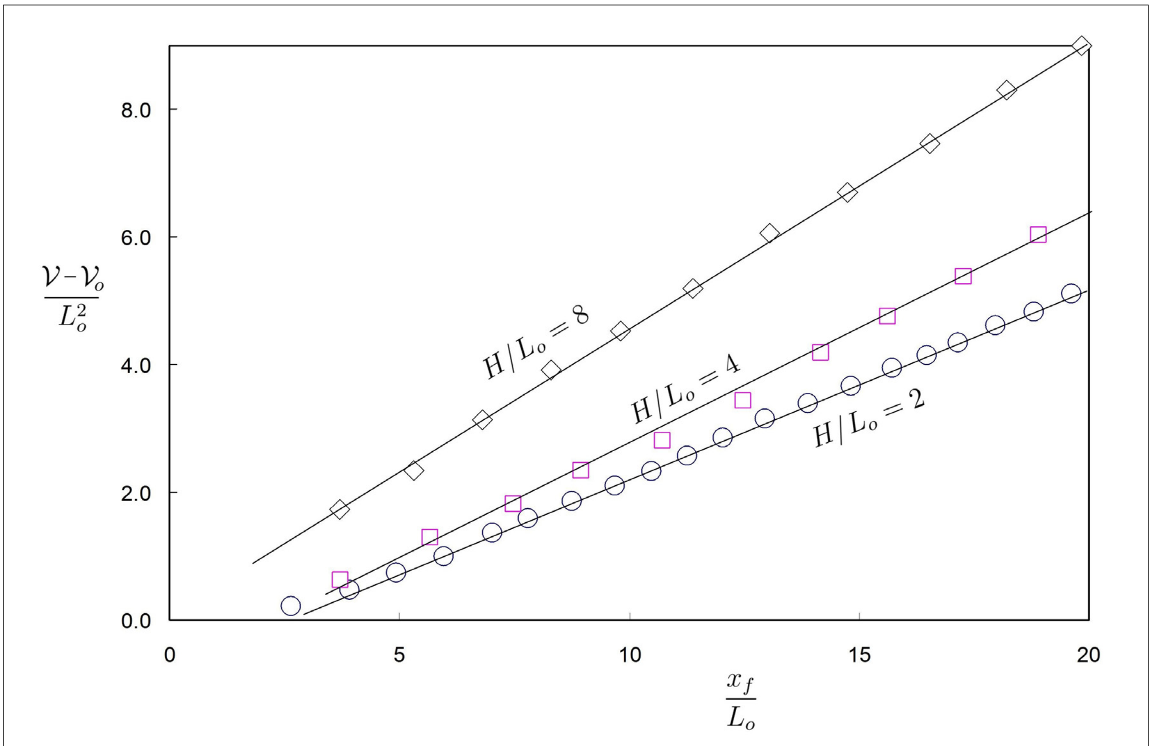


**Figure 4**. The entrained volume of fluid in the gravity-current head that increases linearly as the current head advance over the distance on the floor from $x_f/L_o$ = 1 to 20.

## 4 VERTICAL FOUNTIAN AND INTERMITTENT GRAVITY-CURRENT HEAD

One strategy in the disposal of the desalination effluent is to discharge vertically in the form of a negatively buoyant jet, as shown in Figure 5. The dense fluid rises and falls. Part of the falling fluid is than re-entrain back into the jet. The re-entrainment of the falling fluid is an asymmetrical and unsteady process that occurs within a region in the near field known as the fountain (Hunt and Burridge, 2015). The dense fluid pumping out of the bubbling fountain is intermittent. It is directed on the one side and then on the other side by the flapping motion of the negatively buoyant jet. The intermittent action produces trains of gravity-current heads on the seafloor moving away from the fountain. Each current head has its own mixing layer to draw fluid from its surrounding. The entrainment of the fluid is due to the development of the Kelvin-Helmholtz instability along the mixing layer above each current head. In the simulation, the dense (negatively buoyant) effluent is from a line source. The effluent with a negative reduced gravity ($g_o'$) is discharged vertically with a velocity ($V_o$) through a slot of width ($2b_o$). The pumping of the dense fluid from the bubbling fountain produces the intermittent advancement of the gravity current on the seafloor. This action is defined by the volume flux ($q_o$), buoyancy flux ($f_o$), and momentum flux ($m_o$) per unit length of the plane plume. The fluxes are related to $g_o'$, $V_o$ and $2b_o$, as follows:

$$q_o = 2b_o V_o \qquad [4]$$

$$f_o = 2b_o V_o g'_o \qquad [5]$$

$$m_o = 2b_o V_o^2 \qquad [6]$$

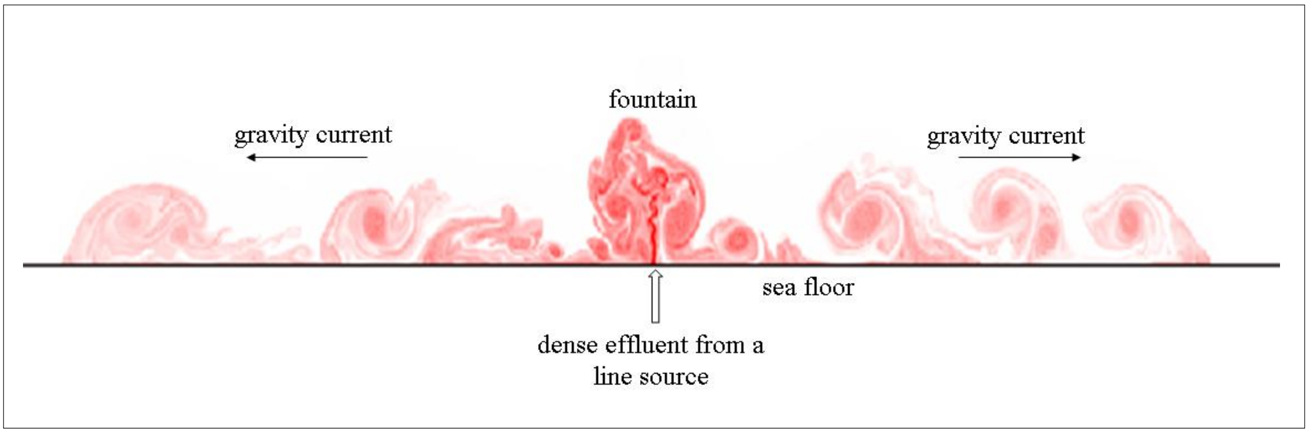


**Figure 5**. The desalination effluent from a line diffuser due to the vertical discharge upward to produce the negatively buoyant plane jet in a bubbling fountain and the train of the gravity-current heads on the seafloor.

The dimensionless parameter derived from these fluxes is:

$$\frac{m_o^{3/2}}{q_o^{3/2} f_o^{1/2}} = \frac{V_o}{\sqrt{2b_o g'_o}} \qquad [7]$$

which is proportional to the densimetric Froude number:

$$\mathrm{Fr} = \frac{V_o}{\sqrt{b_o g'_o}}. \qquad [8]$$

The dependence on $q_o$ is negligible for the negative buoyant jet of sufficiently high densimetric Froude number, as explained by Zhang and Baddour (1997). As a first approximation, the numerical simulation results are presented and normalized using the time scales, $t_s$, length scale, $t_s$, and velocity scale, $v_s$, defined by the buoyancy flux ($f_o$), and the momentum flux ($m_o$) as follows:

$$t_s = \frac{m_o}{f_o}, \qquad \ell_s = \frac{m_o}{f_o^{2/3}}, \qquad v_s = f_o^{1/3} \qquad [9]$$

4.1 Grid refinement

The tank is 17.28m long and 1.08m high in the simulation of the fountain and the gravity-current heads on the seafloor. The computation stops when the front of the gravity current arrives at the end of the tank. The entrainment of the fluid from the ambient dilutes the brine and hence increases the volume of the brine in the fountain and the gravity-current heads. The total volume of the brine per unit length of the line source, V, is determined using the Lagrangian block simulation method by Chu and Altai (2001; 2012; 2015; 2016; 2017). Figure 6 shows the dimensionless volume and its relation with the dimensionless time obtained from the simulations using two different grids and block sizes. The coarse grid has 96 x 1536 cells while the refined grid 192 x 3072 cells. The solid symbols denote of the simulation results obtained using the refined grid with 192 x 3072 cells. The open symbols are the results obtained using the coarse grid of 96 x 1536 cells. The results obtained using the coarse grid is not detectably different from those using the refined grid for both the discharge with the densimetric Froude number of $\mathrm{Fr}_o$ = 11.9 and $\mathrm{Fr}_o$ = 5.96. These grid independent results are remarkable achievement of the Lagrangian block simulation (LBS) that is not possible to attain by the traditional finite volume method (FVM). The difficulty with the FVM is due to its Eulerian formulation. To find the numerical solution, fluxes are estimated on the face of the finite volume using the truncation series. Spurious numerical oscillations and artificial numerical diffusion are the consequences of the truncation (Karimpour and Chu, 2015). The problem is particularly severe in the regions across the flow discontinuities.

Occasional switching to a diffusive upwind scheme, for example, was one classic strategy in FVM to manage the numerical oscillations. As the spurious oscillations and false diffusive error are eliminated, the LBS offers the most effective and accurate method for turbulent flow modeling and simulation. Similar LBS method has been employed to calculate the advance of wet water on dry bed (Tan and Chu, 2010; 2012) and to capture the turbulent interface in shear flow (Chu and Altai, 2001; 2012; 2015). In the absence of spurious oscillations and false diffusion, the best possible model of the gravity-current head is constructed by the LBS method.

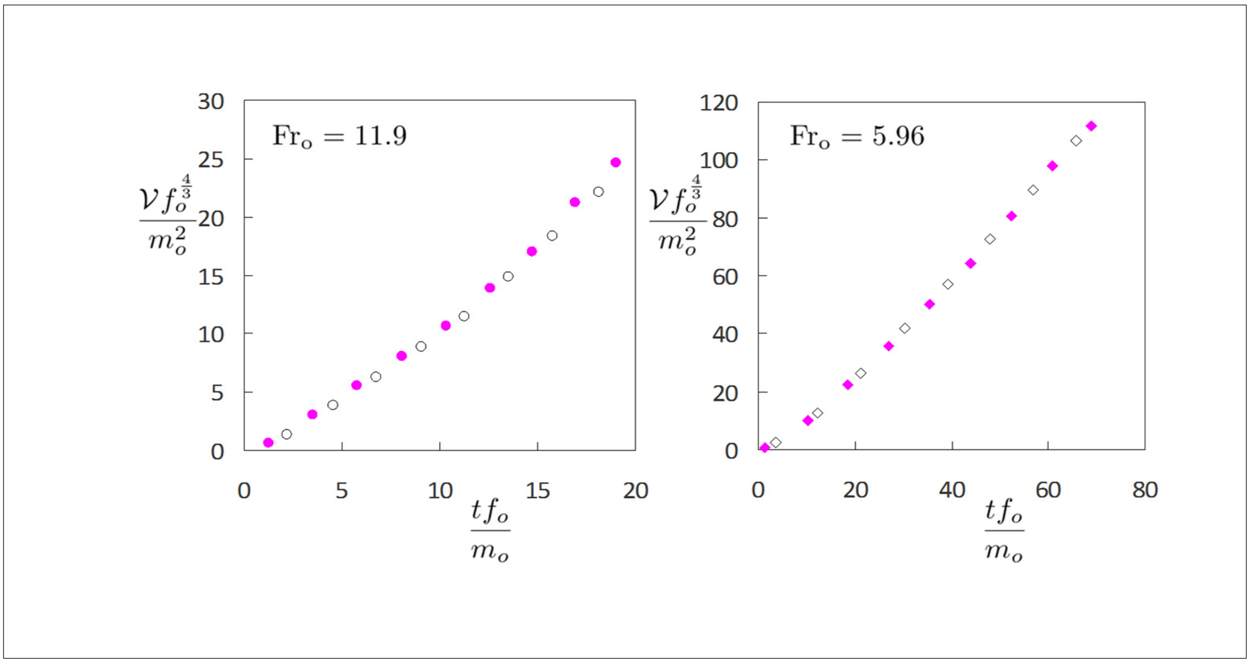


**Figure 6**. Growth of the brine volume per unit length with time for two densimetric Froude numbers, $\mathrm{Fr_o}$ = 11.9 (left) and $\mathrm{Fr_o}$ = 5.96 (right). The volume and time scales for the normalization are based on the initial buoyant flux and momentum flux of the effluent.

4.2 Speed of advance of the density-current head on the sea floor

Figure 7 shows the dimensionless distance between the fronts of the gravity currents on the two sides of the diffuser for the two densimetric Froude numbers, $\mathrm{Fr_o}$ = 5.96 and 11.9 using the refined grid. The rate of increase of this distance determines the speed of the advance. The best fit of the data shown in Figure 7 gives:

$$\frac{dx_{\mathrm{front}}}{dt} = 0.94 f_o^{\frac{1}{3}}, \qquad [10]$$

which is proportional the buoyancy flux to the one-third power at the source, and almost independent of the source momentum flux. According to this formula, large facility with large source buoyant flux would produce density current of great speed that could be dominant in comparison with the current speed due to the tides and winds in the surrounding sea.

4.3 Dilution ratio and turbulent entrainment

Figure 8 shows how the volume of the brine, V, increases continuously with time, *t*, at a greater rate than the rate at the source, $q_o t$. The parameter that measures the rate of the turbulent entrainment is the dilution ratio, V /($q_o t$), which increases the dimensionless time ($tf_o/m_o$). The initial dilution takes place within the fountain is the intercept. The fraction of the dilution subsequently as the density current advance along the sea floor is the more significant fraction that is not negligible.

 

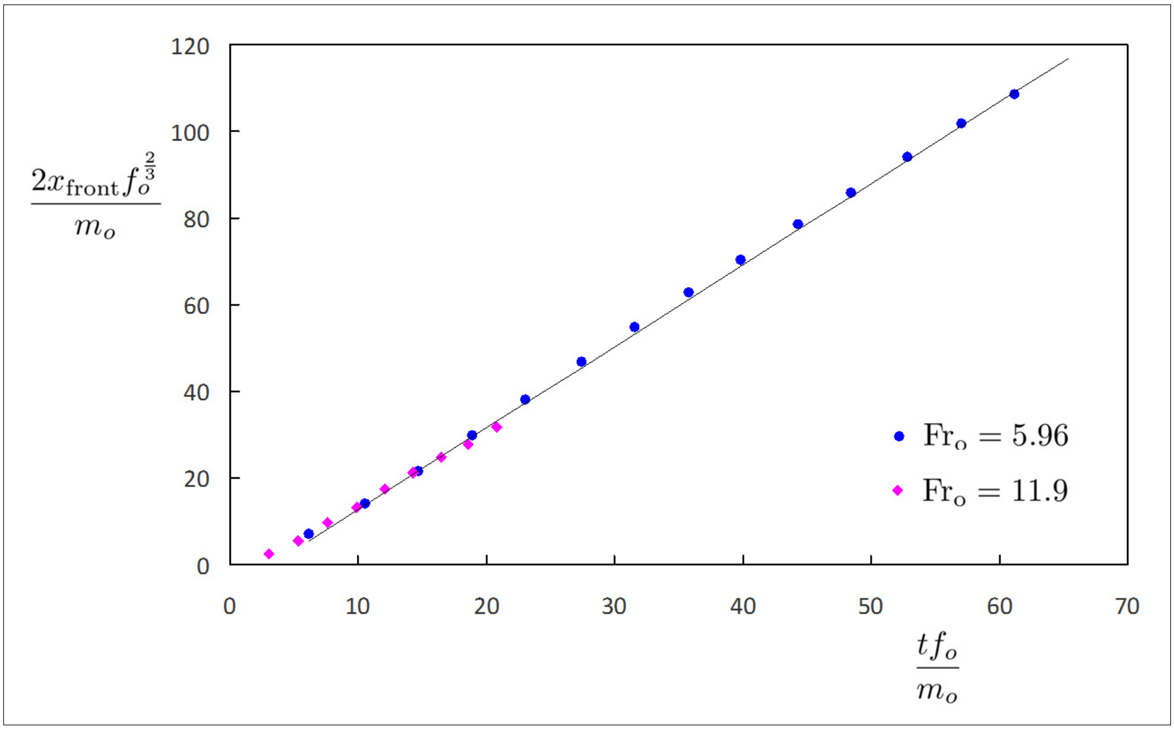


**Figure 7**. Dimensionless distance between the fronts of the density current and its variation with the dimensionless time for two densimetric Froude numbers of $Fr_o$ = 11.9 and 5.96. The straight line is Equation 9.

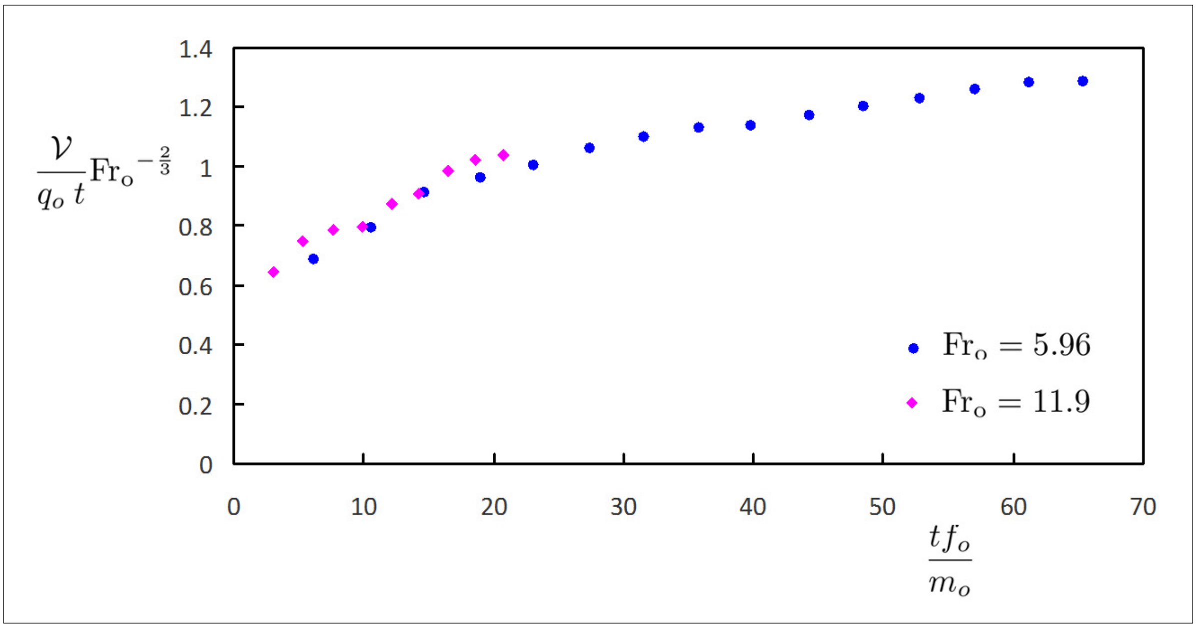


**Figure 8**. Overall dilution ratio over the period time as the density current advances to the end of the tank for the two densimetric Froude numbers of $Fr_o$ = 11.9 and 5.96.

The data in Figure 8 is normalized by the Froude number to the power of 2/3 to get similarity in the results of the simulations for both Froude numbers. Best fit of the two sets of data in Figure 4 gives:

$$\frac{V}{q_o t} \text{Fr}_o^{-\frac{2}{3}} \cong 0.5 \quad \text{as} \quad \frac{t f_o}{m_o} \to 0 \qquad [11]$$

$$\frac{V}{q_o t}\mathrm{Fr_o}^{-\frac{2}{3}} \cong 1.3 \quad \text{as} \quad \frac{t f_o}{m_o} \to \infty \qquad [12]$$

Equation 11 gives the dilution ratio produced by mixing within the fountain. Equation 12 defines the asymptotic far field mixing that occurs on the seafloor. The dilution within the fountain as given by Equation 10 follows consistently with the laboratory measurement of the dilution ratio in the negatively buoyant plane jets by Voustrou et al. (2015). According to the simulation given in Equations 11 and 12, the dilution by the negatively buoyant jet within the fountain in near field is only 38% while the dilution on the seafloor is the greater 62% fraction of the overall dilution. Far field dilution clearly is significant notwithstanding that the effluent in this simulation is advancing on a smooth horizontal seafloor.

## 5 CONCLUSIONS

A series of simulations for the dilution of gravity current on horizontal seafloor are conducted using the method of the Lagrangian block simulation. In one simulation, the gravity-current head is produced by the release of the effluent from an instantaneous source. In the other simulation, the gravity-current head is produced by a continuous but intermittent source. These simulations have demonstrated the effective mixing by the Kelvin-Helmholtz instability along the mixing layer above the gravity-current head. The natural seafloor has hills and valleys. Much greater dilution is attainable as the current interact with the irregularity on the seafloor. Judicious selection of the disposal site by locating the diffuser on the ridge of the sea floor for example can increase the overall dilution as the gravity current flows downhill from the ridge. Raising the height of diffuser pipe to an elevation above the sea floor also should promote the mixing. The detailed knowledge of the current over a large area surrounding the site is necessary to evaluate correctly the impact of the desalination effluent on the marine environment. The simulation must resolve the interfacial mixing by the Kelvin-Helmholtz instability developing in the train of multiple current heads on the natural seafloor. This may require a computational intensive three-dimensional Lagrangian block simulation model.

## REFERENCES

Ahmad, N. & Baddour, R.E. (2012). Dilution and Penetration of Vertical Negatively Buoyant Thermal Jets. *Journal of Hydraulic Engineering*, 138(10), 850-857.

Ahmad, N. & Baddour, R.E. (2014). Minimum Return Dilution Method to Regulate Discharge of Brine from Desalination Plants. *Canadian Journal of Civil Engineering*, 41(5), 389-395.

Chu, V.H. (1975). Turbulent Dense Plumes in Laminar Cross Flow. *Journal of Hydraulic Research*, 13(3), 263–279.

Chu, V.H. & Altai, W. (2001). Simulation of Shallow Transverse Shear Flow by Generalized Second Moment Method. *J. Hydraulic Research*, 39(6), 575-582.

Chu, V.H. & Altai, W. (2012). Advection and Diffusion Simulations Using Lagrangian Blocks. *Computational Thermal Sciences*, 4(4), 351-363.

Chu, V.H. & Altai, W. (2015). Lagrangian Block Simulation of Buoyancy at Turbulence Interfaces. *Computational Thermal Sciences*, 7(2), 181-189.

Chu, V.H. & Altai, W. (2017). A Two-Dimensional Inviscid Model of the Gravity Current Head by Lagrangian Block Simulation. *Environmental Fluid Mechanics*, 1-16. https://link.springer.com/article/10.1007/s10652-017-9519-y

Hallworth, M.A, Huppert, H.E., Phillips, J.C. & Sparks, R.S.J. (1996). Entrainment into Two-Dimensional and Axisymmetric Turbulent Gravity Currents. *J. Fluid Mech*., 308, 289-311.

Hunt, G.R. & Burridge, H.C. (2015). Fountains in Industry and Nature. *Annual Review of Fluid Mechanics*, 47, 195–220.

Jirka, G.H. (2008). Improved Discharge Configuration for Brine Effluents from Desalination Plants. *Journal of Hydraulic Engineering*, 134(1), 116-120.

Karimpour Ghannadi, S. & Chu, V.H. (2015). High-Order Interpolation Schemes for Shear Instability Simulations. *International Journal of Numerical Methods for Heat & Fluid Flow*, 25(6), 1340-1360.

Kikkert, G.A., Davidson, M.J. & Nokes, R.I. (2007). Inclined Negatively Buoyant Discharges. *Journal of Hydraulic Engineering*, 133(5), 545-554.

Lai, C.C. & Lee, J.H. (2012). Mixing of Inclined Dense Jets in Stationary Ambient. *Journal of Hydro-Environment Research*, 6(1), 9-28.

Marti, C.L., Antenucci, J.P., Luketina, D., Okely, P. & Imberger, J. (2011). Near- Field Dilution Characteristics of a Negatively Buoyant Hypersaline Jets Generated by a Desalination Plant. *Journal of Hydraulic Engineering*, 137(1), 57–65.

Nogueira, H.I., Adduce, C., Alves, E. & Franca, M. (2014). Dynamics of the Head of Gravity Currents. *Environ. Fluid Mech.*, 14(2), 519–540.

 

Roberts, P.J.W., Ferrier, A. & Daviero, G. (1997). Mixing in Inclined Dense Jets. *Journal of Hydraulic Engineering*, 123(8), 693–699.

Roberts, P.J.W. & Toms, G. (1987). Inclined Dense Jets in Flowing Currents. *Journal of Hydraulic Engineering*, 113(3), 323–341.

Tan, L.W. & Chu, V.H. (2010). Wave Runup Simulations Using Lagrangian Blocks on Eulerian Mesh. *J. Hydro-Environ. Res.*, 3(4), 193-200.

Tan, L.W. & Chu, V.H. (2012). Two-Dimensional Simulation of Shallow-Water Waves by Lagrangian Block Advection. *Computers and Fluids*, 65, 35-43.

Winter, D. (2015). For Drinking Water in Drought, California Looks Warily to Sea. New York Times, April 11, 2015. http://www.nytimes.com/2015/04/12/science/drinking-seawater-looks-ever-more-palatable-to-californians.html?_r=0

Voustrou, M.K., Yannopoulos, P.C. & Christodoulou, G.C. (2015). Experiments on Plane Negatively Buoyant Jets. *E-proceedings of the 36th IAHR World Congress*, 28 June - 3 July 2015, The Hague, the Netherlands.

Zeitoun, M.A., Mcllhenny, W.F. & Reid, R.O. (1970). *Conceptual Designs of Outfall Systems for Desalting Plants*, Research and Development Progress Rep. No. 550, Office of Saline Water, U.S. Dept. of Interior, Washington D.C.

Zhang, H. & Baddour, R.E. (1997). Maximum Vertical Penetration of Plane Turbulent Negatively Buoyant Jets. *Journal of Engineering Mechanics*, 123(10), 973-977.

 

Proceedings of the 37th IAHR World Congress
August 13 – 18, 2017, Kuala Lumpur, Malaysia

# MODELING THE TRANSPORT AND FATE OF PHOSPHORUS FROM A POINT SOURCE IN THE LAKE MICHIGAN NEARSHORE ZONE

HECTOR R BRAVO[1], HARVEY BOOTSMA[2] & BAHRAM KHAZAEI[3]

[1,3] Department of Civil and Environmental Engineering, University of Wisconsin-Milwaukee,
[2] School of Freshwater Sciences, University of Wisconsin-Milwaukee
hrbravo@uwm.edu; hbootsma@uwm.edu; bkhazaei@uwm.edu

## ABSTRACT

Nutrient loading into Lake Michigan can produce algal blooms, hypoxia, beach closures, clogging of water intakes, and reduced water quality. Addressing those problems requires the understanding of the transport and fate of phosphorus in lakes. Research has shown that reducing tributary phosphorus loading may reduce *Cladophora* abundance near tributary sources. There is active research on the influence of dreissenid mussel filtering on water clarity and phosphorus bioavailability in the nearshore, and the importance of nearshore-offshore phosphorus exchange. None of the existing models specifically accounts for the role of mussels in the phosphorus cycle despite evidence that this role is significant. We developed a computer model that simulates the hydrodynamic and biogeochemical processes relevant to the transport of phosphorus in the nearshore zone. We then used the Milwaukee Metropolitan Sewerage District (MMSD) South Shore Wastewater Treatment Plant (SSWWTP) as a case study, applying the model to simulate the transport of phosphorus released by the plant. The 3D model consists of a hydrodynamic model linked with a biogeochemical model. The hydrodynamic component is a high-resolution model of the lake nearshore zone around Milwaukee, nested into the National Oceanic and Atmospheric Administration Lake Michigan model. The biogeochemical model consists of three linked modules. The *Cladophora* module simulates near-bottom dissolved phosphorus uptake and respiration, and sloughing. The mussel module simulates near-bottom particulate phosphorus grazing, excretion to near-bottom dissolved phosphorus, and egestion to sediment storage. The sediment storage module simulates the particulate phosphorus settling and resuspension. The model was validated against the field measured water temperature, total and particulate phosphorus, *Cladophora* biomass, and phosphorus content. The study included the laboratory testing phosphorus samples with low detection limit and analysis of *Cladophora* trends in the nearshore zone. The model is being applied as a management tool to test the scenarios of SSWWTP nutrient loading, determining the effluent phosphorus limits for the treatment plant.

**Keywords:** Laurentian Great Lakes; limnology; nearshore processes; modeling, nutrients.

## 1 INTRODUCTION

Nutrient loading into Lake Michigan can produce algal blooms, hypoxia, beach closures, clogging of water intakes, and reduced water quality. Pauer et al. (2011) summarized the enactment of a total phosphorus (TP) concentration target for Lake Michigan. The original Great Lakes Water Quality Agreement (GLWQA) (International Joint Commission, 1972;1978) and its revision in 1978 (Great Lakes Water Quality Board, 1978) were enacted mainly due to eutrophication concerns in the Great Lakes. Although Lake Michigan was never regarded as eutrophic, lake-wide total phosphorus (TP) concentrations of 9.0 μg $L^{-1}$ and summer average chlorophyll-a concentrations of 2.0 μg $L^{-1}$ in the late 1960s and early 1970s (Thomas et al., 1980) were a concern. The GLWQA targets for Lake Michigan were 5600 MT annually for TP loading and 7 μg $L^{-1}$ lakewide mean TP concentration for spring, resulting in a chlorophyll-a concentration of 1.8 μg $L^{-1}$ (Thomas et al., 1980).

Research has shown that reducing tributary phosphorus loading to the nearshore may reduce *Cladophora* abundance near tributary sources (Bootsma, 2009; Auer et al., 2010; Higgins et al., 2012), but questions remain unanswered.

Active research on Lake Michigan nearshore biogeochemistry includes:

- The influence of dreissenid mussel filtering on water clarity and phosphorus bioavailability in the nearshore, and
- The importance of nearshore-offshore phosphorus exchange on nearshore biogeochemistry.

Previous phosphorus modeling research includes:

- Whole-lake models for Lake Michigan (Pauer et al., 2011) and Lake Erie (Schwab et al., 2009),
- Nearshore model of Lake Ontario (Leon et al., 2012), and
- Particle tracking model developed by Tetra Tech (2014) for the Milwaukee Harbor area.

 

None of these models specifically account for the role of dreissenid mussels in the phosphorus cycle despite evidence that this role is significant (Bootsma and Liao 2013).

The objectives of the present study were:

(a) To develop a computer model that simulates the hydrodynamic and biogeochemical processes relevant to the transport of phosphorus in the nearshore zone of Lake Michigan.
(b) To use the Milwaukee Metropolitan Sewerage District (MMSD) South Shore Wastewater Treatment Plant (SSWWTP) as a case study, applying the model to simulate the transport of phosphorus released by the wastewater treatment plant.
(c) To apply the model as a management tool to test various scenarios of SSWWTP nutrient loading, and determine effluent phosphorus limits for the wastewater treatment plant.

## 2 APPROACH

The 3D model consists of a hydrodynamic model linked with a biogeochemical model. The hydrodynamic component is a high-resolution model of the nearshore zone of Lake Michigan around Milwaukee, nested into the National Oceanic and Atmospheric Administration (NOAA) Lake Michigan model of the Great Lakes Coastal Forecasting System (GLCFS). The Lake Michigan model uses a grid size of 2 km and 131 x 251 cells in the EW and NS directions, respectively, and 20 vertical depth intervals (sigma layers). The coastal area of interest, simulated by the nested model, extends 45.5 km in the longshore direction, and offshore roughly to the 30 m isobath. The nested model had a grid size of 100 m, 120 x 445 cells in the cross-shore and alongshore directions, respectively, and 20 equally-spaced sigma layers. The hydrodynamic model is based on the Princeton Ocean Model and was expanded to simulate the transport of particulate phosphorus (PP) and dissolved phosphorus (DP) in the water column. The biogeochemical model consists of three linked modules: a mussel model, a *Cladophora* model, and a sediment dynamics model (Fillingham, 2015). The *Cladophora* model simulates the processes of near-bottom dissolved phosphorus uptake and respiration, and sloughing. The mussel model simulates near-bottom particulate phosphorus grazing, excretion to near-bottom dissolved phosphorus, and egestion to sediment storage. The sediment storage model simulates particulate phosphorus settling and resuspension. Figure 1 depicts the components of the hydrodynamic and biogeochemical models developed in this study and the links among them.

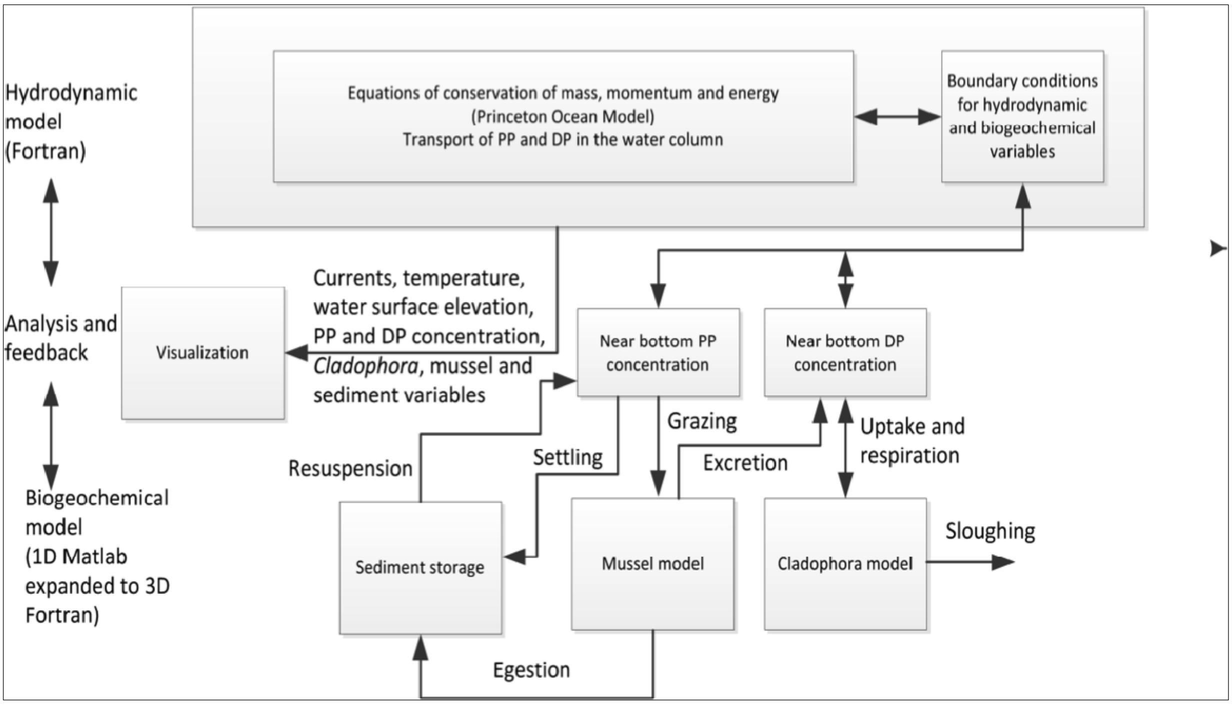


**Figure 1.** Sketch of the hydrodynamic and biogeochemical model components and their links.

The linked models were applied to determine the influence of MMSD SSWWTP phosphorus loading compared to mixing with the lake offshore. Simulations were focused on the time of year for *Cladophora* growth, detachment, and shoreline fouling between May and September. Figure 2 shows the locations of the SSWTP and the Atwater (ATW) sampling stations in Lake Michigan.

The first modeling step was the implementation of hydrodynamic transport in the water column of PP and DP released by SSWWTP outfall. The mussel, sediment dynamics, and *Cladophora* components of the biogeochemical model were linked sequentially to the hydrodynamic model. The linked models were first implemented into a simulated uniform flow field running south through the SSWWTP plant site, then validated with the real meteorological forcing, and 3D flow and temperature fields against measurements made at the Atwater and SSWWTP sites in 2013 and 2015. The model was then used to estimate the assimilative capacity of phosphorus from the SSWWTP.

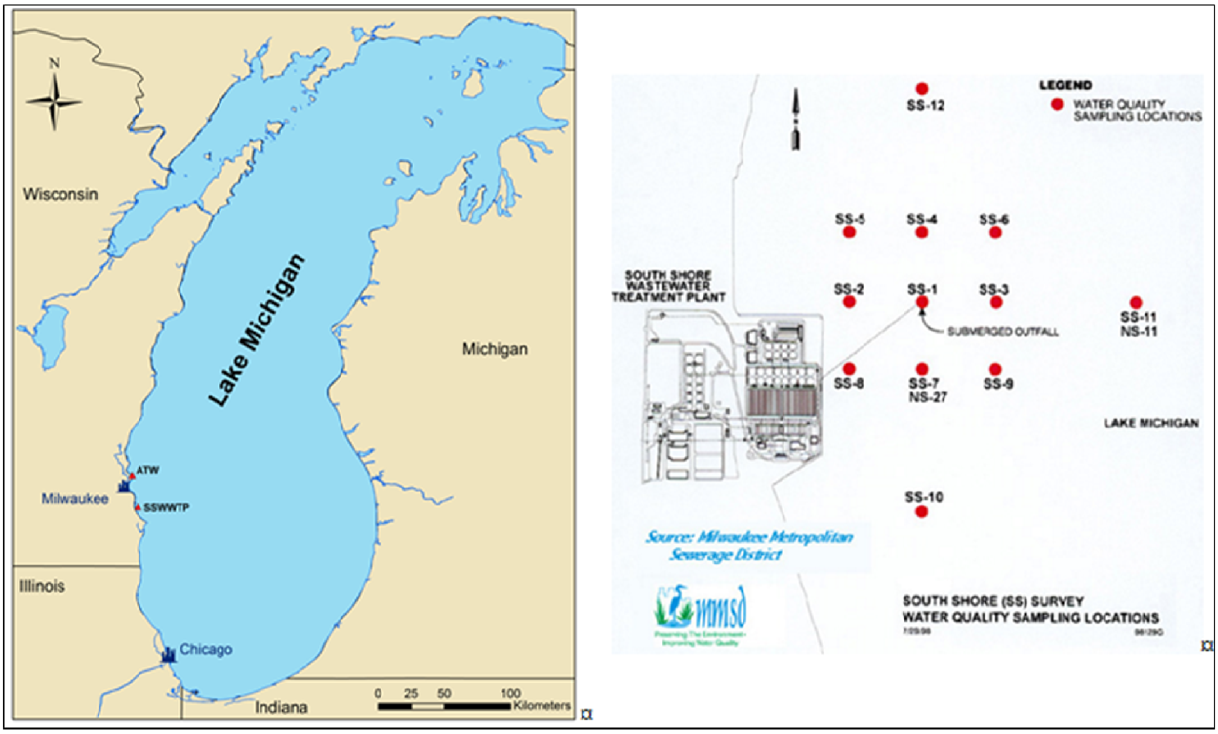


(a) (b)

**Figure 2.** (a) Map of Lake Michigan showing the SSWWTP and ATW water quality sampling sites. (b) Detail of sampling sites around the MMSD WWTP.

## 3 RESULTS

3.1 Testing with lower detection limit of the P samples collected in 2015 by MMSD, and analysis of Cladophora trends in the nearshore zone

During the summer of 2015, we completed sampling cruises, measuring *Cladophora* biomass and *Cladophora* particulate phosphorus content at five sites, with a lower detection limit that was previously used by MMSD. The red dots in Figure 3a show the sites, namely Atwater, Cudahy, Oak Creek, South Milwaukee and Texas Rock, from N to S. One counterintuitive result (Figure 3b) showed high P content corresponding to low biomass. The interpretation is that high P content sites are low light (turbid) sites. The management implication is that we must consider how management actions affect both P supply and water clarity. Clearer water can offset gains resulting from lower P loads.

3.2 Model validation against measurements made at the Atwater sites in 2013 and 2015

Figure 4 illustrates the measured and calculated concentrations of DP and PP at the ATW location in 2013 and 2015. Both simulations showed reasonably good agreement with measurements. The DP simulations showed a significant difference in the patterns of variations when comparing the results of 2013 and 2015. The 2013 simulation showed relatively small fluctuations in DP concentration, which does not exceed the lake background value of 2 µg/L. In contrast, DP concentrations showed larger fluctuations in 2015, reaching higher values around 5 µg/L. The effects of mussels and *Cladophora* could explain the difference. It is plausible that mussels and algae have produced a large amount of DP by excretion and respiration, respectively, during those two years, leading to the accumulation of DP in the bottom of the lake. Also, lake circulation can transport DP from offshore areas to the nearshore zone.

The simulation results for PP showed a smaller range of variation than that of DP, and the calculated concentrations are similar in 2013 and 2015. One difference is that PP concentrations showed more frequent spikes of concentration in 2013 because of resuspension events that year. More frequent resuspension can be explained by the meteorological variability of the study area, with stronger winds in 2013.

 

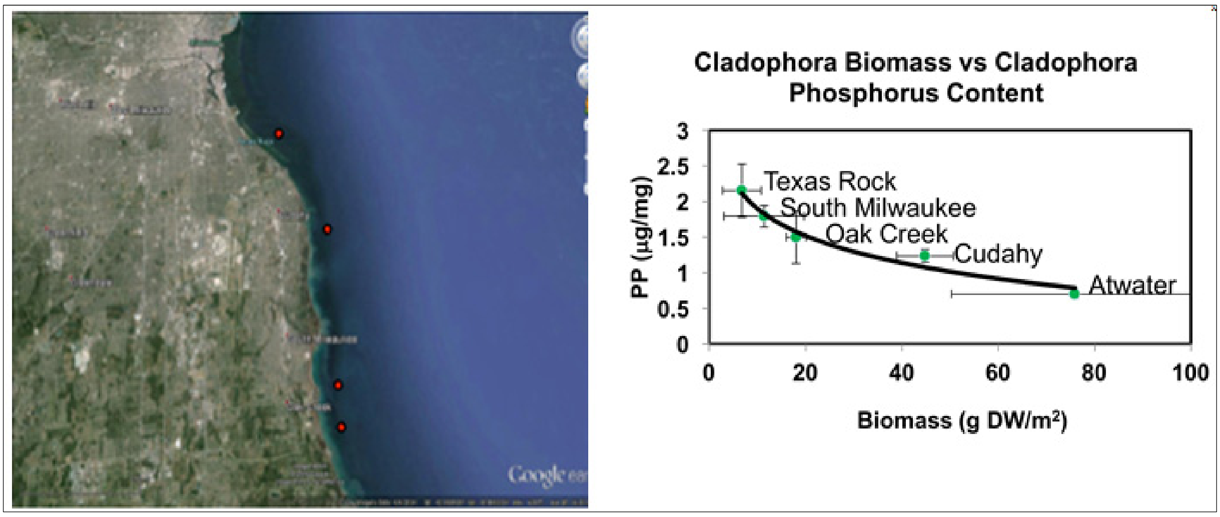


(a) (b)

**Figure 3.** (a) Locations of Atwater, Cudahy, Oak Creek, South Milwaukee and Texas Rock sampling stations shown, N to S, by red dots. (b) *Cladophora* biomass vs. *Cladophora* particulate phosphorus content in 2015 cruises.

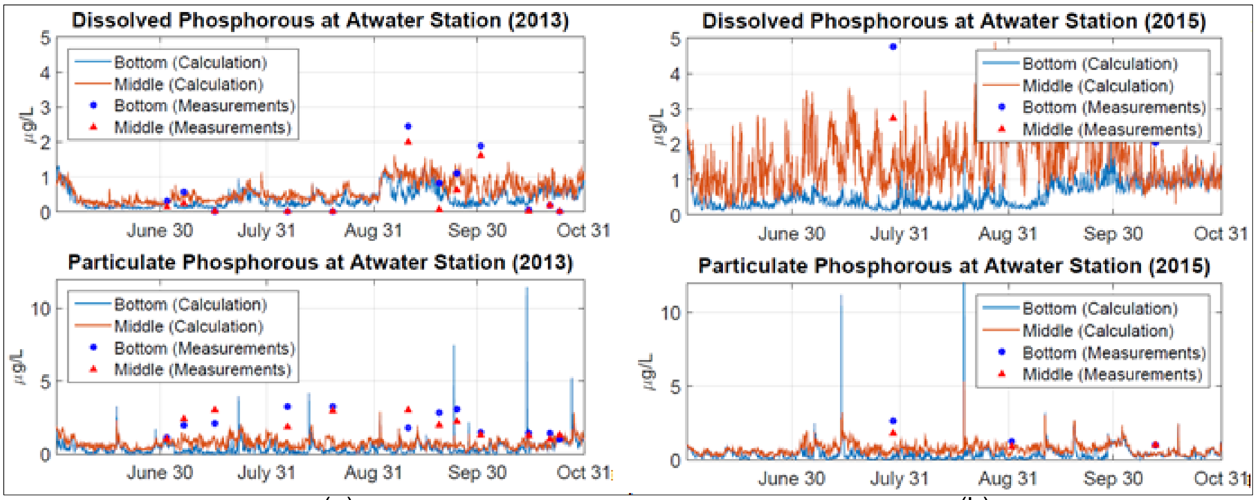


(a) (b)

**Figure 4.** Comparison of dissolved and particulate phosphorus at the Atwater station, measured near the bottom and the middle of the water column (blue and red symbols, respectively) and predicted by the model (blue and red lines). a) 2013 comparison; b) 2015 comparison.

*Cladophora* interactions have a significant influence on DP concentrations in Lake Michigan. Figure 5 shows a reasonable agreement between the measured and calculated *Cladophora* biomass and phosphorous content at ATW in 2013 and 2015. According to the simulation results, *Cladophora* biomass peaks during June, September, and October. The main reason is because of variations in the lake bottom water temperature (not shown). When the temperature is higher than an optimum value of 17 ˚C, *Cladophora* starts sloughing and the biomass decreases. The temperature is most often higher than 17 ˚C between June and Oct of 2013, and during that time period sloughing restricts the growth of *Cladophora* biomass.

The seasonal trends in *Cladophora* biomass were similar in 2013 and 2015, but simulations showed significantly higher biomass in 2015. The reasons could be climate variability and interaction with higher DP concentration in water, as shown in Figure 4. *Cladophora* phosphorous content did not show a significant difference between 2013 and 2015, except for a slight increase in September and October of 2015.

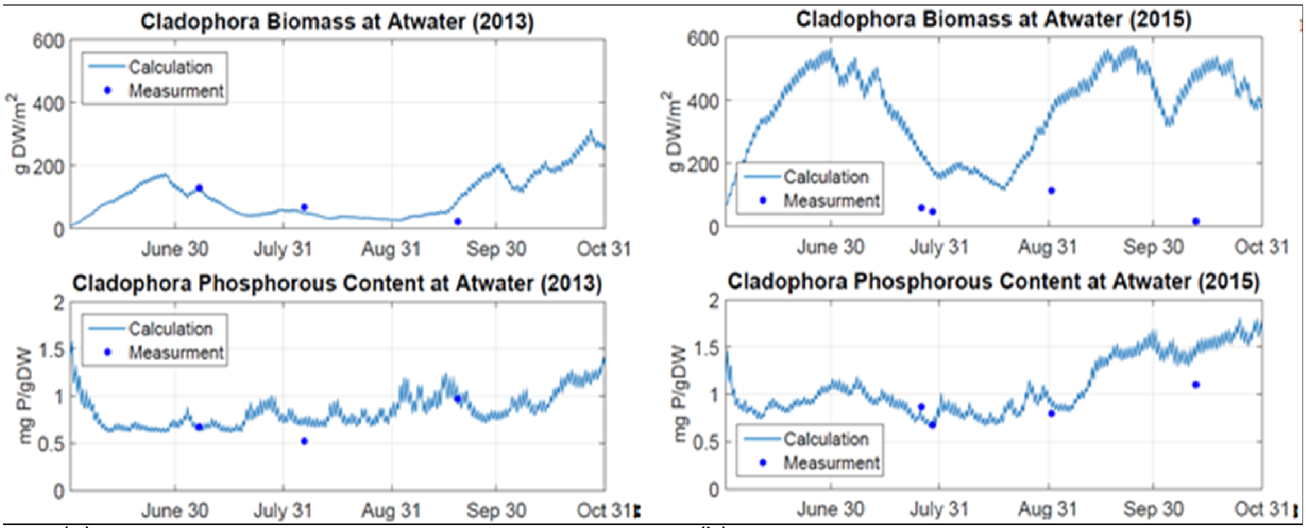


(a) (b)

**Figure 5.** Comparison of *Cladophora* biomass and *Cladophora* phosphorus content at the Atwater station, measured (blue symbols) and predicted by the model (blue lines). (a) 2013 comparison and (b) 2015 comparison.

Figure 6 illustrates DP and PP concentrations at the lake bottom, from the SSWWTP outfall loads measured by MMSD, and DP and PP the concentrations calculated by the model at the middle of the water column during the June to October 2013 and 2015 periods. The concentrations in the bottom layer are much higher than that in the upper layers because the outlet is near at the bottom. The loading patterns in 2013 and 2015 were different from each other, especially in July and September. The average outfall discharge concentrations of DP and PP were 273 μg/L and 251 μg/L in 2013 and 2015, respectively. The peak concentrations released in 2015 were, however, significantly higher than those released in 2013. The outfall concentrations reached values of 1500 μg/L or higher in the last weeks of July and September of 2015.

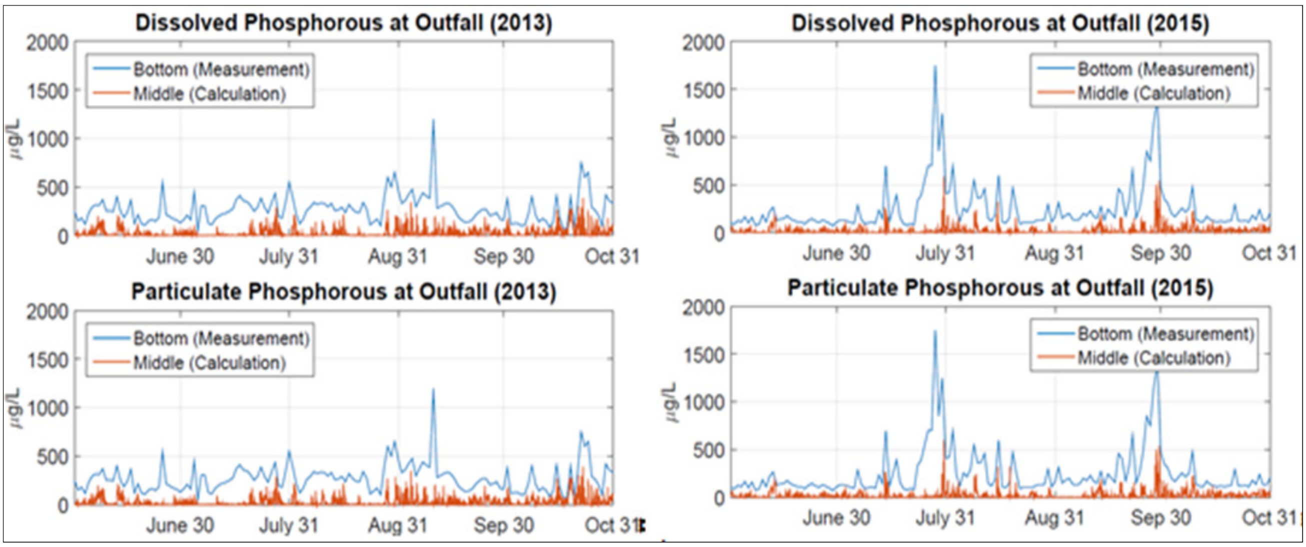


(a) (b)

**Figure 6.** June-October 2013 (a) and 2015 (b) measured DP and PP concentrations at the lake bottom, from SSWTP outfall loads measured by MMSD (blue lines), and DP and PP the concentrations calculated by the model at the middle of the water column (red lines).

3.3 Estimation of the assimilative capacity of the lake

One of the main goals of the study was to apply the model as a management tool to test various scenarios of SSWWTP nutrient loading, and determine effluent phosphorus limits for the wastewater treatment plant. Effluent phosphorus limits can be determined using the concept of assimilative capacity of the lake, defined as the difference between the total, whole-lake average phosphorus target of 7 μg $L^{-1}$ and the lake background concentration. Application of the concept involves a control volume, an averaging period, and a point source loading rate. The limit-loading rate can be calculated as the loading rate that when diluted over the control volume reaches the assimilative capacity, on average over the averaging period. In order to

  / ISSN 1562-6865 (Online) - ISSN 1063-7710 (Print)

estimate the limit-loading rate, we are preparing of maps that show the locations where the TP criterion of 7 μg $L^{-1}$ is exceeded under historical SSWWTP phosphorus load discharges. The maps will show the spatial distribution of total phosphorus criterion exceedance by contour lines of the percentage of time that the criterion is exceeded during the summer season (June to October).

Model simulations showed that TP exceeds the concentration target of 7 μg $L^{-1}$, in particular in areas near the outfall. We calculated the footprints where the SSWTP outfall produces concentrations higher that the 7 μg $L^{-1}$ target during different percentages of the summer season. For example, Table 1 shows the lake volumes and areas affected more than 25% of the time for the model layers located at the surface, middle, and bottom of the water column.

**Table 1**. Total volumes and areas of lake's water affected by TP higher than 7 μg $L^{-1}$ more than 25% of the time.

| Model Layer | Total Area ($km^2$) | | Total Volume ($\times10^6$ $m^3$) | |
|---|---|---|---|---|
| | **2013** | **2015** | **2013** | **2015** |
| Surface | 3.55 | 1.94 | 0.90 | 0.50 |
| Middle | 3.14 | 1.85 | 0.79 | 0.46 |
| Bottom | 1.72 | 1.64 | 0.43 | 0.26 |
| All layers | - | - | 14.12 | 8.09 |

In general, TP concentrations higher than the target occur over larger areas near the water surface than near the bottom of the lake. The difference in affected areas along the water column could be explained by the action of algae and mussels at the bottom of the Lake that can decrease TP concentration, and by the presence of stronger currents in the upper layers that can disperse phosphorous farther. In other words, hydrodynamics is the most significant process near the surface, while the effects of hydrodynamics and biogeochemical processes counteract each other near the bottom. Biogeochemical processes can reduce the TP concentration near the bottom of the lake.

Figure 7 shows the areas affected by TP higher than 7 μg $L^{-1}$ in 2013 and 2015. For example, the alongshore lengths of the surface layer-footprints of TP higher than the target during 25% of the summer season, were approximately 27 and 22 Km in 2013 and 2015, respectively. The difference in the size of the footprint could be explained by the different loading patterns in those two years, and by lower average discharge concentration in 2015. In addition, the areal density of *Cladophora* biomass was larger in 2015, possibly resulting in larger P uptake and lower TP concentrations near the bottom of the lake.

## 4 CONCLUSIONS

A model was developed with the goal of contributing to the understanding the nearshore transport and fate of nutrients, particularly phosphorus, in the Laurentian Great Lakes. That understanding is necessary to address excessive nutrient loading into Lake Michigan, which can produce algal blooms, hypoxia, beach closures, clogging of water intakes, and reduced water quality.

The 3D model consists of a hydrodynamic model linked with a biogeochemical model. The biogeochemical model consists of three interrelated modules: a mussel module, a *Cladophora* module, and a sediment dynamics module. The *Cladophora* module simulates the processes of near-bottom dissolved phosphorus uptake and respiration, and sloughing. The mussel module simulates near-bottom particulate phosphorus grazing, excretion to near-bottom dissolved phosphorus, and egestion to sediment storage. The sediment storage module simulates particulate phosphorus settling and resuspension. The model was validated against field measured water temperature, total and particulate phosphorus, *Cladophora* biomass and *Cladophora* phosphorus content.

The model is being applied as a management tool to test various scenarios of Milwaukee Metropolitan Sewerage District South Wastewater Treatment Plant nutrient loading, in order to determine effluent phosphorus limits for the plant. The limiting loading rate is being estimated using the concept of assimilative capacity of the lake, defined as the difference between the whole-lake phosphorus concentration target and the lake background concentration.

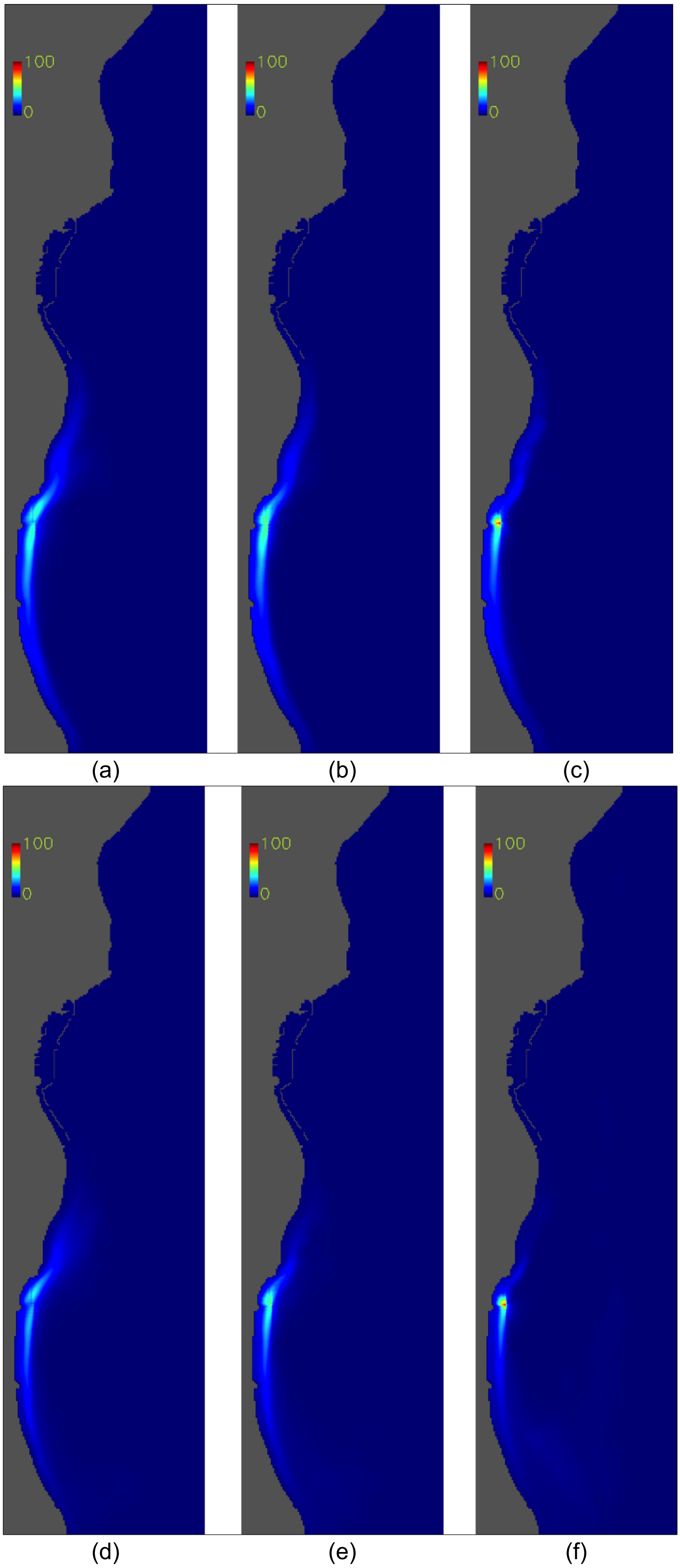


**Figure 7.** Footprints of exceedance of TP target concentration in 2013 (surface, middle and bottom layers in a, b and c, respectively) and 2015 (surface, middle and bottom layers in d, e and f, respectively).

**ACKNOWLEDGEMENTS**

The NSF I/UCRC on Water Equipment and Policy funded the research reported herein. The authors would like to thank Wisconsin Department of Natural Resources and MMSD staff for their involvement in the project.

**REFERENCES**

Auer, M.T., Tomlinson, L.M., Higgins, S.N., Malkin, S.Y., Howell, E.T. & Bootsma, H. A. (2010). Great Lakes *Cladophora* in the 21st Century: Same Algae—Different Ecosystem. *Journal of Great Lakes Research*, 36(2), 248–255.

Bootsma, H. & Liao, Q. (2013). *Nutrient Cycling by Dreissenid Mussels, in: Quagga and Zebra Mussels*. CRC Press, 555–574.

Bootsma, H.A. (2009). *Causes, Consequences and Management of Nuisance Cladophora*; Final Report Submitted to the Environmental Protection Agency Great Lakes National Program Office. Chicago, IL.

Fillingham, J.H. (2015). *Modeling Lake Michigan Nearshore Carbon and Phosphorus Dynamics*, Doctoral dissertation, The University of Wisconsin-Milwaukee.

Higgins, S.N., Pennuto, C.M., Howell, E.T., Lewis, T.W. & Makarewicz, J.C. (2012). Urban Influences on Cladophora Blooms in Lake Ontario. *Journal of Great Lakes Research*, 38, 116–123.

International Joint Commission, (1972). *Great Lakes Water Quality Agreement, with Annexes and Texts and Terms of Reference, between the United States of America and Canada*. International Joint Commission, Windsor, Ontario.

International Joint Commission (1978). *The Water Quality Agreement between the United States and Canada on Great Lakes Water*. International Joint Commission, Windsor, Ontario.

Leon, L.F., Smith, R.E.H., Malkin, S.Y., Depew, D., Hipsey, M.R., Antenucci, J.P., Higgins, S.N., Hecky, R.E. & Rao, R.Y. (2012). Nested 3D Modeling of the Spatial Dynamics of Nutrients and Phytoplankton in a Lake Ontario Nearshore Zone. Journal of Great Lakes Research, 38, 171–183.

Pauer, J.J, Anstead, A.M., Melendez, W., Taunt, K.W., Kreis Jr. & R.G. (2011). Revisiting the Great Lakes Water Quality Agreement Phosphorus Targets and Predicting the Trophic Status of Lake Michigan. *Journal of Great Lakes Research,* 37(1), 26–32.

Schwab, D.J., Beletsky, D., DePinto, J. & Dolan, D.M. (2009). A Hydrodynamic Approach to Modeling Phosphorus Distribution in Lake Erie. *Journal of Great Lakes Research,* 35 (2009), 50–60.

Tetra Tech, Inc. (2014*). Potential Approach for Developing Effluent Limits for Wisconsin Phosphorus Dischargers to Lake Michigan*, Technical Report Prepared for U.S. Environmental Protection Agency, Region 5.

Thomas, N.A., Roberston, A. & Sonzoni, W.C. (1980). *Review of control objectives: New target loads and input controls. In: Loehr*, R.C., Martin, C.S., Rast, W. (Eds.), Phosphorus Management Strategies for Lakes. Ann Arbor Science Publishers, Ann Arbor, 61–90.

Proceedings of the 37th IAHR World Congress
August 13 – 18, 2017, Kuala Lumpur, Malaysia

# THREE DIMENSIONAL NUMERICAL MODELING OF LATERALLY CONFINED VERTICAL BUOYANT JETS USING THE GGDH K-E TURBULENCE MODEL

XIAOHUI YAN[1] & ABDOLMAJID MOHAMMADIAN[2]

[1,2] University of Ottawa, Ottawa, Canada
xyan044@uottawa.ca; amohamma@uottawa.ca

## ABSTRACT

For the purpose of efficiently designing an outfall system and accurately assessing the environmental impacts of the system, it is necessary to investigate the mixing processes of a turbulent buoyant jet. When a turbulent buoyant jet is dynamically bounded by boundaries, it can be called a confined turbulent buoyant jet. In the present paper, the mixing properties of a laterally confined vertical buoyant jet is simulated using the GGDH k-ε turbulence model and the results are compared to other models available and present experiments. The results show that the buoyancy-corrected model can improve the accuracy and can be used for investigating the mixing properties of a laterally confined vertical buoyant jet.

**Keywords:** Numerical modeling; lateral confinement; buoyant jet; k-ε GGDH; turbulence model.

## 1 INTRODUCTION

The density of many types of wastewater effluents is lower than the ambient water, and in this sense the wastewater effluents can be named buoyant jets. A very common form of turbulent buoyant jets is liquid waste from desalination plants (Kheirkhah et al., 2014; 2015). It is quite important to adequately dispose the buoyant jets, as the jets have significant negative impacts on the environment (e.g., Huai et al., 2010; Drami, et al., 2011; Lattemann & Höpner, 2008). Typically, a submarine buoyant jet is affected by boundaries, and this sort of buoyant jet is confined buoyant jet.

The mixing processes of confined buoyant jets can be studies in three different ways: theoretically, experimentally and numerically. Numerical simulations of laterally confined vertical buoyant jets have rarely been reported in the literature. Numerical simulations on confined jets have rarely been done, and require further investigation. Numerous researchers have developed and employed integral models for turbulent buoyant jets (Jones et al., 2007; Chu, 1985). The model has been validated using extensive high-resolution laboratory data and proved to be a convenient and efficient tool for surface discharge jet analysis. 3D numerical simulations based on the solutions of the Navier-Stokes equations can provide more reliable and detailed results for confined jets. El-Amin et al. (2010) analyzed a turbulent buoyant confined jet discharged into a cylindrical tank. The distributions of velocity, pressure, temperature and turbulence were measured and modelled using the realizable k-ε turbulence model. The modelled results matched the measurements fairly well. Gildeh et al. (2014) conducted a numerical study on the velocity and temperature fields of the thermal and saline wall jets. The cling length, plume trajectory, temperature dilutions, and temperature and velocity were simulated using different turbulence models. The simulated results showed good agreement with the recent experimental data, and two models performed best among the seven models chosen for the study.

An important cause of uncertainties in numerical simulations is the selection of turbulence models. There are generally three categories of turbulence models: direct numerical simulation (DNS), large eddy simulation (LES) and Reynolds-averaged Navier-Stokes (RANS) simulations. In practice, the RANS simulations are the most widely used method, especially the k-ε turbulence model. However, the standard k-ε turbulence does not take into account the effect of buoyancy on turbulence, which might lead to errors when buoyancy is very important. The GGDH k-ε turbulence model of Daly and Harlow (1970) is a buoyance-modified k-ε turbulence model, which incorporated buoyance source terms based on the generalized gradient diffusion hypothesis.

Therefore, the present paper simulates a laterally confined vertical buoyant jet using the GGDH k-ε turbulence model and compares its performances with other models and data.

  / ISSN 1562-6865 (Online) - ISSN 1063-7710 (Print)

## 2 METHODS

A total of 24 cases are considered in the present study, and the specifications of these cases are summarized in Table 1.

**Table 1.** Parameters of the simulated cases.

| Cases | *D (mm)* | *$D_r$ (mm)* | *$H_r$ (mm)* | *$T_j$ (°C)* | *$T_a$ (°C)* | *Δρ (kg/m3)* | *$W_j$ (cm/s)* | *B* | *Fr* |
|---|---|---|---|---|---|---|---|---|---|
| C1 | 8 | 36 | 120 | 56.7 | 21.4 | 13.1 | 10.6 | 4.3 | 3.3 |
| C2 | 8 | 36 | 120 | 58.7 | 21.4 | 14.1 | 13.3 | 4.3 | 4.0 |
| C3 | 8 | 36 | 120 | 55.9 | 21.4 | 12.7 | 15.9 | 4.3 | 5.0 |
| C4 | 8 | 36 | 120 | 57.6 | 21.3 | 13.5 | 21.6 | 4.3 | 6.5 |
| C5 | 8 | 36 | 120 | 45.4 | 21.1 | 7.9 | 21.4 | 4.3 | 8.6 |
| C6 | 8 | 36 | 120 | 47.0 | 21.2 | 8.6 | 31.8 | 4.3 | 12.3 |
| C7 | 10 | 64 | 150 | 51.4 | 17.8 | 11.3 | 10.2 | 2.8 | 3.1 |
| C8 | 10 | 64 | 150 | 39.5 | 17.3 | 6.3 | 31.2 | 2.8 | 12.6 |
| C9 | 10 | 64 | 200 | 55.6 | 19.9 | 12.8 | 13.6 | 3.7 | 3.9 |
| C10 | 10 | 64 | 200 | 42.3 | 19.6 | 6.0 | 25.8 | 3.7 | 9.9 |
| C11 | 10 | 36 | 200 | 58.7 | 19.7 | 14.4 | 19.0 | 7.7 | 5.1 |
| C12 | 10 | 36 | 200 | 59.7 | 19.8 | 14.9 | 22.6 | 7.7 | 5.9 |
| C13 | 10 | 36 | 150 | 46.1 | 16.9 | 9.1 | 10.2 | 5.8 | 3.4 |
| C14 | 10 | 36 | 150 | 46.9 | 16.8 | 9.4 | 12.0 | 5.8 | 3.9 |
| C15 | 10 | 36 | 150 | 55.6 | 16.7 | 13.4 | 19.0 | 5.8 | 5.2 |
| C16 | 10 | 36 | 150 | 55.9 | 16.6 | 13.6 | 24.5 | 5.8 | 6.7 |
| C17 | 10 | 36 | 150 | 38.1 | 16.3 | 6.0 | 20.4 | 5.8 | 8.4 |
| C18 | 10 | 36 | 150 | 39.0 | 16.9 | 6.2 | 31.2 | 5.8 | 12.7 |
| C19 | 8 | 21 | 120 | 55.5 | 21.2 | 12.5 | 10.6 | 9.2 | 3.4 |
| C20 | 8 | 21 | 120 | 57.1 | 21.5 | 13.3 | 13.3 | 9.2 | 4.1 |
| C21 | 8 | 21 | 120 | 58.2 | 21.5 | 13.8 | 15.9 | 9.2 | 4.8 |
| C22 | 8 | 21 | 120 | 57.4 | 21.8 | 13.3 | 21.3 | 9.2 | 6.6 |
| C23 | 8 | 21 | 120 | 44.6 | 21.1 | 7.6 | 21.4 | 9.2 | 8.8 |
| C24 | 8 | 21 | 120 | 45.7 | 21.2 | 8.0 | 31.8 | 9.2 | 12.7 |

*D* = Jet diameter; $D_r$ = Riser diameter; $H_r$ = Riser height; $T_j$ = Jet temperature; $T_a$ = Ambient temperature; *Δρ* = Source density deficit; $W_j$ = Jet velocity; *B* = Confinement index; *Fr* = Densimetric Froude number

The governing equations of the numerical simulations can be expressed as (Gildeh et al. 2015):

$$\frac{\partial u}{\partial x}+\frac{\partial v}{\partial y}+\frac{\partial w}{\partial z}=0 \tag{1}$$

$$\frac{\partial u}{\partial t}+u\frac{\partial u}{\partial x}+v\frac{\partial u}{\partial y}+w\frac{\partial u}{\partial z}=-\frac{1}{\rho}\frac{\partial P}{\partial x}+\frac{\partial}{\partial x}\left[\nu_{eff}(\frac{\partial u}{\partial x})\right]+\frac{\partial}{\partial y}\left[\nu_{eff}(\frac{\partial u}{\partial y})\right]+\frac{\partial}{\partial z}\left[\nu_{eff}(\frac{\partial u}{\partial z})\right] \tag{2}$$

$$\frac{\partial v}{\partial t}+u\frac{\partial v}{\partial x}+v\frac{\partial v}{\partial y}+w\frac{\partial v}{\partial z}=-\frac{1}{\rho}\frac{\partial P}{\partial y}+\frac{\partial}{\partial x}\left[\nu_{eff}(\frac{\partial v}{\partial x})\right]+\frac{\partial}{\partial y}\left[\nu_{eff}(\frac{\partial v}{\partial y})\right]+\frac{\partial}{\partial z}\left[\nu_{eff}(\frac{\partial v}{\partial z})\right]-g\frac{\rho-\rho_0}{\rho} \tag{3}$$

$$\frac{\partial w}{\partial t}+u\frac{\partial w}{\partial x}+v\frac{\partial w}{\partial y}+w\frac{\partial w}{\partial z}=-\frac{1}{\rho}\frac{\partial P}{\partial z}+\frac{\partial}{\partial x}\left[\nu_{eff}(\frac{\partial w}{\partial x})\right]+\frac{\partial}{\partial y}\left[\nu_{eff}(\frac{\partial w}{\partial y})\right]+\frac{\partial}{\partial z}\left[\nu_{eff}(\frac{\partial w}{\partial z})\right] \tag{4}$$

with

$$\nu_{eff}=\nu_t+\nu \tag{5}$$

where u, v, and w are Reynolds-averaged velocities; x, y (vertical direction), and z are the Cartesian coordinate axes. t is time, ρ is the fluid density and ρ0 is the reference fluid density. Pressure is represented by P. veff denotes the effective kinematic viscosity, vt is the turbulent kinematic viscosity, and v is the kinematic viscosity. g is the gravity acceleration.

The k-ε model of Jones and Launder (1972) is the most widely used turbulence model as it is accurate as well as efficient, so it is called the standard k-ε turbulence model hereafter.

It is a two-equation model, where the turbulence kinetic energy *k and its* dissipation rate *ε* are calculated from their respective transport equations:

 

$$\frac{\partial k}{\partial t}+U_i\frac{\partial k}{\partial x_i}=\frac{\partial}{\partial x_i}\left[(\frac{\nu_t}{\sigma_k}+\nu)\frac{\partial k}{\partial x_i}\right]+G-\varepsilon \tag{6}$$

$$\frac{\partial k}{\partial t}+U_i\frac{\partial k}{\partial x_i}=\frac{\partial}{\partial x_i}\left[(\frac{\nu_t}{\sigma_k}+\nu)\frac{\partial k}{\partial x_i}\right]+G-\varepsilon \tag{7}$$

$$\frac{\partial \varepsilon}{\partial t}+U_i\frac{\partial \varepsilon}{\partial x_i}=\frac{\partial}{\partial x_i}\left[(\frac{\nu_t}{\sigma_\varepsilon}+\nu)\frac{\partial \varepsilon}{\partial x_i}\right]+c_{1\varepsilon}\frac{\varepsilon}{k}G-c_{2\varepsilon}\frac{\varepsilon^2}{k} \tag{8}$$

With

$$G=\nu_t(\frac{\partial U_i}{\partial x_j}+\frac{\partial U_j}{\partial x_i})\frac{\partial U_i}{\partial x_j} \tag{9}$$

and

$$\nu_t=c_\mu\frac{k^2}{\varepsilon} \tag{10}$$

where $U_i$ is the instantaneous velocity component in the direction $x_i$, $G$ is the production of turbulence due to shear. The model constants $c_\mu$, $c_{1\varepsilon}$, $c_{2\varepsilon}$, and $\sigma_k$, $\sigma_\varepsilon$ are given the standard values of 0.09, 1.44, 1.92, 1, and 1.3.

The $k$-$\varepsilon$ GGDH turbulence model can be expressed as:

$$\frac{\partial k}{\partial t}+U_i\frac{\partial k}{\partial x_i}=\frac{\partial}{\partial x_i}\left[(\frac{\nu_t}{\sigma_k}+\nu)\frac{\partial k}{\partial x_i}\right]+G+\hat{B}-\varepsilon \tag{11}$$

$$\frac{\partial \varepsilon}{\partial t}+U_i\frac{\partial \varepsilon}{\partial x_i}=\frac{\partial}{\partial x_i}\left[(\frac{\nu_t}{\sigma_\varepsilon}+\nu)\frac{\partial \varepsilon}{\partial x_i}\right]+c_{1\varepsilon}\frac{\varepsilon}{k}G+c_{1\varepsilon}(1-c_{3\varepsilon})\frac{\varepsilon}{k}\hat{B}-c_{2\varepsilon}\frac{\varepsilon^2}{k} \tag{12}$$

with

$$\hat{B}=-\frac{3}{2}\frac{\nu_t}{\sigma_t\rho k}\left(\overline{u_i'u_j'}\frac{\partial\rho}{\partial x_j}\right)\left(\frac{\partial P}{\partial x_i}+\rho_0 g_i\right) \tag{13}$$

where $\hat{B}$ is the production of turbulence due to the buoyancy effect. $\overline{u_i'u_j'}$ denotes the velocity fluctuation. It is numerically found that there are no significant differences in the results when $c_{3\varepsilon}$ and $\sigma_t$ vary between 0.6 and 1, so these coefficients are set to 0.8 and 1.0 respectively.

However, the standard k-ε turbulence model was not developed for variant density flows. In order to improve the accuracy of numerical simulations, source terms should be added to the transport equations to account for the buoyancy introduced by the turbulence. There are two popular hypotheses for adding the source terms; one is the simple gradient diffusion hypothesis (SGDH), and the other one is the general gradient diffusion hypothesis (GGDH). In the present paper, the GGDH method is utilized since it is more accurate than the SGDH method.

The governing equations can be solved using finite element, finite difference, or finite volume method. In the present paper, the finite volume method is used, as it is the most convenient one for describing the movement of a fluid. The simulations are conducted using the OpenFOAM (Open Source Field Operation and Manipulation), which is an open source computational fluid dynamics code. The solver is called pisoFoamIIII, which is developed at the University of Ottawa based on the standard pisoFoam solver. The pisoFoamIIII solver incorporates the Boussinesq term, salinity and temperature transport equations. The buoyancy-corrected turbulence model is developed on the basis of the standard k-ε turbulence model and the general gradient diffusion hypothesis.

The model for numerical simulations is based on an experimental setup, the outline dimensions of which are 1 m long, 1 m wide, and 0.45 m deep. Models with different port diameters, densimetric Froude numbers, and confinement indices are simulated to investigate the impacts of these parameters. The computational domain can be discretized using either a structured mesh or un-structured mesh. In the present paper, a structured mesh is used as it makes the simulations more stable. However, variant grid sizes are used in order to save computational costs; for example, the girds are finer near the riser but relatively coarser far from the riser.

 

## 3 RESULTS AND DISCUSSION

### 3.1 Grid sensitivity

The grid resolution can cause large uncertainties in a numerical simulation, so it is necessary to test the grid-independence. The 2% criteria is adopted, which means that a grid resolution is accepted if a finer grid resolution does not change the results by 2%.

The grid resolution of each simulation in the present study is determined in the following manner:

First, a preliminary simulation with relatively coarse grid resolution was established, and then simulations with finer resolution were conducted (until the model achieves the 2% confidence criteria).

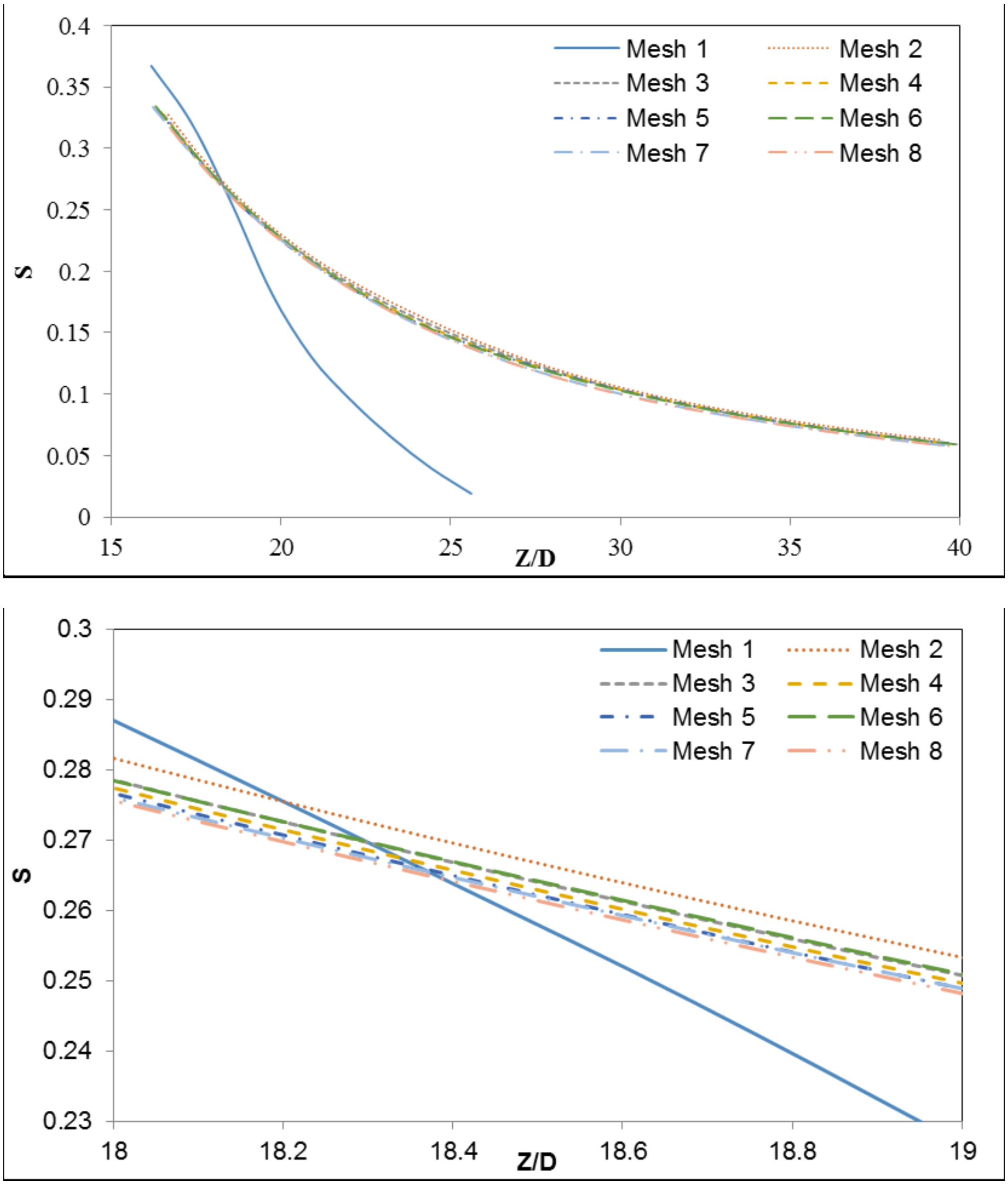


**Figure 1.** Concentration Profile of Confined Buoyant Jet, S versus Z/D for Case C1; a) Z/D = 15~40; (b) Z/D = 18~19. $S = (C-C_a)/(C_j-C_a)$, where $C$ is concentration at a particular location is, $C_a$ is ambient concentration, $C_j$ is jet initial concentration.

Taking Case 1 as an example; eight different meshes were tested, as shown in Figure 1 and Table 2. The employed procedure can be summarized as follows.

A preliminary simulation was performed with mesh 1, which contains about 0.256 × 106 grid cells.

Another simulation was performed with mesh 2. The mesh contains about 0.699 × 106 grid cells and its level of grid resolution is 1.4 (that is, the number of grid cells in each block is multiplied by a factor of 1.4 compared to that of mesh 1). The two simulations were compared. As can be observed in Figure 1, the difference between the mesh 1 and mesh 2 simulations is significant; thus, mesh 1 is not considered acceptable.

A new simulation was conducted using mesh 3, which has a level of grid resolution of 1.5. As one can see in Figure 1, the outputs of the mesh 2 simulation do not deviate far from those of the mesh 3 simulation, so a quantitative analysis is necessary.

The quantitative comparison comprises two steps: first, the results are interpolated to make the x, y, and z values consistent; second, the deviation between the two simulations is calculated.

As summarized in Table 2, the deviation is –2.013%, which exceeds the 2% criteria. The results from mesh 3 deviate from those of mesh 4 within only 2%, but the error regarding interpolation for mesh 4 exceeds 2%. Thus, the results were not considered reliable; neither mesh 5 nor mesh 6 was adopted due to the same concern (interpolation error).

Finally, mesh 7 and mesh 8 met the 2% standard, and the results were deemed reliable. To be conservative, the results from mesh 8 were employed.

### 3.2 Qualitative validation

Figure 2 shows the central plane of a laterally confined vertical buoyant jet in the present experiments. Experiments with other parameters are conducted and it can be concluded that: 1) the dilution decreases when the densimetric Froude number increases, since the buoyancy force becomes smaller compared to the inertial force when the densimetric Froude number increases; and 2) the dilution decreases when the confinement index increases, since the intrusion of ambient water is more restricted when the confinement index increases.

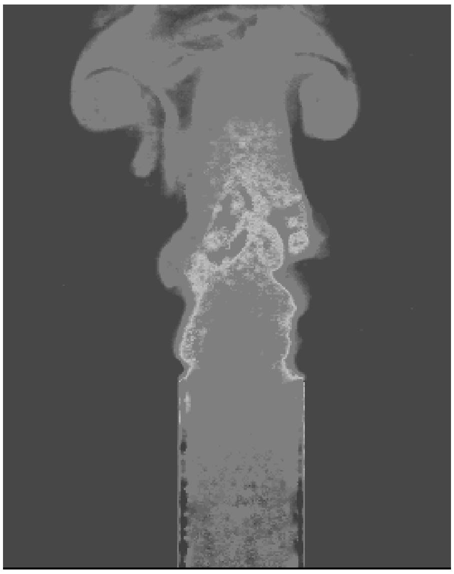

**Figure 2.** The central plane of a laterally confined vertical jet in the present experiment.

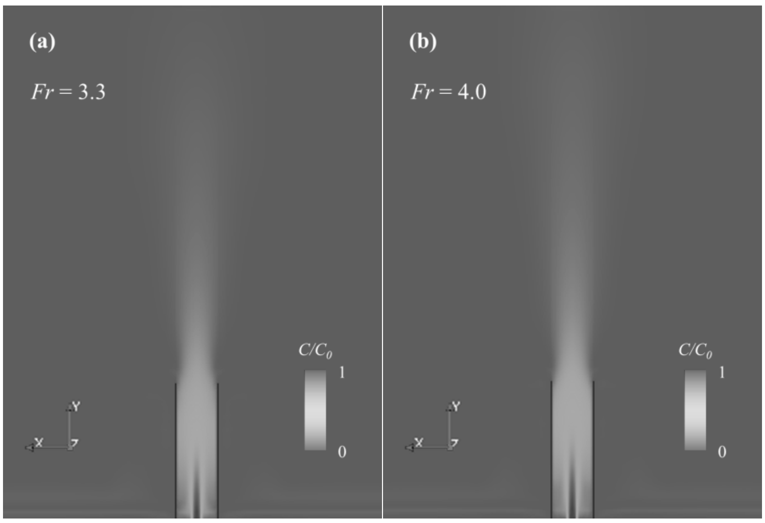


**Figure 3.** Comparison of the mixing properties of two jets with different densimetric Froude numbers (the confinement index is 4.3).

 

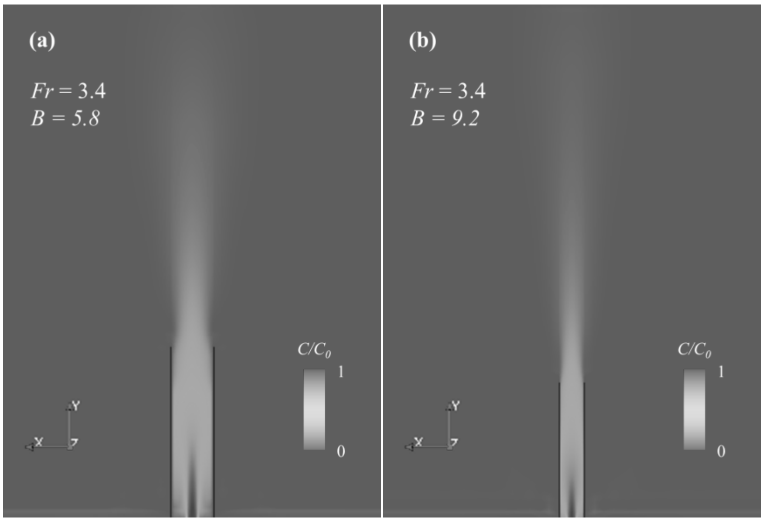


**Figure 4.** Comparison of the mixing properties of two jets with different confinement indices.

Figure 3 shows a comparison of the mixing properties of two jets with different densimetric Froude numbers. The jets have a confined index of 4.3, but the one in Figure 3 (a) has a densimetric Froude number of 3.3 while the one in Figure 3 (b) is 4.0. It can be seen that the dilution of the jet in Figure 3(b) is weaker than that in Figure 3 (a), which is in accordance with the conclusion obtained from the experiments. A comparison of the mixing properties of two jets with different densimetric Froude numbers is shown in Figure 4. The two jets have a same densimetric Froude number of 3.4, but the one in Figure 4 (a) has a confinement index of 5.8 while the one in Figure 4 (b) is 9.2. As can be observed, the dilution of the jet in Figure 4 (b) is weaker than that in Figure 4 (a), which agrees with the conclusion drawn from the experimental observations that the dilution becomes weaker when the confinement index increases.

3.3 Quantitative Validation

The above analysis demonstrates that the numerical models can correctly predict the qualitative properties of the mixing processes of laterally confined vertical buoyant jet. Figure 5 shows the quantitative results of comparisons between experimental and numerical observations.

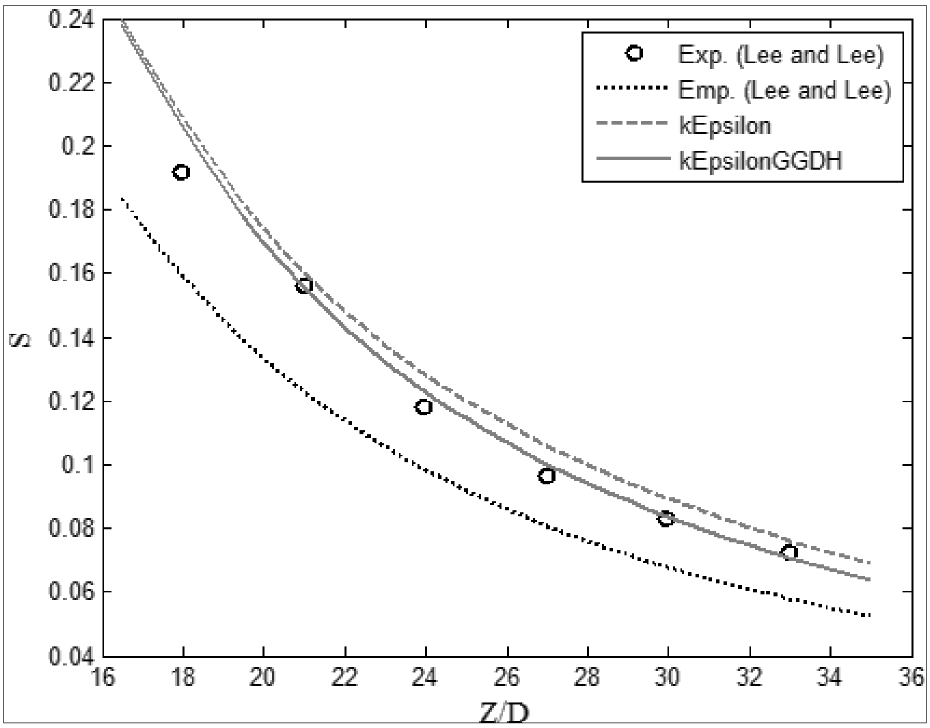


**Figure 5.** Concentration profiles of a laterally confined vertical buoyant jet with a confinement i ndex of 4.3 and a densimetric Froude number of 3.3.

 

Figure 5 shows the concentration profiles of a laterally confined vertical buoyant jet, the confinement index and densimetric Froude number of which is 4.3 and 3.3, respectively. In the figure, Z represents the vertical location, D is the riser diameter, and S is the centerline dilution, which can be expressed as:

$$S = \frac{C - C_a}{C_j - C_a} \tag{14}$$

where C is the concentration at a location, $C_a$ is the ambient concentration, and $C_j$ is the initial concentration of the jet. The empirical results are calculated using the regression equation from Lee and Lee (1998), which is

$$F_r(C - C_a)/(C_j - C_a) = (2.594B + 1.978)(Z/D/F_r)^{-5/3} \tag{15}$$

As can be seen from Figure 5, both the standard and buoyancy-corrected k-ε turbulence models can satisfactorily replicate the experimental measurements but the k-ε GGDH model results are closer to the measurements. The empirical estimation deviates farther from the measurements compared to the simulated results.

3.4 Concentration properties

Concentration properties are one of the most important parts of the analysis of a laterally confined vertical buoyant jet, especially in terms of environmental impact assessment. In the present study, six representative cross sections are investigated, the Z/D values of which are 16, 24, 28, 32, 36, and 40, respectively. The concentrations at these representative cross sections are extracted, normalized by the maximum concentrations, and compared to the normalized transverse distance. The results for a laterally confined buoyant jet with a confinement index of 4.3 and a densimetric Froude number of 3.3 are shown in Figure 6. In the figure, C represents the concentration at a location, $C_m$ is the maximum concentration at a representative cross section, r is the radial distance of a location from the centerline, and $b_{gc}$ is the half width, which is equal to the distance from the centerline to a location where the concentration is 1/e of the maximum concentration at the corresponding respective cross section.

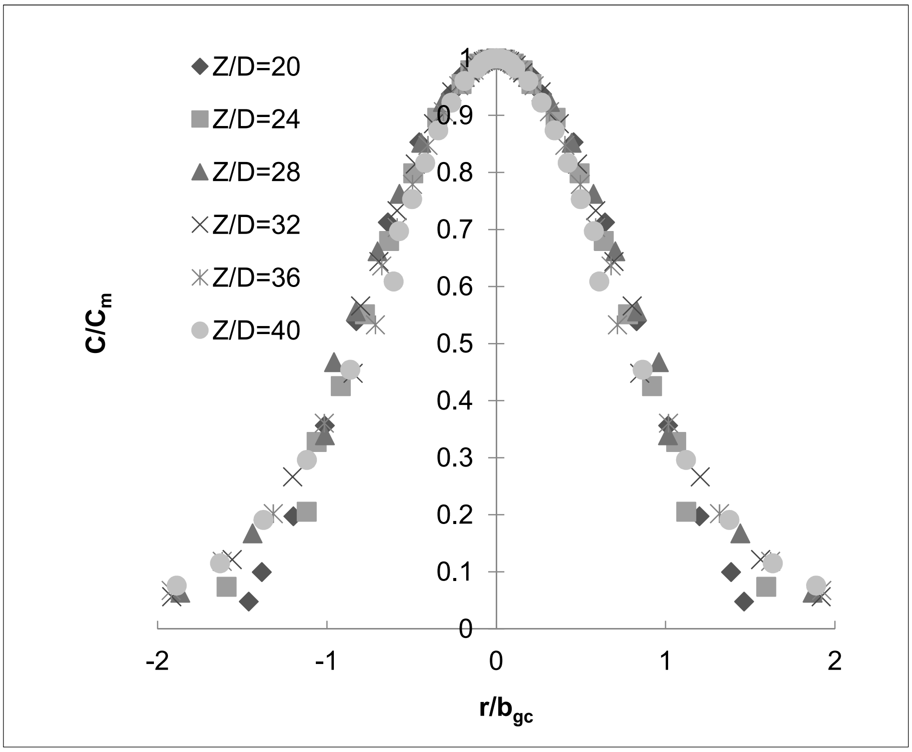


**Figure 6.** Dimensionless concentration profiles at various cross sections for a laterally confined buoyant jet with a confinement index of 4.3 and a densimetric froude number of 3.3.

As can be observed in Figure 6, the transverse distribution pattern is Gaussian, which can be approximately expressed as:

  / ISSN 1562-6865 (Online) - ISSN 1063-7710 (Print)

$$\frac{C}{C_m} = e^{-(r/b_{gc})^2} \tag{16}$$

For every case, the Gaussian manner of transverse concentration distribution exists at all of the representative cross sections.

- Velocity characteristics

  The velocity distributions can be obtained based on the k-ε GGDH model results. The normalized streamwise velocity $U_y/U_0$ at each cross section along the centerline is extracted and plotted against the vertical location of the corresponding cross section Z in Figure 7.

  From the figure, it can be observed that the jet could be divided into different zones based on the characteristics of velocity magnitude decay. In zone 1, the streamwise velocity magnitudes increase along the centerline, which is attributed to the positive buoyancy and process of flow establishment. In zone 2, the streamwise velocity magnitudes decrease significantly because of the rapid dilution in this region and the shear stresses induced by the riser wall. At the end of zone 2, impingement occurs, where the jet hits the riser wall, and the flow is deflected towards to the centerline. Therefore, the streamwise velocity magnitudes increase to a small degree due to the discrease of the jet cross-section areas in zone 3. Note that zone 3 does not exist for case C7 and C8, the confinement index of which are both 2.8. In zone 4, the velocities decay gradually and continuosly, caused by the momentom transfer and jet dilution.

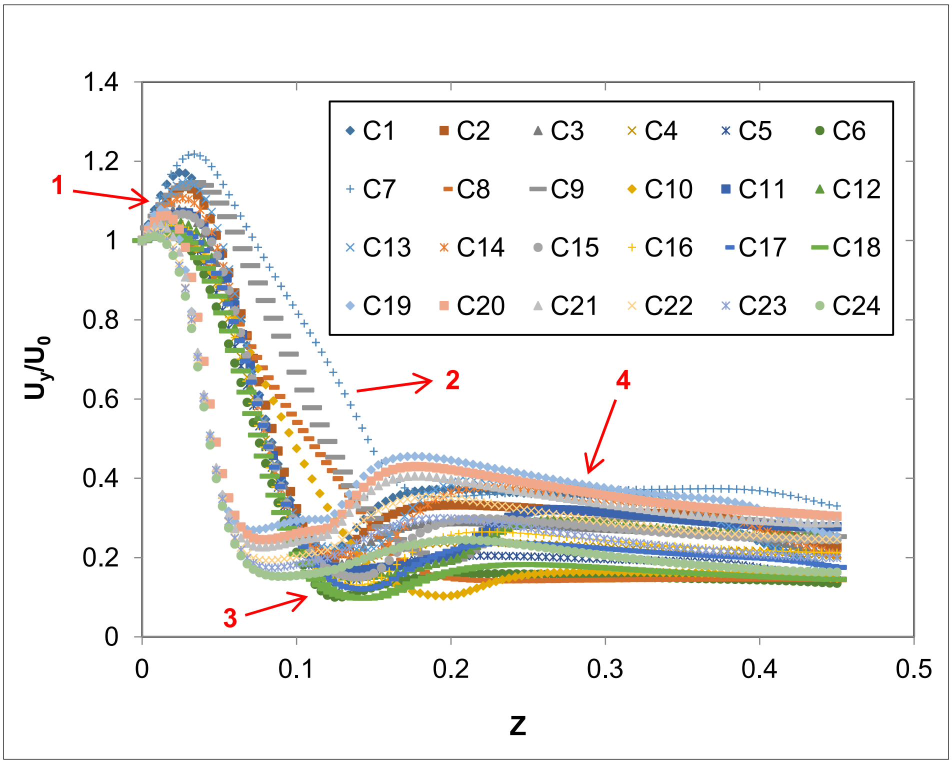


**Figure 7.** Normalized streamwise velocity $U_y/U_0$ at various cross sections.

## 4 CONCLUSIONS

Three-dimensional simulations of laterally confined vertical buoyant jets are conducted using the standard and buoyancy-modified k-ε turbulence models (GGDH k-ε turbulence model). The comparisons between the experimental measurements and simulated results validated these two models and demonstrated that the buoyancy-modified k-ε turbulence model can provide with better results. The concentration properties of the jets are further investigated using the buoyancy-modified k-ε turbulence model, and it is found that the transverse distribution of concentration is approximately Gaussian, and the jet spread width increases with distance. Further studies can also be conducted, such as the quantitative comparisons of the performance of the two different turbulence models, the impact of the confinement index and densimetric Froude number on the agreement between the simulated results and Gaussian profile, and calculations of the jet spread width rate for more cases.

**ACKNOWLEDGEMENTS**

The research was supported by NSERC (Natural Sciences and Engineering Research Council of Canada) and QNRF (Qatar National Research Fund). The first author would like to thank the China Scholarship Council for financial support of this research.

**REFERENCES**

Chu, V.H. (1985). Oblique Turbulent Jets in a Crossflow. *Journal of Engineering Mechanics*, 111(11), 1343-1360.

Daly, B.J. & Harlow, F.H. (1970). Transport Equations in Turbulence. *Physics of Fluids,* 13(11), 2634-2649.

El-Amin, M.F., Sun, S., Heidemann, W. & Müller-Steinhagen, H. (2010). Analysis of a Turbulent Buoyant Confined Jet Modeled using Realizable K–Ɛ Model. *Heat and mass transfer*, 46(8-9), 943-960.

Jones, G.R., Nash, J.D., Doneker, R.L. & Jirka, G.H. (2007). Buoyant Surface Discharges into Water Bodies. I: Flow Classification and Prediction Methodology. *Journal of Hydraulic Engineering*, 133(9), 1010-1020.

Kheirkhah Gildeh, H., Mohammadian, A., Nistor, I. & Qiblawey, H. (2014). Numerical Modeling of Turbulent Buoyant Wall Jets in Stationary Ambient Water. *Journal of Hydraulic Engineering*, 140(6), 1-17.

Kheirkhah Gildeh, H., Mohammadian, A., Nistor, I., Qiblawey, H. & Yan, X. (2015). CFD Modeling and Analysis of the Behavior of 30° And 45° Inclined Dense Jets–New Numerical Insights. *Journal of Applied Water Engineering and Research*, 4(2), 112-127.

Lee, A.W.T. & Lee, J.H.W. (1998). Effect of Lateral Confinement on Initial Dilution of Vertical Round Buoyant Jet. *Journal of Hydraulic Engineering*, 124(3), 263-279.

 

Proceedings of the 37th IAHR World Congress
August 13 – 18, 2017, Kuala Lumpur, Malaysia

# TRANSIENT GROWTH OF PERTURBATIONS IN SHALLOW FLOWS

YARZAR TUN [1] & ABDOLMAJID MOHAMMADIAN[2]

[1,2]University of Ottawa, Ottawa, Canada
ytun054@uottawa.ca; majid.mohammadian@uottawa.ca

## ABSTRACT

A linear stability analysis and nonmodal stability analysis is conducted for an open channel flow to study the conditions under which perturbations growth and develop into large scale lateral motion or "transverse motion". Linear stability analysis is widely used in the analysis of shallow flows. However, it is well known that linear stability analysis is not reliable when it comes to shear driven flows. Nonmodal stability analysis, on the other hand, gives a more complete picture of instabilities. A hyperbolic tangent velocity profile, which is commonly used to approximate shallow mixing layers, is analyzed. Some nonmodal stability metrics are used as an indication of finite time instability and confirmed by plotting the energy in the perturbations over time. It is shown that some linearly stable cases presented in literature do in fact exhibit transient energy growth, which can be significant enough to generate coherent turbulent structures and may take some time for it to dissipate.

**Keywords:** Shallow water; hydrodynamic instability; pseudospectra; nonmodal analysis.

## 1 INTRODUCTION

Natural fluid flows such as the oceans, rivers, estuaries, and even the atmosphere are shallow flows and they play an important role in the ecosystem. Large scale turbulent structures are commonly observed in shallow flows. The small depth to width ratio of shallow flows may lead to the development of large scale structures in the horizontal plane. These quasi two-dimensional structures contribute to lateral transverse motion which in turn leads to the transfer of mass, momentum and energy in the flows. It is very important to understand the conditions under which these structures can be generated.

Large scale lateral motion in channels has been analyzed by means of numerical simulations, laboratory experiments and stability analyses (Jirka, 2001). This paper will mainly focus on stability analyses, more specifically linear stability analysis and nonmodal stability analysis. Many researchers have used linear stability analysis in open channel shallow flows over many decades with reasonable success in quantifying the necessary conditions for the generation of instabilities in a parameter space (Chu et al., 1991; van Prooijen and Uijttewaal, 2002; Chen and Jirka, 1998; Kolyshkin and Ghidaoui, 2003; Ghidaoui and Kolyshkin, 1999; Chen and Jirka, 1997). In conducting linear stability analysis, a steady state base flow is assumed in the open channel and infinitesimally small wave-like perturbations are added to the flow. The main outcome of this analysis is to evaluate if these perturbations will grow in time and generate flow structures, or rapidly decay, having no effect on the flow. The present paper will build on the works of Chu et al. (1991), which describes the effect of bed friction, bottom topography and streamwise base flow velocity profile in the generation of transverse shear instabilities.

Many researchers have used linear stability analysis in a variety of fluid mechanics problems, but the results are not in agreement with experimental studies in shear driven flows (Trefethen et al., 1993; Schmid, 2007). These discrepancies have been attributed to the linearization itself but Trefethen et al. (1993) argues that the problem may come from the nonnormality of the linear operator that shear driven flows produce. Nonmodal stability analysis is a relatively newer method in the field of hydrodynamic instabilities which looks at the energy growth in the perturbation (Schmid, 2007). It is shown that linear stability can only show asymptotic stability, but significant energy growth can occur at finite times (Schmid, 2007).

In this present study, a linear stability analysis was conducted on a shallow water open channel using a baseflow velocity profile, corresponding to a shallow mixing layer, commonly used (Chu et al., 1991; Ghidaoui and Kolyshkin, 1999). A further investigation was done using nonmodal stability analysis to show the transient and asymptotic fates of the perturbations. Some studies using nonmodal stability analysis has been published in studying sedimentary bed forms (Vesipa et al., 2012; Camporeale and Ridolfi, 2011; 2009), but it has not been applied to lateral motion in open channels, to the best of the authors' knowledge.

In the next section, the problem is formulated and the mathematical derivation of the linear stability and nonmodal stability analyses is presented. Section 3, then presents the results of linear stability analysis and compares it to Chu et al. (1991) for verification of the model. Section 4 presents the nonmodal analysis of the selected asymptotically stable cases. Section 5 generalizes the stability behavior of the system into asymptotically stable regions and contours of finite time instability, followed by a conclusion in section 6.

 

## 2 PROBLEM FORMULATION

The equations governing the current problem are the Saint Venant's equations describing shallow water and can be written as follows:

$$\frac{\partial \tilde{u}h}{\partial x}+\frac{\partial \tilde{v}h}{\partial y}=0 \tag{1}$$

$$\frac{\partial \tilde{u}}{\partial t}+\tilde{u}\frac{\partial \tilde{u}}{\partial x}+\tilde{v}\frac{\partial \tilde{u}}{\partial y}=-\frac{\partial \tilde{p}}{\partial x}-\frac{c_f}{h}\tilde{u}\sqrt{\tilde{u}^2+\tilde{v}^2} \tag{2}$$

$$\frac{\partial \tilde{v}}{\partial t}+\tilde{u}\frac{\partial \tilde{v}}{\partial x}+\tilde{v}\frac{\partial \tilde{v}}{\partial y}=-\frac{\partial \tilde{p}}{\partial y}-\frac{c_f}{h}\tilde{v}\sqrt{\tilde{u}^2+\tilde{v}^2} \tag{3}$$

Equation 1 is the continuity equation while 2 and 3 are the momentum equation in the streamwise and cross-stream directions, $x$ and $y$, respectively. The variables $\tilde{u}$ and $\tilde{v}$ represents the $x$ and $y$ velocities. The pressure is given by $\tilde{p}$ , the water depth by $h$ and the time by $t$. The bottom friction coefficient $c_f$ represents the Chezy coefficient. The variables are dimensionless and the details for the nondimensionalization can be found in Chu et al. (1991).

### 2.1 Linear Stability

In order to conduct linear stability analysis, the flow variables are decomposed into mean variables and infinitesimally small perturbations. The problem considered here is a channel with a streamwise steady state unidirectional mean flow, and so the cross-stream velocity does not have a mean component. The decomposition is given as below:

$$\tilde{u}=U+u' \tag{4}$$

$$\tilde{v}=v' \tag{5}$$

$$\tilde{p}=P+p' \tag{6}$$

The mean variables U and P describe the base flow velocity profile and the mean pressure respectively. The prime variables $u', v'$ and $p'$ are the small perturbations. The decomposed variables (Eq 4,5 and 6) are substituted into the system in (Eq 1,2, and 3) and the second order perturbation terms are considered to be negligible. The pressure gradient is taken as $\frac{\partial P}{\partial x}=\frac{c_f U^2}{h}=\mathrm{G}$ because the flow is parallel. The resulting system describes the dynamics of the perturbations.

$$\frac{\partial u'h}{\partial x}+\frac{\partial v'h}{\partial y}=0 \tag{7}$$

$$\frac{\partial u'}{\partial t}+U\frac{\partial u'}{\partial x}+v'\frac{\partial U}{\partial y}=-\frac{\partial p'}{\partial x}-\frac{c_f U}{h}u' \tag{8}$$

$$\frac{\partial v'}{\partial t}+U\frac{\partial v'}{\partial x}=-\frac{\partial p'}{\partial y}-\frac{c_f U}{2h}v' \tag{9}$$

Further mathematical manipulation is done to derive the modified version of the Orr-Sommerfeld equation (Dewals et al., 2008). The derivative with respect to y was taken for Eq 8 and that with respect to $x$ was taken for Eq 9 and the difference of these equations results in the elimination of the pressure terms. Eq 7 was used to write the final equation in terms of only $v'$. A normal mode solution $v'=\hat{v}\exp[k(x-ct)]$ is assumed for the perturbation, where $k$ is the wavenumber and $c=c_r+ic_i$ is a complex number whose real component $c_r$ is the wavespeed and the imaginary part $c_i$ is the growth rate of the perturbation when multiplied by $k$. The resulting system given below:

$$ikv_{yy}c-ikUv_{yy}+ikvU_{yy}-ik^3vc+ik^3Uv-U\frac{(c_f)_y v_y}{h}-\frac{c_f U_y v_y}{h}-\frac{c_f U v_{yy}}{h}+\frac{c_f U k^2 v}{2h} \tag{10}$$

The hat notation has been dropped for simplicity and the subscript $y$ indicates the derivative with respect to $y$. Eq 10 can be rewritten as a generalized eigenvalue problem of the form $\boldsymbol{Av}=c\boldsymbol{Bv}$, where $\boldsymbol{A},\boldsymbol{B}$ are the matrix operators. The parameter $kc_i$ is the growth rate of the perturbation, meaning that a positive value indicates the exponential growth of the perturbation, leading to the generation of instabilities.

 

The base flow velocity presented in this paper is the hyperbolic tangent profile, commonly used to approximate shallow mixing layers, given as:

$$U(y) = U_a + \frac{1}{2}(1 + \tanh(y)) \tag{11}$$

The base flow velocity $U$ is a function of the cross-stream distance $y$ and the ambient velocity parameter $U_a$. The presence of an inflection point is a necessary condition for instability (Ghidaoui and Kolyshkin, 1999). Fig. 1 shows the hyperbolic tangent velocity profile.

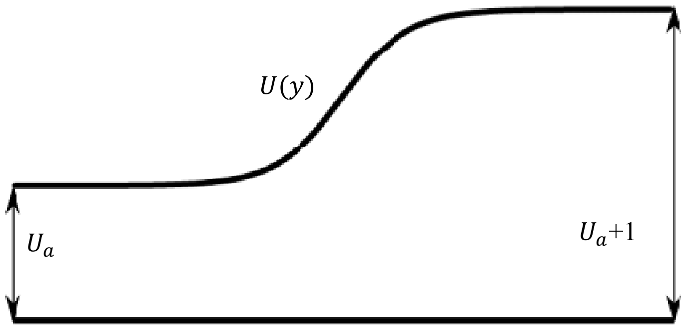


**Figure 1.** Hyperbolic tangent velocity profile

2.2 Nonmodal Stability

Despite the advancements in the field of hydrodynamic stability, there are still some issues that exist in linear stability analysis. One example is the disagreement of the transition Reynold's number between linear stability analysis and experimental studies. The discrepancies between the results of linear stability and laboratory experiments are very common in shear driven flows. This reason for this problem is traditionally attributed to the linear assumption itself and those nonlinear terms should be assessed. However, Trefethen et al. (1993) stated that the problem is due to the nonnormality of the matrix operator and that linear stability only predicts asymptotic stability. Shear driven flows result in non-normal matrix operators and therefore, the results of linear stability may not give a complete picture of the stability behaviour. Nonmodal stability analysis uses parameters such as pseudospectra, numerical abscissa and growth functions to evaluate the evolution of energy in the perturbations in time.

- Pseudospectra

Similar to the spectra or the set of eigenvalues of linear operator used in linear stability analysis, psedospectra or pseudoeigenvalues are used in nonmodal stability analysis. Pseudospectra is a concept introduced by Trefethen et al. (1993) and due to the highly mathematical nature and the many definitions that exist, only one will be presented here for simplicity. The pseudospectra of a matrix A, denoted by $\sigma_\varepsilon(A)$, is defined as the set of eigenvalues obtained by perturbing the matrix $\boldsymbol{A}$ with a matrix $\boldsymbol{E}$ whose norm is $\varepsilon$.

$\sigma_\varepsilon$ is a set of $\lambda \epsilon \mathbb{C}$ such that, $\lambda \in \sigma(\boldsymbol{A} + \boldsymbol{E})$ for some $\boldsymbol{E} \in \mathbb{C}^{N \times N}$ with $||\boldsymbol{E}|| < \varepsilon$

Visually, pseudospectra are plotted as contour lines in conjunction with the spectra and can be seen as the extent of potential perturbation of the eigenvalues. The size of the pseudospectra corresponding to a particular order of perturbation reflects the sensitivity of the eigenvalues to the perturbation of that order.

- Transient growth

Another important concept in nonmodal analysis is the energy in the perturbation. Since linear stability analysis can only predict asymptotic stability, i.e. stability as $t \to \infty$, it is necessary to evaluate the evolution of perturbation energy in time since most relevant physical phenomena occurs in finite time.

$$G(t) = \max_{q_0} \frac{\|q(t)\|}{\|q_0\|} = \max_{q_0} \frac{\left\|e^{-iCt} q_0\right\|}{\|q_0\|} = \left\|e^{-iCt} q_0\right\| \tag{12}$$

The time scale and the extent of energy growth may be very important in the stability behavior as significant energy amplification may happen in finite time.

- `Measure of nonnormality

Nonnormality of the matrix operator, whose eigenvectors are not orthogonal to each other, results in transient energy growth and is a attributed to the reason why discrepancies exist in the analysis of shear flows (Trefethen et al., 1993; Schmid, 2007). The measure of nonnormality is a complex mathematical issue and a topic beyond the scope of this paper. However, Trefethen & Embree, (2005) suggested the use of the condition number to get an idea of the nonnormality of the operator and many other literature that used this concept also exits.. The condition number is defined as:

$$\kappa = \|\boldsymbol{V}\|\|\boldsymbol{V}^{-1}\| = \frac{s_{max}}{s_{min}} \tag{13}$$

where $\boldsymbol{V}$ is a matrix whose column vectors are the eigenvectors of eigenvalue problem of interest and $s_{max}$ and $s_{min}$ are the maximum and minimum singular values of $\boldsymbol{V}$ respectively.

## 3 VERIFICATION OF MODELS

The linear stability analysis done in this study, which is the basis of nonmodal stability analysis that will follow, is verified by comparing to the results presented in Chu et al., (1991). The normalized growth rate is calculated as $\frac{(kc_i)_{max}}{U_y}$ and the bed friction number at the inflection point is $S = c_f U/2hU_y$. The maximum growth rate values decreased as bed friction number values increased until all growth rates across all wavenumbers are negative, which are in reasonable agreement with Chu et al., (1991) with a few differences resulting from the different solution methods.

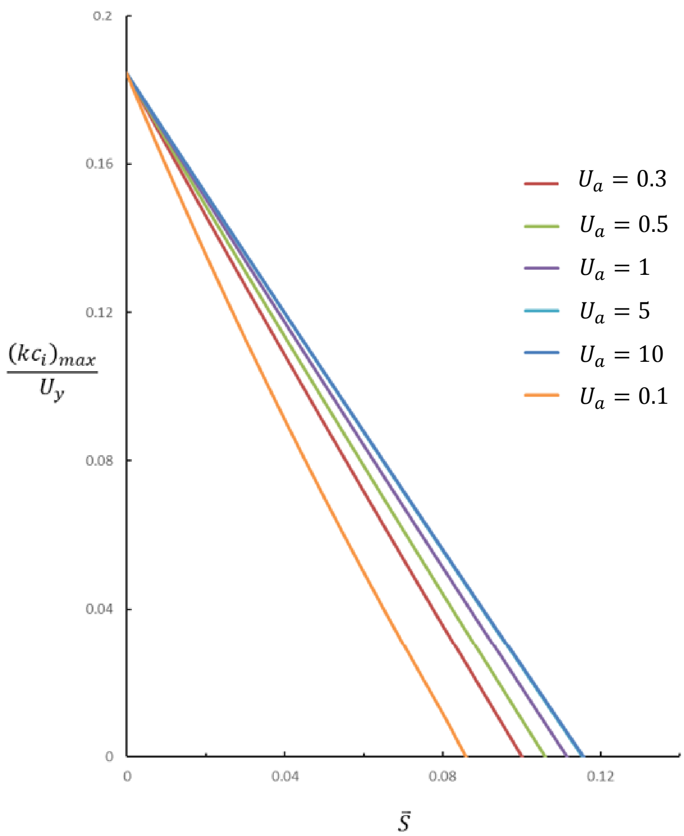


**Figure 2.** Growth rate vs Bed Friction Number

The plots of bed friction number vs growth rate shown in Fig. 2 is very similar to the one presented in Chu et al. (1991) with the cases with higher ambient velocities in the current study having smaller critical values.

## 4 ASYMPTOTICALLY STABLE CASES

The critical cases obtained from linear stability analysis presented in Chu et al., (1991) are referred to as asymptotically stable cases in current paper and the three higher ambient velocity cases $U_a = 1{,}5{,}10$ are further analyzed.

 

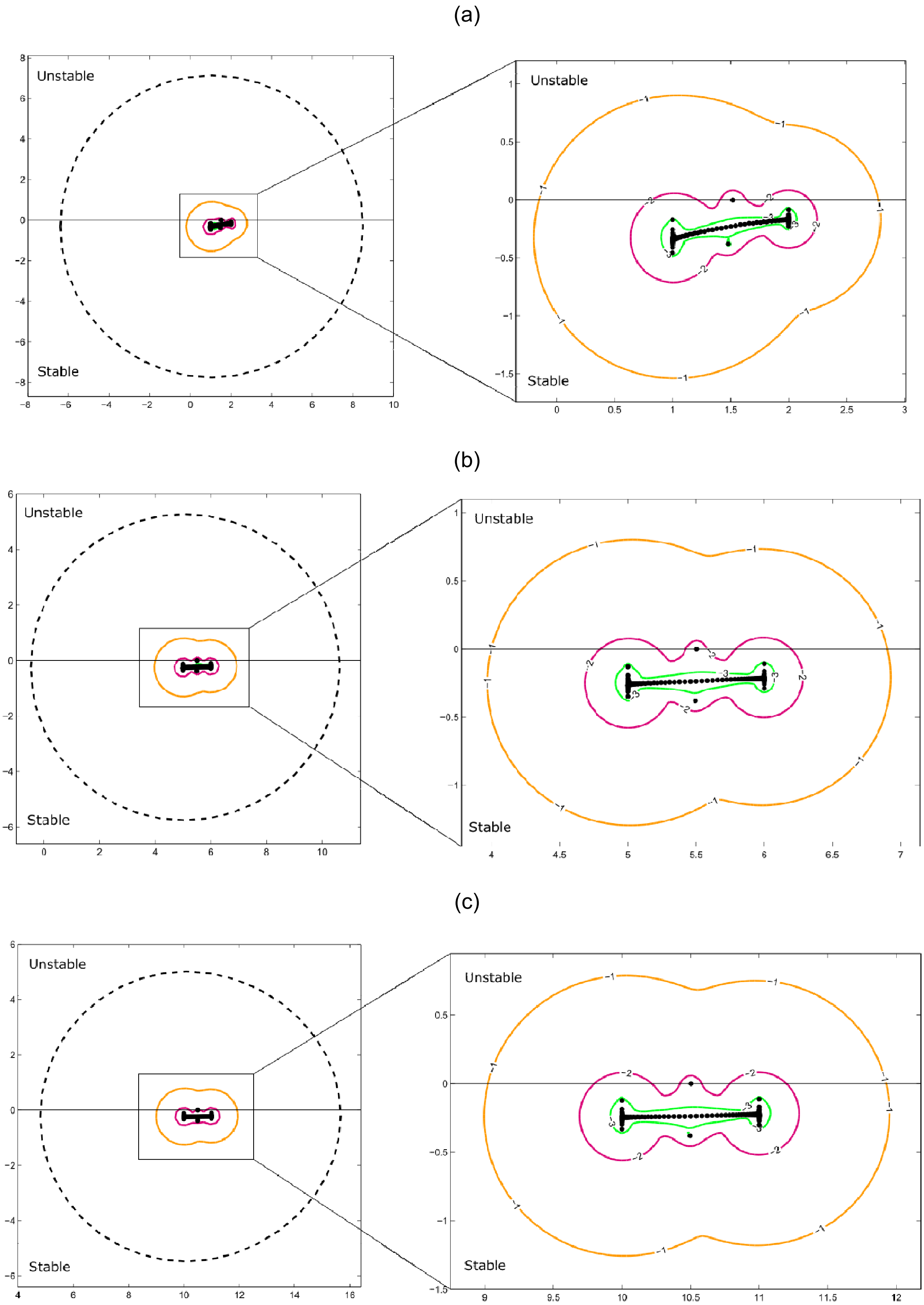


**Figure 1.** Spectral and pseudospectral portraits of hyperbolic tangent velocity profile. Subplots (a) correspond to the cases of $\boldsymbol{U_a = 1}$; (b) to $\boldsymbol{U_a = 5}$; and (c) to $\boldsymbol{U_a = 10}$

Fig. 3 shows the spectral portraits of the system when the base velocity profile is hyperbolic tangent profile and the depth is constant for three ambient velocities $U_a = 1{,}5{,}10$. The left plot in each subfigure shows the numerical range of the linear operator, which is significantly larger and protrudes into the unstable region. The numerical abscissa, which is the maximum value of the numerical range extending into the unstable region, is proportional to the slope of perturbation energy growth and so higher values means that the initial energy growth will be high. The right plot in each subfigure shows a close-up view of the pseudospectra for

$\varepsilon = 10^{-1}, 10^{-2}, 10^{-3}$ shown on the log scale. It is shown that for perturbations of the order $\varepsilon = 10^{-1}$ and , $10^{-2}$ may make the eigenvalues shift into the unstable regions.

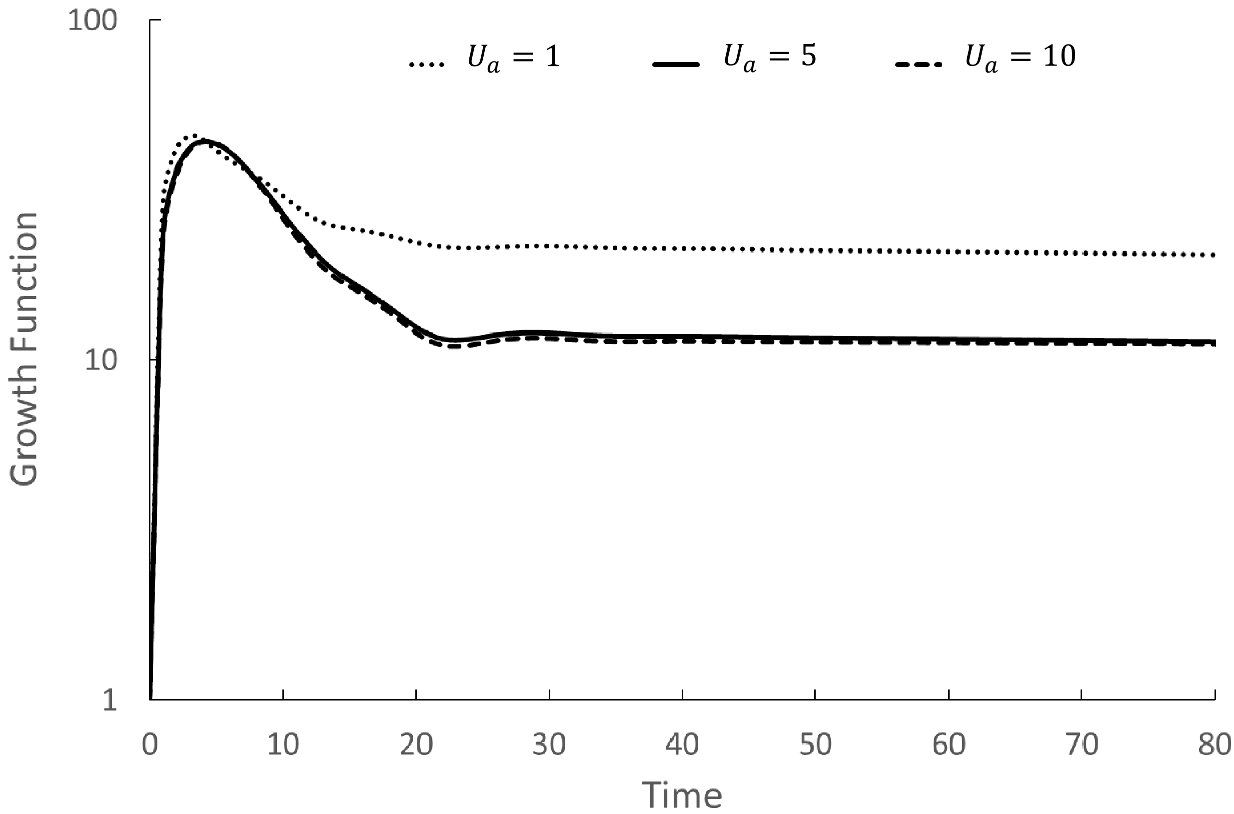


**Figure 2.** Transient energy plot showing the presence of initial energy growth

The energy contained in the perturbation and its temporal progression is calculated using the growth function mentioned in Section 2.2 and plotted in Fig. 4. As expected, initial energy growth can be observed in in all three ambient velocity cases. In all cases, the energy growth is significantly high and the dissipation is gradual. The dissipation of perturbation energy is more gradual in the cases of $U_a = 1$ and faster in $U_a = 5$ and $10$ with little difference between the latter two. It is clearly shown that these cases are indeed may be unstable with high energy growths.

## 5 STABILITY REGIONS

Traditionally, stability regions are plots showing the critical values of growth rate and the corresponding wavenumbers obtained from linear stability analysis. In Schmid, (2007), plots of stability region obtained from linear stability and nonmodal stability analyses are superimposed. Nonmodal stability regions display the critical values numerical abscissa values. However, in this study, we have superimposed the contours of numerical abscissa values on the traditional stability regions, since the critical values do not exist within the range of interest in the $S$- $k$ space.

 

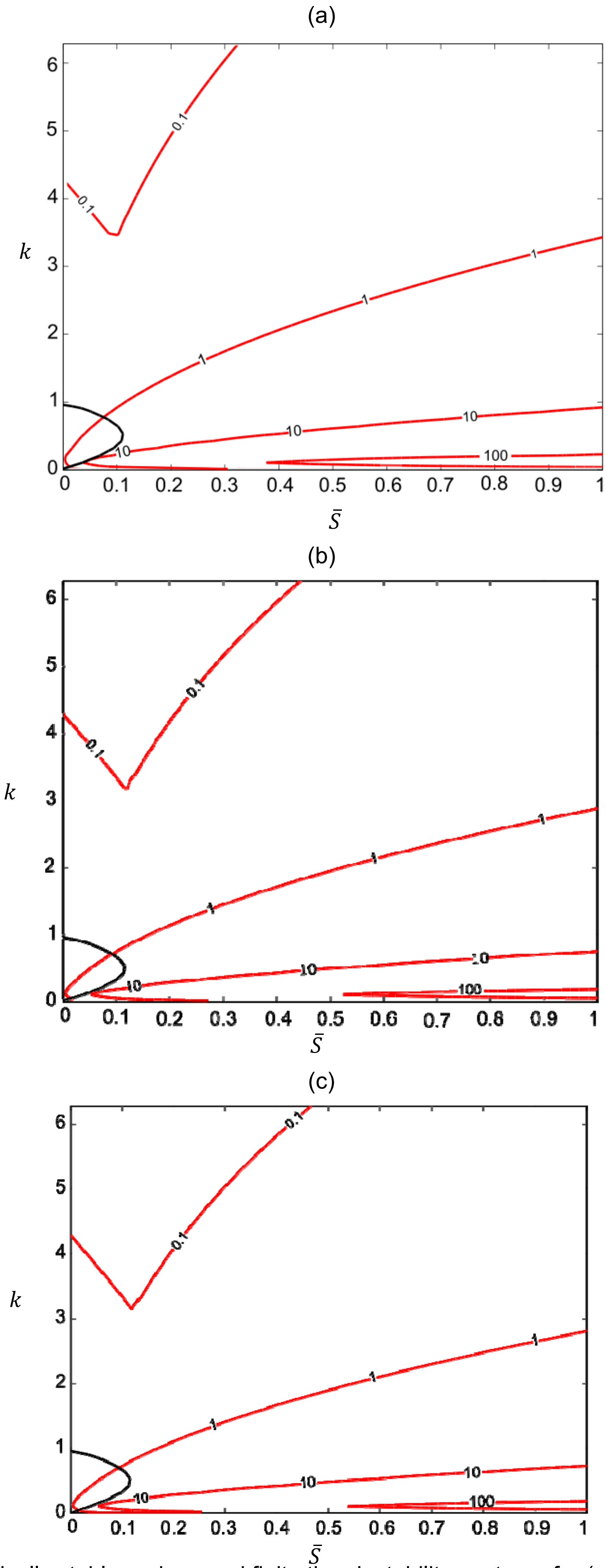


**Figure 3.** Asymptotically stable regions and finite time instability contours for (a) $\boldsymbol{U}_{\mathbf{a}} = \mathbf{1}$,(b) $\boldsymbol{U}_{\mathbf{a}} = \mathbf{5}$, (c) $\boldsymbol{U}_{\mathbf{a}} = \mathbf{10}$

Fig. 5 shows the traditional stability regions in black and the contour lines of the numerical abscissa values on the log scale in red. The linearly stable regions are hyperbolic and are in agreement with Chu et al. (1991). All three cases showed that in the space shown here, initial energy growth can be expected for all sets of $S$ and $k$. The contour lines are almost identical to each other suggesting that the highest energy growth happens at higher friction number and lower wavenumbers.

## 6 CONCLUSIONS

The development of transverse shear instabilities is studied using linear stability and nonmodal stability analysis. The results of linear stability have been shown to differ from experimental studies in shear driven flows. Using nonmodal stability, the sensitivity of the system to perturbations is evaluated in terms of energy and its growth in finite time. Pseusdospectral plots of the linearly stable or asymptotically stable cases presented in Chu et al. (1991) show that transient energy growth can be expected. The growth function is used to plot the evolution of perturbation energy and for the presented cases, significant energy growth is observed. Generalizing the results into stability regions in the $S$-$k$ space, it is shown that transient energy growth can be expected in a much larger area. In fact, in the range of $S$-$k$ presented in this paper, energy growth can be expected everywhere. Higher energy growth may occur at higher $S$ and lower $k$.

## REFERENCES

Camporeale, C. & Ridolfi, L., (2011). Modal Versus Nonmodal Linear Stability Analysis of River Dunes. *Physics of Fluids*, 23(10).

Camporeale, C. & Ridolfi, L., (2009). Nonnormality and Transient Behavior of The De Saint-Venant-Exner Equations. *Water Resources Research*, 45(8), 1–12.

Chen, D. & Jirka, G.H., (1997). Absolute and Convective Instabilities of Plane Turbulent Wakes in a Shallow Water Layer. *Journal of Fluid Mechanics*, 338, 157–172.

Chen, D. & Jirka, G.H., (1998). Linear Stability Analysis of Turbulent Mixing Layers and Jets in Shallow Water Layers. *Journal of Hydraulic Research*, 1686(July).

Chu, V.H. et al. (1991). Stability of Transverse Shear Flows in Shallow Open Channels. *Journal of Hydraulic Engineering*, 117(10), 1370–1388.

Dewals, B.J. et al. (2008). Experimental and Numerical Analysis of Flow Instabilities in Rectangular Shallow Basins. *Environmental Fluid Mechanics*, 8(1), 31–54.

Ghidaoui, M.S. & Kolyshkin, A.A., (1999). Linear Stability Analysis of Lateral Motions in Compound Open Chennels. *Journal of Hydraulic Engineering*, 125(August), 871–880.

Jirka, G.H., (2001). Large Scale Flow Structures and Mixing ProcessesiIn Shallow Flows. *Journal of Hydraulic Research*, 39(6), 567–573.

Kolyshkin, A.A. & Ghidaoui, M.S., (2003). Stability Analysis of Shallow Wake Flows. *Journal of Fluid Mechanics*, 494, 355–377.

van Prooijen, B.C. & Uijttewaal, W.S.J., (2002). A Linear Approach for The Evolution of Coherent Structures in Shallow Mixing Layers. *Physics of Fluids*, 14(12), 4105–4114.

Schmid, P.J., (2007). Nonmodal Stability Theory. *Annual Review of Fluid Mechanics*, 39(1), 129–162.

Trefethen, L. & Embree, M., (2005). *Spectra and Pseudospectra: The Behavior of Nonnormal Matrices and Operators.* Princeton University Press.

TREFETHEN, L., Trefethen, A., Reddy, S. & Driscoll, T. (1993). Hydrodynamic stability without eigenvalues. *Science*, 261(5121), 578-584.

Vesipa, R., Camporeale, C. & Ridolfi, L. (2013). Transient Growths of Stable Modes in Riverbed Dynamics. *EPL (Europhysics Letters)*, 100(6), 64002.

 

# THE ANALOGIES BETWEEN PARTIAL DIFFERENTIAL EQUATIONS (PDE), CELLULAR AUTOMATA (CA) AND UNSTRUCTURED CELLULAR AUTOMATA (UCA)

YU-QING LIN [1], QIU-WEN CHEN [2], ARTHUR MYNETT [3], CHENG CHEN [4], LEI TANG [5] & GANG LI [6]

[1,2,4,5] Center for Eco-Environment Research, Nanjing Hydraulic Research Institute, China,
yqlin@nhri.cn
[3] Unesco-IHE Institute for Water Education, Delft, Netherlands
[6] Center of Water Resources Information, Bureau of Hydrology, Ministry of Water Resources, China

## ABSTRACT

Cellular Automata (CA) is a non-linear dynamical system which discrete in time and space. Cellular automata constitute many simple components, each of them starts from an initial state and all the cells update their states synchronously every discrete step according to the simple local rule. Compared to partial differential equations (PDE), Cellular automata are rule-based methods with the advantages of homogeneity, local interactions, discrete states and parallelism, so that they are often considered as an alternative approach in modelling nonlinear systems with large degrees of freedom. Moreover, Unstructured cellular automaton (UCA) has been proposed based on the unstructured meshes with advantages which are missing in CA. UCA allows varying sizes of elements, permits accurate representation of boundaries and it avoids mapping results from unstructured grid into structured grid during cellular automata process. Compared with classical CA, UCA contains unequal cells, the object cell and its neighbors differ from each other. The aim of this article is to show the analogies between discrete solutions of PDEs and equivalent approaches derived from CA and UCA. Finite difference methods have been used to deduce transition rules for CA-modelling from PDE-based approaches. Specific types of partial differential equations (diffusion equation, wave equation) have been reviewed as a reference for evaluating the equivalent performance of CA simulations. Since UCA can have varying neighborhood properties in contrast with classical CA, Finite Volume Method has been used to deduce transition rules for UCA-modelling and the influence of cell size in UCA has been analyzed in this paper. A characteristic parameter —min distance of UCA– has been put forward and tested by several numerical experiments on different types of meshes (rough meshes, locally refined meshes, globally refined meshes) in order to demonstrate the usefulness of this parameter.

**Keywords:** Unstructured cellular automata; partial differential equations; characteristic parameter; analogies.

## 1 INTRODUCTION

Wolfram (Wolfram, 1985) showed that Cellular Automata and differential equations are related in the case of continuum models for physical, chemical and biological processes (Hu, 2003). Differential equations based models have advantages of high accuracy and conservation laws. But mathematical analyses are sometimes very difficult, and analytical solutions do not always exist. There are several popular numerical algorithms for partial differential equations. This ncludes Finite Difference methods which work very well for many problems but have some disadvantages in dealing with irregular geometries. There are also Finite Volume and Finite Element methods which can deal with irregular geometries, and Partial differential equations are only suitable for systems with only a small degree of freedom. By contrast, Cellular Automata are often considered as an alternative mathematical approach in modelling nonlinear systems with large degrees of freedom. (Ganguly, 2003; Chen, 2004).

CA uses vast numbers of cells or nodes that can take a number of states which always cause a mass of computational loads, and sometimes CA-based modelling is not as accurate and conservative as PDE models. However, Cellular Automata has the advantage in that they can represent discrete entities directly (Bennett,1985), and CA can reproduce the emergent properties of behaviors (Fathy, 2013). Furthermore, CA has universal computability and the nature of parallel implementation (Chen, 2008); it is powerful and is gradually becoming an essential part of numerical computation.

Cellular Automata are sometimes considered as an alternative approach in numerical modelling. There are many references to, for example, cellular automata being used to solve the Navier-Stokes equation by Lattice-gas CA (Rorhman, 1997). However, Lattice-gas CA holds a microscopic view and is thus restricted to very small scales. For real applications, Lattice-gas CA is less practical for solving the full Navier-Stokes equations (Chen, 2004). In this research, special attention was paid to exploring the differences and analogies between CA and PDEs.

## 2 GENERAL COMPARISON OF CA AND PDE

Partial Differential Equations (PDEs) have a history of several centuries. Famous scientists like Euler, Lagrange, Laplace, Poisson and so on, made many outstanding contributions. PDEs are the language of modern science used in many important fields of applied science.

Typical features of PDEs are that they represent a space-time continuum based modelling:

**Table 1.** Differences between CA based modelling and PDE based modelling

| | **PDE model** | **CA model** |
|---|---|---|
| Degree of freedom | Small | Big |
| Variable State | Continuum | Discrete |
| Variable Value | Spatial Mean value | Individual (could be) |
| Emergent properties | No | Yes (could be) |
| Self-reproducing | No | Yes |
| Accurate / Conservative | Yes | No (could be) |
| Parallel implementation | No | Yes |

The advantage of partial differential equations is that they can have accurate quantitative solutions, often in closed analytical form in case of simplified geometries. But modern digital computing is based on discrete representations of space-time co-ordinates leading to discrete solutions of PDEs, in close resemblance to CA. Still, CA models are different since (i) in CA the state variables are also discrete, providing the possibility to represent individuals rather than a continuum, and are therefore very well suited for population dynamics simulation; (ii) CA has very simple transition rules but can lead to rather complex behaviour patterns in both time and space (Guinot, 2002).

Furthermore, cellular automata modelling has the advantage of being easily understood, and being highly suitable for parallel computing, allowing the perspective of the model to multiple local views.

However, continuum-based partial differential equations can easily be used to describe conservation principles in science and engineering and even in biological and ecological modelling (Bartlett & Hiorns, 1973). Recently, there has been research done on using cellular automata as an alternative to (partial) differential equations. But when using a CA approach, one must face the problem of deducing the transition rules from continuum-based models (Guinot, 2002). The emphasis of the next section is on discussing the relationships between partial differential equations and cellular automata, and how to get the transform rules for cellular automata modelling from the physical concepts underlying partial differential equation models.

## 3 ANALOGIES BETWEEN PDES DISCRETE SOLUTIONS AND EQUIVALENT CA APPROACHES

We first choose the 1D diffusion equation for demonstration purposes:

$$\frac{\partial C}{\partial t} = D\frac{\partial^2 C}{\partial x^2} \qquad [1]$$

where, $D$ is the diffusion coefficient; $C$ is the substance concentration.

The Finite Difference method (FDM) of discretizing a differential equation on a regular grid with the evolution of states at discrete time steps has similarities with a classical cellular automata approach on the evolution of state variables with a finite number of values on a regular grid at discrete time steps (Chopard, 1991; Chopard, 1998). If the number of states of a cellular automaton is comparable to that of the related finite difference equation, then it can be expected that the results should also be comparable. Using a Forward-Time Central-Space (FTCS) scheme to discrete the 1D diffusion equation, we get:

$$C_i^{t+1} = C_i^t + D\frac{\Delta t}{\Delta x^2}(C_{i+1}^t - 2C_i^t + C_{i-1}^t) \qquad [2]$$

If the exact solution $C_i$ satisfies the equation, then the error value $\varepsilon_i^t$ should also meet the discretion equation:

$$\varepsilon_i^{t+1} = \varepsilon_i^t + D\frac{\Delta t}{\Delta x^2}(\varepsilon_{i+1}^t - 2\varepsilon_i^t + \varepsilon_{i-1}^t) \qquad [3]$$

Expressing

$$\varepsilon(\mathrm{x}) = \sum_{m=1}^{M} A_m \mathrm{e}^{\mathrm{i}k_m \mathrm{x}} \qquad [4]$$

where, $k_m = \frac{\pi m}{L}$ ; $m=1,2,\ldots.M$ ; $M = \frac{L}{\Delta x}$

and the amplitude $A_m$ as a function of time t,

$$\varepsilon(\mathrm{x},\mathrm{t}) = \sum_{m=1}^{M} e^{at} \mathrm{e}^{\mathrm{i}k_m \mathrm{x}} \quad [5]$$

in which the coefficient a is constant, viz.

$$\varepsilon_m(\mathrm{x},\mathrm{t}) = e^{at} e^{iK_m X} \quad [6]$$

Then

$$\varepsilon_m(\mathrm{x},\mathrm{t}) = e^{at} e^{iK_m X} \quad [7]$$

$$\varepsilon_i^{t+1} = e^{a(\mathrm{t}+\Delta \mathrm{t})} e^{iK_m X} \quad [8]$$

$$\varepsilon_{i+1}^{t} = e^{at} \mathrm{e}^{\mathrm{i}k_m(\mathrm{x}+\Delta \mathrm{x})} \quad [9]$$

$$\varepsilon_{i-1}^{t} = e^{at} \mathrm{e}^{\mathrm{i}k_m(\mathrm{x}-\Delta \mathrm{x})} \quad [10]$$

which leads to

$$\varepsilon_i^{t+1} = \varepsilon_i^t + D\frac{\Delta t}{\Delta x^2}(\varepsilon_{i+1}^t - 2\varepsilon_i^t + \varepsilon_{i-1}^t) \quad [11]$$

so that

$$e^{a\Delta t} = 1 + D\frac{\Delta t}{\Delta x^2}(e^{iK_m \Delta X} + e^{-iK_m \Delta X} - 2) \quad [12]$$

since

$$\cos(k_m \Delta x) = \frac{e^{iK_m \Delta X} + e^{-iK_m \Delta X}}{2} \quad [13]$$

$$\sin^2 \frac{k_m \Delta \mathrm{x}}{2} = \frac{1-\cos\left(k_m \Delta x\right)}{2} \quad [14]$$

we obtain

$$\mathrm{e}^{\mathrm{a}\Delta \mathrm{t}} = 1 - 4D\frac{\Delta \mathrm{t}}{\Delta \mathrm{x}^2}\sin^2\left(\mathrm{k_m}\Delta \mathrm{x}/2\right) \quad [15]$$

defining

$$G = \frac{\varepsilon_\mathrm{i}^{\mathrm{t}+1}}{\varepsilon_\mathrm{i}^{\mathrm{t}}} \quad [16]$$

taking into account the stability criterion

$$|G| \le 1 \quad [17]$$

 

with

$$G = \frac{e^{a(t+\Delta t)} e^{ik_m x}}{e^{at} e^{ik_m x}} = e^{a\Delta t} \qquad [18]$$

and

$$G = 1 - 4D\frac{\Delta t}{\Delta x^2}\sin^2\left(k_m \Delta x / 2\right) \qquad [19]$$

$$\left|1 - 4D\frac{\Delta t}{\Delta x^2}\sin^2\left(k_m \Delta x / 2\right)\right| \le 1 \qquad [20]$$

so

$$0 \le D\frac{\Delta t}{\Delta x^2} \le \frac{1}{2} \qquad [21]$$

if

$$D\frac{\Delta t}{\Delta x^2} = \frac{1}{2} \qquad [21]$$

$$C_i^{t+1} = \frac{1}{2}(C_{i+1}^t + C_{i-1}^t) \qquad [22]$$

This computational stencil is similar to a structured cellular automaton in one dimension with two-neighbouring cells having equal weight. The truncation error can be analysed from the discrete steps of the partial differential equations as follows:

$$C_{i+1}^t = C_i^t + \left(\frac{\partial C}{\partial x}\right)_i^t \Delta x + \frac{1}{2}\left(\frac{\partial^2 C}{\partial x^2}\right)_i^t \Delta x^2 + \frac{1}{3!}\left(\frac{\partial^3 C}{\partial x^3}\right)_i^t \Delta x^3 + \ldots \qquad [23]$$

$$C_{i-1}^t = C_i^t - \left(\frac{\partial C}{\partial x}\right)_i^t \Delta x + \frac{1}{2}\left(\frac{\partial^2 C}{\partial x^2}\right)_i^t \Delta x^2 - \frac{1}{3!}\left(\frac{\partial^3 C}{\partial x^3}\right)_i^t \Delta x^3 + \ldots \qquad [24]$$

$$C_i^{t+1} = C_i^t + \left(\frac{\partial C}{\partial t}\right)_i^t \Delta t + \frac{1}{2}\left(\frac{\partial^2 C}{\partial t^2}\right)_i^t \Delta t^2 + \frac{1}{3!}\left(\frac{\partial^3 C}{\partial t^3}\right)_i^t \Delta t^3 + \ldots \qquad [25]$$

$$C_i^{t+1} - C_i^t = \left(\frac{\partial C}{\partial t}\right)_i^t \Delta t + \frac{1}{2}\left(\frac{\partial^2 C}{\partial t^2}\right)_i^t \Delta t^2 + \frac{1}{3!}\left(\frac{\partial^3 C}{\partial t^3}\right)_i^t \Delta t^3 + \ldots \qquad [26]$$

$$\frac{C_i^{t+1} - C_i^t}{\Delta t} = \left(\frac{\partial C}{\partial t}\right)_i^t + \frac{1}{2}\left(\frac{\partial^2 C}{\partial t^2}\right)_i^t \Delta t^1 + \frac{1}{3!}\left(\frac{\partial^3 C}{\partial t^3}\right)_i^t \Delta t^2 + \ldots \qquad [27]$$

$$\left(\frac{\partial C}{\partial t}\right)_i^t = \frac{C_i^{t+1} - C_i^t}{\Delta t} - \left(\frac{\partial^2 C}{\partial t^2}\right)_i^t \frac{\Delta t}{2} + \ldots \qquad [28]$$

$$C_{i+1}^t + C_{i-1}^t = 2C_i^t + \left(\frac{\partial^2 C}{\partial x^2}\right)_i^t \Delta x^2 + \left(\frac{\partial^4 C}{\partial t^4}\right)_i^t \frac{\Delta x^4}{12} \ldots \qquad [29]$$

$$\left(\frac{\partial^2 C}{\partial x^2}\right)_i^t = \frac{C_{i+1}^t - 2C_i^t + C_{i-1}^t}{\Delta x^2} - \left(\frac{\partial^4 C}{\partial t^4}\right)_i^t \frac{\Delta x^2}{12} + \ldots \qquad [30]$$

 

$$\frac{\partial C}{\partial t}-D\frac{\partial^2 C}{\partial x^2}=0=\frac{C_{\mathrm{i}}^{\mathrm{t+1}}-C_{\mathrm{i}}^{\mathrm{t}}}{\Delta \mathrm{t}}-D\frac{C_{\mathrm{i+1}}^{\mathrm{t}}-2C_{\mathrm{i}}^{\mathrm{t}}+C_{\mathrm{i-1}}^{\mathrm{t}}}{\Delta \mathrm{x}^2}+\left[-\left(\frac{\partial^2 C}{\partial \mathrm{t}^2}\right)_{\mathrm{i}}^{\mathrm{t}}\frac{\Delta \mathrm{t}}{2}+D\left(\frac{\partial^4 C}{\partial x^4}\right)_{\mathrm{i}}^{\mathrm{t}}\frac{\Delta \mathrm{x}^2}{12}+..\right. \quad [31]$$

If we write the discrete diffusion equation as

$$\frac{C_{\mathrm{i}}^{\mathrm{t+1}}-C_{\mathrm{i}}^{\mathrm{t}}}{\Delta \mathrm{t}}=D\frac{C_{\mathrm{i+1}}^{\mathrm{t}}-2C_{\mathrm{i}}^{\mathrm{t}}+C_{\mathrm{i-1}}^{\mathrm{t}}}{\Delta \mathrm{x}^2} \quad [32]$$

then the truncation error is

$$\frac{C_{\mathrm{i}}^{\mathrm{t+1}}-C_{\mathrm{i}}^{\mathrm{t}}}{\Delta \mathrm{t}}=D\frac{C_{\mathrm{i+1}}^{\mathrm{t}}-2C_{\mathrm{i}}^{\mathrm{t}}+C_{\mathrm{i-1}}^{\mathrm{t}}}{\Delta \mathrm{x}^2} \quad [33]$$

which is $\mathrm{O}\left[\Delta \mathrm{t},(\Delta \mathrm{x})^2\right]$.

The cellular automata system is by nature a discrete system, so there is no discretization error. But, one should realize that the truncation error should always accounted for if we use CA to simulate a partial equation, because the CA rules were deduced from the discrete equation.

## 4 ANALOGIES BETWEEN PDES DISCRETE SOLUTIONS AND EQUIVALENT UCA APPROACHES

### 4.1 UCA and Finite volume methods (FVM) for 2D diffusion equation

For the 2D diffusion equation:

$$\frac{\partial C}{\partial t}=\mathrm{D}\ \left(\frac{\partial^2 C}{\partial x^2}+\frac{\partial^2 C}{\partial y^2}\right) \quad [34]$$

the discretization based on the triangular mesh using the FVM method becomes

$$\frac{C_i^{t+1}-C_i^t}{\Delta t}V_i=\sum F_{ij}=\sum_{j=1}^{3}\frac{L_{ij}}{d_{ij}}D_{ij}(\mathrm{C}_j^t-\mathrm{C}_i^t) \quad [35]$$

$$\frac{V_i}{\Delta t}C_i^{t+1}=\left(\frac{V_i}{\Delta t}-\sum_{j=1}^{3}\frac{L_{ij}}{d_{ij}}D_{ij}\right)C_i^t+\sum_{j=1}^{3}\frac{L_{ij}}{d_{ij}}D_{ij}C_j^t \quad [36]$$

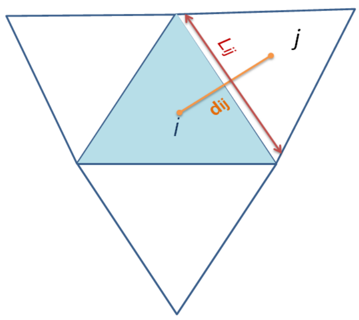


**Figure** 1. The discretization scheme ba on the triangular mesh using the method

Where: $C_i^t$ ---the concentration of element *i* at time step *t*; $F_{ij}$ ---the normal flux of diffusion; $V_i$ --- the area of the triangular elements *I*; $L_{ij}$--- the edge length of edge *ij*; $d_{ij}$--- the normal projection of the distance between the centre of *i* and *j*; $D_{ij}$--- the diffusion coefficient between element *i* and *j*;

For stability reasons, it is required that

$$\sum_{j=1}^{3}\frac{L_{ij}}{d_{ij}}D_{ij}\le\frac{V_i}{\Delta t} \quad [37]$$

which implies that every element i and its neighbouring element j should satisfy the stable conditions:

$$\frac{L_{ij}}{d_{ij}}D_{ij}\le\frac{1}{3}\frac{V_i}{\Delta t} \quad [38]$$

 

$$\frac{L_{ij}}{d_{ij}} D_{ij} \frac{\Delta t}{V_i} \leq \frac{1}{3} \quad [39]$$

$$D_{ij} \frac{\Delta t}{d_{ij}} \frac{L_{ij}}{V_i} \leq \frac{1}{3} \quad [40]$$

$$\Delta t \leq \frac{1}{3} \frac{d_{ij}}{D_{ij}} \frac{V_i}{L_{ij}} \quad [41]$$

Because

$$V = \frac{1}{2} L h \quad [42]$$

In which *h* is the height of the triangular element.

Then we have

$$\Delta t \leq \frac{1}{6} \frac{h_{ij}}{D_{ij}} d_{ij} \quad [43]$$

If $h_{ij} \geq 2D_{ij}$
then we obtain

$$\Delta t \leq \frac{1}{3} d_{ij} \quad [44]$$

This result shows that $\Delta t$ is related to the value $d_{ij}$ which is the distance between neighbouring elements. Using the parameter $d_{min}$ which is the minimum value of the $d_{ij}$ among all the triangular elements, Equation could be simplified as:

$$\Delta t \leq \frac{1}{3} d_{\min} \quad [45]$$

Since there are no $\Delta t$ concepts in cellular automata schemes, for every execution step the CA rules were based only on cell neighbour radius. In the numerical experiments of this paper, the numerical value $\frac{1}{3} d_{min}$ was used instead of $\Delta t$ in order to satisfy the stability condition:

$$C_i^{t+1} = (1 - \frac{\Delta t}{V_i} \sum_{j=1}^{3} \frac{L_{ij}}{d_{ij}} D_{ij}) C_i^t + \frac{\Delta t}{V_i} \sum_{j=1}^{3} \frac{L_{ij}}{d_{ij}} D_{ij} C_j^t \quad [46]$$

$$C_i^{t+1} = C_i^t + \frac{\Delta t}{V_i} \sum_{j=1}^{3} \frac{L_{ij}}{d_{ij}} D_{ij} (C_j^t - C_i^t) \quad [47]$$

$$C_i^{t+1} = C_i^t + \frac{1}{3} \frac{d_{\min}}{V_i} \sum_{j=1}^{3} \frac{L_{ij}}{d_{ij}} D_{ij} (C_j^t - C_i^t) \quad [48]$$

4.2 Effects of cell size in Unstructured Cellular Automata (UCA)

In this research, we used UCA to simulate a diffusion equation (Ostrov,1996; Rucker, 2003). For a given cell i at some time t, our cell states typically a real-number value $C_i$, and our UCA update scheme typically has the form $C^{t+1}$=Update *($C^t$,).*

Ideally, any simulation result should be grid independent as the result should be stable even when calculated on different computational grids. But, CA modelling considers one cell as a participant element, and executes the same rules synchronously for every element. If we use small grids instead of large grids and run the same rules, the result shows different patterns since the smaller elements cause more executing steps among the calculating area. Especially for UCA modelling which is based on unstructured meshes, the size of every element is different. The size effect should be an important factor in the UCA rules.

To analyse the effects of variable meshes, the numerical experiments were carried out based on two groups of meshes. The first mesh set is the original mesh with local refinement; the second type of meshes is the rough mesh compared with the global refined meshes.

The evolution rule for UCA which is derived from diffusion equation based on the unstructured triangular meshes could be described as follow:

$$C_i^{t+1} = C_i^{t+1} + d_{min} \frac{1}{3V_i} \sum_{i=1}^{3} D_{ij} \left(C_j^t - C_i^t\right) \frac{L_{ij}}{d_{ij}} \qquad [49]$$

In order to eliminate the effects of cell size, the parameter $d_{min}$ was used in numerical experiments. Firstly, the distance $d_{ij}$ between every central element was calculated, and the parameter $d_{min}$ is the minimum value among those distances. The diffusion coefficient *D* in this equation will be set as a constant. The results of numerical experiments show that the minimum distance between the cells can serve as a characteristic parameter for unstructured cellular automata.

4.2.1 Original meshes & Locally refined meshes

It was supposed that we should get the same results from two sets of meshes: one is the original, and the other is the mesh with local refinement. Figure 2 shows the original mesh on a circular area, while Figure 3 gives the local refined meshes based on the Figure 4.

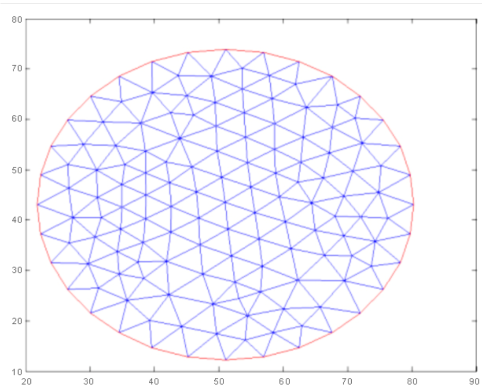

**Figure 2**. Original Meshes

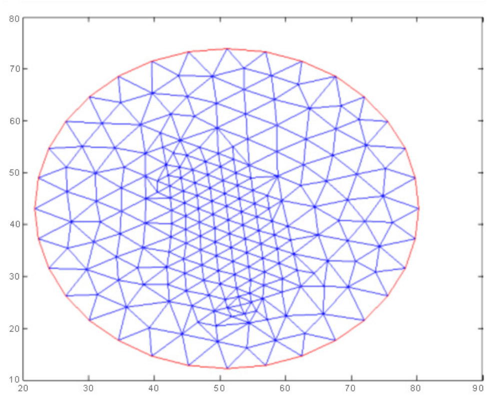

**Figure 3**. Locally refined Mesh

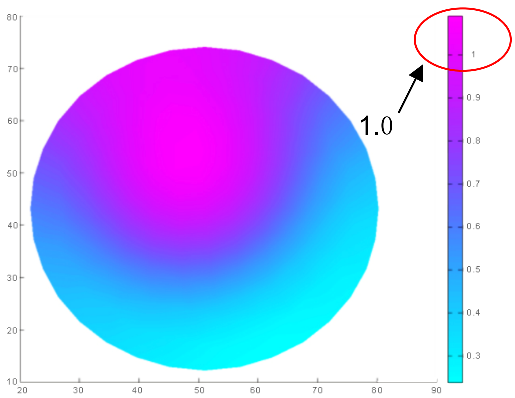


**Figure 4**. Diffusion on Original Meshes

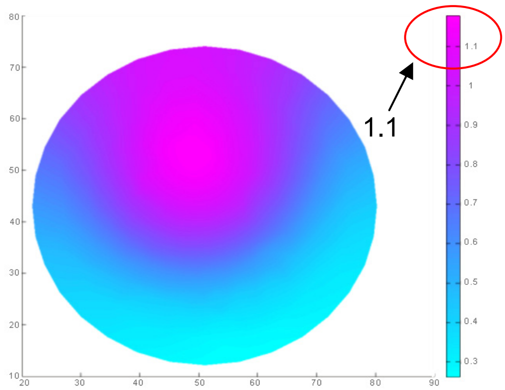


**Figure 5**. Diffusion on refined Meshes

In this case, after the local refinement, the $d_{min}$ equals 0.8605. **Error! Reference source not found.**ure 4 and Figure 5 are snapshots at 900 steps from the experiments. In these two experiments, $d_{min}$=0.8605 was adopted. The results show similar diffusion values (maximum concentrations 1.0 compared with 1.1) and alike diffusion patterns, which means under this rule and parameter, UCA modelling can be cell independent. After running several experiments, it was found that if the original meshes use the same $d_{min}$ as the locally refined meshes, the results of simulation from two sets of meshes are comparable. The diffusion patterns and concentration values are both similar, and the difference between them decreased with the time steps.

4.2.2 Rough meshes & Globally refined meshes

In this part, the experiments are executed separately on the rough mesh and global refined mesh.

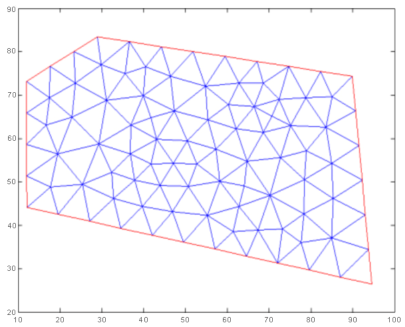

**Figure 6**. Rough Mesh

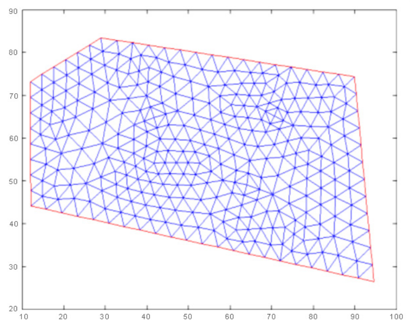

**Figure 7**. Globally refined Mesh

Figure 6 illustrates the rough mesh, while the mesh shown in Figure 7 is a globally refined mesh generated based on the rough mesh.

*Using separate* $d_{min}$

For these sets of meshes, we keep their own $d_{min}$ separately in the modelling. The $d_{min}$ which belongs to the rough meshes (Figure 6) equals 2.5851, while the $d_{min}$ of the fine mesh (Figure 7) is reduced to 1.066 after global refining. If we calculate the ratio between these two $d_{min}$ values, the ratio is around 2.4 times.

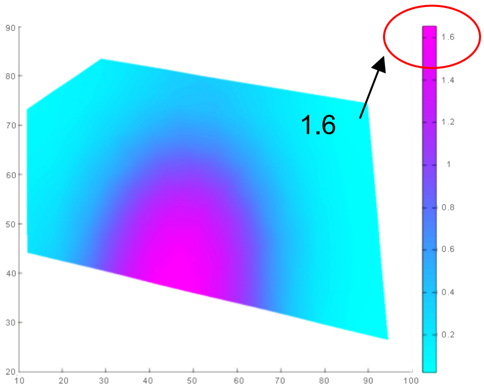


**Figure 8**. Rough Meshes in 250 steps

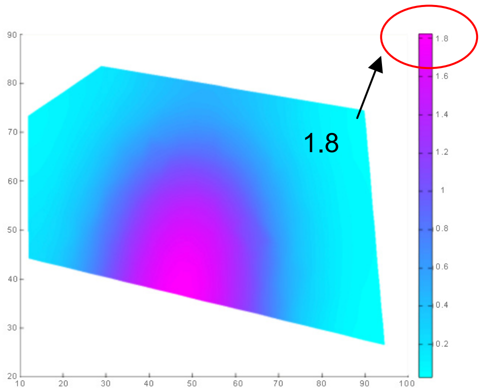


**Figure 9**. Refined Meshes in 600 steps

Running the models and making a snapshot after 250 steps (Figure 8) and a snapshot at 600 steps (Figure 9) separately, it can be seen that similar diffusion patterns and comparable concentration values appear. The proportion approximates the ratio value from $d_{min}$. For example, Figure 8 /Figure 9 = 600steps / 250steps= 2.4 (which was mentioned in last paragraph).

*Using same* $d_{min}$

In Figure 6 and Figure 7, we change the parameter to $d_{min}$=1.066, which is the minimum characteristic distance belonging to the globally refined mesh. With this parameter and executing the model for 800 steps, the results are shown in Figure 10 and Figure 11.

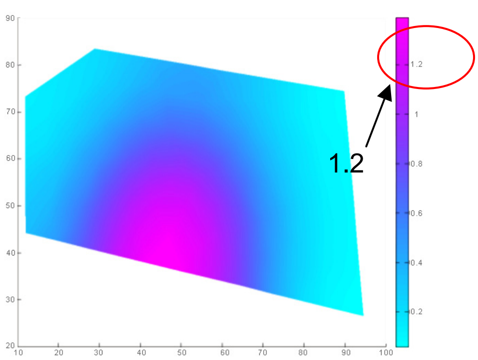


**Figure 10**. Rough Meshes at 800 steps

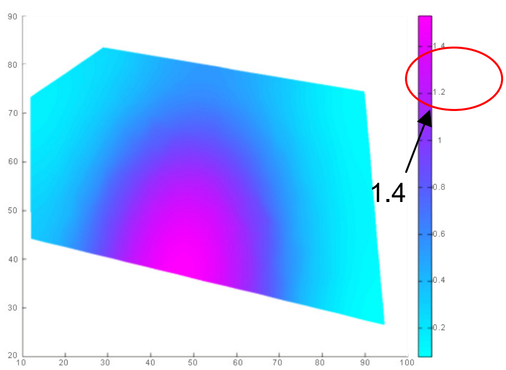


**Figure 11**. Refined Meshes at 800 steps

 

The results in Figure 10 and Figure 11 show similar diffusion patterns. From the graphs, it can be seen that using the same characteristic parameter, UCA modelling under different meshes leads to almost the same diffusion process.

## 5 DISCUSSION

Usually, when developing models one needs to understand the basic underlying processes which is why partial differential equations are commonly used to model conservation processes. But in some cases, partial differential equations may have limitations. In contrast, complex nonlinear systems can be modelled by CA with a good computing efficiency. This research gives some description of the computational theory of unstructured cellular automata, and a comparison is made between Partial Differential Equation and Unstructured Cellular Automata modelling.

Compared with PDE-based models, Cellular Automata has the advantage in that they can represent discrete entities directly and can reproduce emergent properties of behaviors with a large number of degrees of freedom. Another unique characteristic of CA-based modelling is that CA could generate dynamics patterns that are self-reproducing. It also should be mentioned that CA has universal parallel computing characteristics, which is powerful and has become an essential part in numerical computations.

The emphasis of this research is on deducing the transition rules for cellular automata modelling from the PDE equivalent using the finite difference method. The result shows that under certain rules, the CA evolution results could be compared with the PDE performance. Taking into consideration that UCA has varying neighbours in contrast with classical CA, the influence of cell size in UCA is analyzed in this paper by the means of Finite Volume Method. The characteristic parameter —min distance of UCA— is put forward. Followed by several numerical experiments which were validated on different kinds of meshes (Rough meshes & local refined meshes & Global refined meshes), the characteristic parameter (min distance) for UCA proved to be useful to eliminate effects from varying neighbours and the simulation results turned out to be grid-independent.

From simulation scenarios, it is proposed to use the characteristic parameter in identifying UCA transition rule. Sometimes the characteristic parameters have their own physical meanings, especially in the CA-based ecosystem modeling. In this case,he characteristic parameter $\mathrm{d_{min}}$ might be relevant to the spatial features of ecosystem (Chen, 2002; Chen, 2003; Ratze, 2007).

## 6 CONCLUSIONS

In this research, the minimum distance $d_{min}$ is adopted as a characteristic parameter in unstructured cellular automata modelling. The results show that in most cases, the performance of UCA is comparable even based on different sets of meshes. Generally speaking, the results obtained show similar concentration values and diffusion patterns at the same time step if the same $d_{min}$ was adopted. On the first set of meshes, we used the $d_{min}$ which belongs to the locally refined meshes, and in the case of the second type of meshes, the parameter $d_{min}$ was calculated from globally refined meshes. With the same parameter, the results from rough meshes and globally refined meshes are very similar. Meanwhile, if the $d_{min}$ from rough meshes and globally refined meshes are used separately, the results are still comparable but proportional to the time scale, which is related to the ratio of $d_{min}$.

This research explored the relationships between PDE-based modelling and Unstructured Cellular Automata. Numerical experiments were carried out, but additional simulations using measured data needs to be carried out as well to verify and compare the two approaches.

## REFERENCES

Bartlett, M. S. & Hiorns, R. W. (1973). Mathematical Theory of the Dynamics of Biological Populations. *Academic Press*, London, 225-347

Bennett, C. & Grinstein, G. (1985). Role of Irreversibility in Stabilizing Complex and Nonenergodic Behavior in Locally Interacting Discrete Systems. *Physical Review Letters*, 55(7), 657-660.

Chen, Q. W. (2004). Cellular Automata and Artificial Intelligencein Ecohydraulics Modelling. PhD, Delft University of Technology, the Netherlands.

Chen, Q. W. (2008). Cellular Automata Handbook of Ecological Modelling and Informatics: *WIT Press*, Southampton, UK, 283-306.

Chen, Q. W. & Mynett. A.E. (2003). Effects of Cell Size and Configuration in Cellular Automata Based Prey–Predator Modelling. *Simulation Modelling Practice and Theory*, 11(7-8), 609–625.

Chen, Q. W., Mynett. A.E. & Minns, A.W. (2002). Coupling of Scales in Finite State Cellular Automata with Applications to Ecohydraulics Modelling. *Hydroinformatics Conference*, Cardiff, UK, 500-506.

Chopard, B. & Droz, M. (1998). Cellular Automata Modelling of Physical Systems. *Cambridge University Press*, 407-433.

Chopard, B. & Droz, M. (1991). Cellular Automata Model for the Diffusion Equation. *Journal of Statistical Physics*, 64(3-4), 859-892.

Fathy, A. H. F. & Aghababa, A.B. (2013). *Cellular Learning Automata and Its Applications*, Emerging Applications of Cellular Automata, 6, 85-111.

Ganguly, N., Sikdar, B.K., Deutsch, A., Canright, G., Chaudhuri, P. (2003). A Survey on Cellular Automata. *Neurocomputing*, 58(3-4), 321-354.

Guinot, V. (2002). Modelling Using Stochastic, Finite State Cellular Automata Rule Inference from Continuum Models. *Applied Mathematical Modelling*, 26, 701-714.

Hu, R. C. & Ruan, X.G. (2003). Differential Equation and Cellular Automata Model. *Robotics Intelligent Systems and Signal Processing International Conference*. 1-2

Ostrov, D. N. & Rucker, R. (1996). Continuous-Valued Cellular Automata for Nonlinear Wave Equations. *Complex Systems*, 10, 91-119.

Ratze, C., Gillet, F., Muller, J.-P. & Stoffel, K. (2007). Simulation Modelling of Ecological Hierarchies in Constructive Dynamical Systems. *Ecological Complexity*, 4(1-2), 13-25.

Rorhman, D. H. & Zeleski, S. (1997). Latice-Gas Cellular Automata: Simple Model of Complex Hydrodynamics. *Cambridge University Press*, 599-632.

Rucker, R. (2003). Continuous-Valued Cellular Automata in Two Dimensions. In D. Griffeath, Moore, C. (Ed.), New Constructions in Cellular Automata, *Oxford University Press*, 167-186.

Wolfram, S. (1985). Twenty Problems in the Theory of Cellular Automata. *Physica Scripta*, T9, 170-183.

 

# A PIPELINE OIL LEAKAGE MODEL FOR OILFIELDS IN SHALLOW WATER

ZHIGANG LI(1), MEIRONG JIANG(2), JIANXING YU(3), KONGZHONG LIU (4), YING JIANG(5) & CHANGTAO WANG(6)

(1, 2, 5, 6) CNOOC Research Institute & Offshore Oil Engineering Co., Ltd., CNOOC, Beijing, China,
meirongjiang@live.cn
(1, 2, 3) State Key Laboratory of Hydraulic Engineering Simulation and Safety, Tianjin University, Tianjin, China,
yjx2000@tju.edu.cn
(4) CNOOC Limited (Shanghai), Shanghai, China,
liukzh@cnooc.com.cn

## ABSTRACT

Due to ship anchoring and operation, the oil leakage of the submarine pipeline has often occurred offshore. If oil spill can be predicted, it will provide reference for the accident treatment and promote the quick resolution of the leakage. Based on the pressure drop and liquid holdup formula, the process calculation of the pipeline was carried out by the Three-Fluid model for an oilfield in shallow water. Different leakage apertures were considered to analyze the influence on the leakage velocity, amount and the inlet pressure. Then, on account of the process result, a verified hydrodynamic model with the $k-\varepsilon$ turbulence equations was introduced to simulate a typical subsea pipeline leakage condition. Different water depths were considered to study the diffusing form and the arriving time to the surface. The lateral drifting distance and the diffusion range were also introduced to do the investigation quantitatively. The results show that, with the increase of the leakage aperture, the leakage amount increase obviously, but the decreasing amplitude of the leakage velocity and the inlet pressure are much smaller. The verified model can reflect the diffusion of the pipeline oil spill very well. With the increase of the water depth, the arriving time to the sea surface is increased significantly. But, for the lateral drifting distance and the diffusion range, different trends with the depth are appeared at different time instants. The oil leakage model can do preliminary calculation and analysis for the spill trajectory and the diffusion range. It clearly shows the valuable ability to predict the submarine oil leakage in the shallow water area. This quantitative analysis could help in clean-up activities.

**Keywords:** Oil leakage; submarine pipeline; shallow water; hydrodynamic model; water depth.

## 1 INTRODUCTION

In the coastal and offshore areas, oil leakage accidents of the submarine pipeline have often occurred due to ship anchoring and operation. If the pipeline oil spill can be simulated and predicted, it will provide reference for the accident treatment and the accurate predictions could promote the quick resolution of the oil spill accident.

In the recent 30 years, people's consciousness on the destructive influence of the oil leakage for the environment has been gradually enhanced. As to the modeling of the oil spill on the sea surface, large amounts of research have been done to evaluate the fate and transport of the oil. More than 50 models have been developed to predict the behavior and fate of the oil spill (Yapa et al., 1997; Wang, 2008). The correct forecast of the spilling trajectories and diffusion range can provide timely information for the handling of the oil spill accidents. However, relative to the large amounts of studies on the sea surface, the numerical work of the oil spill underwater is much less up to present.

Research on the prediction models for the subsea oil spill has been carried out from 1960s. Theoretical and experimental studies were made on two classes of buoyant jet problems (Fan, 1967). In general, the observed experimental jet forms agreed well with the calculated trajectories. Fannelop and Sjoen (1980) established the oil spill model for the oil well and the gas expansion was taken into account. But, it was only limited to the vertical oil spill and did not consider the effect of water flow. Bemporad (1994) simulated buoyant jet trajectory from the round orifice in stratified flow environment. Based on Lagrangian integral method, a relatively perfect oil spill model was established by Yapa et al. (1997) and Zheng and Yapa (1998). This model considered the diffusion and dissolution process of oil spill, but did not consider emulsifying process. For deep water blowouts, Johansen (2000) established a Lagrangian plume model, named DeepBlow. It was applied to multiphase discharges in the formation of water, oil and gas in a stratified water column with variable currents. A numerical simulation was built up by Reed et al. (2003) to estimate pipeline oil spill volumes, which was composed of a Release Module and a Near Field Module. On the basis of the Goncharov model, a numerical model was simulated about the spilled oil/gas from a single orifice under water and influence of different parameters were studied on the formation of oil/air bubbles and their floatation speed (Wang, 2005). Diffusion and drift of spilled oil for subsea pipeline were simulated based on the spill model of Yapa and Zheng and the hydrodynamic model of POM and FVCOM (Wang, 2008). Different operating pressure, current velocities and wave lengths were compared by FLUENT to forecast the trajectory of the spilled oil (Li et al., 2012). Effects of oil density, oil leaking rate, leaking size and water velocity on the oil spill process were examined with FLUENT (Zhu et al., 2014). Socolofsky et al. (2015) compared oil spill model predictions for a prototype subsea blowout with and without subsea injection of chemical dispersants in deep and shallow water, for high and low gas–oil ratio, and in weak to strong cross flows. A three-dimensional coupled model was employed by North et al. (2015) to evaluate the influence of initial droplet size and rates of biodegradation on the subsurface transport of oil droplets. It indicated that improvement in knowledge of droplet sizes and biodegradation processes is important for accurate prediction of subsurface oil spills. Socolofsky et al. (2015) introduced a new subsea oil and gas simulation suite, TAMOC, which including separate modules for particle and plume dynamics.

When the leakage of the submarine pipeline occurs under water, the characteristic and operation condition of the crude oil in the pipeline have a great influence on the diffusion of the oil spill, especially the characteristic of the internal fluid, the leakage amount and the leakage velocity which is the input variable for the simulation of the subsea oil spill and have a direct influence on the oil diffusion. To solve this problem well, there is a need to consider the hydrodynamic diffusion of the oil spill with the process calculation together. So far, however, the related research has been not found yet to the author's knowledge. Therefore, further work should be done in this aspect. This paper takes into account the hydrodynamic analysis and the process calculation to better deal with the problem of typical subsea oil spill. Oil diffusion in shallow waters could be predicted by this model and it would provide some references for the emergency maintenance operation of the pipeline oil spill.

For an oilfield in shallow waters, based on the pressure drop and liquid holdup formula, the process calculation of the pipeline was carried out by the Three-Fluid model. Different leakage apertures were considered to analyze the influence on the leakage velocity, amount and the inlet pressure. On the basis of the process results, a verified hydrodynamic model was introduced to simulate a typical subsea pipeline leakage condition. The $k-\varepsilon$ turbulence model is chosen to solve the Reynolds time-averaged Navier-Stokes equations. Different water depths are proposed to study the diffusing form and the arriving time to the surface. The lateral drifting distance and the diffusion range were also investigated quantitatively.

## 2 THE LEAKAGE MODEL

The oil leakage model for the submarine pipeline is shown in Figure 1. The dimensions of the calculating area are $L$ long ($x$ direction) and $H$ high ($y$ direction), and the water depth is $h$. The crude oil is spilled from the damaged aperture and vertically flows into the sea water with the initial velocity $u_{oil}$, where the width of the leakage aperture is $D$. The velocity of the water flow $u_{water}$ is parallel to the sea floor. The calculation area is consisted of the free surface, the inlet boundary at the left side, the outlet boundary at the right side, the wall and the leakage aperture at the bottom.

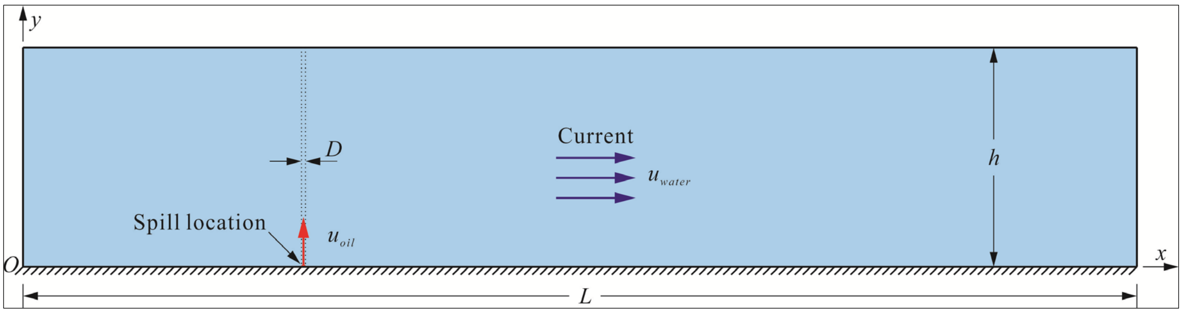


**Figure 1**. The sketch of the oil spill for the submarine pipeline.

The two-dimensional transient incompressible flow field of the oil spill is governed by the continuity equation and the Reynolds time-averaged Navier-Stokes equations.

The $k-\varepsilon$ turbulence is very suitable to provide superior performance for the free flow simulation involving the jet flow and the mixed flow. Therefore, the $k-\varepsilon$ turbulence model is chosen to solve the Reynolds time-averaged Navier-Stokes equations,

$k$ equation:

$$\frac{\partial(\rho k)}{\partial t}+\frac{\partial(\rho k u_i)}{\partial x_i}=\frac{\partial}{\partial x_j}\left[\left(\mu+\frac{\mu_t}{\sigma_k}\right)\frac{\partial k}{\partial x_j}\right]+G_k-\rho\varepsilon \quad [1]$$

 

$\varepsilon$ equation:

$$\frac{\partial(\rho\varepsilon)}{\partial t}+\frac{\partial(\rho\varepsilon u_i)}{\partial x_i}=\frac{\partial}{\partial x_j}\left[\left(\mu+\frac{\mu_t}{\sigma_\varepsilon}\right)\frac{\partial\varepsilon}{\partial x_j}\right]+\rho C_1 E\varepsilon-\rho C_2\frac{\varepsilon^2}{k+\sqrt{\nu\varepsilon}} \quad [2]$$

In which, $\mu$ and $\mu_t$ are coefficients of the fluid kinematic and turbulent viscosity, respectively. $k$ and $\varepsilon$ are the turbulent kinetic energy and its dissipation rate, and

$$\mu_t=\rho C_\mu\frac{k^2}{\varepsilon} \quad [3]$$

$$C_\mu=\frac{1}{A_0+A_s U^* k/\varepsilon} \quad [4]$$

$$C_1=\max\left(0.43,\frac{\eta}{\eta+5}\right) \quad [5]$$

$$\eta=\left(2E_{ij}\cdot E_{ij}\right)^{1/2}\frac{k}{\varepsilon} \quad [6]$$

$$E_{ij}=\frac{1}{2}\cdot\left(\frac{\partial u_i}{\partial x_j}+\frac{\partial u_j}{\partial x_i}\right) \quad [7]$$

Where,

$$\left.\begin{aligned}&A_0=4.0,\ A_s=\sqrt{6}\cos\phi\\&\phi=\frac{1}{3}\cos^{-1}\left(\sqrt{6}W\right),\ W=\frac{E_{ij}\cdot E_{jk}\cdot E_{kj}}{\left(E_{ij}\cdot E_{ij}\right)^{1/2}}\\&U^*=\sqrt{E_{ij}E_{ij}+\tilde{\Omega}_{ij}\tilde{\Omega}_{ij}}\\&\tilde{\Omega}_{ij}=\Omega_{ij}-2\varepsilon_{ijk}\omega_k,\ \Omega_{ij}=\bar{\Omega}_{ij}-\varepsilon_{ijk}\omega_k\end{aligned}\right\} \quad [8]$$

In the equation, $\bar{\Omega}_{ij}$ is the time-averaged rotation velocity tensor which is observed in the reference system with the angular velocity $\omega_k$. Here, the constant $C_2=1.9,\ \sigma_k=1.0,\ \sigma_\varepsilon=1.2$ (Wang, 2004).

The Volume of Fluid method (VOF method) is employed to track the free interface of the multiphase flow (Li et al., 2016). The control equations are discretized by the Finite Volume Method for the flow field and the iterative calculation for the pressure-velocity couple is carried out by the PISO algorithm. The separate solver based on the pressure is selected to do numerical computation. The more detailed information can be found in Li et al. (2016) and Jiang et al. (2016).

Two kinds of reliable experimental (Fan, 1967) and numerical data (Zheng and Yapa, 1998) are introduced to verify the present turbulence model, which is shown in Figure 2. As can be seen from the figure, the moving trajectory of the main body for the oil spill agrees very well with the experimental and numerical data. It is proved that the established model is reliable and can be adopted as the best practice guideline to simulate the oil spill trajectories for the subsea pipeline accurately and effectively.

## 3 NUMERICAL RESULTS

An oilfield from East Sea, named ES3-2, is chosen to do the numerical study. This oilfield is located in the coastal area with an average depth 20 m, which is a typical environmental condition of the shallow water. The selection of various parameters is mainly referred to the overall exploitation program of ES3-2.

 

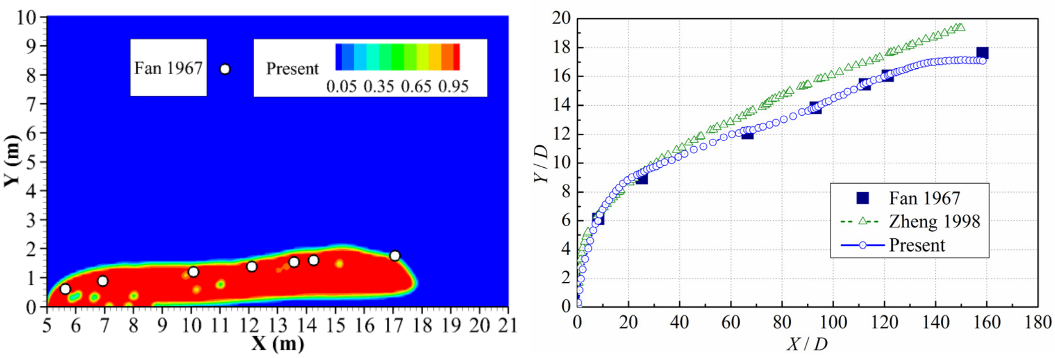


(a) $Fr_0 = 20$ , $R_0 = 4$

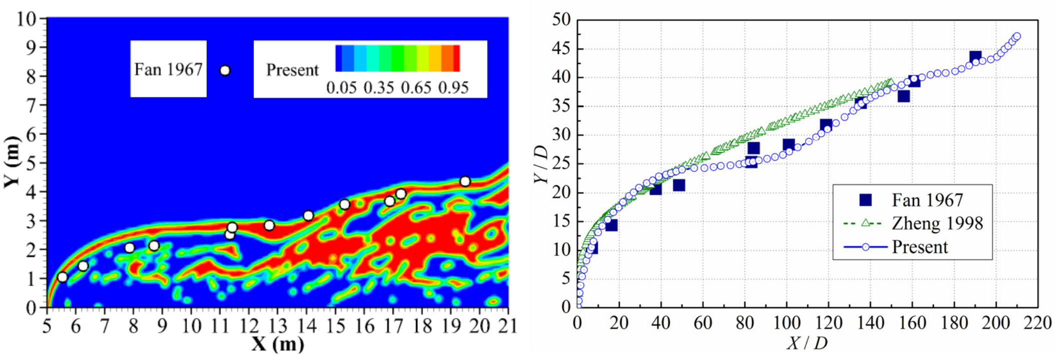


(b) $Fr_0 = 20$ , $R_0 = 8$

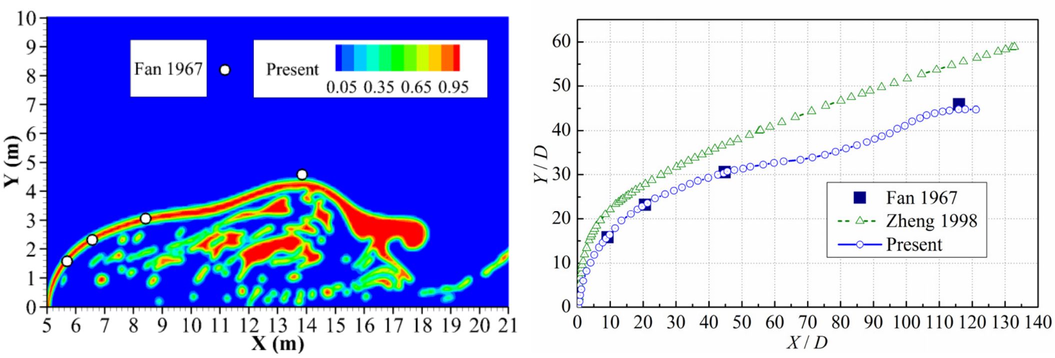


(c) $Fr_0 = 18$ , $R_0 = 12$

**Figure 2.** Comparison of the trajectories between the present model and the experimental and numerical data ($Fr_0$ is the spilling oil jet densimetric froude number, and $R_0$ is the ratio between the magnitudes of the initial oil jet velocity and cross flow velocity).

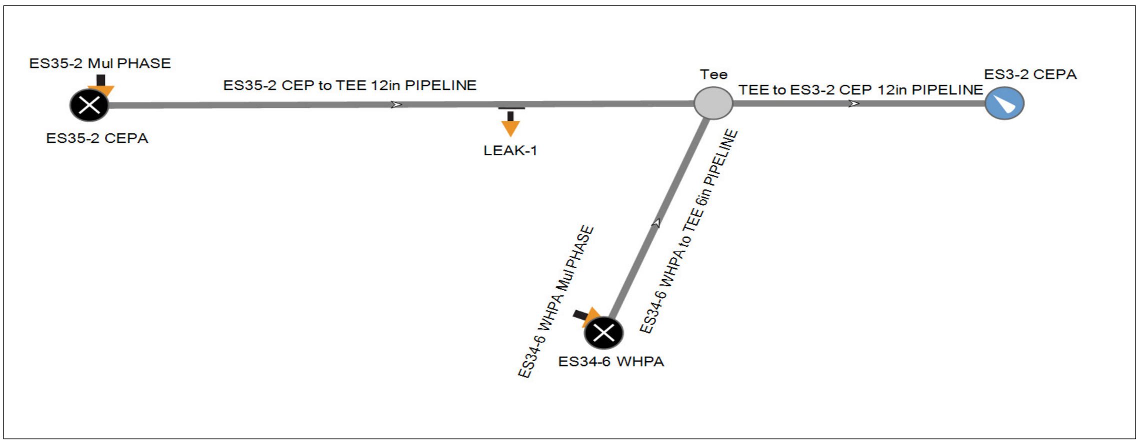


**Figure 3.** The process flow diagram of ES 3-2 oilfield.

  / ISSN 1562-6865 (Online) - ISSN 1063-7710 (Print)

3.1 Process calculation

Based on the pressure drop calculation formula and the liquid holdup formula of the Three-Fluid model, the process simulation is conducted with OLGA. OLGA is currently the world's leading dynamic multiphase flow simulator, which can simulate the flow state of oil, gas and water in wells, pipelines and processing equipment. Its computation result is recognized by the world's major oil companies, which has been widely used in the simulations of feasibility study, engineering design and operation. Here through the transient multiphase flow simulation of the submarine pipeline, different leakage apertures are proposed to study the influence on the leakage velocity, amount and the inlet pressure.

**Table 1.** The leakage aperture and the area of aperture.

| **No.** | **The leakage aperture** $D$ **(mm)** | **The area of aperture** $S$ **(m$^2$)** |
|---|---|---|
| 1 | 7.5 | 4.418E-05 |
| 2 | 10.0 | 7.854E-05 |
| 3 | 12.5 | 1.227E-04 |
| 4 | 15.0 | 1.767E-04 |
| 5 | 20.0 | 3.142E-04 |

The process flow diagram of the oilfield is shown in Figure 3. The crude oil, which contained oil, gas and water, is delivered from ES35-2 CEPA and ES34-6 WHPA platform to ES3-2 CEPA platform by a 12 in pipeline. The distance is 15.3 km from the leak point to ES35-2 CEPA platform. The different leak aperture and the area of aperture are present in Table 1.

3.1.1 The leakage velocity

Figure 4 presents the influence of different leakage apertures on the leakage velocity. The leakage velocity of the oil, gas and water at the leakage point are provided below.

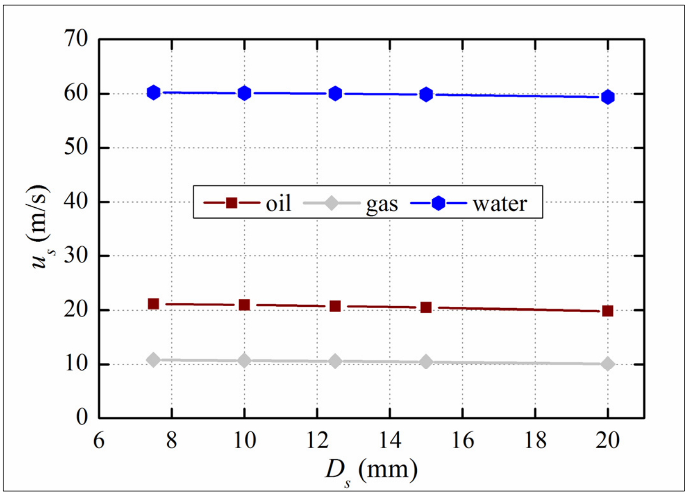


**Figure 4.** The influence of different leakage apertures on the leakage velocity.

As can be seen from the figure, with the increase of the leakage aperture gradually, the leakage velocity of the oil, gas and water decrease slightly. They are relatively stable overall. The leakage velocity of the water is greater than that of the oil and the gas, where the leakage velocity of the water is about three and six times larger than that of the oil and the gas, respectively.

3.1.2 The leakage amount

Figure 5 shows the influence of different leakage apertures on the amount of leakage. The leakage amount of the oil, gas and water at the leakage point are presented in the figure where d in the unit m$^3$/d means day.

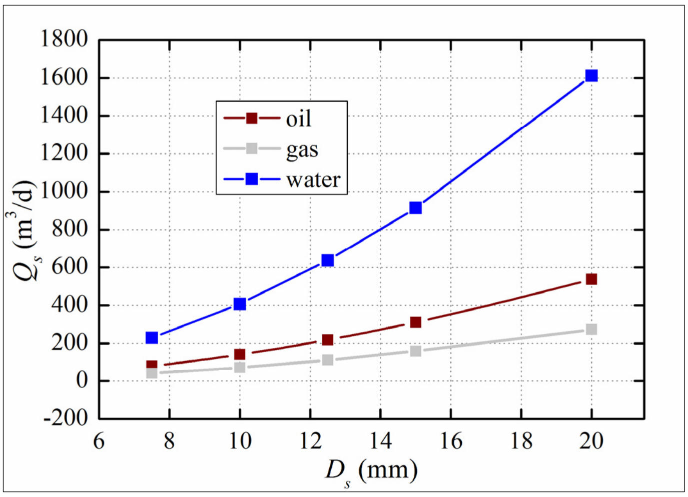


**Figure 5.** The influence of different leakage apertures on the amount of leakage.

Contrary to the overall stable of the leakage velocity, the leakage amount $Q_s$ of the oil, gas and water increase greatly with the increase of the leak aperture. This can be attributed to the invariable outlet pressure and the almost constant leakage velocity and the leakage aperture becomes the primary critical influence on the amount of leakage. As a consequence, the amount grows almost quadratically to the aperture. For the comparison among the oil, gas and water, the same rule is observed between the leakage velocity and the leakage amount; the leakage amount of the water is larger than the other two. Meanwhile, it is can be found that the slope of growth curve for the leakage of water is larger than that of oil and gas. Thus, the leakage increment for the water is greater than the other two.

3.1.3 The inlet pressure

The influence of different leakage apertures on the inlet pressure are presented in Figure 6. The variation of the inlet pressure for the pipeline at the two platforms, ES35-2 CEPA and ES34-6 WHPA, are given in the figure.

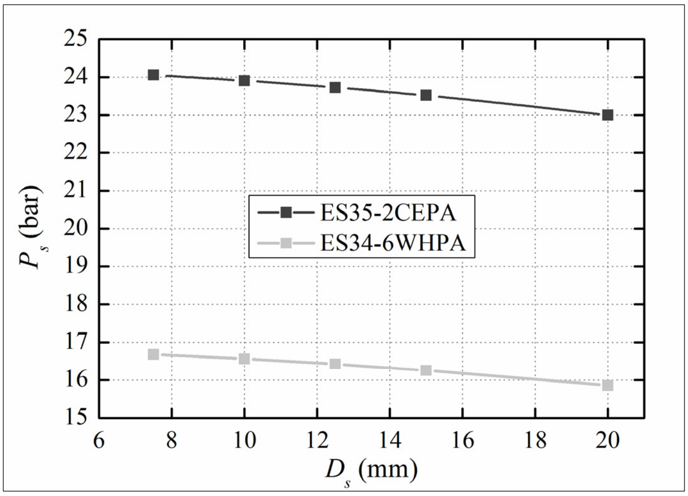


**Figure 6**. The influence of different leakage apertures on the inlet pressure.

As can be seen from Figure 6, with the increase of the leakage aperture, the inlet pressure of the two pipelines decreases gradually. The inlet pressure at ES35-2 CEPA platform is greater than that at the ES34-6 WHPA platform at each leakage aperture.

3.2 Oil spill simulation

On the base of the process results, proper parameters are selected and the verified hydrodynamic model is introduced to simulate a typical subsea pipeline leakage condition. The variation of the diffusing form was described under different water depths. The arriving time to the surface, lateral drifting distance and the diffusion range were investigated quantitatively with the depths.

 

3.2.1 The diffusing form

Figure 7 presents the trajectory of the spilled oil under different environmental water depths. From top to bottom, the depths are 10 m, 20 m, 30 m, 40 m and 50 m, respectively.

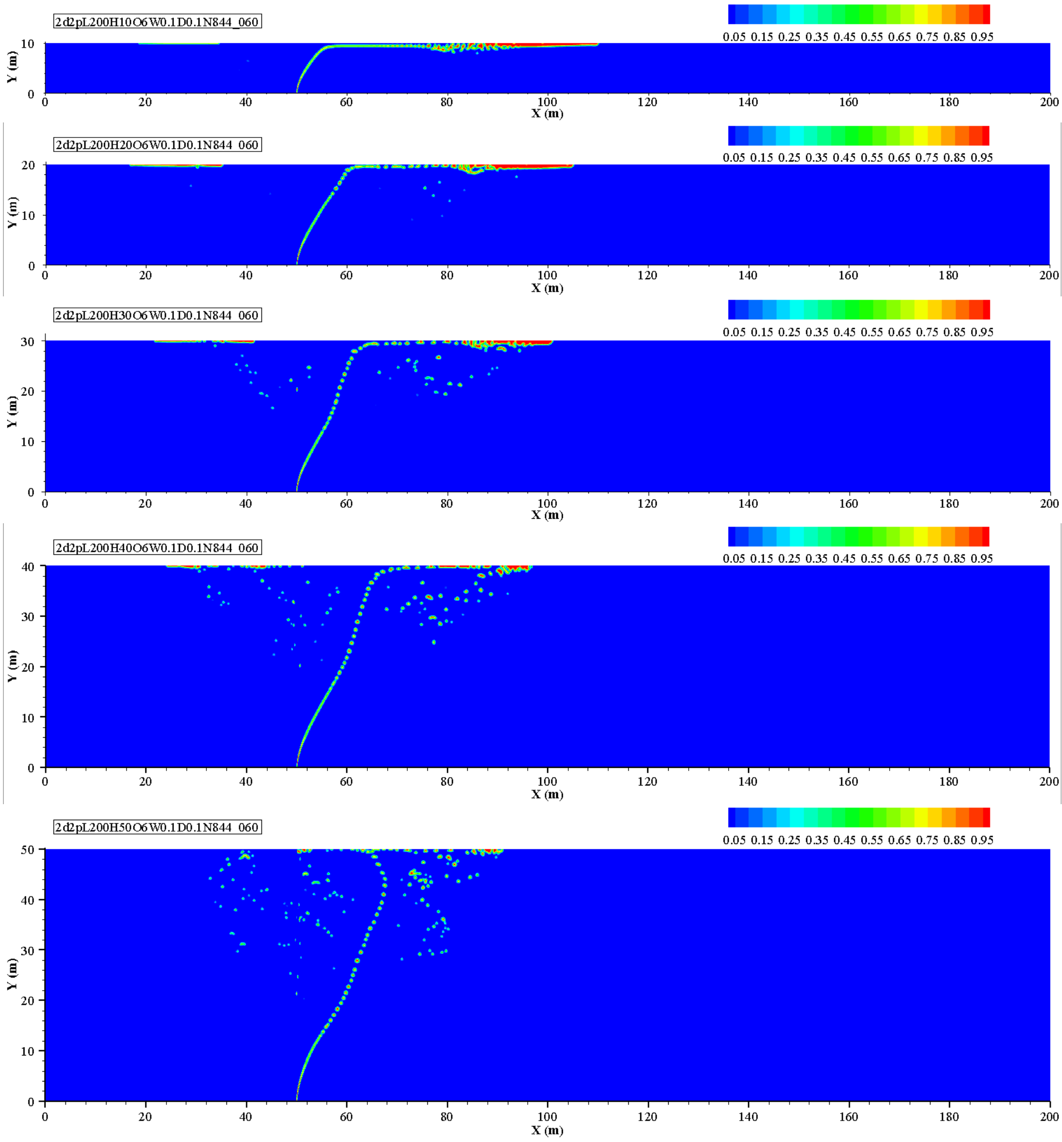


**Figure 7.** The trajectory of the spilled oil under different environmental water depths.

As shown in the figure, the spread trajectories and forms of the spilled oil are very similar under different water depths. At this instant, the form of the spilled oil has been relatively stable under water. Due to the transverse flow of the current, the main body of the spilled oil spreads to the right side and diffuses upward. The spilled oil under different water depths have risen to the sea surface at this point. Most of the spilled oil on the surface drifts to the right side and a small amount of oil spreads to the left side under the action of the free drift. Continuous oil blocks are formed and extend downstream near the sea bed under water. After spreading to a certain height from the sea bed, the spilled oil is mainly in the form of discontinuous oil blocks and oil droplets. Through preliminary comparison, it is found that, the shallower the water depth is, the larger the lateral drift distance on the surface is. And so is the diffusion range.

Moreover, although the same numerical model is used, the diffusing form of the spilled oil in Figure 7 is not the same as that in Figure 2. This is due to the difference of the selected oil and leakage parameter between the two conditions. Figure 2 is to verify the turbulence model with the experimental data, so its chosen oil and leakage parameter have been designated in the previous model test. Compared to Figure 2, Figure 7 is for a sensitive study based on the specific oil filed where the selected parameter is from ES35-2 CEPA platform. Different parameters selected lead to different diffusing forms. Therefore, the trajectory of Figure 7 is distinct from that of Figure 2.

3.2.2 The arriving time to the surface

Figure 8 shows the arriving time to the sea surface of spilled oil $T_a$ under different environmental water depths. The blue scatters are the arriving time to the surface and the red line is the linear fitting result.

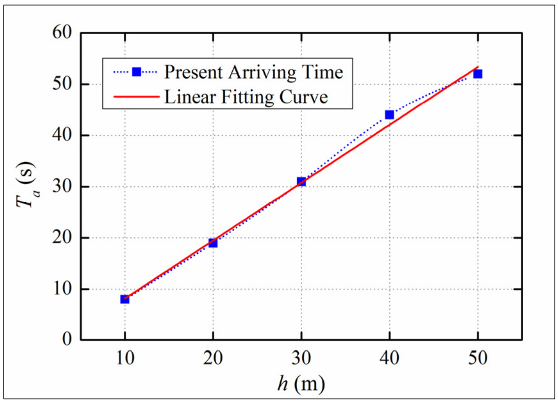


**Figure 8.** The arriving time to the sea surface of spilled oil under different environmental water depths and the linear fitting result.

As shown in the figure, the arriving time to the sea surface increases gradually with the increase of the environmental water depth. In the currently selected five different water depths, the arriving time to the sea surface is in the range of 8 s~52 s. Among the five arriving times, the largest arriving time happens at the most deep depth 50 m which is 52 seconds and the smallest one happens at the most shallow depth 10 m which is 8 seconds. The deviation between the two is 44 seconds which is 84.6% compared to the arriving time at the depth 50 m. The overall trend is close to a linear distribution (The goodness of fit Adj. R-square is 99.39% and the fitting formula is $y = -3.1 + 1.13x$ ).

3.2.3 The lateral drifting distance

Figure 9 shows the comparison of the lateral drifting distance under different water depths. In the figure, $h/D$ , $L_{du}/D$ and $L_{ds}/D$ are dimensionless water depth, lateral drifting distance of the spilled oil under water and on the surface, respectively. As can be seen from the diagram, for the lateral drifting distance, with the increase of the water depth, different trends are appeared at the two different time instants $t$ = 60 s and $t$ = 120 s.

At the time instant $t$ = 60 s, for the different water depths, the lateral drifting distance under water are relatively close to each other (The minimum difference is only 0.4%, and the maximum difference is 19.0%). While the lateral drifting distance on the surface decrease gradually with the increase of the water depth, where the maximum deviation is 31.6%. This is due to the same leakage velocity that results in the same leakage rate in the same spilled time under different depths. Under the transverse current, their lateral spreading velocities are also basically the same. Therefore, the lateral drifting distance are closer under different depths. However, the deeper the depth is, the longer the time of the spilled oil spreading to the surface is. When the overall time is the same, the deeper the depth is, the less the amount of leakage on the surface is, and also the shorter the time of the oil drifting laterally on the sea. As a result, the lateral drifting distance of the spilled oil shows the general trend of decrease with the increase of the water depths.

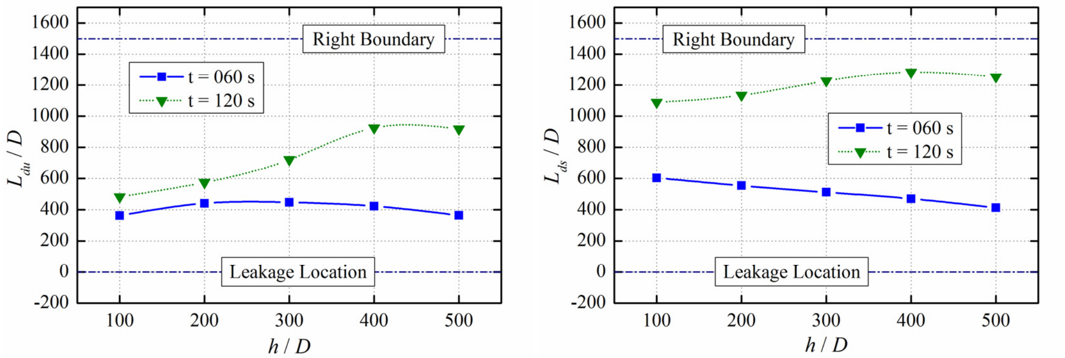


(a) Under water (b) On the surface

**Figure 9.** The lateral drifting distance of the spilled oil under different environmental water depths.

 

When $t$ = 120 s, under the water, the deeper the depth is, the longer the time of the spilled oil spreading under water is; and the accumulated amount of the oil is more and more under water. At the same time, the amount of the spilled oil drifting laterally under water is also increased. As a consequence, the overall trend of the lateral drifting distance of the spilled oil under water increases gradually with the increase of the water depth, where the largest deviation of the distance is 47.9%. While for the spilled oil on the surface at this instant, because the spilled time is relatively long and the oil spill approaches saturation, the sensitivity of the water depth to the spilled oil is reduced. Part of spilled oil propagating horizontally under water before is also spread vertically from under-water to the surface now. Therefore, the lateral drifting distances on the surface are relatively close under different water depth. At this instant ($t$ = 120 s), the minimum difference of the distance between water depths is only 2.1% and the biggest difference is also only 15.1%.

At the same water depth and the same time instant, the lateral drifting distances on the surface are always greater than that under water. It can be concluded that the spilled oil spreads faster on the surface than it diffuses under water.

3.2.4 The diffusion range

Figure 10 shows the surface diffusion range of the spilled oil under different environmental water depths. In the figure, $h/D$ and $A_d/D$ are the dimensionless water depth and diffusion range on the surface. As seen from the figure, the variation trend of the diffusion range and the lateral drifting distance on the surface are basically the same. For the diffusion range, with the increase of the water depth, different trends are appeared at the two different time instants $t$ = 60 s and $t$ = 120 s.

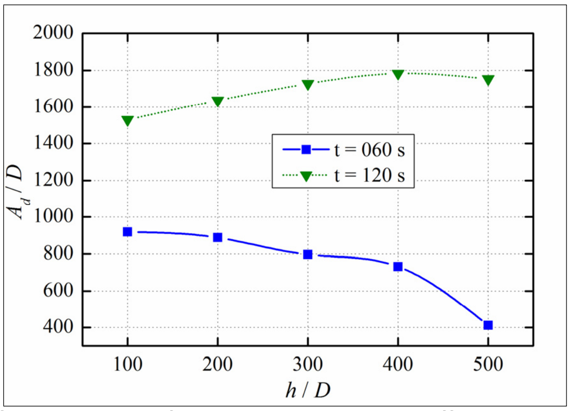


**Figure 10**. The surface diffusion range of the spilled oil under different environmental water depths.

When $t$ = 60 s, the diffusion range decreases with the increase of the water depth. This can be attributed to the same leakage velocity that results in the same leakage rate in the same spilled time under different depths. The deeper the depth is, the longer the time of the spilled oil spreading to the surface is. When the overall time is the same, the deeper the depth is, the less the amount of leakage on the surface is, and also the shorter the time of the oil drifting laterally on the sea. As a result, the diffusion range of the spilled oil decreases with the increase of the water depths.

While at the instant $t$ = 120 s, because the spilled time is relatively long and the oil spill approaches saturation, the sensitivity of the water depth to the spilled oil is reduced. Part of spilled oil propagating horizontally under water before is also spread vertically from under-water to the surface now. Therefore, the diffusion ranges on the surface are relatively close under different water depths. At this instant ($t$ = 120 s), the minimum difference of the diffusion range between water depths is only 1.5% and the biggest difference is also only 14.2%.

## 4 CONCLUSIONS

A Three-Fluid model was adopted to do the process calculation of an oilfield in shallow water. Five different leakage apertures were considered for the submarine pipeline, and the influence on the leakage velocity, amount and the inlet pressure was analyzed. Then, based on the process results, a verified hydrodynamic model with the $k-\varepsilon$ turbulence equations was introduced to simulate a typical subsea pipeline leakage condition. The diffusing forms were described under different water depths. The arriving time to the surface, lateral drifting distance and the diffusion range were investigated quantitatively.

With the increase of the leakage aperture, the leakage amount increased obviously, but the decreasing amplitude of the leakage velocity and the inlet pressure were much smaller. The verified model can reflect the diffusion and spread of the pipeline oil spill very well. With the increase of the water depth, the arriving time to the sea surface is increased significantly. The overall trend is close to a linear distribution. But for the lateral drifting distance and the diffusion range, different trends with the depth appeared at different time instants.

When $t$ = 60 s, the diffusion range decreased with the increase of the water depth; While at $t$ = 120 s, the diffusion ranges were relatively close under different water depths.

The oil spill model can quantitatively consider the oil spill under different leakage, environmental and physical conditions. It can do preliminary calculation and analysis for the prediction of the spill trajectory and the diffusion range. The presented model clearly shows the valuable ability to predict the submarine oil spill in the shallow water area, especially for the oilfield development project in Bohai and East Sea. This quantitative analysis could help in clean-up activities.

## ACKNOWLEDGEMENTS

The authors acknowledge the valuable comments of the reviewers and the editor. This work was financially supported by National Natural Science Foundation of China (51609168), Open Fund of State Key Laboratory of Coastal and Offshore Engineering (LP1608), National Key Basic Research Program of China (2014CB046804) and CNOOC Limited (Shanghai) (C-0816133).

## REFERENCES

Bemporad, G.A. (1994). Simulation of Round Buoyant Jet in Stratified Flowing Environment. *Journal of Hydraulic Engineering*, 120, 529-543.

Fan, L.N. (1967). *Turbulent Buoyant Jets into Stratified or Flowing Ambient Fluids,* Pasadena, Calif.: W.M. Keck Laboratory for Hydraulics and Water Resources, California Institute of Technology, Rep. KH-R-18.

Fannelop, T.K. & Sjoen, K. (1980). Hydrodynamics of Underwater Blowouts. *Norwegian Maritime Research*, 4, 17-33.

Jiang, M.R., Li, Z.G., Yu, J.X., Yin, H.J. & Jiang, Y. (2016). A Comparative Study of Different Grid Models for an Oil Spill Under Water. *Proceeding of the 35th International Conference on Ocean, Offshore and Arctic Engineering*, 2016 June 19-24, Busan, South Korea: ASME, 25.

Johansen, Ø. (2000). DeepBlow–A Lagrangian Plume Model for Deep Water Blowouts. *Spill Science & Technology Bulletin*, 6(2), 103-111.

Li, Z.G., Jiang, M.R. & Yu, J.X. (2016). Numerical Simulation on the Oil Spill for the Submarine Pipeline based on VOF Method. *The Ocean Engineering*, 34(6), 101-113.

North, E.W., Adams, E.E., Thessen, A.E., Schlag, Z., He, R.Y., Socolofsky, S.A., Masutani, S.M. & Peckham, S.D. (2015). The Influence of Droplet Size and Biodegradation on the Transport of Subsurface Oil Droplets during the Deepwater Horizon Spill: A Model Sensitivity Study. *Environmental Research Letters*, 10(2), 1-13.

Reed, M., Hetland, B., Emilsen, M.H. & Buffington, S. (2003). Numerical Model for Estimation of Pipeline Oil Spill Volumes. *Environmental Modelling & Software*, 21(2), 178-189.

Socolofsky, S.A., Adams, E.E., Boufadel, M.C., Aman, Z.M., Johansen, Ø., Konkel, W.J., Lindo, D., Madsen, M.N., North, E.W., Paris, C.B., Rasmussen, D., Reed, M., Rønningen, P., Sim, L.H., Uhrenholdt, T., Anderson, K.G., Cooperl, C. & Nedwed, T.J. (2015). Intercomparison of Oil Spill Prediction Models for Accidental Blowout Scenarios with and Without Subsea Chemical Dispersant Injection. *Marine Pollution Bulletin*, 96(1-2), 110-126.

Socolofsky, S.A., Dissanayake, A.L., Jun, I., Gros, J., Arey, J.S. & Reddy, C.M. (2015). Texas A&M Oilspill Calculator (TAMOC): Modeling Suite for Subsea Spills. *Proceeding of the 38th AMOP Technical Seminar on Environmental Contamination and Response*, Vancouver, British Columbia, Canada, 2-4.

Wang, F.J. (2004) Computational Fluid Dynamics Analysis: Theory and Application of CFD Software. *Tsinghua University Press*, Beijing, 26-28, 39-44.

Wang, J. (2006). The Study of the Spread and Diffusion Process of Oil Spilled from Seabed Pipeline. *Dalian: Dalian University of Technology.*

Wang, S.D. (2008). Study on the Forecast Models for Oil Spills in Seas based on Lagrange Tracking. *Dalian: Dalian University of Technology*.

Yapa, P.D. & Zheng, L. (1997). Simulation of Oil Spills from Underwater Accidents I: Model Development. *Journal of Hydraulic Research*, 35(5), 673-687.

Zheng, L. & Yapa, P.D. (1998). Simulation of Oil Spills from Underwater Accidents II: Model Verification. *Journal of Hydraulic Research*, 36(1), 117-134.

Zhu, H.J., Lin, P.Z. & Pan, Q. (2014). A CFD (Computational Fluid Dynamic) Simulation for Oil Leakage from Damaged Submarine Pipeline. *Energy*, 64, 887-899.

 